Predictive Design and Fabrication of Complex Micro and Nano Patterns via Wrinkling for Scalable and Affordable Manufacturing

by

Sourabh Kumar Saha

M. Tech., Mechanical Engineering
B. Tech., Mechanical Engineering
Indian Institute of Technology Kanpur, 2008

Submitted to the Department of Mechanical Engineering
in Partial Fulfillment of the Requirements for the Degree of

Doctor of Philosophy in Mechanical Engineering

at the

MASSACHUSETTS INSTITUTE OF TECHNOLOGY

September 2014

Signature of Author……………………………………………………………………………
Department of Mechanical Engineering
August 29, 2014

Certified by……………………………………………………………………………………
Martin L. Culpepper
Professor of Mechanical Engineering
Thesis Supervisor

Accepted by……..………………………………………………………………………………
David E. Hardt
Professor of Mechanical Engineering
Graduate Officer

Predictive Design and Fabrication of Complex Micro and Nano Patterns via Wrinkling for Scalable and Affordable Manufacturing

by

Sourabh Kumar Saha

Submitted to the Department of Mechanical Engineering
on August 29, 2014 in Partial Fulfillment of the
Requirements for the Degree of Doctor of Philosophy in
Mechanical Engineering

ABSTRACT

There is a demonstrated need for scalable and affordable manufacturing of complex micro and nano scale structures for applications such as fluidics-based medical diagnostics and photonics-based sensing. Although high-rate patterning of these structures is feasible via template/stamp based processes, scalability and affordability are often limited by expensive and slow template fabrication processes. The purpose of this work was to develop a wrinkling-based manufacturing process that eliminates the need for an expensive and slow template fabrication step.

Wrinkling of thin films is a low-cost buckling-driven patterning process that provides an alternate route to manufacturing scale-up. However, this process is currently of limited practical import because predictive design is restricted to a small set of simple/elementary patterns. In this work, predictive models, tools, and techniques were developed to enable the design and fabrication of a variety of complex wrinkled patterns.

The shape and size of wrinkled patterns is determined by the interaction among geometry, material properties, and loading. Complexity in wrinkle patterns often arises due to uncontrolled/undesirable non-uniformities in these process parameters. Due to the confounding effect of simultaneously acting non-uniformities, it is difficult to link wrinkle shape/size to process parameters for such systems. To solve this problem, experimental and computational tools were developed to (i) individually tune/control the non-uniformities in these parameters and (ii) probe the effect of these parameters on the wrinkled pattern. The data generated from these tools was then used to link process parameters to pattern complexity.

Contributions were made in the following specific areas:

(1) Tunable hierarchical wrinkled patterns via geometric pre-patterning

Although complex hierarchical wrinkled patterns have been fabricated via geometric pre-patterning in the past, predictive design of such patterns is not feasible. This is primarily because of lack of appropriate process models that can accurately capture the physical effect of pre-patterns on the wrinkle generation process. Herein, an analytical model was developed and verified to predict the hierarchical patterns that arise due to geometric non-uniformity. This model elucidates and captures the fundamental energetic response of the system to pre-patterns that distinguishes a pre-patterned system from a flat non-patterned system. The ability to capture this essential physics provides valuable insight into the process that is not available via empirical models that are based on a limited data set. This insight enables one to (i) explore the full design space and identify optimal operating regions, (ii) design and fabricate tunable wrinkled patterns that can be deterministically switched across hierarchical and non-hierarchical states and (iii) explain and predict patterns that are theoretically feasible yet practically inaccessible.

(2) Period doubling via high compressive strains

Although period doubling at high compressive strains has been demonstrated in the past, models that accurately predict the onset of period doubling are not available. This is due to the inability of existing models to capture the nonlinear stress versus strain material response as the physical basis for period doubling. For example, existing models erroneously assume that the onset of period doubling is independent of stiffness moduli. Herein, models driven by finite element analysis were developed to accurately link the onset of period doubling to nonlinearities that arise during large deformations. These models enable one to accurately separate the effect of individual process parameters on the onset of period doubling. This enables one to extract valuable process-relevant information from the observation of the period doubling phenomenon that is otherwise not available.

(3) Attractors and repellers as localized material defects for curved wrinkles

Curved wrinkles have been demonstrated in the past during equibiaxial compression of non-uniform materials. However, predictive design of target patterns via curved wrinkles is not feasible at present due to the lack of simple yet effective design rules. Generation of such design rules is hindered by the confounding effect of biaxial compression and localized material non-uniformities. Herein, an elegant design rule for in-plane bending of wrinkles has been generated for the case of uniaxial compression. Based on this, the concept of attractors and repellers as distinct localized material defects has been proposed and experimentally verified. Attractors are relatively compliant defects that pull wrinkles toward them; whereas repellers are relatively stiffer defects that push wrinkles away. These defects may be used as the building blocks to locally alter the in-plane orientation of otherwise uniformly aligned wrinkles during uniaxial compression.

The set of predictive models generated in this work would enable a designer to perform inverse pattern design of complex wrinkled structures, i.e., to select the appropriate set of process parameters that are required to fabricate the desired pattern. By replacing other expensive processes for complex patterning, this would reduce the time and cost of manufacturing a variety of functional micro and nano scale patterns by a factor of ~10 for low-volume applications and by ~10% for high-volume applications.

Thesis Supervisor: Martin L. Culpepper
Title: Professor of Mechanical Engineering

Acknowledgements

When I first started my PhD, I had made a promise to myself to ‘be myself’ and chase my own dreams. I’m very grateful to have been part of the MIT community that has helped me keep that promise. Being part of this community has given me the freedom to choose my own path and at the same time provided me with abundant resources, support, and help to walk that path. I cannot think of any other place that would have made the journey of the past several years as thoroughly enjoyable as this one was.

A major part of my rewarding PhD experience has been shaped by the presence of my thesis advisor Prof. Martin Culpepper. Marty has not just been a thesis advisor but also an excellent mentor to me. I still distinctly remember the first question that he ever asked me, “What do you want to do with your life?” Over the years, this question has formed the basis for a very personalized learning experience that was custom-designed by Marty for me. I’m grateful to have him as a mentor, teacher, and advisor.

I would also like to thank my thesis committee members Prof. Brian Wardle and Prof. David Hardt for their constant feedback and guidance throughout the thesis work. Although I always had a destination for my thesis in mind, the path was seldom clear and the journey often resembled walking through thick early morning fog. Their suggestions and comments were instrumental in making sense of such an environment.

I’m also grateful for the following sources of funding during the course of my PhD: Pappalardo Graduate Fellowship, Mechanical Engineering MIT; Martin Family Society of Fellows for Sustainability, MIT; and National Science Foundation Grant No. 0914790, “Center for Affordable Nanoengineering of Polymeric Biomedical Devices (CANPBD)”.

Also, I’m grateful to my friends and colleagues in the Precision Compliant Systems Lab for their constant support, help, and encouragement. I have learned a lot from working with them all. Specifically, I would like thank Bob (Robert Panas), Mike (Michael Cullinan), and Chris (Christopher DiBiasio) for helping shape key ideas of my research. Special thanks to Nadia Cheng and Maria Telleria for quickly and efficiently introducing me to life at PCSL, MIT, Boston, and the US during my first semester here.

To my friends outside MIT, I’m greatly indebted for being there for me during times of need. Specifically, I’m grateful to Amith Somanath for being a naturally giving person, Puneet Kumar for being the friend that he is, and Prakash Govindan for the countless discussions on life.

Finally, I’m grateful to my parents for their unconditional love and support.

CONTENTS

List of figures

List of tables

Chapter 1

Introduction

1.1 Purpose of thesis

1.1.1 Specific goals

The purpose of this work is to develop an affordable high-rate micro and nano scale manufacturing process based on wrinkling that eliminates the need for an expensive/slow template fabrication step. Currently, template based replication processes are necessary for achieving high rates because a majority of the template-free processes are serial processes. Although these serial processes are highly flexible and have a high resolution, they are too slow and expensive for large volume production [1]. Thus, as a compromise between rate, cost, and flexibility, one is forced to first fabricate a template using these serial techniques and then replicate the pattern for high rate processing.

An alternate low-cost and high-rate template-free scheme may be achieved via parallel processes such as those based on self-assembly and self-organization. Wrinkling of thin films is one such parallel process. However, this approach to manufacturing is currently of limited use because predictive design and fabrication of wrinkled patterns is limited to a small set of elementary geometries. The goal of this work is to develop this alternate scheme by improving the geometric flexibility of the wrinkling-based parallel template-free process. Specifically, the goals of this work are to develop models, tools, and techniques that enable the predictive design and fabrication of high-quality complex tunable patterns via wrinkling.

The shape and size of wrinkled patterns is determined by the interaction among geometry, material properties, and loading. Complexity in wrinkle patterns often arises due to uncontrolled/undesirable non-uniformities in these process parameters. Due to the confounding effect of simultaneously acting non-uniformities, it is difficult to link wrinkle shape/size to process parameters for such systems. To solve this problem, experimental and computational tools were developed to (i) individually tune/control the non-uniformities in these parameters and (ii) probe the effect of these parameters on the wrinkled pattern. The data generated from these tools was then used to link process parameters to pattern complexity. The complexity arising out of these process parameters is summarized in Figure 1.1. Specifically, models were developed to (i) predict hierarchical patterns by capturing the effect of non-flat geometries, (ii) predict the onset of period doubling at high strains by capturing the effect of nonlinear base material, and (iii) predict in-plane bending of wrinkles around localized material defects during uniaxial compression by capturing the effect of defects on the stress state.

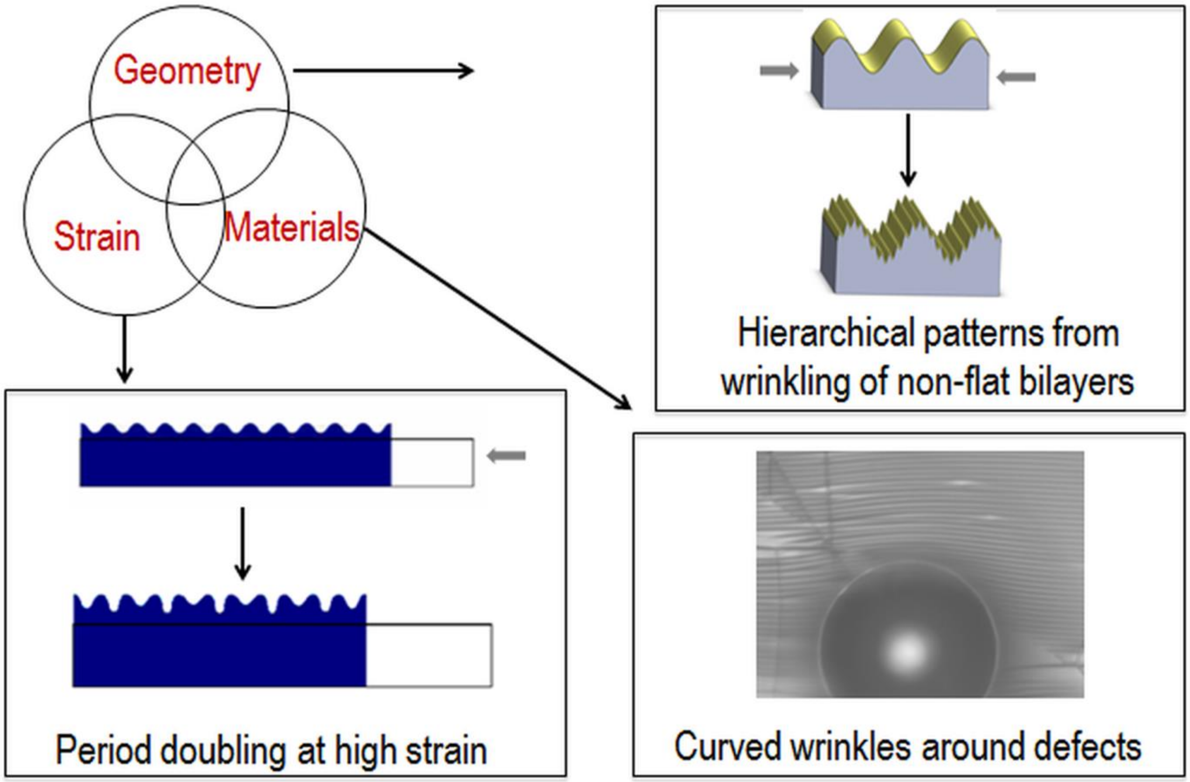

Figure 1.1: Complexity in wrinkled patterns arises due to non-flat geometry, high strain, and localized material defects. Herein, predictive models have been generated to link the input parameters to the corresponding complex wrinkled pattern.

The set of predictive models generated here would enable a designer to perform inverse pattern design of complex wrinkled structures, i.e., to select the appropriate set of process parameters that are required to fabricate the desired pattern. This would reduce the time and cost of manufacturing a variety of functional 2-D micro and nano-structures by a factor of ~10 for low volume applications and by ~10% for high volume applications. This fabrication time/cost reduction would have an impact on the following fields (i) nano-structured assays for drug discovery [2], (ii) micro and nano fluidics based cancer diagnostics [3], (iii) sensors for high sensitivity sensing of toxic chemicals [4] and (iv) research and development of emerging applications such as plasmonics based optical, chemical, and biological sensing [5].

1.1.2 Need for scalable and affordable complex patterning

The functional value of a product is determined by the complexity of the pattern/part. For example, turbine blades for aircraft engines have complex 3-dimensional shapes and as such have a higher value than structural I-beams. In this case, the difference in complexity arises due to differences in both the nominal shape of the parts and the tolerance on deviation of the shape from the nominal values. The desired shapes and tolerances are determined by the applications of these products. This value-complexity dependence is also observed for patterns on the micro and nano scale. For example, as the complexity of patterns increases, the ability of patterns to actively manipulate mass and/or energy on the micro/nano scale also increases. This active manipulation enables using micro/nano-enabled products in applications that have the potential to significantly impact diverse fields such as energy, water, health, and environment among others. To have a meaningful impact of such applications, it is necessary to scale-up the manufacturing of complex micro and nano scale patterns.

1.1.3 Potential of wrinkling

Wrinkling-based pattern formation is a self-organization phenomenon that is commonly observed in natural systems over a wide length scale [6-47]. For example, large scale buckled patterns are observed during ridge formation in the earth’s crust, whereas micro scale wrinkle patterns are observed on white blood cells [10]. Micro and nano scale buckling-induced wrinkle patterns have also been fabricated for applications such as thin film metrology and microfluidics [25, 48]. The mechanism of pattern formation is similar to Euler buckling of beams under compressive loads [17, 49]. Beyond a critical compressive stress, pure compression becomes unstable and wrinkles are formed via periodic bending of the substrate. The period and amplitude of these wrinkles depend on the applied stress, material properties, and the substrate geometry. Thus, periodic patterns of desired period/amplitude may be obtained by controlling these parameters. Some examples of periodic 2-D patterns that were formed via buckling on the micro/nano scale are shown in Figure 1.2 [14, 50]. As areas up to 1-5 cm^2 can be simultaneously patterned via wrinkling, it is a high-rate parallel template-free process for 2-D micro and nano scale patterning.

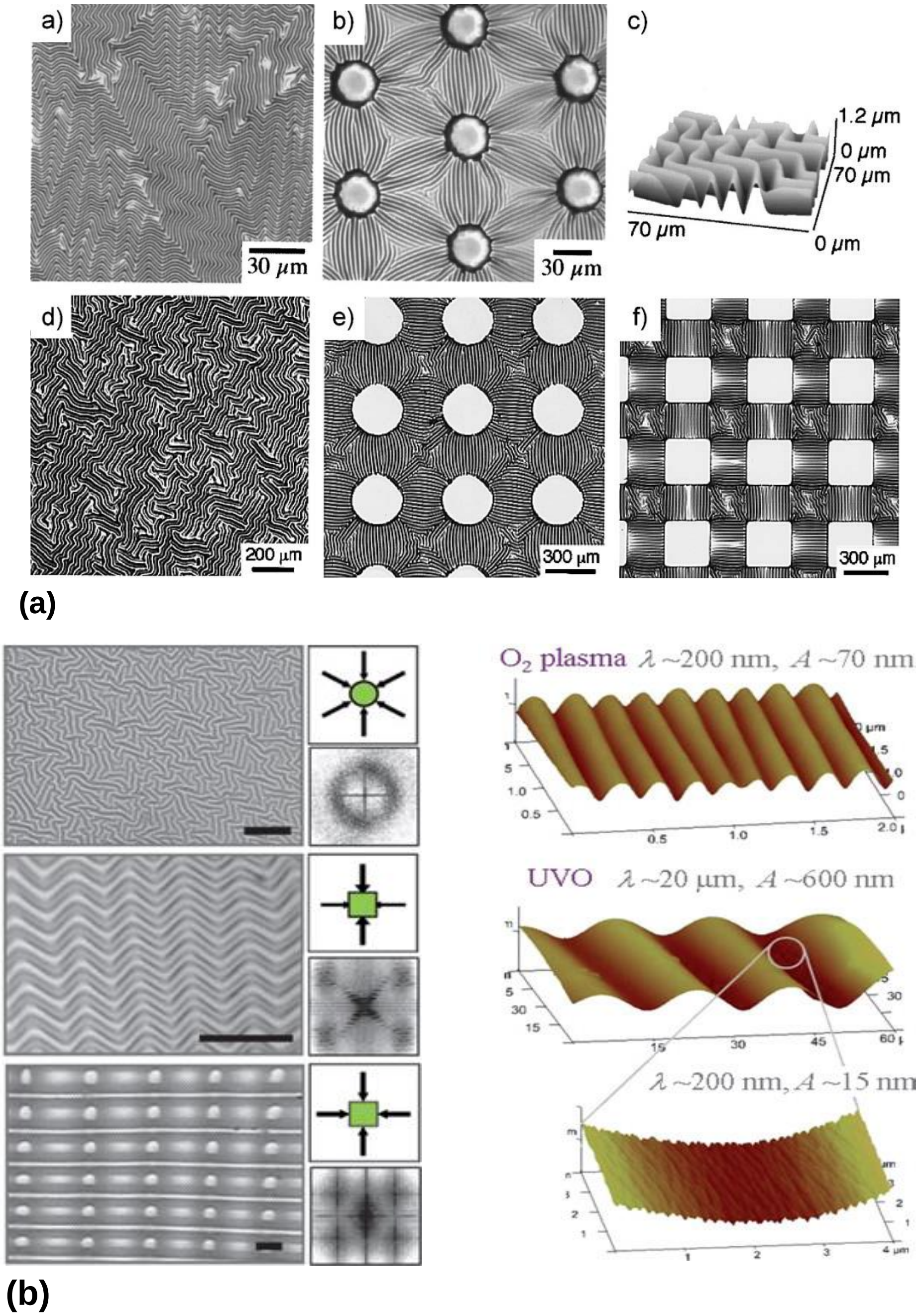

Figure 1.2: Micro and nano scale periodic structures formed via wrinkling. (a) Bowden et al. [14]. Reprinted by permission from Macmillan Publishers Ltd: Nature copyright 1998 (b) Reproduced from Chiche et al. [50] with permission of The Royal Society of Chemistry; scale bars are 20 μm long.

1.1.4 Limitations of wrinkling

Although high-rate template-free fabrication is feasible via wrinkling, it has not yet developed into a robust manufacturing process. This is primarily because only a limited set of patterns can be fabricated via wrinkling. Wrinkled patterns are dictated by the geometry, material properties, and the applied strains. As these parameters cannot be simultaneously and readily altered during processing, only a limited set of pattern geometries can be generated via wrinkling. Additionally, practical quality-based issues such as inaccurate and non-uniform patterning render this process unsuitable for manufacturing. The purpose of this work is to overcome these manufacturing limitations. Manufacturing limitations of the buckling-based process can be broadly divided into two types: flexibility based limitations and quality based limitations. For flexibility, (i) the ability to generate complex patterns and (ii) the ability to perform feature tuning are of primary concern. For quality, (i) pattern accuracy and (ii) pattern uniformity are of primary concern.

1.2 Complex patterning

1.2.1 Pattern complexity in manufacturing

The complexity of a pattern or a part can be measured in terms of the length of the specification required to fully describe it [51]. This is illustrated in Figure 1.3. Within the context of manufacturing, the description of a pattern/part involves specifying (i) the nominal shape, size, and location of the features with respect to a reference and (ii) the acceptable tolerance of deviation of these parameters from the nominal values. A pattern is considered more complex than the others if describing it would require more information. For example, a circular arc is a more complex shape than a line segment as three points are required to define an arc whereas only two points are required to define a line segment. Similarly, a feature with a tighter dimensional tolerance, i.e., higher precision, has a longer specification and is therefore more complex than one with a lower tolerance. Thus, manufacturing complex patterns requires the ability to (i) generate complex shapes and (ii) control the shapes within desired specifications based on predictive knowledge of pattern generation.

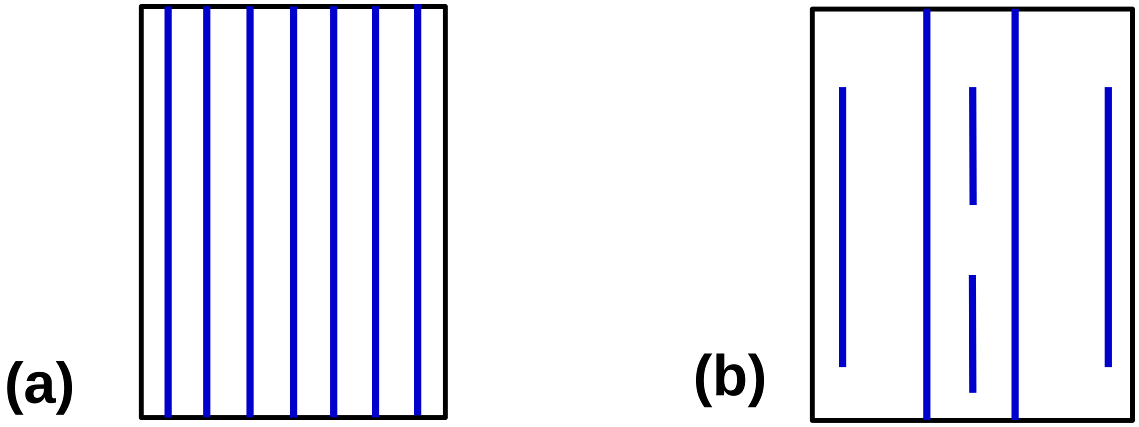

Figure 1.3: Pattern complexity is determined by the size of the specification required to describe it. (a) A relatively simple pattern that is defined by location of one line and the period. (b) A relatively complex pattern that requires information beyond period to fully describe it.

1.2.2 Scalability versus complexity trade-off

In conventional pattern generation processes a trade-off exists between manufacturing scalability and complexity of patterns as shown in Figure 1.4. As the complexity of patterns increases, it becomes more difficult to scale-up the fabrication. This trade-off exists because of the serial/sequential nature of the conventional processes. In general, fabrication cost and time increases with the complexity of a pattern. As only small regions of the pattern are generated at once via serial processes, this increase in cost/time depends on the total path length that the tip/beam of a serial process must traverse to generate the pattern. Thus, scalability of manufacturing a pattern decreases with its complexity.

In contrast, the cost/time for fabricating a complex pattern via a parallel/simultaneous process does not scale with its size. Therefore, an increase in the pattern complexity does not have a significant effect on scalability of these processes. However, such ideal parallel processes for complex patterning do not exist today. Self-assembly and instability driven self-organization processes such as wrinkling come close this ideal as these processes can generate ordered patterns over large areas. However, patterns generated via these processes are often limited to elementary ordered structures. Developing predictive design and fabrication tools for wrinkling is a step toward developing ideal processes for scalable complex patterning.

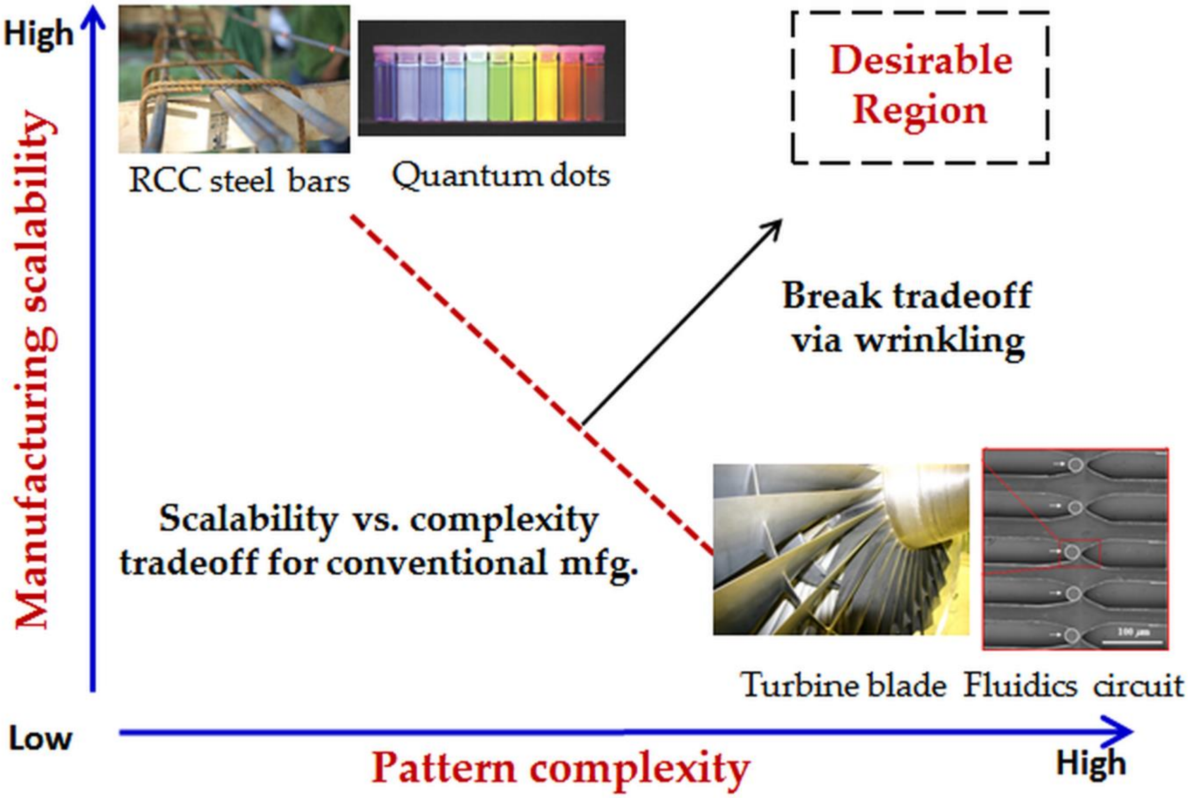

Figure 1.4: In conventional manufacturing, a trade-off exists between scalability of manufacturing a pattern and its complexity. As similar manufacturing principles are being used for micro/nano scale manufacturing today, such a tradeoff also exists for micro/nano scale manufacturing. This tradeoff limits the availability and affordability of micro/nano-enabled products. The goal of this work is to develop understanding of key aspects of wrinkling that demonstrate that wrinkling can be an alternate manufacturing process that breaks this scalability-complexity trade-off. Quantum dots from Han et al. [52]. Reprinted by permission from Macmillan Publishers Ltd: Nature Biotechnology copyright 2001. Fluidics circuit from Boukany et al. [3]. Reprinted by permission from Macmillan Publishers Ltd: Nature Nanotechnology copyright 2011.

1.2.3 Existing manufacturing processes

Nano-scale patterning processes can be broadly divided into two types: pattern generation and pattern replication. During pattern replication, the part is fabricated using a pre-existing physical copy of the pattern, i.e., via a template/stamp; whereas, pattern generation involves creating the first physical copy of the desired pattern. Thus, template-free processes are used for pattern generation, whereas template-based processes are used for pattern replication. Template-free processes can be further divided into two types: serial processes and parallel processes. In a template-free serial process, localized transfer of mass or energy occurs via nano scale interactions with the substrate. For example, mass/energy transfer via a probe tip or a focused beam. The desired 2-D pattern is achieved by scanning the tip or the focused beam on the substrate surface. Template-free parallel processes are those in which a large area can be simultaneously affected in order to produce the desired pattern. Wrinkling-based pattern formation is an example of template-free parallel processing.

Manufacturing metrics for some of the popular template-free and template-based processes are shown in Figure 1.5. These metrics may be used as a guide to select a process that is appropriate for the desired application. For example, template-free serial processes demonstrate high flexibility in terms of the pattern geometry and have a high resolution, i.e., these processes can produce parts with small features (~10 nm). However, the serial nature of the processes severely limits the processing rate. Thus, serial processes are generally used for low-volume applications such as for fabricating high-quality templates/masks.

On the other hand, template based processes are fast and economical techniques for high-volume production. As large areas can be simultaneously patterned via these processes, high rates of part production can be achieved. Also, the cost of an expensive template may be easily recovered if a large number of replicate parts are produced. However, a major drawback of such processes is that the pattern geometry is limited by the template and even minor modifications in the pattern would require a new template. Thus, geometric flexibility of the processes is limited by the availability of templates. If the volume of production is not sufficiently high and a variety of different patterns are required, the cost and fabrication time of the templates would dominate the overall production rate and cost.

There are several applications of 2-D nano patterns that do not necessarily require large volume manufacturing. Instead, moderate quantities of several different types of patterns may be required; for example, during prototype testing of nano-enabled devices such as electronic/fluidic circuits. In these cases, the cost and time spent on fabrication of the templates has a significant effect on the overall cost and rate. Thus, there is a need to develop template-free processes that are: (i) fast, (ii) low-cost and (iii) flexible in terms of the pattern geometry.

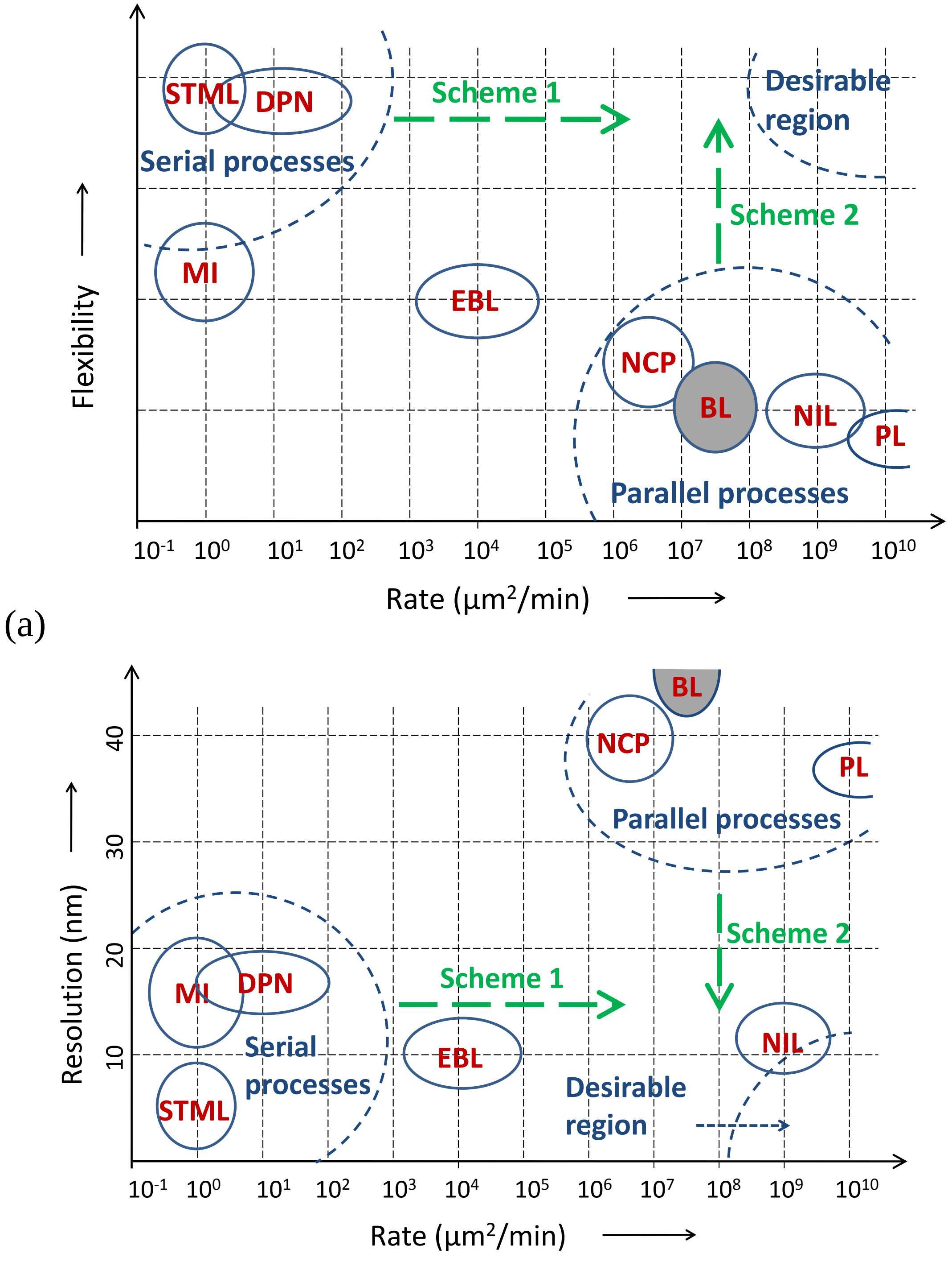

Figure 1.5: Manufacturing metrics of commonly used 2-D nanomanufacturing processes (a) flexibility versus rate and (b) resolution versus rate. Schemes 1 and 2 are generic schemes for modifying the existing processes. Processes are: Dip pen nanolithography (DPN), Scanning tunneling microscope lithography (STML), Mechanical indentation (MI), E-beam lithography (EBL), Nano-imprint lithography (NIL), Nano contact printing (NCP) , Photolithography (PL) and Buckling/wrinkling lithography (BL).

1.2.4 Affordability versus flexibility of manufacturing

For conventional macro scale manufacturing, affordability is improved by performing manufacturing in two steps: (i) template fabrication via a high-cost pattern generation process and (ii) part fabrication via a low-cost pattern replication process. The effectiveness of this strategy in reducing the overall cost is dependent on (i) the number of replicate parts that are produced for each template (***N***) and (ii) the ratio of cost of pattern generation to cost of pattern replication (***R***). If the cost of template fabrication is C_T and the fabrication cost for each replicate part is C_p, then the net cost for part fabrication (C_n) is given by:

$$C_n = C_p + \frac{C_T}{N} \tag{1.1}$$

The ratio of cost of template fabrication to part replication (***R***) is given by:

$$R = \frac{C_T}{C_p} \tag{1.2}$$

The fraction of net part cost that is contributed by the template (f_T) is given by:

$$f_T = \frac{C_T}{C_n} \tag{1.3}$$

This fraction is a measure of the 'affordability of flexibility' of a manufacturing scheme. A scheme that has a low f_T value can be affordably adapted to manufacture different types of parts; whereas a scheme with a high f_T value makes it economically difficult to alter the part type. This is because changing the part requires changes in the relatively expensive templates. From Eqs. (1.1), (1.2), and (1.3) , this fraction can be evaluated as:

$$f_T = \frac{1}{1 + RN} \tag{1.4}$$

The relationship of Eq. (1.4) is graphically represented in Figure 1.6. For large volume manufacturing, the net part cost is insensitive to the cost of the template. However, for low to moderate volume manufacturing, the contribution of template cost to net part cost is highly sensitive to the ratio of template generation cost to replication cost (***R***). For micro/nano scale fabrication, these two factors co-exist: (i) the ratio ***R*** is of the order of 1,000 and (ii) the number of parts (***N***) that can be replicated per template is low. The number ***N*** is often limited to 100 to

200 parts either due to practical process constraints that limit the number of reliable replications that are feasible per template or due to limited demand for a unique pattern. This practical replication limit is labeled in Figure 1.6. Due to these two factors, the net cost of micro/nano scale parts is dominated by the cost of the template. Thus, affordability of micro/nano scale processes can be improved by reducing the cost of the templates. A wrinkling based process has an ***R*** value of about 10 as wrinkling is 100-1000 times less expensive than the existing cleanroom techniques. Therefore, wrinkling based processes can be affordable alternatives to the existing cleanroom based fabrication processes if the geometric flexibility of wrinkling is improved.

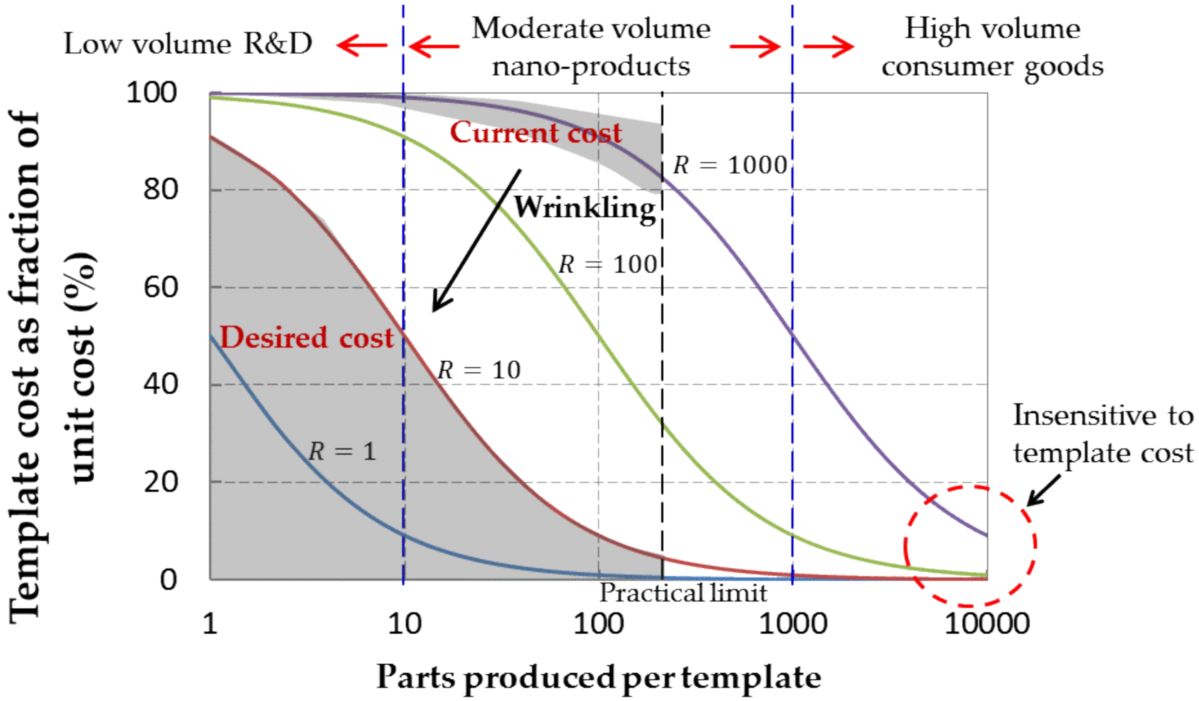

Figure 1.6: Fraction of net part cost that is contributed by the template for different operating conditions. For micro/nano scale manufacturing, the net cost of the part is dominated by the cost of templates.

1.2.5 Limitations of existing processes

At present, template-free processes that are fast, low-cost and flexible do not exist. Thus, one would need to either develop a new process or modify the existing ones. To modify the existing processes one may choose those processes that already satisfy one or more of the requirements. Schemes for modifying the existing template-free processes can be divided into two types: (i) increase the rate of serial template free processes that are low-cost and flexible (Scheme 1 in

Figure 1.5) or (ii) improve the quality and geometric flexibility of the existing parallel template free processes that are low-cost and high-rate (Scheme 2 in Figure 1.5).

In past work, focus had been on the first approach: i.e., on increasing the rate of a low-cost and flexible process. Specifically, the dip pen nanolithography process that is a tip based template-free serial process was modeled and characterized [53-55]. The goal was to increase the rate by several orders of magnitude (~10^5 times). However, it was found that the diffusion based process mechanism puts a fundamental limit on the rate. The rate is limited to about 20 times the typical processing rate, and falls much short of the desired value [55]. In this work, the focus is on the second approach, i.e., on improving the flexibility of high rate parallel template-free processes. Specifically, the focus in on developing predictive models and fabrication tools for the wrinkling process.

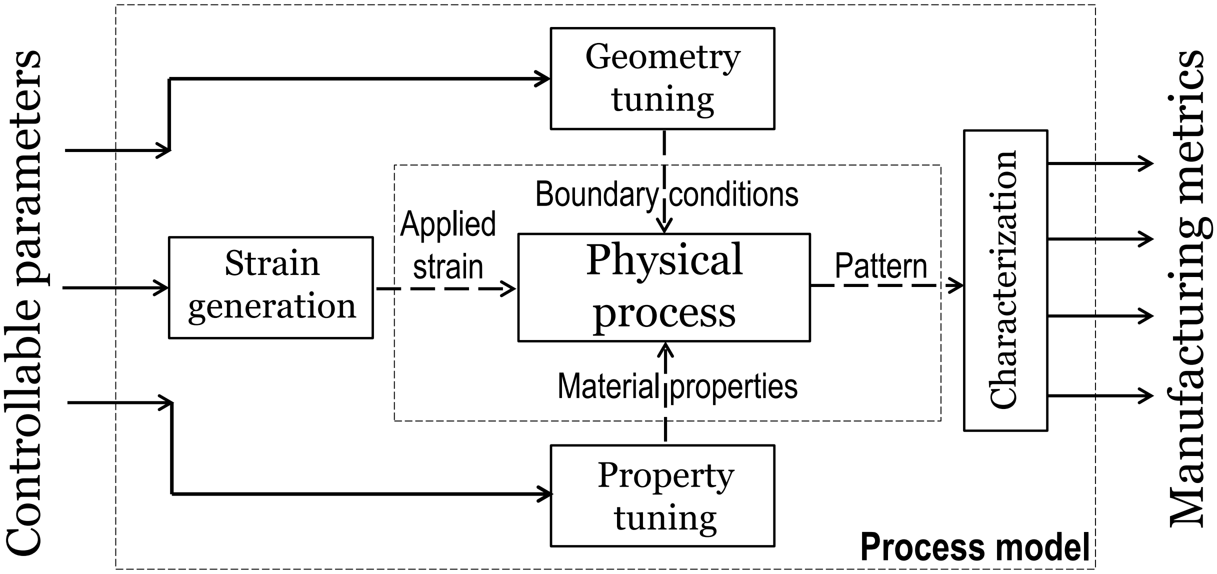

Figure 1.7: Parameters of the wrinkling process.

1.3 Wrinkling process

1.3.1 Process parameters

The wrinkled pattern depends on several factors such as the material behavior, material properties, geometry of the substrates and the compressive stresses. A model of the wrinkling process depicting the inputs and outputs to the process is shown in Figure 1.7. Several different techniques have been used in the past for modifying/controlling the input parameters of the process. These techniques are listed in Table 1.1. Different configurations may be obtained by combining these techniques. A schematic of one such configuration is shown Figure 1.8. This configuration forms the basis of the work presented here. It consists of forming/depositing a thin stiff layer on top of a pre-stretched thick soft elastomeric material. Wrinkled patterns are formed on the surface when the pre-stretch is released. The period (λ) and amplitude ($\boldsymbol{A}$) of the wrinkles may be estimated in terms of the thickness of the top stiff layer thickness, ratio of Young's modulus of the base and the top film, and the applied compression.

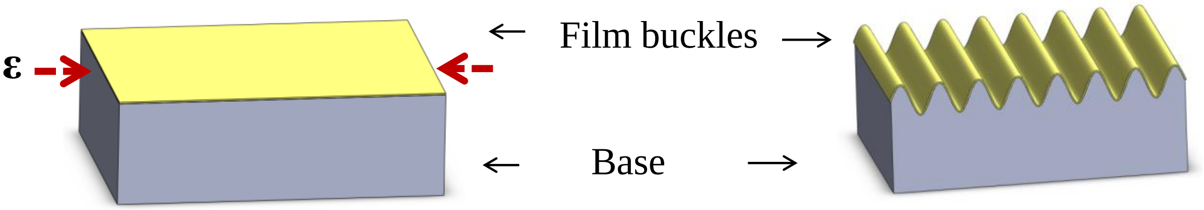

Figure 1.8: Schematic of the wrinkling process. Periodic wrinkles are formed upon compression of a bilayer that consists of a thin stiff layer resting on a thick compliant base.

Table 1.1: Techniques for controlling the parameters of the wrinkling process

Material behavior	Techniques for stress generation	Techniques for tuning geometry	Techniques for tuning material properties
Elastic [15, 50]	Mechanical stretching [50, 56]	Metal deposition or thin film transfer [14, 46]	Plasma/UVO treatment [50, 56]
Viscous [57]	Thermal expansion [14, 15]	Plasma/UVO treatment [50, 56]	Photo-curing [16]
Viscoelastic [58]	Hydrogel swelling [37, 45]	Pre-patterned surfaces [14, 16]	Temperature dependent properties [59]

1.3.2 Wrinkling as a manufacturing process

Suitability of a manufacturing process for a specific patterning application may be evaluated in terms of the manufacturing metrics, i.e., flexibility, quality, rate, and cost. The current and desirable performance of the wrinkling-based process on these manufacturing metrics is listed in Table 1.2. A significant gap exists between the current and desirable performance on two of these metrics: *flexibility and quality*. This is because of the limited ability to globally and locally control all/some of the input parameters to the process. Thus, the focus of this work is on improving upon these metrics.

Table 1.2: Current and desirable manufacturing metrics for wrinkling-based patterning

Manufacturing metric		Current value	Desirable value
Flexibility	Types of features	Periodic structures	General complex structures
Quality	Accuracy	Unknown	> 1-5 % dimensional tolerance
	Resolution	$\lambda \sim 100$ nm—1μm	$\lambda < 100$ nm
Rate	Area processing rate	10^7—10^8 μm^2/min	~ 10^8 μm^2/min
	Cycle time	Minutes	Seconds—minutes
Cost	Equipment cost	~ 10,000 US$	< 10,000 US$

For the wrinkling process, geometric flexibility has two interpretations: (i) the *extent* to which the geometric properties of the pattern such as shape and size may be modified and (ii) the *ease* with which the geometric properties of pattern may be modified. In this work, the focus is on both of these aspects of flexibility. Similarly, the quality metric has multiple interpretations that are relevant to manufacturing. These are: (i) accuracy of the pattern, (ii) uniformity of the pattern over a given area during a single run in terms of the long range ordering and short range defects and (iii) resolution, i.e., the lowest achievable wavelength and amplitude. As the wrinkling period resolution is already ~100 nm and the amplitude resolution is ~10 nm, the focus of this work is on improving the accuracy of feature prediction and quantifying and improving the pattern uniformity.

Affordability and scalability of wrinkling

Herein, the fabrication cost and rate have been used as a measure of the affordability and scalability of a manufacturing process. As wrinkling-based processes already satisfy the requirements for high-rate and low-cost of processing, further improvements in these two metrics are not necessary. The area processing rate during wrinkling-based patterning is determined by the rate at which the strain is applied and by the area over which ordered structures can be obtained. This rate is marginally less than template-based soft lithography processes and is about 10^7—10^8 μm^2/min. A first-order estimate of the processing cost may be made using the cost of the equipment. The cost of the equipment for wrinkling-based patterning is dominated by the cost of the equipment used for depositing the top layer. This is about 100-1000 times less than the cost of equipment used for e-beam lithography. As such, wrinkling-based processes are affordable and scalable techniques for generating micro and nano scale patterns.

1.3.3 Predictive design and fabrication of complex patterns

Complex wrinkled patterns are often the result of uncontrolled/undesirable non-uniformities in the process parameters. Thus, the complexity in the fabricated pattern is a result of the effect of multiple coupled ‘non-simple’ process parameters. Due to this, it is difficult to decipher the relationship between non-uniformity or complexity of individual parameters and the complexity of the patterns. To solve this problem, here tools and techniques have been developed to (i) individually tune and control the non-uniformity of the process parameters that determine geometry, material properties, and loading and (ii) probe the effect of these process parameters on the wrinkled patterns. This has resulted in predictive models that capture the complexity arising out of (i) non-flat bilayer geometry, (ii) high compressive strains, and (iii) localized material defects.

1.4 Organization of thesis

This thesis is organized into two parts: (i) tools for fabricating and predicting wrinkled patterns and (ii) effect of individual process parameters on pattern complexity.

Chapter 2 provides a summary of the design and fabrication of a biaxial stretch stage, in-situ metrology system, and the characterization of the process steps involved in fabricating ‘simple’ 1-D periodic wrinkle patterns.

Chapter 3 provides a description of the finite element modeling process that was employed for numerically predicting wrinkled patterns. Verification of the codes based on internal self-consistency tests and comparisons to analytical models and experiments is also provided in this chapter.

Chapter 4 provides a description of the process of fabricating and predicting hierarchical wrinkles that are generated via compression of non-flat bilayers. An analytical model has been developed and verified against experiments and finite element simulations to predict the transition of pre-patterned bilayers into hierarchical modes.

Chapter 5 provides a description of the process of fabricating and predicting the wrinkling mode that is generated when high compressive strains are applied to bilayers. The higher mode manifests as a period doubling mode and can be predicted via finite element methods.

In Chapter 6, the concept of attractors and repellers as distinct localized material defects has been introduced. These localized defects either attract or repel wrinkles during 1-D loading. Attractors and repellers have been physically demonstrated and a parametric analysis has been performed via finite element methods to quantify the attraction/repulsion effect of the localized defects.

Chapter 2

Tools for wrinkling: Fabrication

2.1 Introduction

Complex wrinkled patterns are commonly observed in natural systems over a wide length scale [25]. Due to the inherent affordability and manufacturing scalability, pattern generation via wrinkling is an attractive potential alternative to more expensive cleanroom-based techniques such as e-beam lithography. However, the practical import of this process is limited by the lack of flexibility, i.e., due to the inability to predictively design and fabricate a variety of different complex patterns. Predictive design and fabrication of complex wrinkled patterns is hindered by the lack of appropriate fabrication tools and techniques. For example, current tools and techniques (i) have limited ability to independently tune the process parameters over a large design space, (ii) lack a set of well-characterized process steps, and (iii) do not provide in-situ metrology/visualization of wrinkle formation. This prevents one from developing predictive models by systematically probing the wrinkling process and empirically observing the effect of control parameters on the process performance. Herein, a set of fabrication tools has been developed and characterized to enable systematic empirical studies of the wrinkling process. Later in Chapters 4–6, application of these tools is demonstrated for predictive design and fabrication of complex wrinkled patterns.

2.1.1 Limitations of existing experimental tools

Although current experimental tools form a valuable toolkit for predictive design and fabrication of wrinkled patterns, they are still inadequate in satisfying the need for a variety of complex patterns. This is primarily due to the (i) limited design space that is accessible via existing experimental techniques and (ii) inability to independently probe and study the effect of individual process parameters.

The set of achievable patterns is limited by the feasible range and types of compressive loads. For example, (i) complex higher modes cannot be achieved below a threshold strain [60] and (ii) only a limited set of complex 2-D modes can be achieved via equibiaxial strains [46]. Existing techniques that rely on thermal expansion [14-16] or volumetric swelling [37, 45] to generate strains can provide only a limited set of loads. For example, mismatched thermal expansion of an isotropic film on an isotropic base leads to equibiaxial strains. Due to this, exploring the design space for large uniaxial or non-equibiaxial loads becomes a material selection problem. This coupling between loading and materials can be eliminated by using mechanical stages to introduce strains. However, existing biaxial mechanical stages are often too large to use within plasma oxidation or metal deposition chambers that are required during wrinkle fabrication. Thus, there is a need to develop a mechanical extension stage that (i) has a small form factor and (ii) is capable of applying large non-equibiaxial strains.

The ability to independently probe and study the effect of process parameters is limited by the absence of in-situ metrology for visualization of the wrinkling process. As the tools for generating compressive strains are usually incompatible with imaging systems, imaging is often done via offline techniques. This limits the ability to continually probe the effect of strain release on the wrinkled surface. Additionally, the inability to accurately scan the wrinkled surface over a large area prevents one from studying the spatial variation due to non-uniformity of process parameters. Thus, there is a need to develop an in-situ metrology system that would enable process monitoring over a large area.

2.1.2 Goals

The goal of the work presented in this chapter is to (i) design and build equipment for control of process parameters, (ii) characterize the fabrication steps of the process to reduce variations in the process parameters, (iii) set up in-situ metrology for visualization of wrinkle formation, and (iv) verify the accuracy of the fabrication tools. These goals have been achieved by (i) designing and fabricating a compact mechanical extension stage that enables providing accurate, large, and non-equibiaxial mechanical strains and (ii) setting up an in-situ metrology system consisting of a CMOS camera mounted on an X-Y-Z translation stage that enables visualizing the effect of the stretch release process on the wrinkled surfaces. Additionally, the fabrications steps of the wrinkling process have been characterized to enable process control. Specifically, the bilayer generation process has been quantified and optimized so as to enable tuning of wrinkles via control of material properties and geometry of the bilayer.

2.2 Wrinkling fabrication process

2.2.1 Process physics

Wrinkling of compressed bilayers is an affordable fabrication technique for generating 1-D periodic micro and nano scale patterns. The period and amplitude of these patterns can be tuned by controlling the relevant process parameters. For the bilayer system shown in Figure 2.1, these parameters are: (i) thickness of the top layer, (ii) compression of the top stiff layer, and (iii) ratio of stiffness of the top and the bottom layers. Several analytical models for 1-D wrinkling of bilayer systems are available in the literature. These models differ in terms of small [17, 50] versus large compression [61] and linear [17, 50] versus nonlinear material models [61, 62]. For linear elastic materials at low compressive strains, the period (***λ***) and amplitude (***A***) of the wrinkles may be estimated in terms of the top stiff layer thickness (***h***) as [50]:

$$\lambda = 2\pi h (c\eta)^{1/3} \tag{2.1}$$

$$A = \frac{\lambda}{\pi}(\varepsilon - \varepsilon_c)^{1/2} \tag{2.2}$$

Here, ***c*** and ***η*** are non-dimensional ratio of material properties, ***ε*** is the applied compression, and $\boldsymbol{\varepsilon_c}$ is the critical compression beyond which wrinkled patterns are observed. The critical compression is determined entirely by the material properties and is given by [50]:

$$\varepsilon_c = -\frac{1}{4}(c\eta)^{-2/3} \tag{2.3}$$

The ratio ***c*** is the ratio of Poisson's ratio of the two layers ($\boldsymbol{v_{f,s}}$) and is given by [50]:

$$c = \frac{1}{9}\left(\frac{1-\nu_s^2}{1-\nu_f^2}\right) \tag{2.4}$$

The ratio η is the ratio of stiffness moduli of the layers ($E_{f,s}$) and is given by [50]:

$$\eta = \left(\frac{3E_f}{E_s}\right) \tag{2.5}$$

In Eqs. (2.4) and (2.5), the subscripts ***f*** and ***s*** refer to the film and the base substrate, respectively. This simplified model captures the essential physics of the wrinkling process: (i) length scale is determined by the thickness of the top film, (ii) effect of material properties is through the ratio of properties of the top and bottom layers, and (iii) amplitude depends on the applied compressive strain. Thus, to fabricate the desired wrinkle patterns one must be able to tune and/or control these three parameters: top layer thickness, material properties, and applied strain.

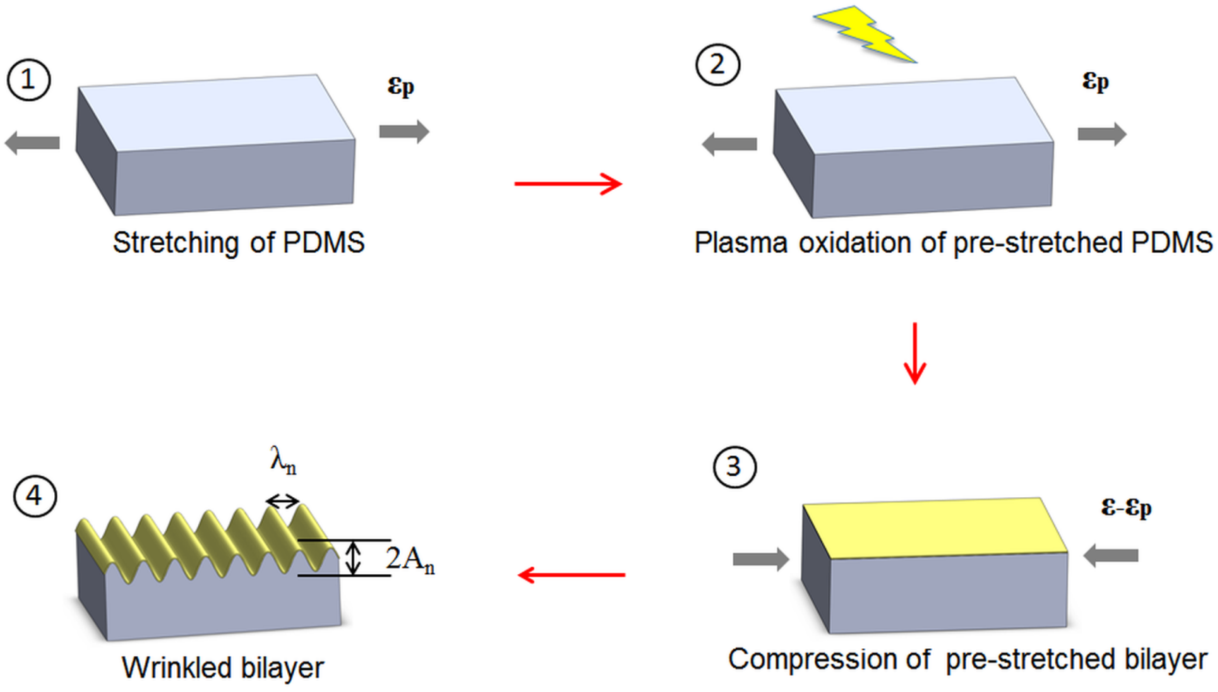

Figure 2.1: Schematic of the wrinkling process

2.2.2 Process steps and equipment

To enable the fabrication and tuning of wrinkle patterns, one must solve these sub-problems: (i) fabrication of a bilayer system with the desired material properties and geometry, (ii) loading/unloading to compress the top stiff layer, (iii) visualization of pattern formation, and (iv) material transfer across different steps of the process. Herein, a summary of the process steps and the equipment that were designed and fabricated to solve these sub-problems is presented.

Stretchable bilayers with large stiffness ratio can be fabricated by attaching or growing a thin stiff film on top of a thick elastomeric base. For example, plasma oxidation of a polydimethylsiloxane (PDMS) film leads to the formation of a thin glassy layer on top of the exposed PDMS surface via oxidation [15]. Alternately, a metallic [14, 63] or polymeric [64, 65] thin film may be deposited on top of PDMS to obtain the desired bilayer. The top layer thickness may be controlled by controlling the plasma oxidation or the deposition process; whereas the stiffness ratio may be tuned by selecting appropriate top/bottom materials. Here, PDMS was used as the elastomeric base material and plasma oxidation process was used to generate the thin glassy film. PDMS films were fabricated by thermal curing of a commercially available two-part silicone resin. Tuning of material properties was achieved by tuning the PDMS curing and the plasma oxidation processes.

Wrinkles are observed on compression of the top stiff layer in the glass/PDMS or metal/PDMS bilayer. Compression of the top layer can be achieved by either directly compressing the bilayer or by generating a residual compressive stretch in the top layer. As direct compression of the bilayer requires sustained loading to maintain the wrinkles, residual compression is often the preferred loading scheme. During mechanical loading, residual compression can be generated by first stretching the PDMS base and then attaching/growing the stiff film on top of this pre-stretched base. On releasing the pre-stretch in the PDMS, the top layer undergoes compression that leads to wrinkle formation. Here, the pre-stretch release mechanism has been used to generate the wrinkles. A mechanical biaxial extension stage has been designed and fabricated to perform these stretch and stretch release operations.

The steps of the fabrication process are summarized in Figure 2.2. The steps are (i) fabricating a PDMS film, (ii) loading the PDMS film on to the extension stage, (iii) extension of the PDMS film, (iv) plasma oxidation of the stretched PDM film, and (v) unloading of the pre-stretched PDMS film. The role of the extension stage is to provide the means to (i) control the stretch in the PDMS film, (ii) hold the pre-stretch during plasma oxidation, and (iii) perform a controlled release of the pre-stretch. Additionally, the stage has alignment features to register it to a vision system before and after plasma oxidation to enable in-situ visualization of wrinkle generation. The vision system consists of a CMOS camera mounted on an X-Y-Z stage and enables visualizing the formation of wrinkles during stretch release. Details on the process steps and the equipment are discussed in the subsequent sections.

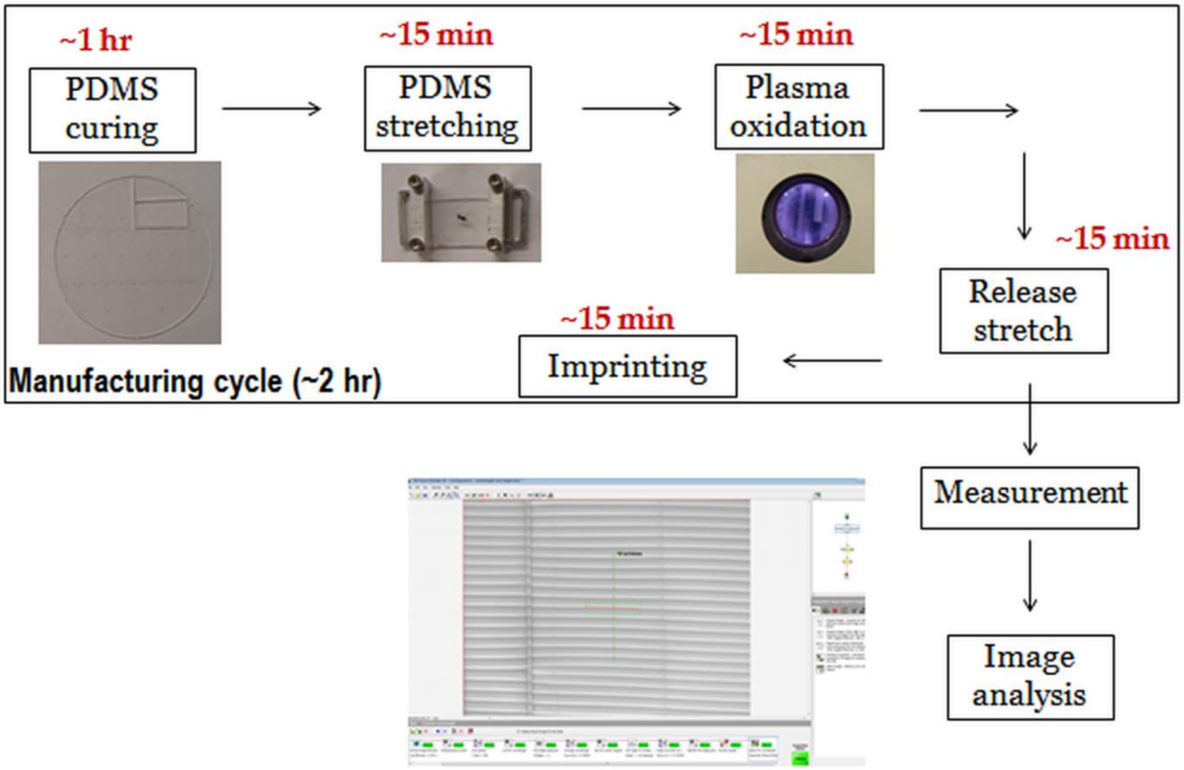

Figure 2.2: Fabrication steps during wrinkling

2.3 PDMS casting and sample design

The PDMS casting process influences wrinkle formation via the geometry and the material properties of the sample PDMS film. Herein, a protocol for casting and sample generation has been developed to (i) tune the geometry and material properties of the film and (ii) reduce variations in these parameters across a single PDMS sample and across multiple samples. The parameters that are controlled during the casting process are (i) thickness of the PDMS film, (ii) length of the stretched section of the film, (iii) flatness of the film surface, and (iv) shear modulus of the PDMS film. Control of these parameters is achieved by controlling the casting and curing process and by standardizing the sample geometry.

2.3.1 PDMS casting and curing

PDMS films were fabricated by thermally curing the commercially available Sylgard 184 two-part silicone elastomer mixture. As the wrinkling process performance depends on the mechanical properties of PDMS, it is important to ensure a well-controlled process for fabricating the PDMS base. Thus, a standard protocol was developed for curing of PDMS. The protocol is summarized here. Salient features of the protocol are: (i) use of two-step thermal curing cycle, (ii) incorporation of alignment features into the molds, (iii) use of conduction based thermal curing via a hot plate, and (iv) mixing of the two parts at non-stoichiometric ratios to optimize mechanical properties of PDMS.

The steps of the curing process are:

[1] Determine amount of resin and curing agent for the desired resin to agent ratio *r (w/w)*
[2] Thoroughly mix appropriate amounts of resin and curing agent
[3] Degas the mixture for $\boldsymbol{t_g}$ minutes under vacuum pressure $\boldsymbol{P_d}$
[4] Slowly pour the mixture into the mold to minimize the formation of air bubbles
[5] Place the mold on top of a hot plate held at a temperature of $\boldsymbol{T_{c,1}}$ for $\boldsymbol{t_{c,1}}$ minutes
[6] Increase the temperature of hot plate to $\boldsymbol{T_{c,2}}$ and hold for $\boldsymbol{t_{c,2}}$ minutes
[7] Remove the mold off the hot plate and place it on a thermal sink at room temperature.

Based on trial runs, the following parameters were selected: $\boldsymbol{P_d} \leq -28.5$ inHg, $\boldsymbol{t_g}=20$ min, $\boldsymbol{t_{c,1}}=20$ min, $\boldsymbol{t_{c,2}}=15$ min; $\boldsymbol{T_{c,1}}=65\ {}^0\mathrm{C}$ and $\boldsymbol{T_{c,2}}=130\ {}^0\mathrm{C}$. The curing ratio (***r***) was varied over the range of 6 to 15 to achieve the desired mechanical properties. The effect of curing ratio on mechanical properties of PDMS is discussed later in Sec. 2.3.4.

A two-step thermal curing technique was adopted to reduce the curing cycle time and the volume shrinkage during gelation [66]. Low curing temperature before gelation ensures that the volumetric shrinkage during curing is low; whereas a high curing temperature after gelation ensures a fast post-gelation curing. The gelation time corresponds to the time it takes for the mixture to undergo a phase transition. The first thermal period ($\boldsymbol{t_{c,1}}$) was selected based on the experimental observation of a gelation time of ~6 min.

2.3.2 Molds for PDMS coupons

Custom molds for casting PDMS films were fabricated out of aluminum to reduce variations in the geometric parameters of the PDMS films. Separate molds were used for casting films for 1-D loading and for 2-D loading. Schematic of these molds is shown in Figure 2.3. Each mold consists of a cylindrical casting reservoir that is 150 mm in diameter and a nominal height of 2 mm. The casting reservoir is surrounded by an overflow reservoir that holds any excess PDMS that overflows from the casting reservoir. This feature ensures that the maximum thickness of the PDMS films is limited to the height of the casting reservoir. Films below this thickness may be fabricated by controlling the amount of pre-cured PDMS that is poured into the casting reservoir.

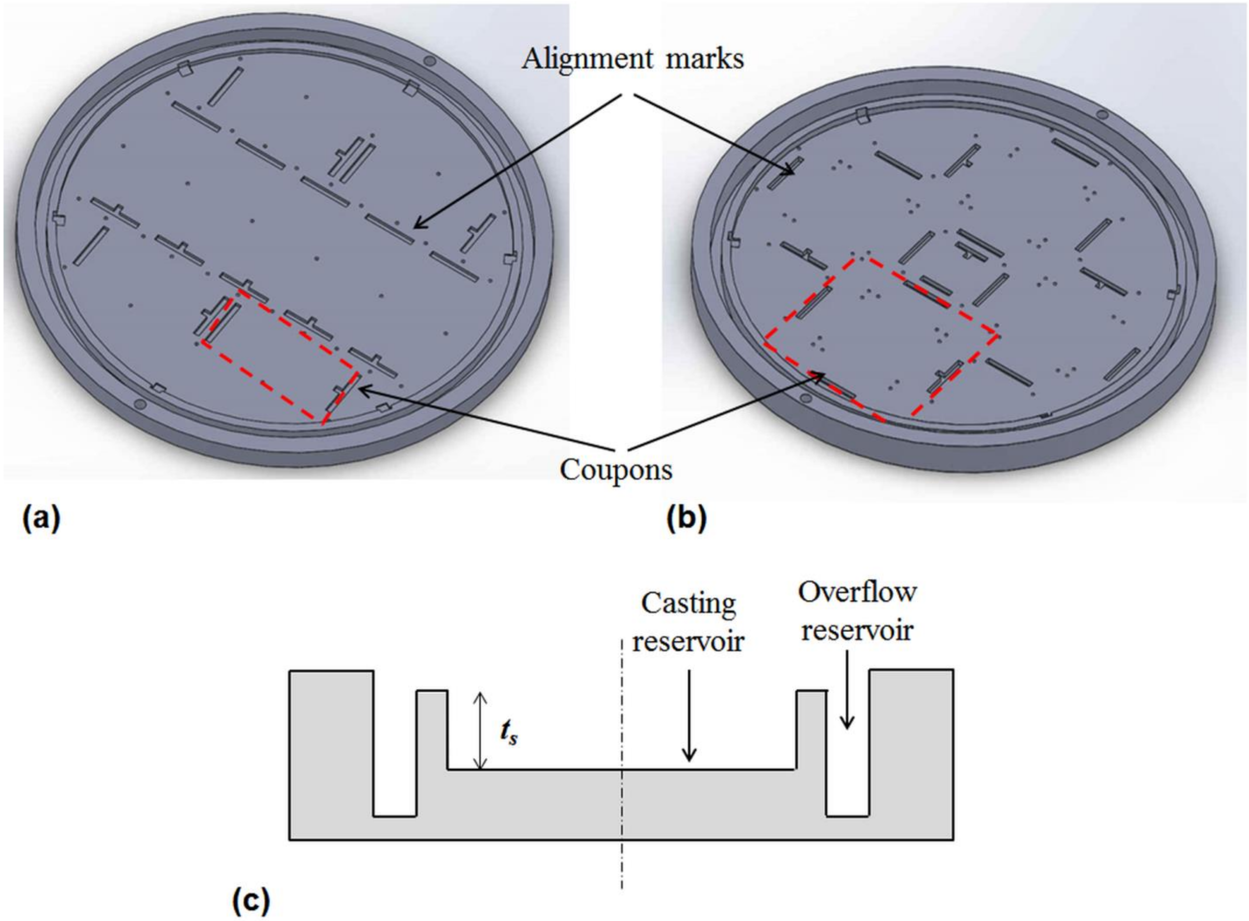

Figure 2.3: Custom molds that were used for fabricating the PDMS films. (a) Mold for 1-D loading, (b) Mold for 2-D loading, (c) Schematic of the mold reservoir geometry. Each mold has a casting reservoir surrounded by an overflow reservoir. Alignment features for the stretching operation are built into the molds.

Variations in thickness across the casting surface were reduced by holding the mold surface level with respect to the gravitational field. This was achieved by performing the thermal curing operation on a hot plate that was itself kept on top of an optical table. To ensure that featureless flat films were available for patterning, only the top surface of the films were used for patterning wrinkles. The stretched length of the films is held uniform across different samples by incorporating alignment features into the molds as indicated in Figure 2.3. These mold features ensure that each PDMS sample has well characterized alignment features built into it during the casting/curing process.

2.3.3 PDMS coupon design

PDMS coupons of pre-determined shape and size were used during fabrication of wrinkles. The size of these PDMS coupons was determined by microfluidics based applications wherein the chip/device is about a cm to an inch square. Rectangular films were used for uniaxial stretching and star shaped films were used for biaxial stretching. The geometry of the coupons is shown in Figure 2.4; numerical values of the geometrical parameters are listed in Table 2.1. Each clamped edge of the coupon is provided with a feature on the bottom surface to align the edge to clamps during mechanical stretching. The “negatives” of these features were designed and built into the metal molds that were used for casting the PDMS films. These alignment features ensure that the length of the stretched section is accurately known during stretching. Separate metal molds were used to fabricate the PDMS films for coupons that were used in 1-D loading and 2-D loading. The 1-D mold yields nine coupons and the 2-D mold yields four coupons for each casting cycle. The coupons were manually cut out of the cast PDMS films using a razor blade.

Table 2.1: PDMS coupon size

Loading type	Stretched length	Thickness
1-D	37.5 mm	1.9-2.2 mm
2-D	43 mm	

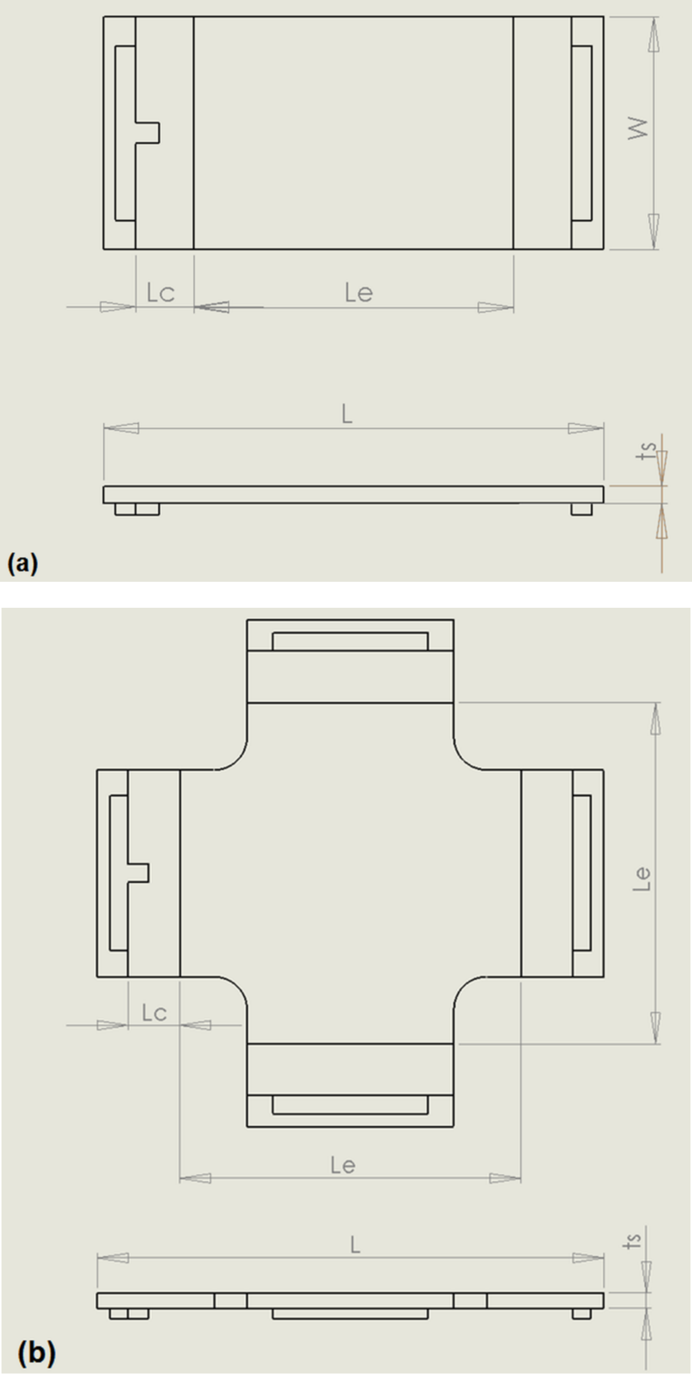

Figure 2.4: Geometry of an individual coupon that is stretched during wrinkling. (a) 1-D coupon, (b) 2-D coupon.

2.3.4 Mechanical properties of PDMS

Measurement of properties

The mechanical properties of PDMS that are relevant to the wrinkling process are: (i) Young's modulus and (ii) failure stretch. The Young's modulus of PDMS affects the period of the wrinkles; whereas the failure stretch determines the maximum prestretch that can be applied to generate wrinkles. Both of these properties were measured during uniaxial tension on an Instron 5869 tensile testing machine with a ±1 kN load cell. Young's modulus was measured as the slope of the engineering stress versus stretch curve at the zero extension point. Failure stretch was measured as the stretch at which the PDMS coupon tears. These measurements for a representative coupon are summarized in Figure 2.5. For these tests, 1-D PDMS coupons of a nominal length of 37.5 mm, width of 20 mm, and thickness of 2 mm were used. A low stretch rate of 0.05 mm/s was used during stretching to ensure quasi-static loading conditions.

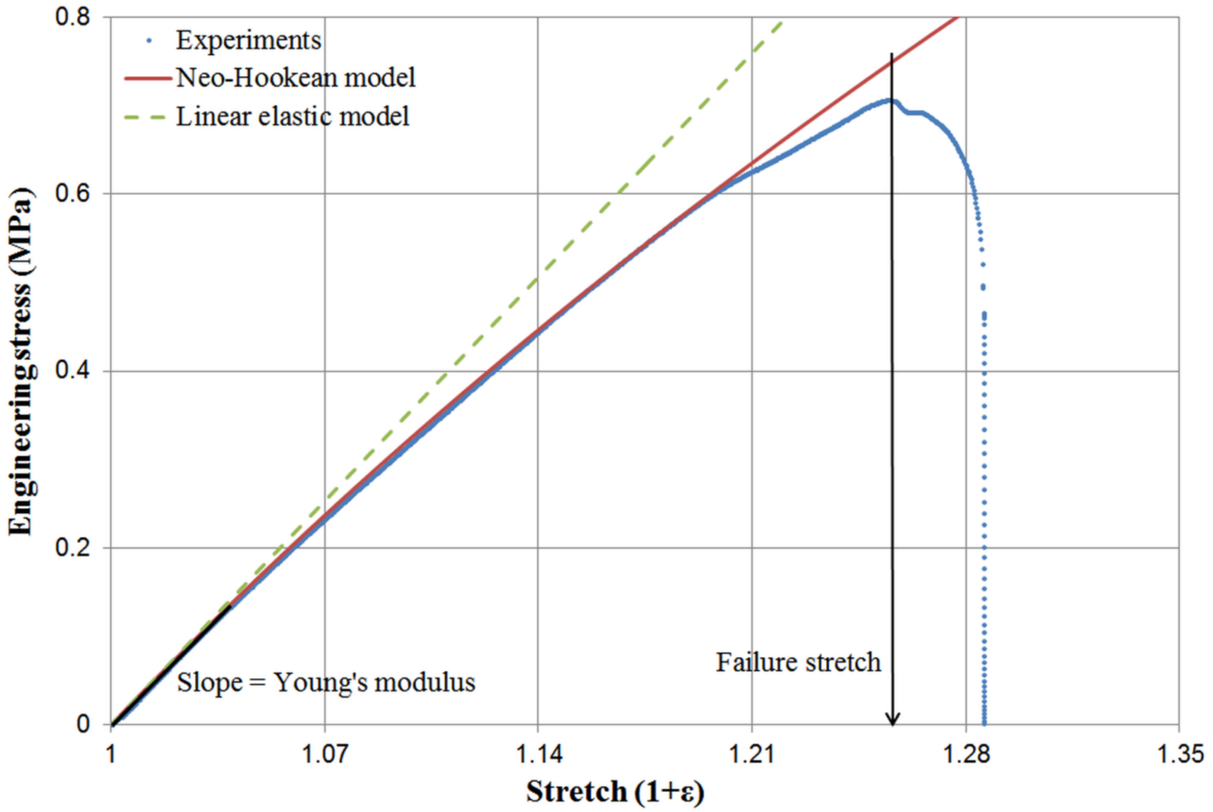

Figure 2.5: Engineering stress versus stretch response of a 1-D PDMS coupon of curing ratio 8:1. The slope of the curve at zero extension, i.e., at stretch=1 is 3.62 MPa.

PDMS material behavior

In addition to the Young's modulus and failure stretch, the uniaxial tensile test also provides important information about material nonlinearity. As is evident from Figure 2.5, PDMS exhibits nonlinear stress versus stretch response at large stretch values. The linear stress versus stretch approximation is accurate only at low extension values that are less than about 5%. At moderate extension values of about 5−20%, the Neo-Hookean nonlinear material model prediction is more accurate than the linear estimate. For large extension values, it is observed that the Neo-Hookean model overestimates the engineering stress by about 5%. The corresponding overestimation by the linear material model is about 29%. As wrinkling is performed at moderate stretch values, the Neo-Hookean material model has been used for setting up the computational models in this work.

For an incompressible material, i.e., for Poisson's ratio $\boldsymbol{\nu}$=0.5, the engineering stress ($\boldsymbol{S}$) in a Neo-Hookean material during uniaxial stretching is related to the extension ($\boldsymbol{\varepsilon}$) as:

$$S = \frac{E}{3}\left(1+\varepsilon-\frac{1}{(1+\varepsilon)^2}\right) \tag{2.6}$$

Here, $\boldsymbol{E}$ is the Young's modulus of the material and (1+$\boldsymbol{\varepsilon}$) is the stretch. The stretch is given by:

$$1+\varepsilon = \frac{L}{L_o} \tag{2.7}$$

Here, $\boldsymbol{L}$ is the final stretched length of the sample and $\boldsymbol{L_o}$ is the initial unstretched length.

Effect of curing ratio

The mechanical properties of PDMS may be tuned and optimized by altering the curing ratio [66]. Therefore, experiments were performed to quantify the effect of curing ratio on the Young's modulus and failure stretch of PDMS. The results of these experiments are summarized in Figure 2.6. It is observed that the Young's modulus of PDMS decreases as the curing ratio deviates away from the stoichiometric curing ratio of 10:1. This observation suggests that both over-crosslinking and under-crosslinking lead to a decrease in the elastic modulus. The failure stretch is observed to be higher for curing ratios that are higher than the stoichiometric ratio, i.e., for mixtures with an excess of the resin material. This indicates that the failure stretch is higher when there is lower PDMS cross-linking. Based on the results of these tests, the operating curing ratio was selected to be 12:1 and 15:1. This selection ensures a higher limit to failure during prestretch.

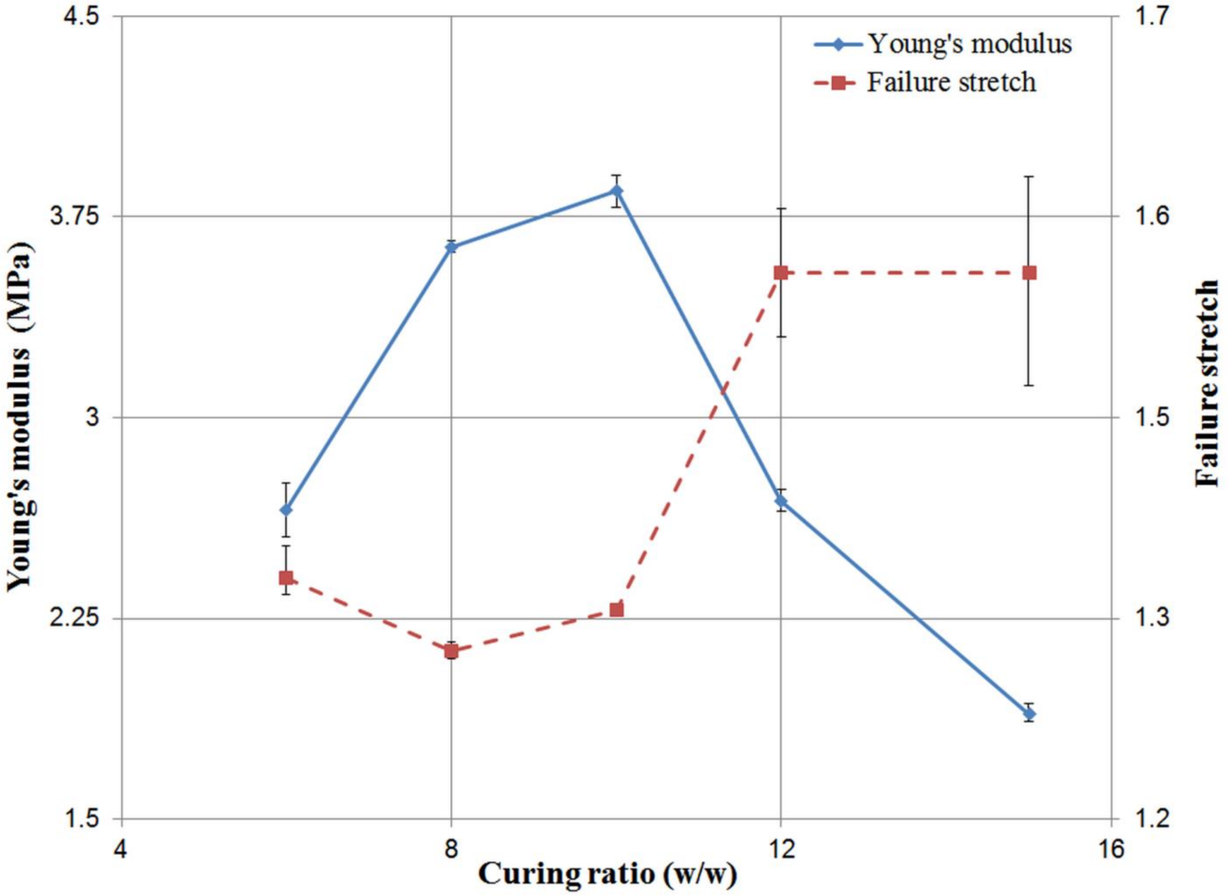

Figure 2.6: Effect of curing ratio on the mechanical properties of PDMS. Three coupons from the same six inch cast PDMS film were used to obtain the data points corresponding to each curing ratio. Error bars indicate the maximum and minimum values of the measured parameters.

2.4 Stretch stage

Large non-equibiaxial compressive stress states are necessary for fabricating complex wrinkled structures. As these stress states are not accessible via techniques that are based on thermal and/or hygroscopic volumetric expansion, developing an alternate technique is necessary. In general, mechanical stretching and stretch release is an easily controllable and fast technique for generating a variety of large non-equibiaxial stress states. However, existing commercial mechanical stretch stages are unsuitable for integration into a wrinkle fabrication system. This is primarily because these stages have a large form factor relative to the sample size. This prevents one from (i) using such stages inside a metal deposition or plasma oxidation chamber and (ii) performing in-situ metrology during wrinkle formation. Herein, a compact yet accurate biaxial mechanical stretch stage has been designed and fabricated that overcomes these limitations. The small form factor of the stage enables one to integrate the stretching and stretch-release operations with the thin film generation process. Additionally, the stage has been registered to a metrology frame that enables performing in-situ visualization of wrinkle formation during stretch release. This section summarizes (i) the design and fabrication of the stage, and (ii) the performance of the stage.

2.4.1 Functional requirements

The purpose of the mechanical stage is to implement well-controlled uniaxial and biaxial stretching and stretch-release of PDMS films. A well-controlled stretching operation is one in which (i) loading conditions are close to the idealized uniaxial/biaxial loading conditions, (ii) errors during loading and/or clamping that have a significant influence on the wrinkle formation are low, and (iii) stretch values are accurately controlled. Here, ‘close to ideal ’, ‘low errors’ and ‘accurate’ are relative terms and scale with the desired precision and fabrication tolerance of the wrinkles. For example, when low amplitude wrinkles are desired, the accuracy of the strain must be of the order of the critical bifurcation strain that lies in the 0.1-0.2% range.

Stretching driven requirements

During uniaxial stretching, the desired stage motion is a translation along a fixed axis with no additional translations or rotations. Errors may arise due to (i) parasitic motions of the stage along the non-actuated directions, (ii) misalignment of the plane of clamping to the actuated direction, and (iii) misalignment of clamp ends with respect to each other. Misalignment of the clamp ends occurs when the clamping surfaces on the two ends are on different planes; this leads to undesirable out-of-plane bending of the PDMS film during clamping and stretching. The misalignments are schematically demonstrated in Figure 2.7. During biaxial stretching, the desired motion is a set of independent translations along two orthogonal axes. To enable this, clamping should be such that at each edge only the actuated direction is constrained. In addition to the errors during uniaxial stretching, the deviation from orthogonality due to misalignment of the actuated directions is another source of error during biaxial stretching.

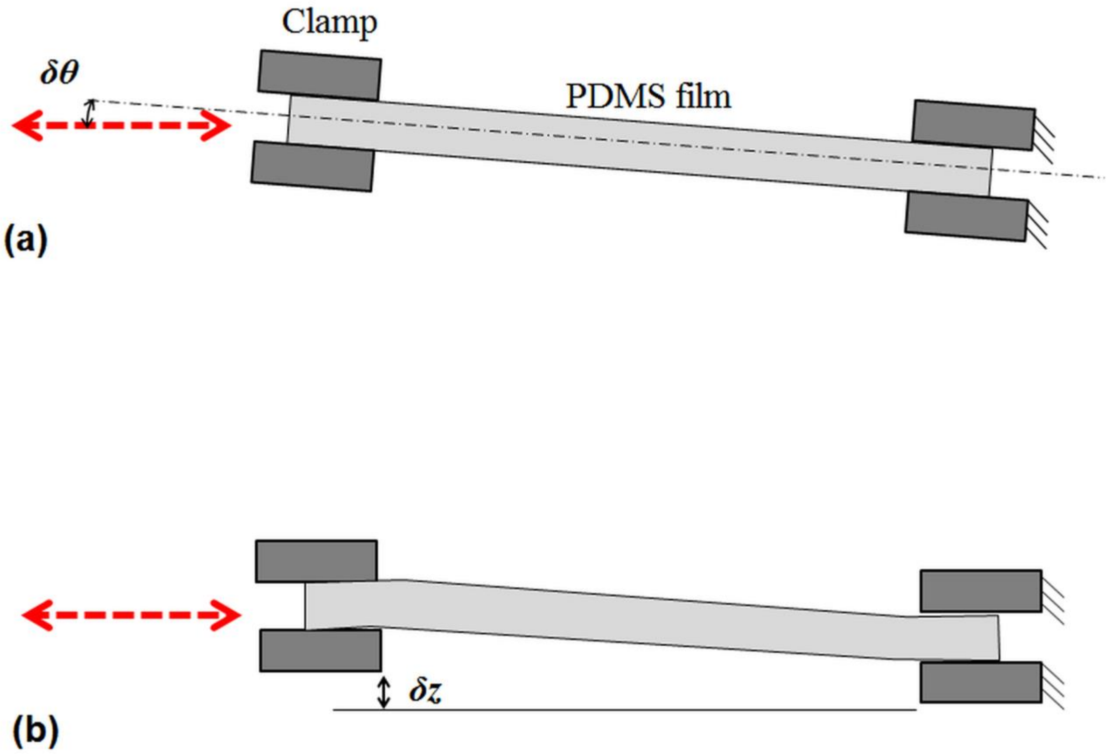

Figure 2.7: Schematic representation of the misalignment between clamped PDMS film and the stretch direction. (a) Angular misalignment between the stretch direction and plane of clamping. (b) Misalignment between the two clamped surfaces of the film.

Process driven requirements

In addition to motion based requirements, the stage must also satisfy the functional requirements that would enable successful integration with other steps of the fabrication process. These requirements are: (i) the device footprint must be smaller than the size of the plasma oxidation chamber and (ii) the ability to accurately register the stage to the vision/metrology system. The need for registration arises out of the need to perform in-situ process monitoring of wrinkle formation during stretch release. As the stage must be moved into the plasma chamber between the stretch loading and unloading steps, repeatable and accurate registration of the stage to the vision system is critical.

2.4.2 Stage design and fabrication

Here, a system has been designed and fabricated that satisfies the functional requirements for performing and visualizing wrinkle formation during uniaxial and biaxial stretching. A photograph of the system is shown in Figure 2.8. It consists of (i) a CMOS camera mounted on an X-Y-Z translation stage that forms the metrology frame and (ii) the biaxial stretch stage that is registered to the metrology frame.

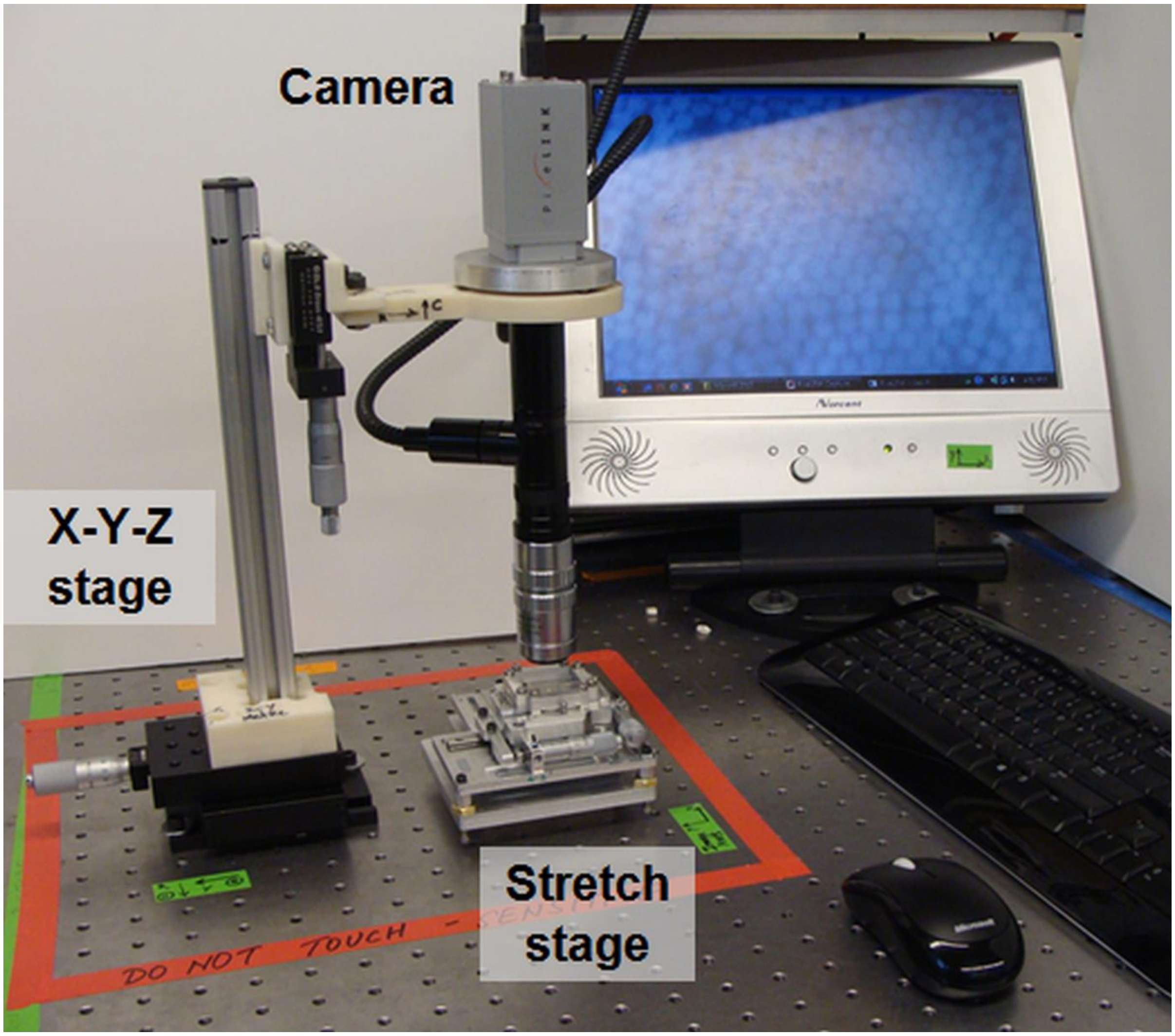

Figure 2.8: Photograph of the experimental set-up

System modules

The biaxial stage may be functionally separated into distinct modules as shown in Figure 2.9. These modules are: (i) fixtures to clamp and hold the PDMS film onto the stage, (ii) linear bearings for guiding motion, (iii) actuators for stretch/displacement control, (iv) base with kinematic coupling for registration, and (v) the structural frame. The purpose of the film clamping fixtures is to hold the edges of the PDMS film stationary along the actuated direction while allowing motion along the orthogonal in-plane direction. This is achieved by holding the film with custom fabricated compression clamps and then attaching these clamps onto the stage platforms via miniature linear ball bearings. This design implements rolling boundary condition at each clamped edge. The stage platforms are mounted on linear bearings and actuated individually and manually by micrometer heads. The purpose of kinematic couplings in the base is to implement a quick and accurate attach/detach mechanism to register the stage to the metrology frame. The structural frame serves the purpose of maintaining structural rigidity and providing alignment features for assembling the modules of the stage.

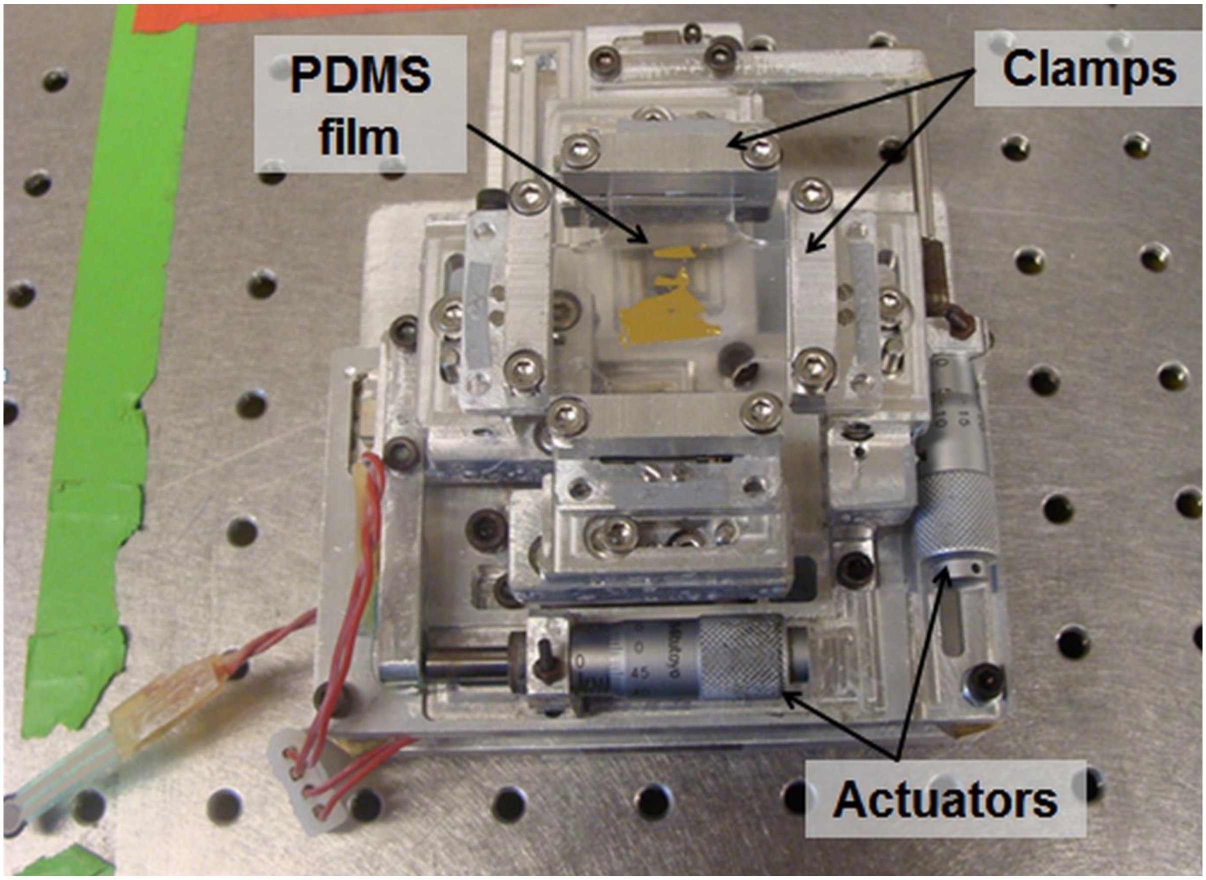

Figure 2.9: Photograph of the compact biaxial stretch stage. The bolt holes on the table are on a 1 inch square spacing. The PDMS film is partially coated with gold for visual clarity.

Film clamping

The edges of the PDMS coupon are held onto the stage platforms via custom-made compression clamps. These clamps were designed to provide a sufficiently high and repeatable compression during clamping. The clamping mechanism is shown in Figure 2.10. Each clamp consists of a set of two halves that when bolted together leave a fixed gap between them. The gap between the two parts is less than the thickness of the PDMS films. Thus, when the PDMS film is clamped between these parts, the amount of clamping compression in the film is repeatable and is determined by the difference in the film thickness and the predetermined gap between the clamp halves. A low clamping force is desirable so as to reduce the edge effects during wrinkle formation. However, the clamping force must be high enough to prevent film slippage along the clamps during stretching. Based on these considerations, the gap between the clamps (**g_c**) and the film thickness (**H**) are related to the maximum stretch (**ε_{max}**) as:

$$\frac{H-g_c}{H} > \frac{1}{\mu}\left(\frac{H}{l_c}\right)\varepsilon_{\max} \tag{2.8}$$

Here, **μ** is the coefficient of static friction between the clamp and PDMS, and **l_c** is the length of the PDMS film that is clamped in between the top and bottom halves of the clamp.

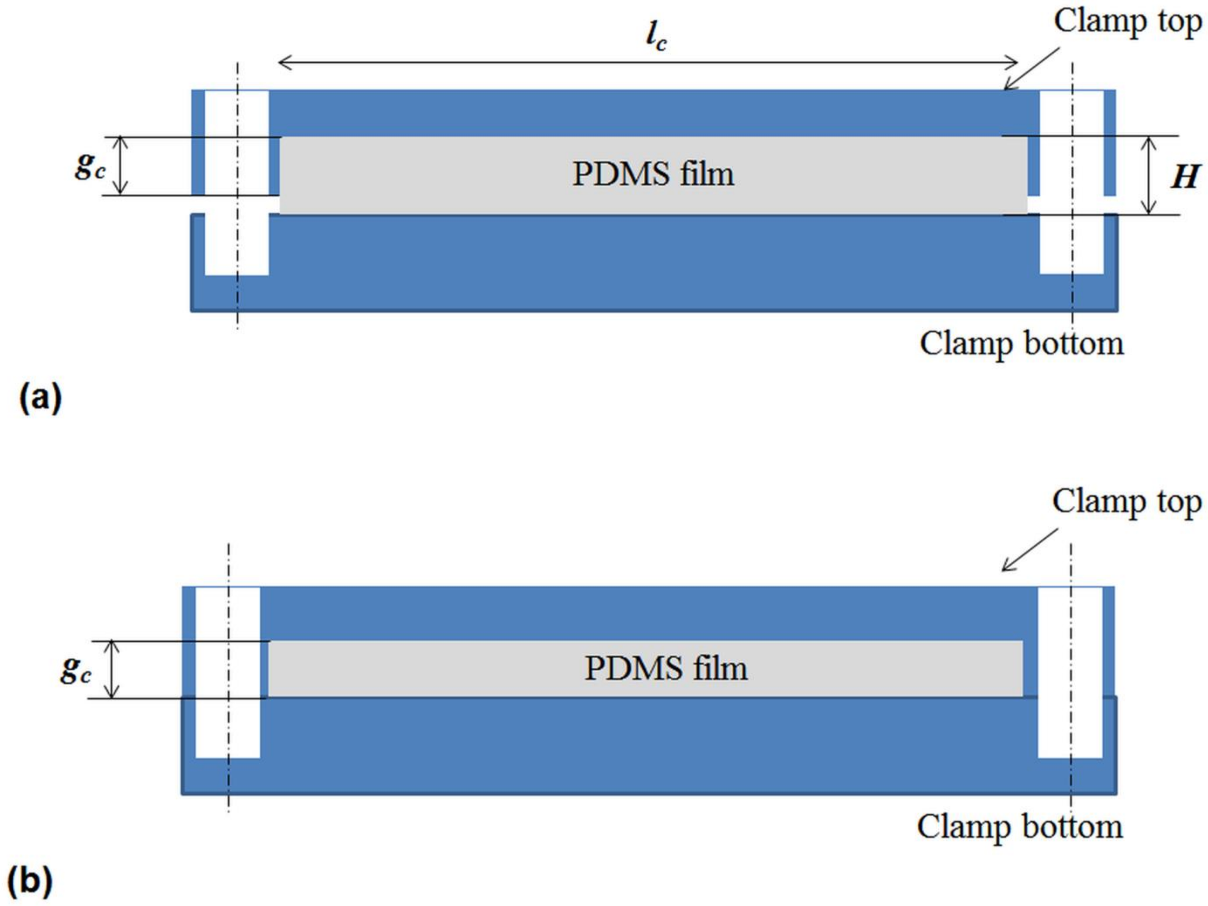

Figure 2.10: Clamping mechanism for holding PDMS coupons during stretching. (a) Cross-sectional view of the unclamped PDMS film located in between the top and bottom clamps. (b) PDMS film that has been clamped by compressing the film in between the top and bottom clamps.

Rolling edge conditions

To prevent over-constraint during biaxial stretching, it is necessary to allow the movement of edges along the non-actuated direction. For example, edges oriented along the ***X*** direction must be free to move along the ***X*** axis whereas edges along the ***Y*** direction must be free to move along the ***Y*** axis. When all four edges are clamped, over-constraint can be prevented by implementing rolling edge conditions at each of the edges. Rolling edge conditions were implemented by introducing miniature linear ball bearings between each of the clamps and the corresponding platforms. The bearings are oriented along the edges, thereby allowing linear motion between the stage and the clamp along the direction of the edges. To assemble these bearings, linear rails were mounted onto the stage platforms and the bearing stages were mounted onto the clamps. During biaxial loading, these roller bearings ensure that the stretches along the two axes are independent of each other.

Motion stage

The purpose of the motion stage is to provide the desired stretching motion while minimizing the errors. Based on the tradeoff for range versus accuracy, linear bearings based on the ball guide and rail mechanism were selected to guide motion along the two stretch axes. The linear guides along the two axes are oriented perpendicular to each other and can be independently actuated to stretch the PDMS film. To stretch the film, two orthogonal edges of the film are clamped onto stationary platforms and the corresponding opposing edges are clamped onto the moving platforms that are mounted on the linear guides. Actuation of each moving platform is performed manually via a micrometer head. As the two axes can be independently actuated, the stage may be used for both uniaxial and biaxial stretching. A CAD rendering of the designed stage is illustrated in Figure 2.11.

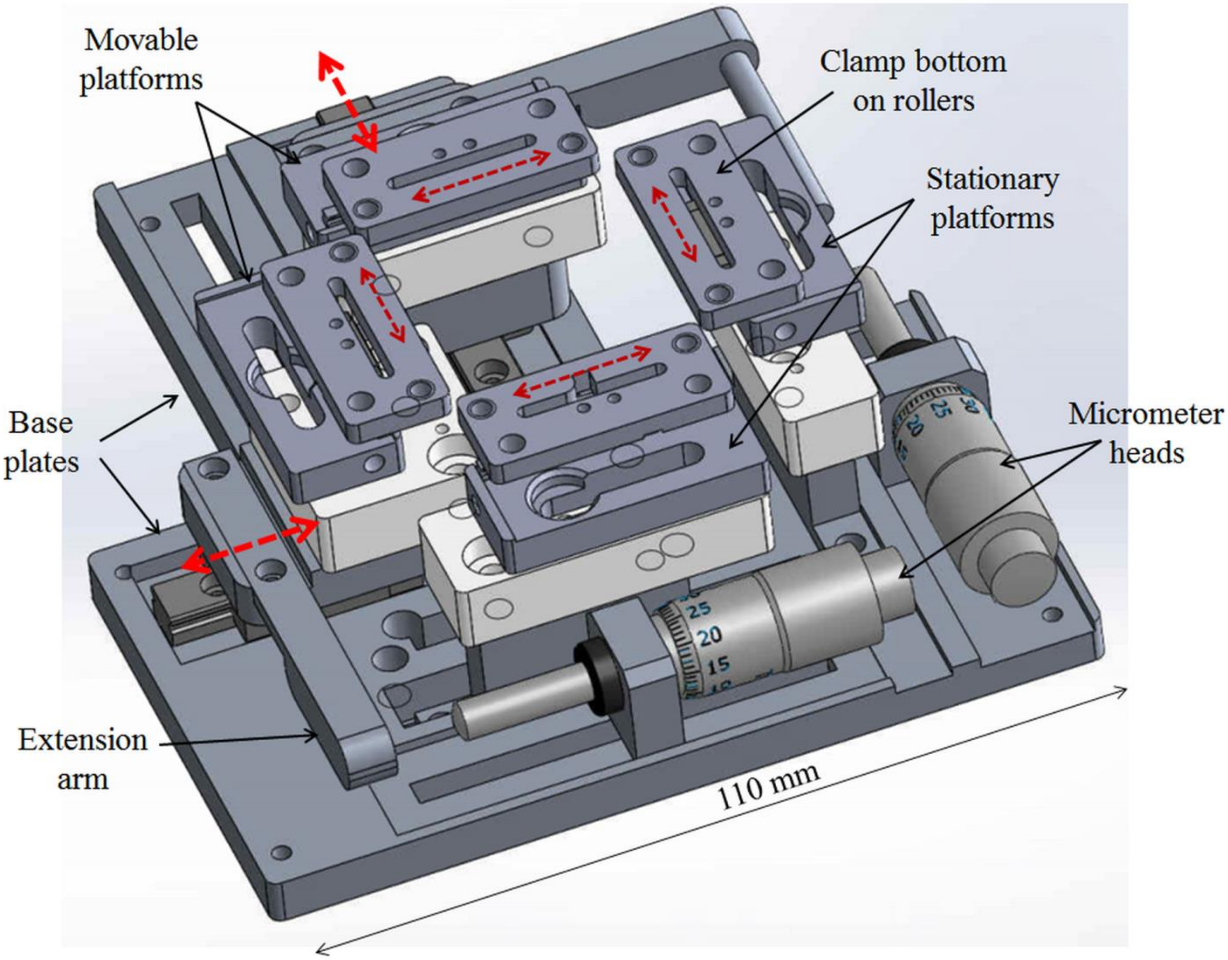

Figure 2.11: CAD rendering of the designed motion stage. The motion stage has two independently actuated axes. Each axis consists of a pair of stationary and movable platforms. PDMS films are clamped on top of these platforms and stretched by manually actuating the micrometer heads. Dashed arrows indicate the degree of freedom for the platform/clamp.

Alignment and stacking of motion stages

Machined alignment features and mating of precision machined surfaces were used to align and stack the two motion stages. Alignment features were used to perform in-plane alignment of (i) stationary platform perpendicular to the linear rail, (ii) actuation direction parallel to linear rails, and (iii) the two linear rails perpendicular to each other. To do so, linear bearings and the stationary platforms were first mounted and aligned onto separate base plates and then the two base plates were aligned to each other. On each plate, rail seat was first machined out and then this seat was used as a reference for machining out all in-plane alignment features. To ensure that all of the moving and stationary platforms are at the same height to within ±25 um, the following measures were taken: (i) platforms were fabricated to nominal dimensions such that stacking of the components of each platform would lead to the same nominal height and (ii) shim stock was used during assembly of the platforms. The final heights

Stage actuation

Micrometer heads that are mounted on each of the base platforms are used to manually and independently actuate the two movable stages. The resolution of these micrometer heads is 10 um and the maximum stretching that can be achieved is 13 mm. To reduce the overall size of the stretch stage and to integrate the heads onto the platforms, mechanical couplings between the micrometer heads and the movable platforms were eliminated. Instead, the micrometer heads push directly onto the extension arms of the movable platforms. Each micrometer head sits in between the movable and stationary platforms and sets the minimum distance between the two platforms. As the heads are not rigidly connected to the movable platforms, they are incapable of pulling the platforms. Therefore, during actuation the movable platforms are free to move away from the stationary platforms, but not toward them. When PDMS films are mounted onto the stage and stretched, tension in the film provides the restoring force to the actuation motion. This restoring force on the movable platform keeps it from moving further away while the platform’s position is held by the micrometer head. The PDMS film can be stretched further by actuating the micrometer to push onto the movable platform; whereas the tension can be released by actuating the micrometer in the opposite direction. Thus, actuation of the micrometer head can be used to control the tensile stretching of the film but cannot be used to apply compression.

The unidirectional actuation capability of the micrometer head arrangement has been used to accurately identify the zero stretch point during film stretching. During stretching and stretch release, the movable platform tracks the micrometer head and stays in contact with it as long as the restoring force due to tension exists. This restoring force has been measured as the contact force between the micrometer head and the movable stage using a force dependent resistor in half-bridge Wheatstone arrangement. The zero stretch point is identified within a tolerance band by measuring this contact force during displacement ramp-up or ramp-down. As a finite contact force is measured, the zero stretch point corresponds to a configuration with a small tensile stretch. Close to the zero stretch point, the tensile force may be comparable to the bearing friction. However, as the actuators are displacement controlled, a tensile component always exists in the measured contact force. Thus, the extension values corresponding to measurements of the micrometer head are never higher than the actual extension but could be lower by as much as the zero point tolerance. The actual extension (***ε***) is related to the measured extension (***ε*****m**), the contact force corresponding to the zero point tolerance (***δF***), the stiffness of the film (***k***), and the clamped length of the film (***l*****c**) by:

$$\max(\varepsilon) = \varepsilon_m + \frac{\delta_F}{l_c k} \tag{2.9}$$

For the system designed here, the smallest force that can be accurately measured is 100 mN. For the stamp size used here, this corresponds to an error of 0.06% in the zero point of the stretch (***ε***). This is about 2 to 5 times less than the critical strain for wrinkling bifurcation and is substantially less than the operating strains of 5-15%.

Registration to metrology frame

Kinematic couplings were used to implement a quick and repeatable attach/detach mechanism to register the stage to the metrology frame. One half of the kinematic coupling is aligned and rigidly attached to the metrology frame whereas the other half is aligned and attached to the stretch stage. Preload to the coupling is provided by a pair of permanent magnets that are attached to the coupling halves. The stage can be registered to the vision system by engaging the two halves of the coupling. Registration of the stage to the metrology frame involves aligning and locating the coordinate frames of the two systems with respect to each other. This requires: (i) aligning the in-plane axes (***X***-***Y***) of the scanning stage of the vision system along the in-plane axes of the stretch stage, (ii) aligning the ***X***-***Y*** plane of the vision system, i.e., the focal plane of the microscope to the ***X***-***Y*** plane of the stretched film surface, and (iii) locating a point in the ***X***-***Y*** plane of the stretched film within the ***X***-***Y*** focal plane of the vision system. To enable quick registration, alignment is performed in two steps. First, an initial alignment is performed to achieve these registration requirements; then the kinematic couplings are used to maintain the registration during repeated engagement/disengagement of the stage from the metrology frame.

Thermal management

The film generation step of plasma oxidation is the primary source of heat during the wrinkling process. This step may impact the process performance by generating undesirable thermal strains that distort the intentionally applied mechanical strain. Additionally, the positional accuracy during imaging may be adversely affected due to thermal expansion of the stage. Here, passive thermal management schemes have been used to ensure that the mechanical stretch is minimally distorted by thermal strains and to hold positional accuracy during imaging.

Thermal strains during film generation were managed by (i) performing intermittent plasma oxidation with a maximum continuous exposure time of five minutes to prevent overheating of the stage and (ii) limiting the rise in temperature by increasing the thermal mass of the stage. The thermal mass of the stage was increased by attaching strips of a phase change material with a transition temperature of 50 ^{0}C on the exposed surfaces of the stage. These schemes minimize the thermal errors associated with the film generation process. After film generation, the stage is cooled down to room temperature before performing any subsequent operation. This ensures that heating of the stage has minimal influence on position measurements during imaging.

The goal of thermal strain management was to maintain the thermal strains lower than the critical wrinkling strain ($\boldsymbol{\varepsilon_c}$); under this condition, thermal strains alone would not lead to wrinkled surfaces. Due to the layout of the mechanical constraints, there is no thermal strain in the PDMS due to thermal expansion of PDMS. A stick figure model of the constraint layout of a single stretch axis is shown in Figure 2.12. As the stiffness of PDMS is at least three orders of magnitude less than the stiffness of the base/micrometer, all of the thermal strain in PDMS is due to expansion of the micrometer head and the base of the stage. Thus, the thermal strain ($\boldsymbol{\varepsilon_t}$) in the constrained PDMS film that arises due to a uniform temperature rise of $\boldsymbol{\Delta T}$ is given by:

$$\varepsilon_t = \Delta T\left(\frac{\alpha_b L_b + (L_s - L_b)\alpha_a}{L_s}\right) \tag{2.10}$$

Here, $\boldsymbol{\alpha_a}$ and $\boldsymbol{\alpha_b}$ are the coefficient of linear thermal expansion of the actuator and the base, $\boldsymbol{L_s}$ is length of the prestretched PDMS coupon, and $\boldsymbol{L_b}$ is the distance of the base of the actuator from the fixed platform. The temperature rise necessary for a thermal strain equal to the critical bifurcation strain can be estimated with the following values: $\boldsymbol{L_s}$ =43 mm, $\boldsymbol{L_b}$=18 mm, $\boldsymbol{\alpha_a}$=13e-6/K, $\boldsymbol{\alpha_b}$=22.2e-6/K, and $\boldsymbol{\varepsilon_c}$=0.1%. The maximum allowable temperature of the stage can then be estimated to be 59.3 ^{0}C.

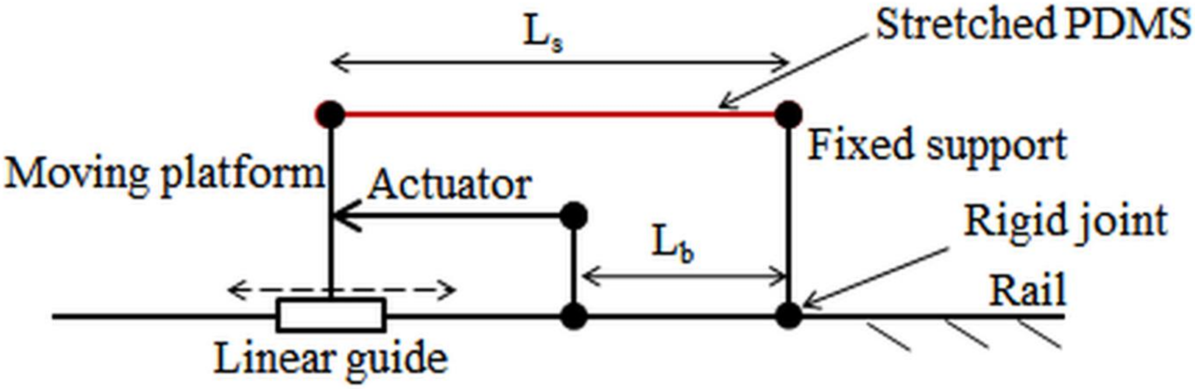

Figure 2.12: Stick figure model depicting the layout of constraints for a single stretch axis. Circles represent rigid connectors. The displacement-based actuator is capable of only pushing onto the moving platform; it cannot pull the moving platform. All straight lines, except the PDMS film, represent rigid members.

To verify the efficacy of the passive thermal management scheme, temperature at various spots on the stage was measured after plasma exposure of an unstretched PDMS film for 90 minutes. The exposure cycle consisted of 5 minutes of continuous exposure followed by a five minute off time. Immediately after the 90 minute exposure cycle, temperature at various spots on the stage was measured using a thermocouple. The temperature was observed to vary from 60 ^{0}C to 50 ^{0}C over the surface of the stage. The maximum temperature was observed on the clamps and the minimum was observed on the exposed surface of the actuation arm. The surface of the exposed PDMS film was examined under an atomic force microscope to verify that no wrinkles were formed under thermal strains. No wrinkles were observed and the surface roughness of the PDMS film was measured as 3.5 nm. This justifies the approximation that the thermal strain effect during plasma oxidation is negligible during mechanical stretching on this stage.

Table 2.2: Performance of the biaxial stretch stage

Metric	**Value**
Resolution	10 um
Range of motion	13 mm
1-D PDMS film length	37.5 mm
2-D PDMS film length	43 mm
Footprint	131 mm X 110 mm X 75 mm

2.4.3 Performance of stage

The performance of the stage is summarized in Table 2.2. With a displacement resolution of 10 um, the corresponding prestretch resolution is 0.027% for a 1-D film and 0.023% for a 2-D film. The maximum prestretch that may be applied to the films is 34.7% for a 1-D film and 30.2% for a 2-D film.

2.5 In-situ metrology

In-situ visualization of wrinkle formation coupled with accurate surface scan provides valuable information about the wrinkling process that is not available via off-line measurement systems. For example, in-situ visualization enables tracking the growth of wrinkle modes as the prestretch in the PDMS film is released. Herein, in-situ metrology is performed via an optical microscope that is mounted on a manually actuated X-Y-Z stage. The X and Y stages enable scanning the sample surface over a 25 mm X 25 mm area with a step size of 10 um along each direction. The Z stage enables focusing the microscope onto the wrinkled surface. The images recorded by the microscope camera were processed using LabVIEW Vision Builder AI 2012 software. These images may be analyzed to quantify (i) the spatial variation of the period and morphology of the wrinkles and (ii) the evolution of period and morphology with prestretch release. The vision system and the protocol for image analysis are discussed in this section.

2.5.1 Vision system

A custom stereomicroscope was assembled to satisfy the need for in-situ visualization of wrinkle formation via a system that enables quick and accurate registration of the metrology frame to the PDMS stretch stage. The microscope consists of (i) optics for image magnification, (ii) an illuminator for coaxial illumination (iii) a 5.0 MP CMOS camera (PixeLINK PL-B777U) to record the magnified image, and (iv) an X-Y-Z stage to scan the sample surface and to focus the microscope. The components of the vision system are indicated in Figure 2.8. As this microscope does not use transmitted light for imaging, there are no microscope components below the lens. Thus, the PDMS stretch stage can be freely positioned in the space below the microscope lens. The stretch stage is registered to this microscope by registering it to the fixed base of the X-Y-Z stage on the microscope. The microscope was calibrated using a 1 mm microscope stage ruler with 10 um divisions (R1L3S2P) that is available from Thorlabs. Specifications of the microscope optics are listed in Table 2.3 and those of the camera are listed in Table 2.4. This system enables recording grayscale reflected-light images of the wrinkled surface with a magnification of 35.1X and a captured area of 163 um X 122 um.

Table 2.3: Specifications of the optical microscope

Parameter	**Value**
Imaging mode	Reflected light stereomicroscope with coaxial illumination
Vendor	Navitar, Ultra Precise Eye
Nominal magnification	36.4X
Calibrated magnification	15.94 pixels in camera image = 1 um in real world
Objective	20X infinity corrected objective with 2X adapter
Numerical aperture	0.42
Working distance	20 mm
Depth of field	~ 4 um
Lateral resolution	~ 0.86 um

Table 2.4: Specifications of the digital camera

Parameter	**Value**
Image acquisition	CMOS sensor with rolling shutter
Sensor pixel pitch	2.2 um X 2.2 um
Frame size	2592 X 1944 pixels
Imaged area	163 um X 122 um
Frame rate	7 Hz
Image type	8 bit grayscale

2.5.2 Image analysis

An automated image analysis protocol was developed to enable quick, repeatable, and reliable analysis of the images. The grayscale image recorded by the camera represents the intensity of the light that is reflected by the wrinkled surface. One such image is shown in Figure 2.13. Wrinkles can be identified in this image as the alternating bands of light and dark regions. These bands correspond to regions of high and low amplitude, i.e., the peaks and valleys of the wrinkles. Thus, each pair of a light and a dark band represents a single wrinkle. The period of wrinkles was measured by counting the number of wrinkles over a fixed length. The angle of wrinkles was measured by recording the angle of the bands with respect to the image axis or to any other reference line. To measure the period and angle of wrinkles based on this scheme, one must first accurately identify and locate the edges of the light or dark bands. LabVIEW Vision Builder AI 2012 software was used to computationally perform these edge identification and location operations. The inset in Figure 2.13 shows the result of one such edge identification operation. The spacing, location, and orientation of the edges was then used to compute the period and angle of the wrinkles.

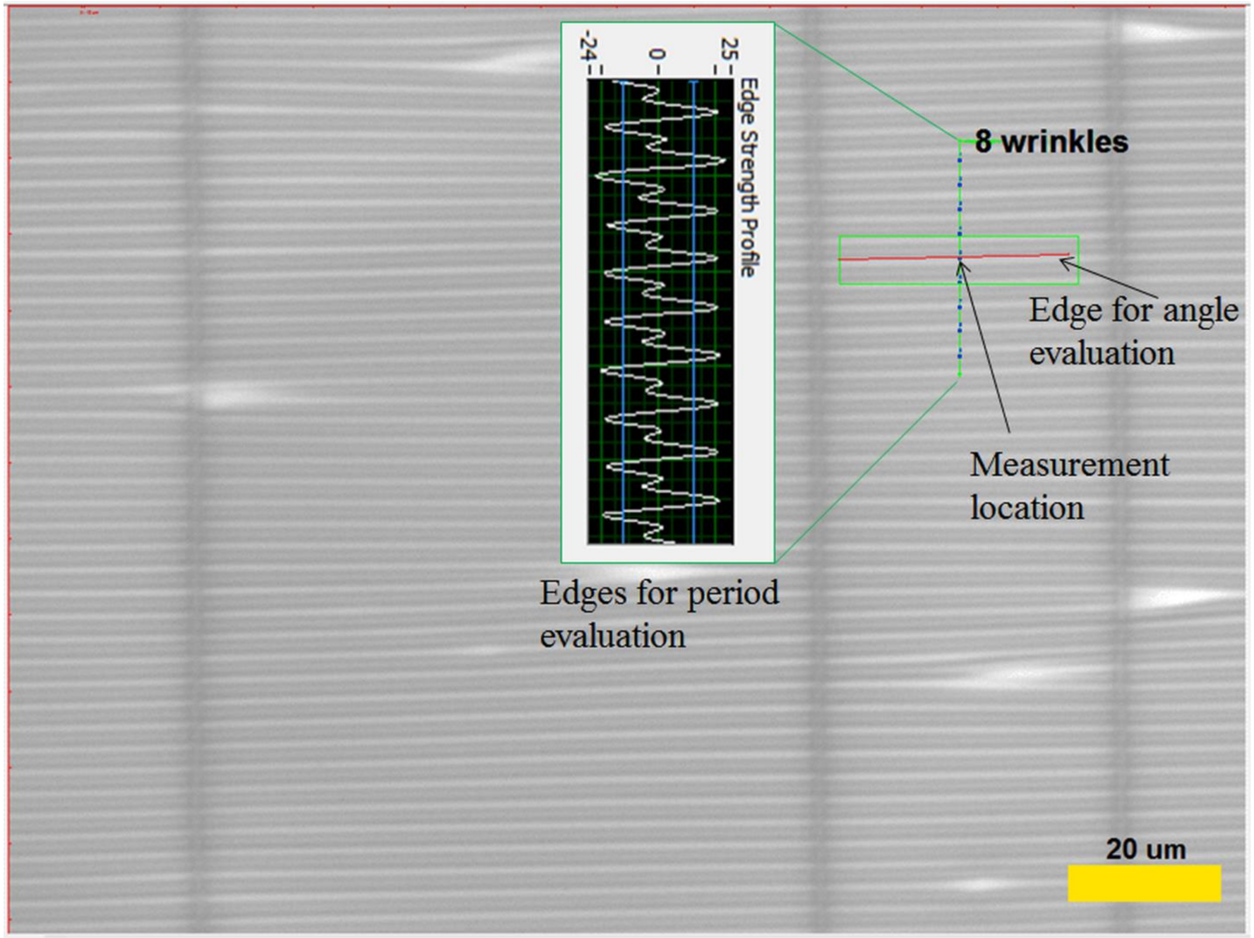

Figure 2.13: Image of a wrinkled surface as captured by the microscope. Inset shows the grayscale intensity profile along a vertical line.

The algorithm for image analysis is summarized in Figure 2.14. For measurement of period and angle of wrinkles at a desired point, the edges of light and dark regions are identified along a vertical line through that point. The angle of wrinkles is evaluated as the angle of the wrinkle edge with respect to the horizontal. The period of wrinkles is first obtained from the average number of wrinkles per unit length along the vertical line and then corrected for the angle of the wrinkles. The measured period (**λ_m**) is given by:

$$\lambda_m = \frac{|y_n - y_1|}{n-1}\cos(\theta_m) \qquad \textbf{(2.11)}$$

Here, **y_i** is the vertical location of the **i^{th}** edge, **n** is the total number of edges and **θ_m** is the angle of the wrinkles with respect to the horizontal as measured at the measurement location. The period is evaluated as an average over at least 7 periods, i.e., n ≥ 8 for all measurements. The standard deviation (**$\delta\lambda_m$**) of the period is given by:

$$\delta\lambda_m = \sqrt{\frac{\sum_{i=2}^{n}\left((y_i - y_{i-1}) - \lambda_m\right)^2}{n-1}}\cos(\theta_m) \qquad \textbf{(2.12)}$$

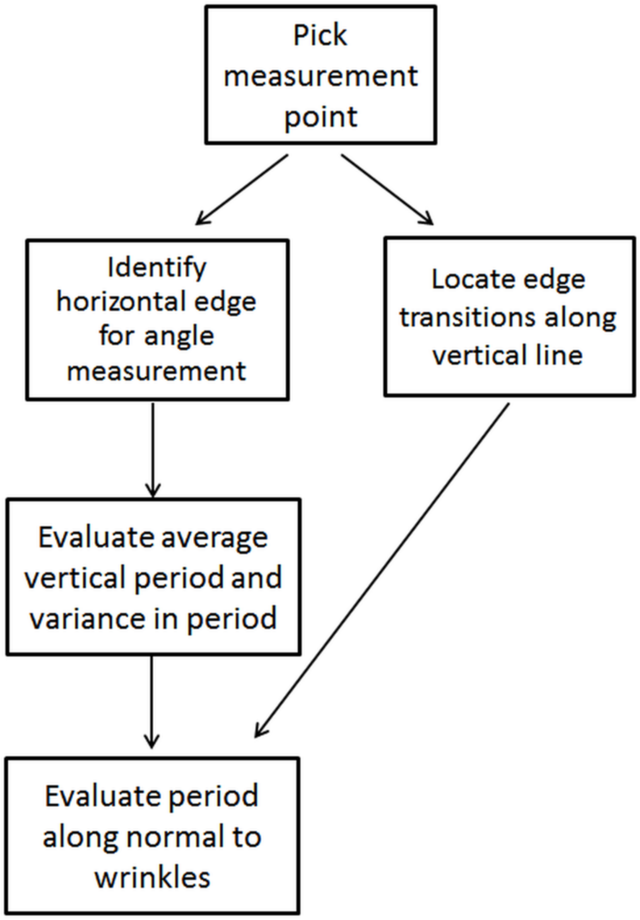

Figure 2.14: Algorithm for image processing.

The in-situ metrology system developed here enables one to study the wrinkle formation process by measuring the period and orientation of wrinkles during prestretch release. If additional information such as amplitude of the wrinkles is required, then one must employ off-line metrology techniques such as an atomic force microscope.

2.6 Plasma oxidation process

When PDMS samples are exposed to air plasma, a thin stiff glassy layer is generated on top of the exposed surfaces of the samples via oxidation of PDMS [15]. The thickness and Young's modulus of this oxidized film can be tuned by controlling the power and exposure time of plasma oxidation. Thus, bilayers of the desired geometry and material properties may be generated by tuning the plasma oxidation process. As such, plasma oxidation is a low-cost technique for generating the bilayers that are required for fabrication of wrinkles. To enable predictive design and fabrication of wrinkles via this technique, one must link the parameters of the plasma oxidation process to the wrinkling process parameters. This section summarizes (i) the calibration process for linking plasma oxidation parameters to period and amplitude of wrinkles, (ii) measurement of the Young's modulus of the thin film, and (iii) quantification of the spatial variation in the period of wrinkles over the surface of the oxidized PDMS film.

2.6.1 Calibration of plasma asher

The effect of the plasma oxidation process parameters on the thin film properties may be indirectly measured by measuring the period and amplitude of the wrinkles. Here, an RF plasma asher has been calibrated to enable controlling wrinkle periods via control of the plasma exposure time and power. The calibration process involves (i) fabricating wrinkled surfaces at different plasma exposure time intervals and power levels and (ii) off-line measurement of the period and amplitude of the wrinkles on an atomic force microscope. The calibration data is summarized in Figure 2.15. All data points were collected at a constant prestretch release of 15% and for a PDMS curing ratio of 12:1. This calibration chart is valid for the exposure time of 1 – 16 minutes. If smaller periods are desired, one must recalibrate the plasma oxidation chamber for low exposure times.

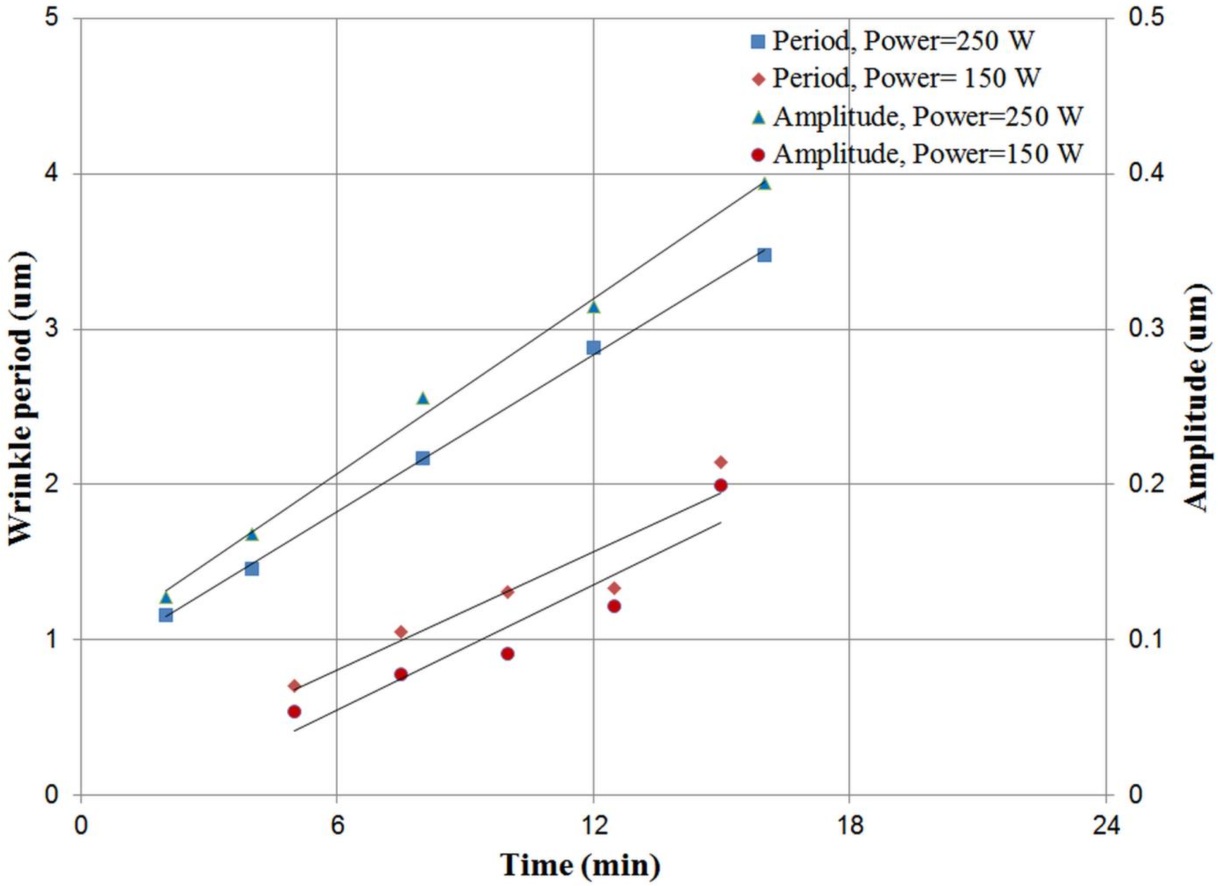

Figure 2.15: Calibration chart for estimating the period of wrinkles from the plasma exposure time. Period and amplitude were measured using an AFM. Error bars are smaller than the data point markers.

2.6.2 Young's modulus of film

The stiffness of the top film is an important process parameter that determines the period and amplitude of wrinkles. However, the stiffness modulus of the top glassy film that is generated via plasma oxidation is not well-known. Hence, the Young's modulus of the top film was measured directly using an atomic force microscope (AFM). This was performed by measuring the force versus displacement response of the top surface of the bilayer during shallow indentations by a sharp AFM tip. The Young's modulus was then obtained by fitting the force versus displacement data to the Hertz contact model. Measurements were performed on an Asylum Research MFP 3D Bio AFM system with a conical silicon tip of tip radius < 10 nm. As the Hertz model is accurate only for small indentations on the order of 5-10% of the film thickness, a sample with a film thickness greater than 150 nm was used. The sample was prepared by exposing unstretched bare PDMS of 12:1 curing ratio to air plasma for 105 minutes.

The Young's modulus obtained from the indentation tests are shown in Figure 2.16. As the indent depth is increased, it is observed that the measured modulus decreases. This is primarily due to the effect of the underlying soft compliant base layer that is "sensed" by the AFM tip during deeper indentations. Thus, shallower depths are necessary for accurate measurements. However, the noise to signal ratio in the measured data increases with a decrease in the indentation depth due to the corresponding decrease in the contact force. As a compromise, an intermediate depth of 8 nm was selected to estimate the Young's modulus of the top film as 3.2 ± 0.78 GPa. This measured modulus is much less than that of fused silica glass (~ 70 GPa) but at-least 1,000 times that of the base layer. Thus, even though the oxidized top layer is not identical to glass, it is sufficiently stiffer than the base layer to produce wrinkles at moderate compressions of 5-20%.

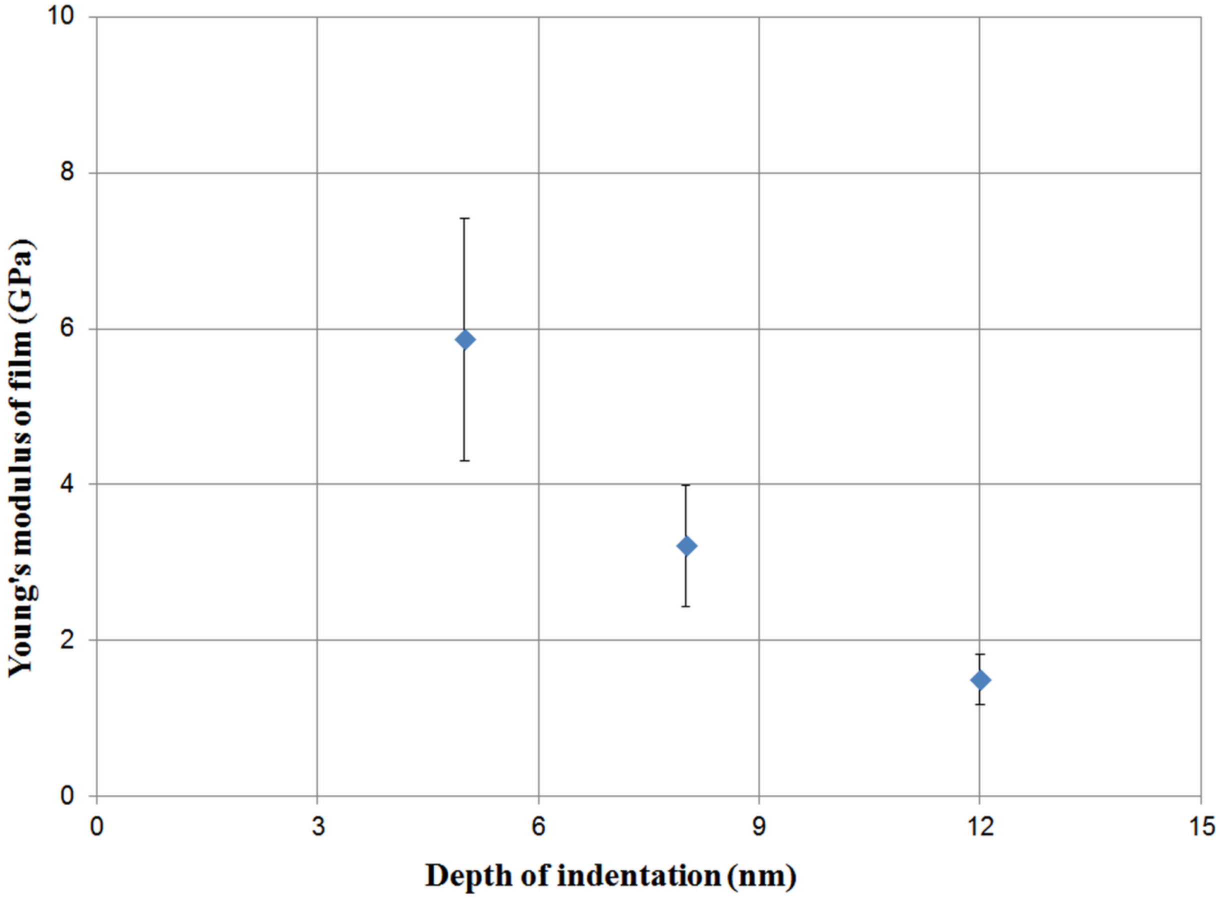

Figure 2.16: Young's modulus of the top film as measured by nano-indentation tests that were performed on an atomic force microscope.

2.6.3 Uniformity of plasma oxidation

Uniformity of patterning is a critical manufacturing metric that must be quantified when predictive design and fabrication of wrinkled patterns is desired over a large area. However, studies in the past have failed to quantify or characterize the uniformity of wrinkle generation. Lack of in-situ metrology has been a major roadblock in characterizing uniformity. Here, the in-situ metrology system has been used to quantify pattern uniformity by (i) mapping the spatial variation of period over the PDMS surface and (ii) tracking the change in period with prestretch release.

The spatial variation of period and the evolution of period with prestretch release are shown in Figure 2.17. It is evident from the figure that the period of wrinkle depends on both the location of the measurement point and the extent of the prestretch release. Thus, the effect of these parameters must be accounted for and/or controlled during any subsequent experiments. One of the techniques used in this work has been to perform experiments at a constant prestretch release and to measure the wrinkle period at a fixed spatial location.

As the observed spatial variation of the wrinkle period is of the same order as the variance in the measured period, a definitive quantitative link between spatial location and period cannot be established. Nevertheless, the following qualitative conclusions may be drawn from the observations: (i) the period of the wrinkles increases with an increase in the distance from the fixed end along the stretch direction and (ii) the period decreases with an increase in the distance from the centerline along the direction orthogonal to the stretch direction. Both of these trends are supported by the expected variation in the prestretch values due to edge effects.

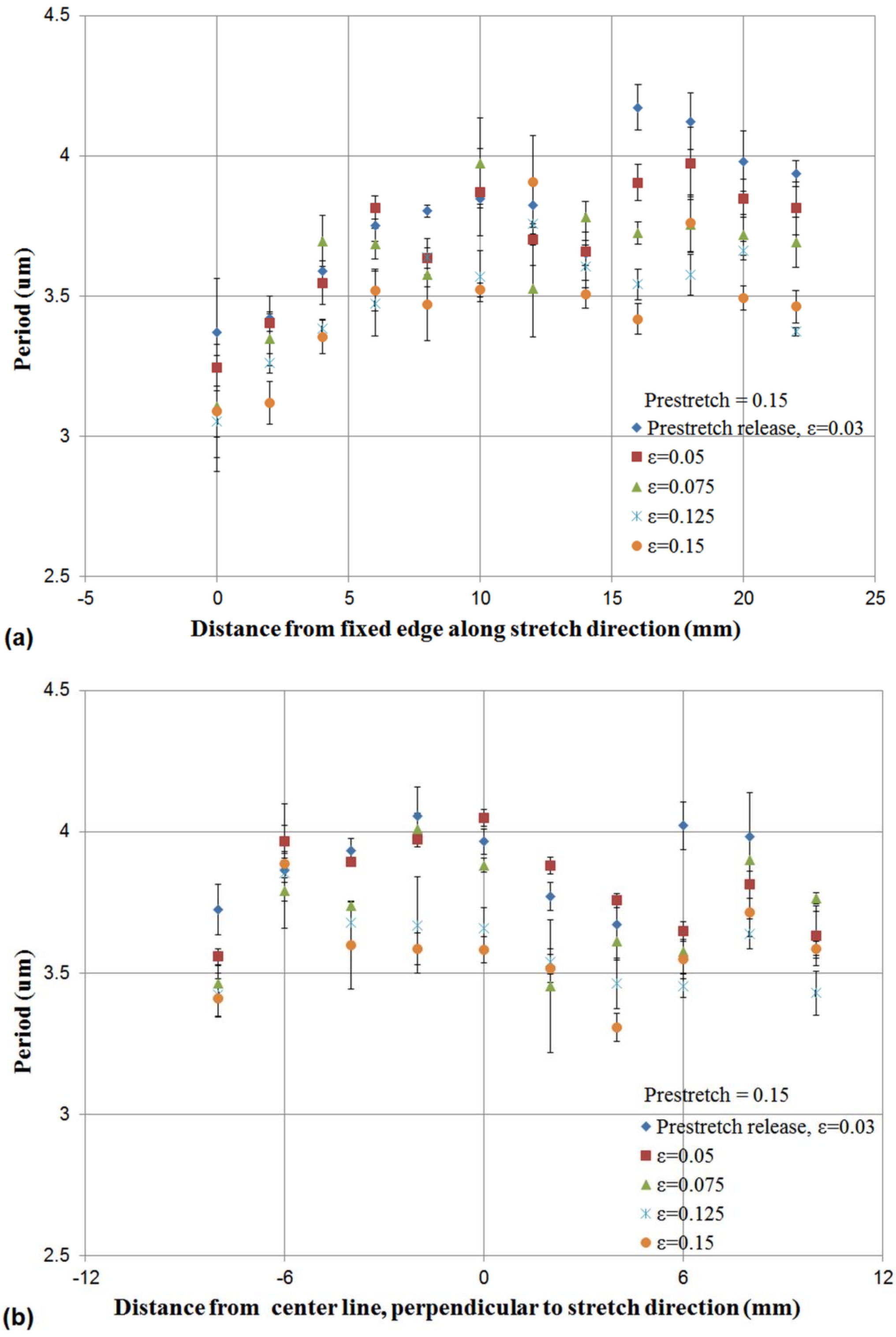

Figure 2.17: Spatial variation of period at different values of prestretch release. (a) Variation of period along the centerline oriented along the prestretch direction, (b) Variation of period along the centerline oriented perpendicular to the prestretch direction. Distances are as measured in the non-deforming metrology frame of reference. Error bars indicate the standard deviation of measured period.

The effect of prestretch release on the period can be separately studied by spatially averaging the period at each of the prestretch release steps. The spatially averaged periods at different prestretch values are shown in Figure 2.18. Error bars in the figure denote the standard deviation in the period that is measured at different locations on the PDMS surface. Thus, error bars quantify the non-uniformity of wrinkle period. This non-uniformity is of the order of 5 – 6.5 %. From the data represented in Figure 2.18, it is also observed that the spatially averaged period decreases as the prestretch is released. This observation is not predicted by the linear elastic model represented by Eq. (1.3) that is based on the non-deforming coordinate system. As the experimental observation of period is based on the deformed configuration of the bilayer, one must use the deformed coordinate system to interpret these observations. On prestretch release, the period decreases due to the compression of the deformed coordinate system. This effect has been studied further in Sec. 2.7.2 by tracking the evolution of period with prestretch release at a single material point.

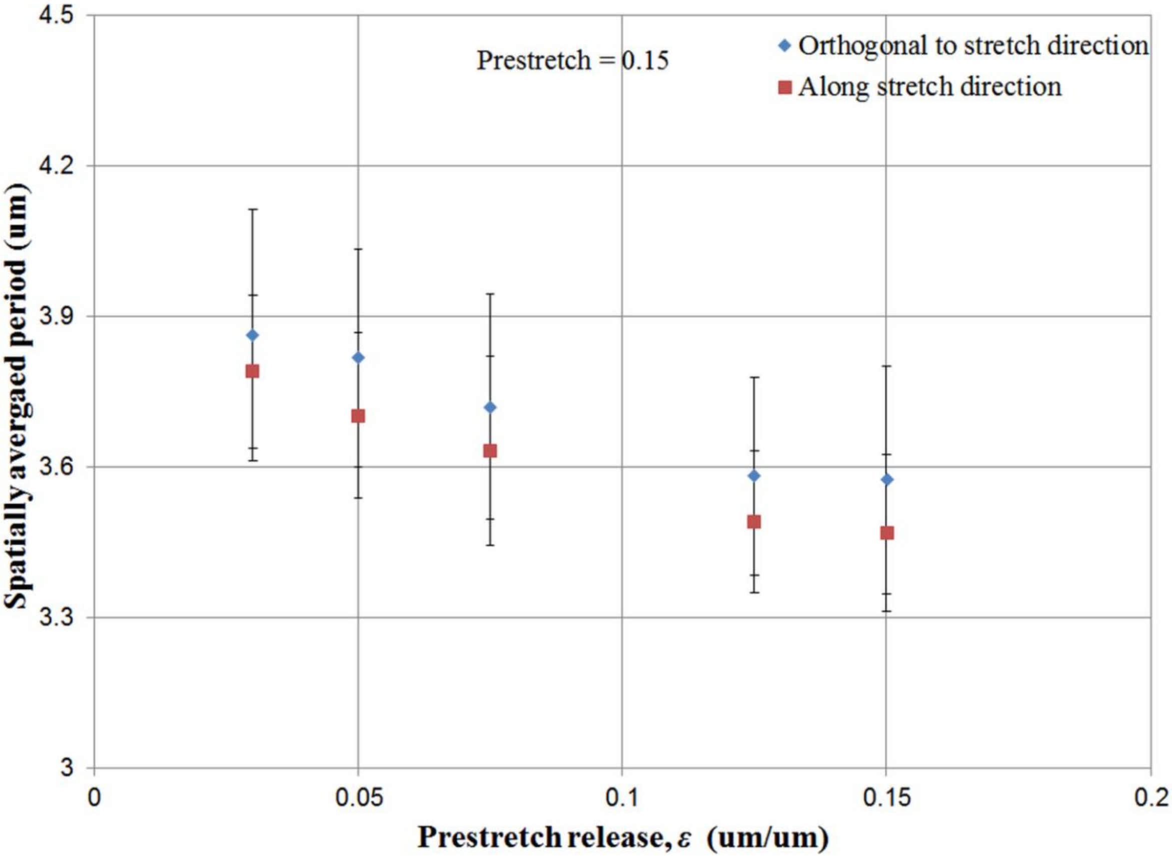

Figure 2.18: Effect of prestretch release on period of wrinkles. Period is obtained by spatially averaging the mean period measured at different locations on the two centerlines of the PDMS film. Error bars indicate the standard deviation of the mean period measured at different locations.

2.7 Parametric analysis

2.7.1 Effect of elastic modulus of base

Elastic modulus of the base is an important process parameter that may be used to tune and/or control the period of wrinkles. As demonstrated in Sec. 2.3.4, tuning the curing ratio of PDMS is a convenient technique for varying the elastic modulus of the base. Here, experiments have been performed to quantify the effect of change in elastic modulus of the base on the period of wrinkles by varying the curing ratio. This quantification would enable one to (i) confirm the 1/3rd power law dependence of period on elastic modulus of the base and (ii) verify whether the effect of curing ratio on wrinkle periods is solely through the elastic modulus of the base. Results of the experiments have been compared with the predictions from finite element analysis and with the linear elastic model. Details of the finite element modeling are discussed later in Chapter 3.

Results of the experiments performed to link the period of wrinkles to the elastic modulus of base are summarized in Figure 2.19. The figure shows that the period decreases with an increase in the shear modulus of the base. Experiments also confirm the 1/3rd power law dependence of period on elastic modulus of the base except for one outlier data point. This outlier point corresponds to the curing ratio of 6:1 and does not conform to the 1/3rd power law. Experiments were repeated several times at this curing ratio to confirm this outlier behavior. A lower-than-expected period was consistently observed at this curing ratio indicating a physical basis for this outlier behavior. Thus, the effect of curing ratio on wrinkles is not solely through the elastic modulus. This outlier behavior has also been observed by others [67] and stems from the over-crosslinked base for the case of a 6:1 curing ratio. This over crosslinking restricts the growth of the top layer and leads to lower than expected period of wrinkles. As such large anomalies have not been observed at other curing ratio, it can be approximated for these cases that the effect of curing ratio on period is entirely via the modulus of the base. Thus, in the operating region of curing ratio of 8:1 to 15:1, tuning the curing ratio is a reliable technique for controlling the wrinkle period.

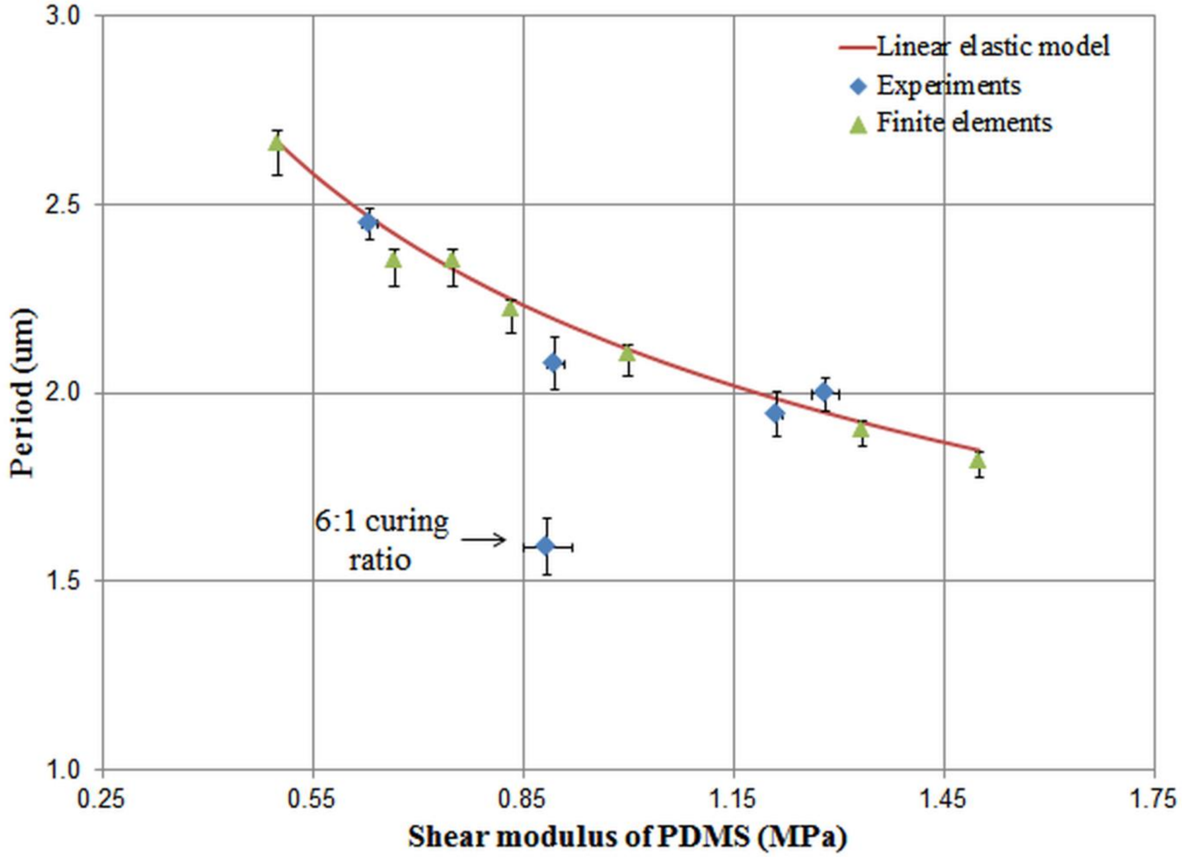

Figure 2.19: Effect of shear modulus of PDMS base on the period of wrinkles. Experiments were performed with 15% base prestretch and full prestretch release. Linear elastic estimate was evaluated by fitting the linear model to the results of the finite element analysis for the case of the lowest shear modulus. Parameter fitting was performed to evaluate properties other than the shear modulus while preserving the 1/3rd power law dependence of period on base shear modulus. The outlier data point is for the case of 6:1 curing ratio.

2.7.2 Effect of prestretch release

As the stretch in the sample is released it is observed that the period of the wrinkles decreases. The analytical model represented by Eqs. (2.1)-(2.3) does not predict this decrease in period with prestretch release. A simple predictive model can be obtained by making the approximation that the number of wrinkles does not change as the prestretch is released. Thus, the period of the wrinkles can be estimated as:

$$\lambda = \lambda_o \left(\frac{1+\varepsilon_p - \varepsilon}{1+\varepsilon_p - \varepsilon_o} \right) \tag{2.13}$$

Here, λ is the period at the current pre-stretch, ε is the current pre-stretch that has been released, and λ_o is the period when a pre-stretch of ε_o is released. This relationship was verified against experiments as shown in Figure 2.20. These experiments were designed to minimize the effect of spatial non-uniformity in the measured period. This was achieved by moving the microscope along with stage actuation. This ensures that the microscope tracks a material point on the wrinkled surface as the prestretch in the base is released. A rigorous model based on the finite deformation effect has been developed by Jiang et al. [61]. However, their model provides only a marginal improvement in predictive accuracy with respect to the elegant model that is based on constant number of wrinkles. Hence, as a first approximation, Eq. (2.13) may be used to predict the change in period of the wrinkles as the prestretch in the base is released.

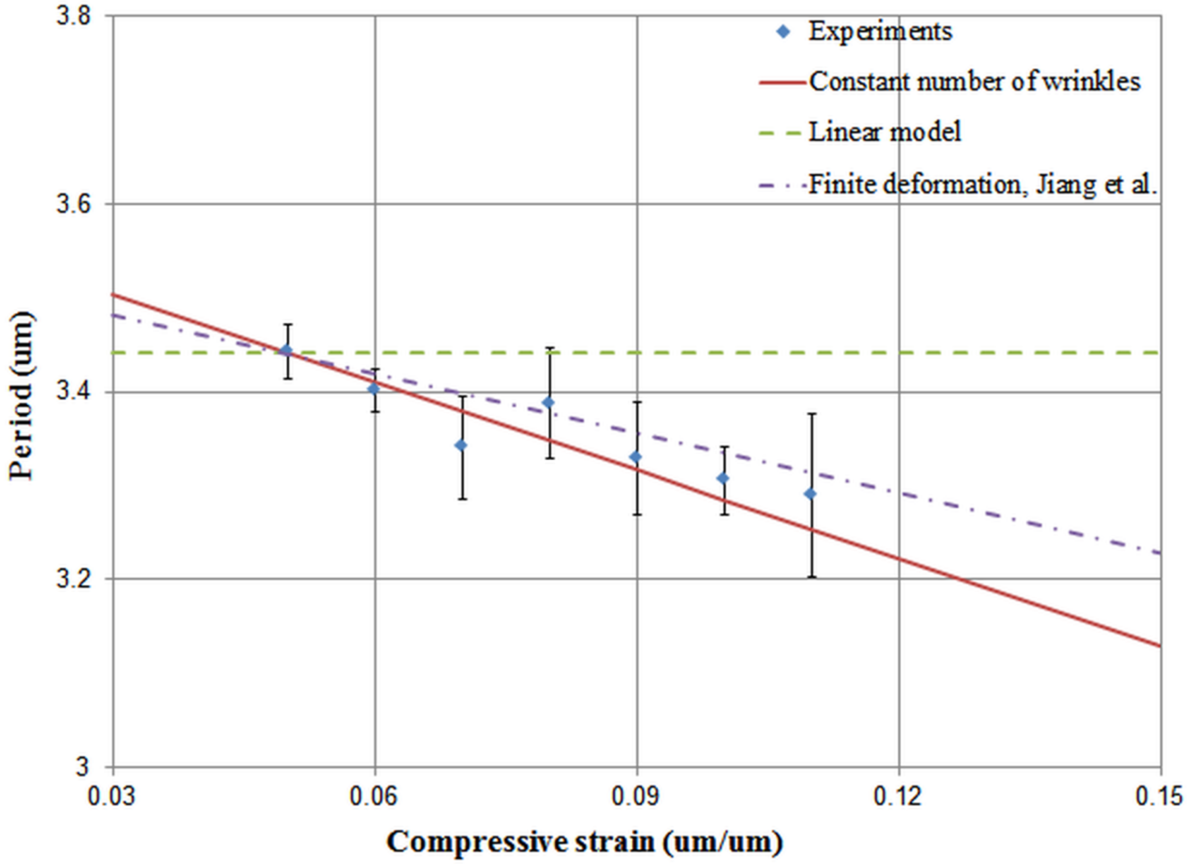

Figure 2.20: Effect of compressive strain generated via prestretch release on the period of wrinkles. A prestretch of 15% was applied to the base. All three models were calibrated using the period measurement at 5% prestretch release.

Chapter 3

Computational tools: Finite element analysis

3.1 Introduction

As currently available analytical models are inadequate for predicting complex wrinkled patterns, Finite Element Analysis (FEA) becomes an important computational tool for predicting such patterns. Complex wrinkle patterns are generated by non-uniform input parameters such as non-uniform geometry or material properties. As analytical models are based on the approximation of uniform geometry and uniform material properties, such models are inappropriate for predicting complex wrinkles. FEA models do not suffer from this limitation and enable one to conveniently run computational experiments with non-uniform input parameters. Additionally, FEA models enable one to probe a system and access system parameters that are not easily accessible during physical experiments. For example, FEA models enable one to track the deformation energy during loading thereby providing additional insight into the wrinkling process. In this work, finite element based computational experiments have been used in conjunction with physical experiments to explore and learn about the process in order to develop predictive models for complex wrinkling.

3.1.1 Goals of this work

Commercially available FEA software packages are insufficient for predicting wrinkled patterns because these packages do not provide in-built toolboxes to perform post-buckling or post-bifurcation analysis. As wrinkled patterns are formed via a bifurcation process, additional computational tools for perturbing the geometry or loading are required to perform accurate post-bifurcation analyses. As such, the lack of well-tested perturbation tools leads to the (i) inability to verify the accuracy of the predictions due to absence of benchmark problems and (ii) the inability to accurately quantify the effect of perturbations on the patterns. This limits the ability to quickly and reliably use commercially available FEA software to predict the formation of wrinkled patterns. Thus, there is a need to develop and test perturbation toolboxes that would enable using FEA packages for predicting wrinkled patterns.

Herein, a computational toolbox has been developed and tested to perturb the mesh of a finite element model. This toolbox has been used in conjunction with the commercially available COMSOL 4.2 FEA package to perform post-buckling analyses of wrinkled patterns. The toolbox enables one to (i) apply arbitrary shaped perturbations to the mesh, (ii) quantify the effect of perturbations on the wrinkle patterns, and (iii) quantify the accuracy of the predicted patterns based on the applied perturbations. The accuracy of the toolbox has been verified by (i) several internal consistency tests and (ii) comparison with analytical models and experimental data. Provided herein is: (i) description of the modeling scheme, (ii) protocol for setting-up the model and for evaluating the results of the analyses, and (iii) the results of the verification tests.

3.1.2 Limitations of existing computational tools

As buckling has traditionally been considered a failure mode, the first step of predicting the onset of bifurcation has received more attention than post-bifurcation analysis. Thus, predictive tools for post-bifurcation analysis of buckled/wrinkled structures are not as readily available as those for predicting the onset. This trend is also reflected in the development of commercially available finite element analysis (FEA) software packages. For example, dedicated stability analysis based modules are available for predicting the onset of bifurcation but modules for post-bifurcation analysis are absent from most FEA packages. Post-bifurcation analysis is essential for an accurate prediction of the wrinkled structures. Hence, computational tools were developed to perform post-bifurcation studies using the commercially available COMSOL 4.2 FEA package. These tools enable one to systematically perform post-bifurcation analyses and run extensive automated parametric analyses.

3.1.3 Need for mesh perturbations

Providing an external perturbation to the system is often necessary for observing buckling bifurcation during numerical simulations. The bifurcation point is characterized by intersection of multiple feasible modes/paths that the system may follow after bifurcation. Out of these paths, one or more may be energetically favorable. In the absence of any imperfection, the system may be unable to “see” and follow any of these alternate paths. Therefore, the system may remain on an energetically unfavorable path even after the bifurcation point.

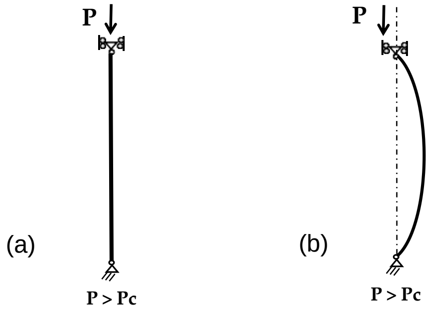

Figure 3.1: Role of imperfection in buckling. Imperfection is essential for buckling bifurcation. (a) A “perfect” column does not buckle even at very high loads. (b) Real column buckles at high loads due to presence of imperfections.

For example, during buckling of a column there are two feasible modes at the bifurcation point (i) pure compression and (ii) bending. Bending is energetically favorable beyond the bifurcation point. However, a ‘perfect’ column with no imperfections would not buckle even beyond the bifurcation load (Figure 3.1). In reality, this ‘non-buckling beyond bifurcation’ phenomenon is never observed due to the presence of imperfections in a real system. However, such non-buckling is routinely observed in an idealized finite element model. Therefore, an imperfection must be applied to the finite element model to ensure that the system follows the energetically favorable post-bifurcation path. The imperfection may be in the form of (i) geometric/mesh imperfection and/or (ii) imperfection in the applied loads and boundary conditions. Herein, this imperfection is provided via geometric perturbations of the mesh.

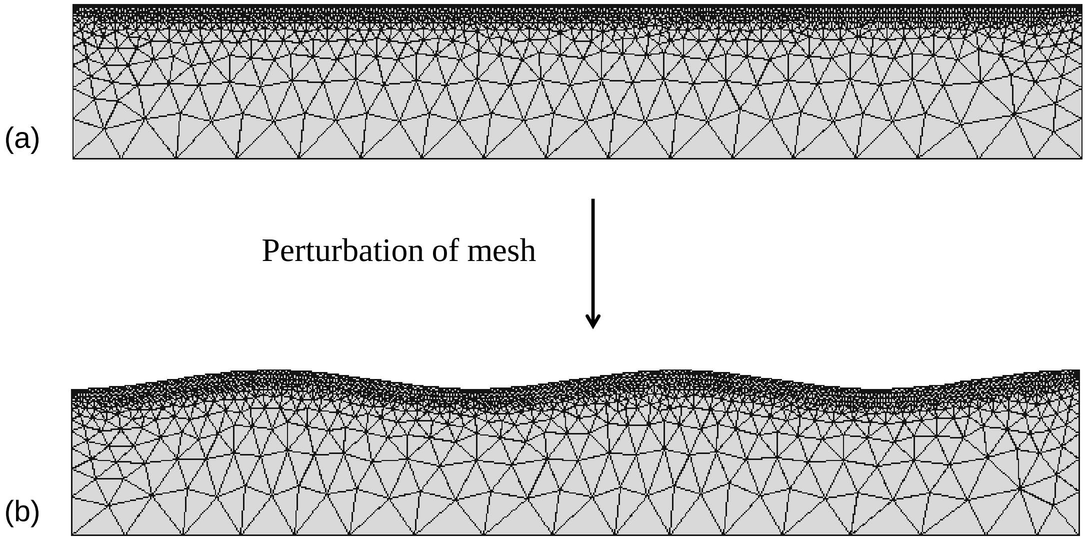

Figure 3.2: Mesh perturbation as imperfection that enables bifurcation. (a) Perfect mesh that does not bifurcate. (b) Perturbed mesh that bifurcates. Perturbation has been exaggerated for clarity. A perturbed mesh can be obtained from a perfect mesh by 'moving' the mesh points around.

Perturbing the mesh is a reliable and sometimes the only feasible technique to introduce imperfections to a system in such a way that the appropriate post-bifurcation behavior is observed. Perturbing a mesh means moving the mesh points around so that the resulting geometry is 'somewhat but not substantially' different from the original geometry. The mesh corresponding to a flat bilayer and a representative perturbed mesh are shown in Figure 3.2. Although mesh perturbation is an important technique for post-bifurcation analysis, it is not available via the existing modules in COMSOL. Therefore, MATLAB codes were developed to perform automated mesh perturbations. Additionally, these codes automate the pre and post processing of the FEA models. These codes enable one to perform (i) post-bifurcation analysis, (ii) studies on sensitivity to mesh imperfections, and (iii) parametric studies that require re-meshing the geometry. The codes that were developed here have been archived and are available for download via an open source license from the MIT DSpace online repository [68].

3.1.4 Need for automated analysis

In addition to the codes to perturb a mesh, to solve a post-bifurcation problem one needs to (i) extract the original mesh, (ii) generate the perturbation shape functions, and (iii) define the COMSOL study files. Although these steps may be performed manually, codes for automated processing are necessary if unattended parametric studies are required. Automation was made possible by (i) using MATLAB LiveLink to transfer data across the MATLAB and COMSOL desktop environments and (ii) using COMSOL model seed files to define a template of the post-bifurcation study.

3.2 Modeling technique

3.2.1 Summary of implementation

Finite element modeling was performed by developing 2-D and 3-D models of wrinkling using the Structural Mechanics module of the COMSOL 4.2 software package [69]. The COMSOL software package was selected because of its ability to link to MATLAB to pre and post process the models. The 2-D models were developed by implementing buckling of wide plates under the plane strain condition; 3-D models were developed by implementing buckling of finite sized plates. In both cases, the top film was modeled as a linear elastic material and the bottom layer as a Neo-Hookean material. A nonlinear strain-displacement relationship was used for both layers to account for large displacements during wrinkling. Also, two different types of loading were applied: (i) pure compression of top and bottom layers and (ii) initial pre-stretch of the bottom layer followed by release of this pre-stretch. The pre-stretch based loading was implemented by applying an initial strain to the top layer that corresponds to a uniaxial/biaxial tension. This was followed by compression of both the layers.

Modeling was performed in two steps: (i) linear pre-buckling analysis to predict the mode shapes, i.e., the period of the wrinkles and (ii) a nonlinear post-buckling analysis to predict the shape and amplitude of the wrinkles after buckling bifurcation. In this two-step process, first the displacements of the 1st mode shape obtained from linear buckling analysis were extracted; then the displacements were added as the initial imperfection to the mesh. The displacements were weighted by a multiple of the top layer thickness. The studies were solved in COMSOL. LiveLink for MATLAB was used to (i) generate the initial weighted imperfections, (ii) set-up the post-bifurcation studies, and (iii) post-process the post-bifurcation analysis. Representative results of the pre-buckling analysis and the post-buckling analysis for the case of compression with no base pre-stretch are shown in Figure 3.3.

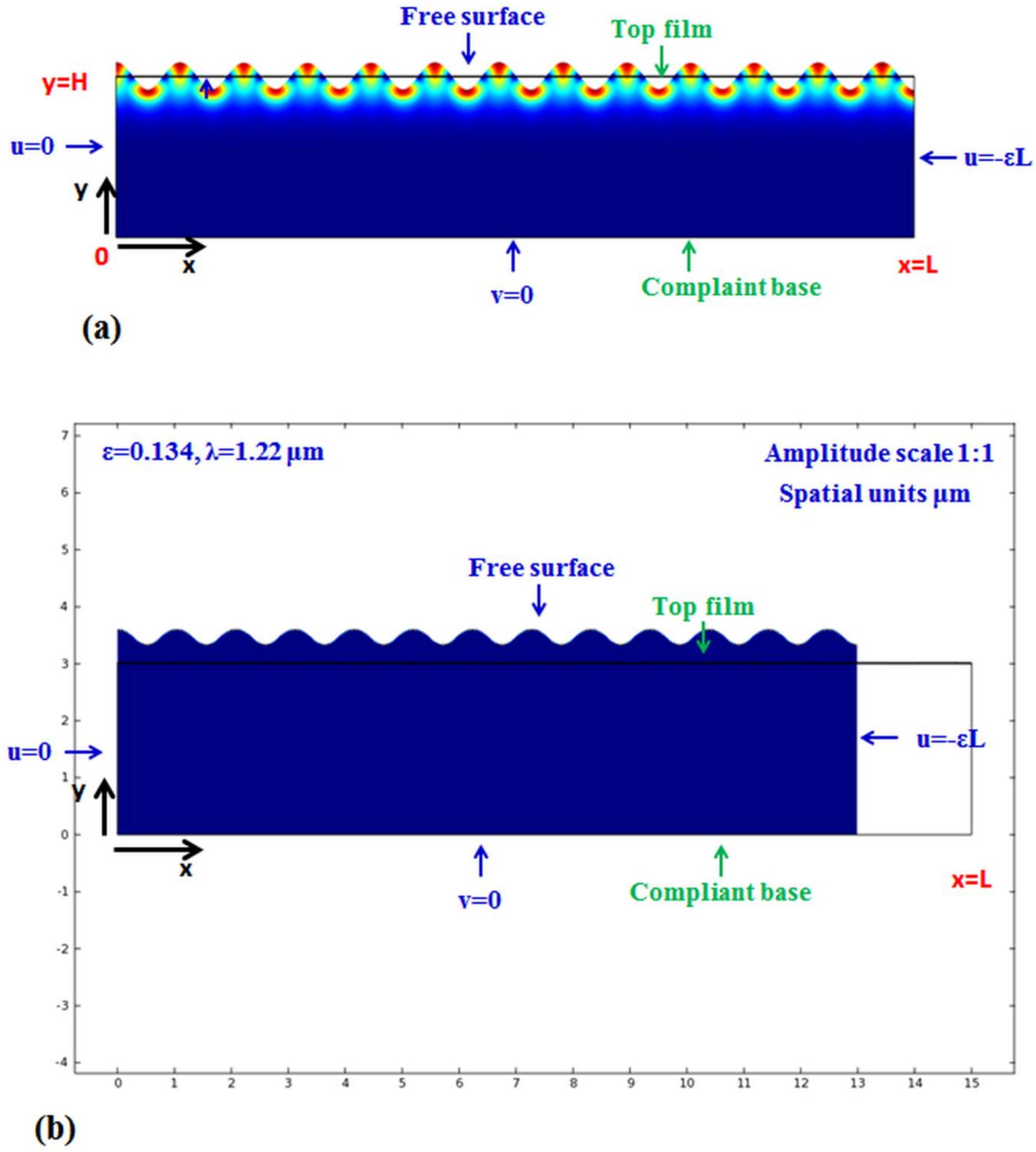

Figure 3.3: Results of finite element analysis. (a) Linear pre-buckling analysis to evaluate mode shapes and (b) nonlinear post-buckling analysis to evaluate the post-buckled deformed configuration. Thickness of top film is 21.4 nm and moduli ratio (η) is 10,500.

3.3 Mesh perturbation

3.3.1 Mathematical background

In the perturbation scheme developed here, the perturbed mesh is generated from the original mesh by displacing the mesh points, i.e., by 'moving around' the nodes. This transformation preserves the connectivity, ordering, total number of nodes, and the type of elements in the mesh. If $X_{i,j}$ are the coordinates of the j^{th} node in the original mesh and $x_{i,j}$ are the coordinates of the same node in the perturbed mesh, the two are related by:

$$x_{i,j} = X_{i,j} + (wh)\bar{u}_{i,j} \tag{3.1}$$

$$\bar{u}_{i,j} = \frac{u_{i,j}}{\max\left|u_{N,j}\right|} \tag{3.2}$$

Here, 'w' is a non-dimensional weight factor, 'h' is thickness of the top layer and '$\bar{u}_{i,j}$' are non-dimensional perturbation shape functions. The perturbation shape functions are generated by non-dimensionalizing the displacement field, $u_{i,j}$, with the maximum out-of-plane displacement. The size of the perturbation is determined by the weight factor and the top layer thickness. The subscript 'i' runs from 1 to N for an N-dimensional system; i.e., N=2 for a 2-D system and N=3 for a 3-D system. The displacement functions $u_{i,j}$ may be chosen arbitrarily or according to a predetermined scheme. Typically, during post-bifurcation analysis, these functions are chosen to be either (i) the Eigen modes of the linear pre-buckling analysis or (ii) the geometric imperfections that are observed in a 'real' system. The codes developed here enable applying both of these two types of mesh perturbations.

3.3.2 Implementation details

In order to implement the perturbation scheme, codes were developed to transform an existing COMSOL mesh into the perturbed mesh. This is achieved by generating a new file with the perturbed mesh data from an existing '.mphtxt' text file that contains the original mesh data. An '.mphtxt' mesh file contains all data that are required to fully define a mesh. Details of the format are available in the COMSOL Reference Guide [70]. The original mesh file can be obtained from a COMSOL study by exporting the undeformed mesh. The perturbed mesh is generated by replacing the mesh point coordinates of the original mesh with the transformed coordinates while keeping the rest of the mesh data intact. To do this, codes were developed to perform (i) file read/write operations to extract and replace mesh point coordinates of an '.mphtxt' file and (ii) mathematical transformations to generate coordinates of the perturbed mesh for a given set of perturbation shape functions. A COMSOL study may then be solved by importing the perturbed mesh and defining the study on this new perturbed mesh.

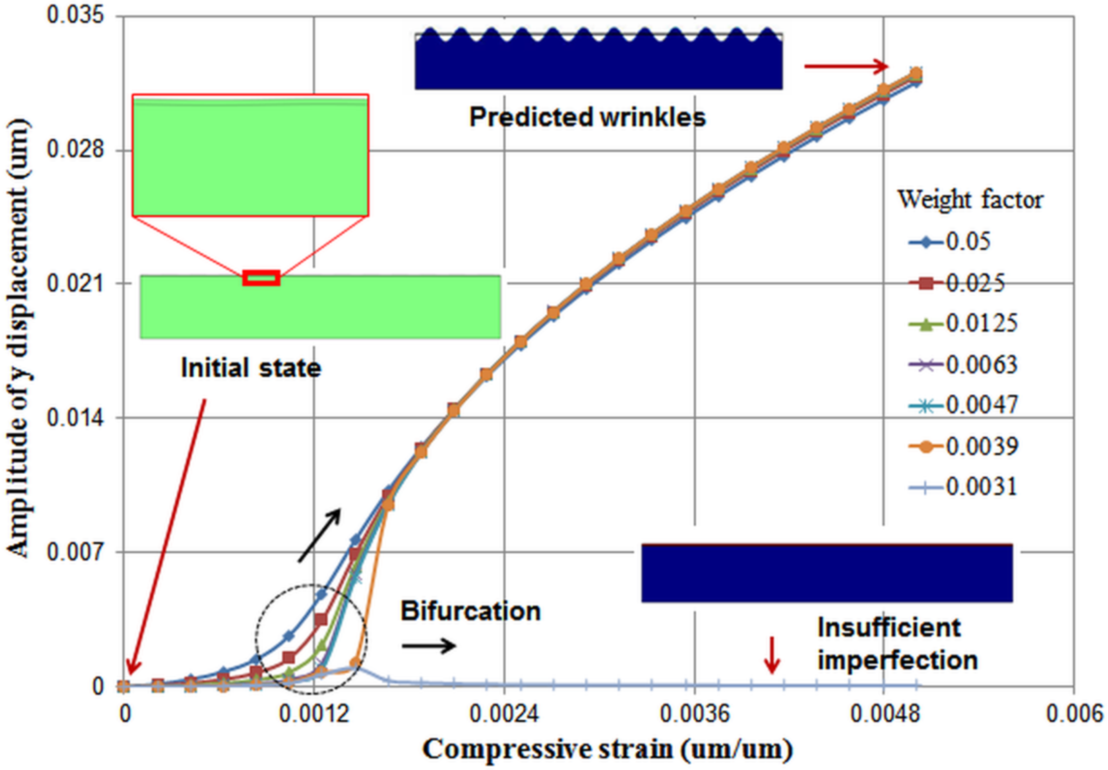

Figure 3.4: Effect of insufficient mesh perturbation on bifurcation behavior. The system does not bifurcate into the wrinkled mode unless a sufficiently large mesh perturbation is provided. Here, base was pre-stretched to 0.5%, film thickness is 20 nm and moduli ratio η=29,165.

3.3.3 Sensitivity to mesh perturbation

As the wrinkle pattern is affected by the mesh perturbations, one must properly select these perturbations to ensure an accurate prediction. The effect of perturbations on wrinkles can be studied at two extremes: (i) when the perturbation is "too low" and (ii) when the perturbation is "too high". With insufficient perturbation, the model does not bifurcate to the wrinkled state. Thus, instead of wrinkles a flat compressed bilayer is observed as shown in Figure 3.4. As the weight factor of the imperfection is increased, one observes transition of the system into the bifurcated mode; this is accompanied with a decrease in the solution/convergence time as illustrated in Figure 3.5. However, in the presence of excessive perturbation the bifurcation behavior changes to the extent that the new system is substantially different from the modeled flat bilayer system. As depicted in Figure 3.6, this difference manifests as (i) a broader bifurcation zone and (ii) a decrease in the final amplitude of the deformation due to the initial non-flat geometry. To ensure bifurcation of the models and to minimize the errors due to perturbations, here perturbations have been selected to lie within 1% and 5% of the top film thickness, i.e., the weight factor $\boldsymbol{w}$ in Eq. (3.1) is 0.01-0.05. For the studies summarized in Figure 3.4 and Figure 3.6, the first Eigen mode from the linear pre-buckling analysis was used as the shape function for mesh perturbations. The effect of non-Eigen mode shapes on the wrinkled patterns is discussed later in Chapter 4.

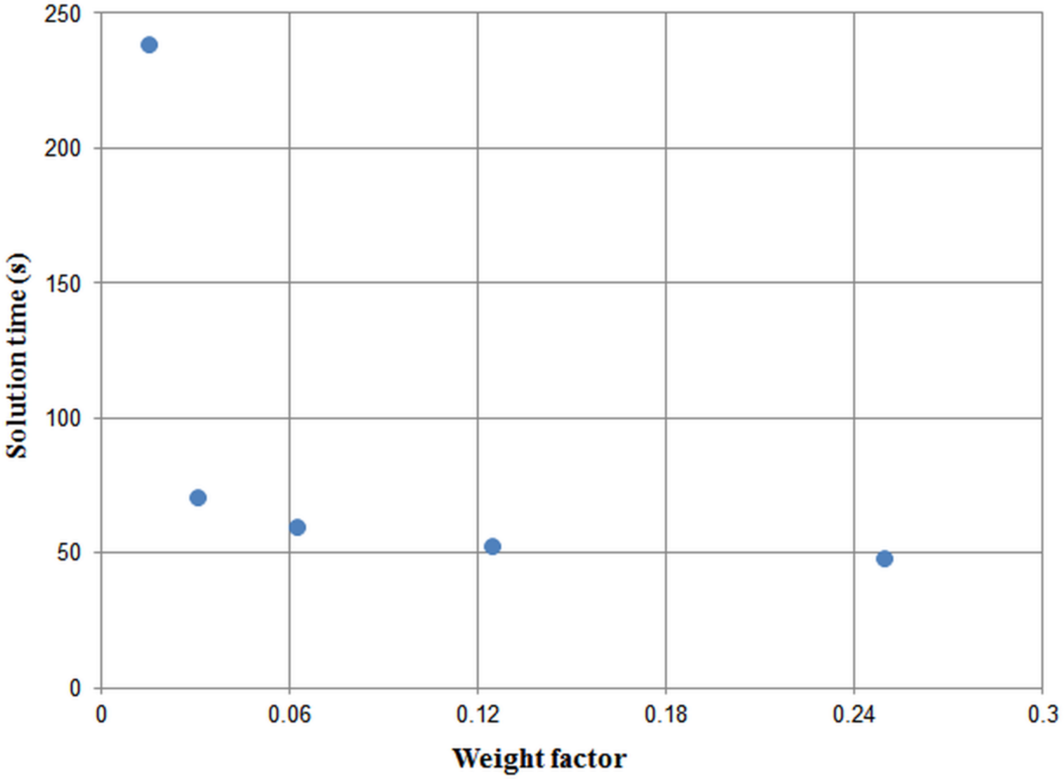

Figure 3.5: Effect of mesh perturbation on solution time. Solution time decreases with an increase in the amplitude of mesh imperfection. Here, base was pre-stretched to 0.5%; film thickness is 20 nm and moduli ratio η is 35,000.

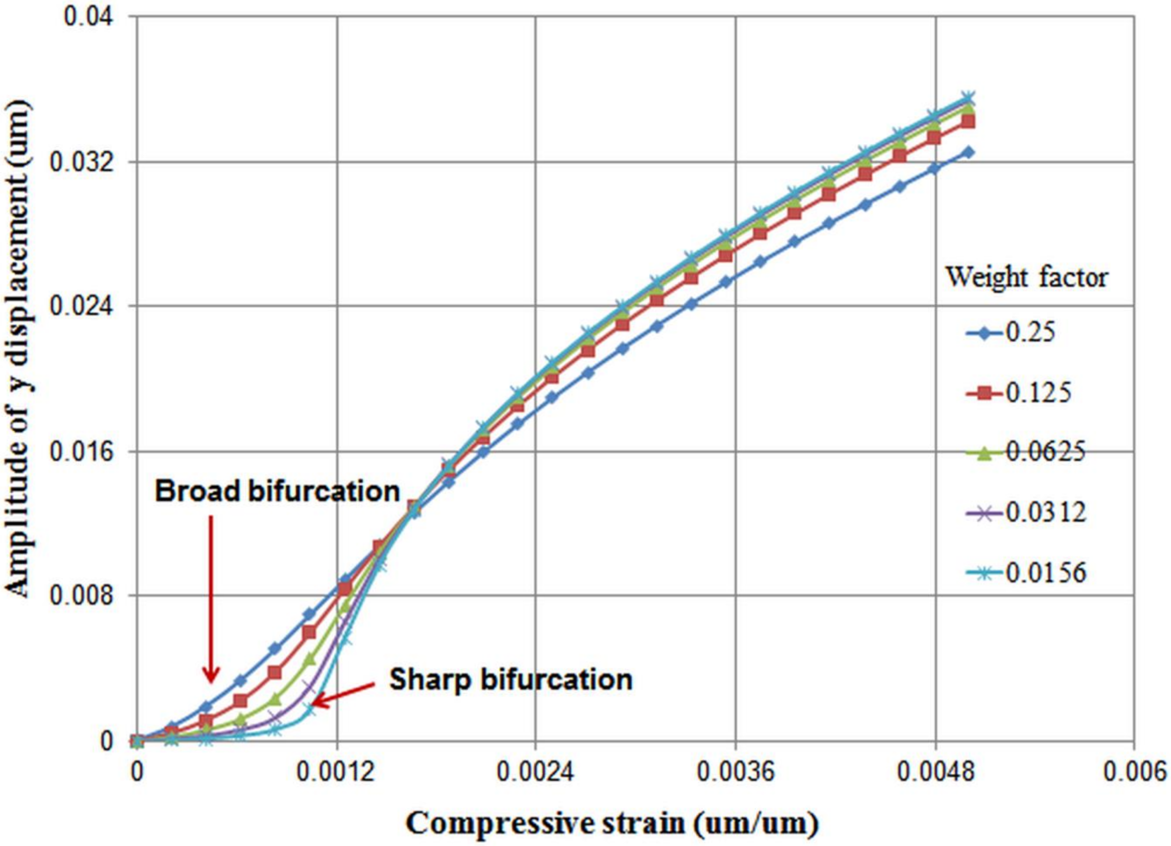

Figure 3.6: Effect of high mesh perturbation on bifurcation behavior. The bifurcation region broadens when large perturbations are used. Observed post-bifurcation deformation decreases with an increase in the perturbation size due to significant changes in the initial geometry of the system. Here, base was pre-stretched to 0.5%; film thickness is 20 nm and moduli ratio η is 35,000.

3.4 Algorithm for automated analysis

3.4.1 With Eigen modes as mesh perturbation

When Eigen modes are used as mesh perturbations, a linear pre-buckling analysis is performed before defining the post-buckling study. The mesh perturbation displacement field in Eq. (3.2) is obtained from Eigen modes of the linear pre-buckling analysis. The perturbed mesh is obtained by performing the transformation of Eq. (3.1) on the original undeformed mesh of the linear pre-buckling analysis. The post-buckling study is then defined on this perturbed mesh. As the amplitude of the modes is undetermined in a linear pre-buckling analysis, only the shape of the modes is used as the perturbation displacement function. The size of the perturbation is determined by the user defined weight factor and is proportional to the top layer thickness. A flowchart of the algorithm is shown in Figure 3.7. Both the linear pre-buckling and the post-buckling studies are solved in the COMSOL environment. However, the studies are defined and post-processed in MATLAB. Data is exchanged between the two environments via the MATLAB LiveLink module of COMSOL.

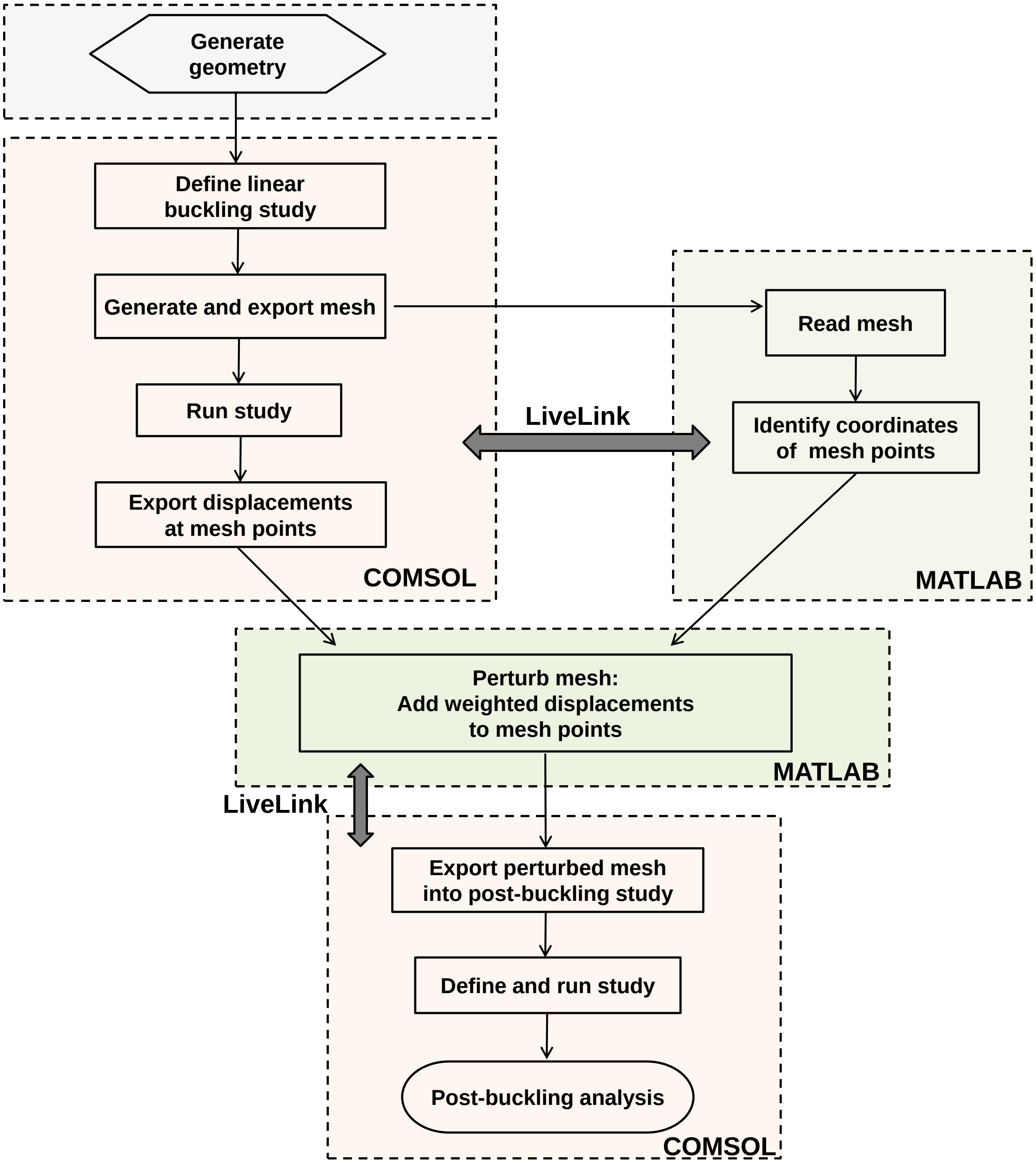

Figure 3.7: Algorithm for performing post-bifurcation analysis wherein the shape of the imperfections is defined by the Eigen modes of the linear pre-buckling analysis.

3.4.2 Externally provided mesh perturbation

Running a linear pre-buckling analysis is not necessary when an external mesh perturbation is applied. Instead, only the original undeformed mesh is extracted from the study and the mesh is then transformed with the external perturbation. The post-buckling study is then defined on this perturbed mesh. For convenience, the schemes and codes developed earlier are reused with these modifications: (i) the linear pre-buckling study is defined to extract the mesh but the study is not solved and (ii) external perturbation displacement field is generated and used to perturb the mesh. The steps are summarized in Figure 3.8.

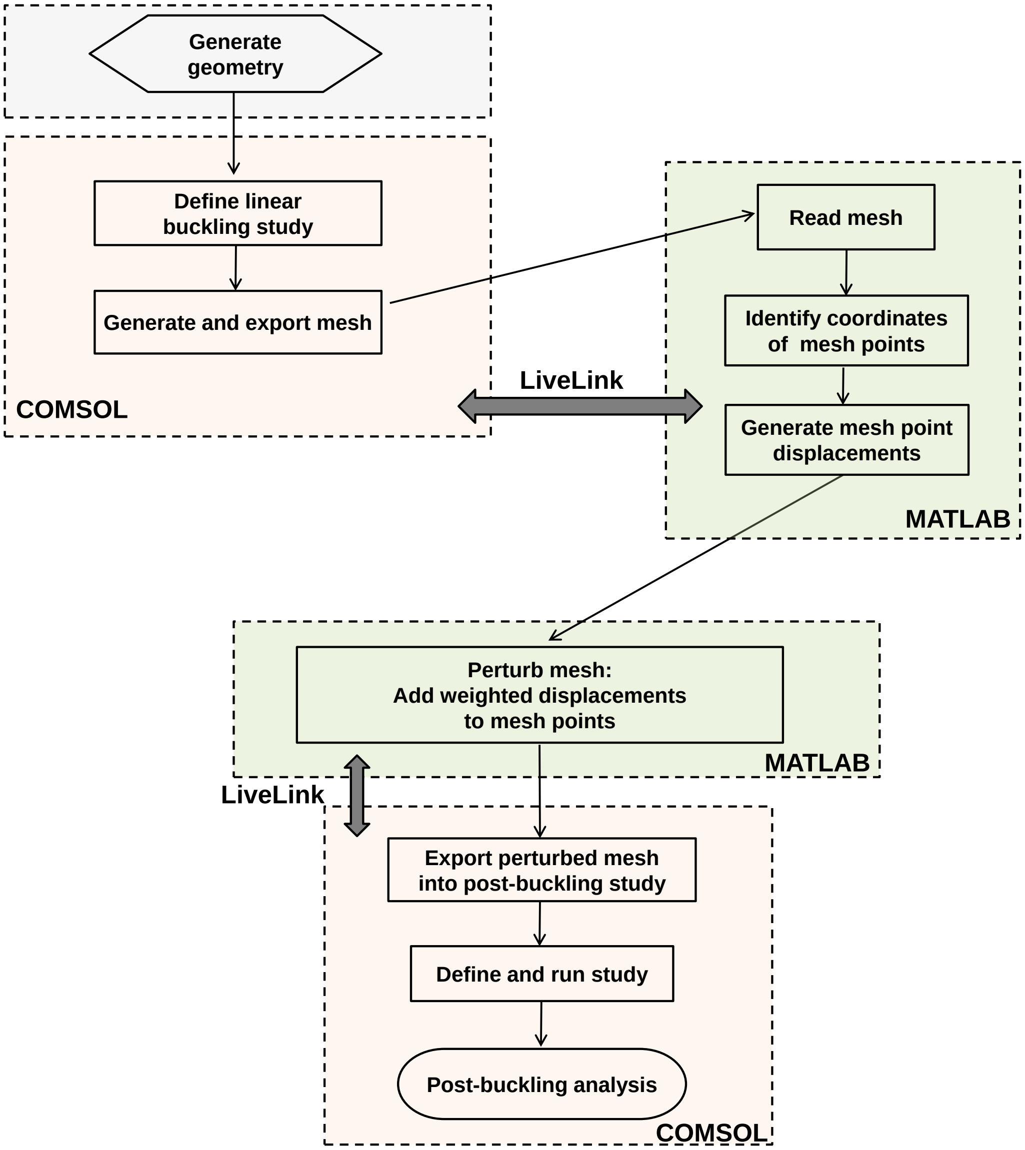

Figure 3.8: Algorithm for performing post-bifurcation analysis wherein shape of the imperfections is not defined by the Eigen modes.

3.4.3 Automation via seed models

During a parametric study that involves varying the geometric parameters, it is necessary to regenerate a perturbed mesh for each combination of parameters. This requires repeatedly solving the linear pre-buckling studies, generating the perturbation displacement field, and defining the post-buckling studies. Automation of this process can substantially reduce the time and effort required to run such parametric analyses. This automation has been achieved by using seed models to define the COMSOL models and LiveLink to exchange data between MATLAB and COMSOL environments.

Seed models

When a geometric parameter is varied, seed models are used to generate the new models. Seed models are the preliminary unsolved COMSOL models that contain all the necessary definitions required to define and solve the model for a specific set of parameters. Seed models are necessary because post-buckling studies are not defined on a geometry; instead, they are defined on an imported mesh. Therefore, changing a geometric parameter requires changing the mesh in the study. The initial linear buckling study in the COMSOL '.mph' format is directly used as the seed model. The seed model for the post-buckling study is obtained by exporting the post-buckling COMSOL study as a MATLAB '.m' script. This script contains the sequence of MATLAB commands required to define the study. The format of commands are available in the COMSOL User's Guide [71]. The linear buckling seed model and the post-buckling MATLAB script can be modified to generate new models whenever the model parameters are changed. When Eigen modes are used as perturbations, the new linear pre-buckling studies are solved to generate the perturbation displacement field. However, when external perturbations are used, the linear models are used only as a source of the initial undeformed mesh.

LiveLink

The LiveLink module of COMSOL has been used to 'connect' the COMSOL desktop environment to the MATLAB environment. Details on this module are available in the COMSOL documentation [72]. This connection enables one to access or modify data in a model from both of these environments. For example, one may define a study and/or modify the parameters via MATLAB scripts and then use COMSOL to solve the study. This connection has been used to automate parametric analysis by implementing these data transfer operations: (i) accessing and modifying parameters of the seed models to generate new models, (ii) extracting the undeformed mesh and perturbation displacement fields from the linear buckling models, (iii) defining a new post-buckling study on the perturbed mesh, and (iv) extracting results of solved models to perform post-processing via MATLAB. Automated data transfer during these steps enables performing parametric studies in a completely unattended mode.

3.4.4 Capability of finite element parametric analysis

The parameters that can be controlled during an automated parametric study are listed in Table 3.1. All of these parameters, except for the length and thickness of the base, are found to have an influence on the wrinkling process. The effect of these parameters on the wrinkling process can be quantified in terms of the observable parameters that are listed in Table 3.2. These observable parameters are the period and amplitude of the wrinkles and the critical compression for bifurcation. The protocol for evaluating these parameters from the deformed configuration of the bilayer is discussed in Sec. 3.5.1. Later in Sec. 3.5.2 and Sec. 3.5.5, the effect of the controllable parameters on the observable parameters is discussed.

Table 3.1: Controllable parameters during finite element analysis

Sensitive parameters	**Non-sensitive parameters**
Thickness of top film ($\boldsymbol{h}$)	Thickness of base ($\boldsymbol{H}$)
Young's modulus ($\boldsymbol{E_f}$) and Poisson's ratio ($\boldsymbol{\nu_f}$) of top film	Length of bilayer ($\boldsymbol{L}$)
Shear modulus of base ($\boldsymbol{\mu_b}$)	
Pre-stretch of base ($\boldsymbol{\varepsilon_p}$)	
Compression of bilayer ($\boldsymbol{\varepsilon}$)	
Step size for compression ramp-up ($\boldsymbol{\delta\varepsilon}$)	

Table 3.2: Observable parameters during finite element analysis

Directly observable	**Evaluated from directly observable parameters**
Deformed configuration of bilayer	Evolution of period with compression
Deformation energy of bilayer	Evolution of amplitude with compression
	Critical compression at bifurcation

3.5 Performance of FEA

3.5.1 Post-processing protocol

Period and amplitude

The results of the post-bifurcation finite element analysis are used to evaluate the period and amplitude of the wrinkles. Period and amplitude are evaluated by extracting the deformed coordinates of the mid plane of the top film. Period is evaluated as the average distance between adjacent peaks and the amplitude is evaluated as average of the half of the peak to valley heights. A representative deformed profile of the mid plane of the top film during 1D loading is shown in Figure 3.9. The cosine profile generated by the average measured period and amplitude matches with the deformed profile of the film over the entire length to within 0.4% accuracy.

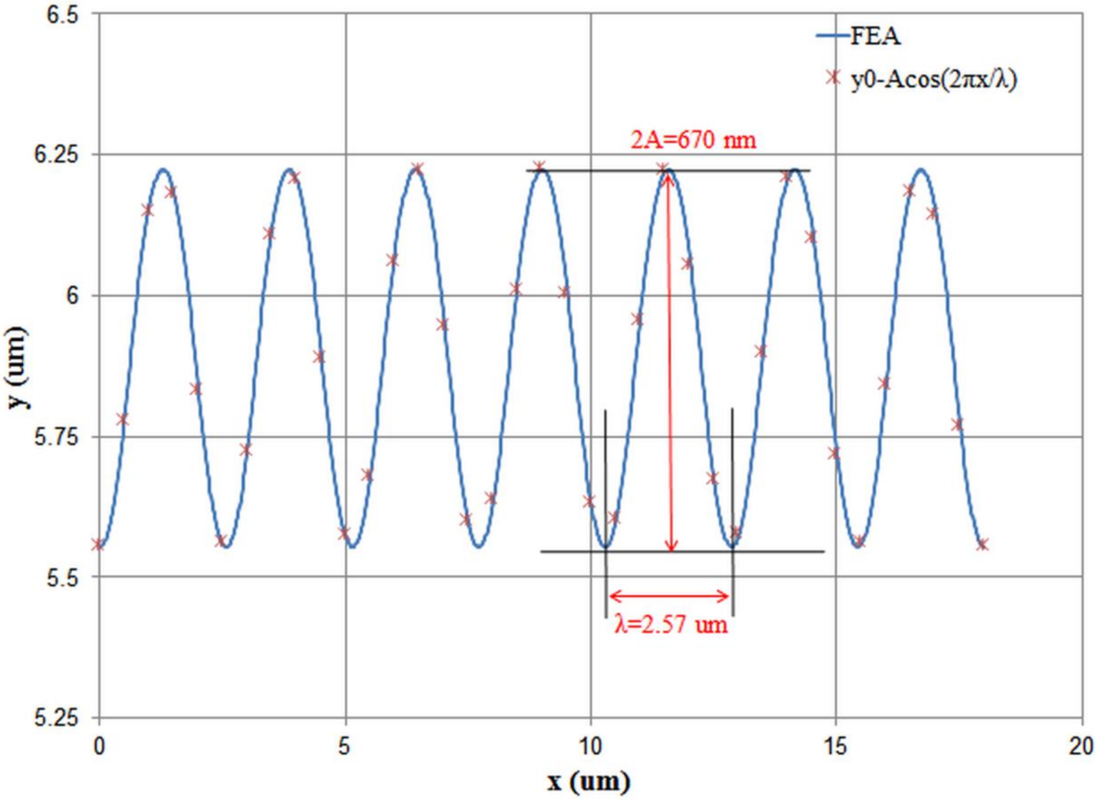

Figure 3.9: Representative wrinkle profile extracted from the deformed configuration of the bilayer. The profile represents the deformed position of the mid-plane of the top film. Period and amplitude are extracted from this profile by evaluating the spacing and height of the peaks and valleys. Here, bilayer compression is 10% with no base pre-stretch; film thickness is 24.6 nm and moduli ratio η is 78,125.

The definition of period and amplitude based on the deformed profile is different from definitions used in developing analytical models. In analytical models that are available in literature [17, 50], period and amplitude are often defined in the undeformed coordinate system. In the undeformed coordinate system, the period of wrinkles does not change with compression; whereas in the deformed coordinate system the period decreases with compression. The quantitative effect of compression on period is discussed later in Sec. 3.5.2. In this work, the deformed coordinates have been used to define the period and amplitude because such a definition is consistent with the analysis of experimental observations of deformed configurations.

Critical compression for bifurcation

The critical compression for bifurcation can be estimated from the bifurcation diagram of the system, i.e., from the evolution of the out-of-plane displacement with compression. For an ideal system, the slope of the displacement versus compression plot is discontinuous at the critical compression. However, this discontinuity is not observed during finite element analysis. Instead, a broad compression region is observed over which the displacement increases from zero to a finite value. The critical compression can be evaluated as the region over which the displacement reaches a cut-off value. The accuracy of estimation of the critical compression can be improved by narrowing the region over which bifurcation occurs. A narrow region can be obtained by using a small imperfection and by increasing the density of the mesh.

3.5.2 Effect of compression

The deformed profile of the wrinkles changes when the bilayer is compressed. As discussed in Sec. 3.5.1, the shape of the wrinkles is accurately captured by the cosine curve. Thus, the effect of compression on the deformed profile can be quantified in terms of effect of compression on the period and amplitude of wrinkles.

During finite element analysis, it is observed that the number of wrinkles in the domain does not change with compression. This constancy of spatial frequency of wrinkles can be used to relate the periods at different compressions as:

$$\lambda(\varepsilon) = \lambda_n \left(1 + \varepsilon_p - \varepsilon\right) \qquad \textbf{(3.3)}$$

Here, $\boldsymbol{\lambda}$ is the period of the wrinkles at a compression $\boldsymbol{\varepsilon}$, $\boldsymbol{\varepsilon_p}$ is the pre-stretch of the base layer, $\boldsymbol{\varepsilon}$ is the compression of the bilayer, and $\boldsymbol{\lambda_n}$ is the period of the wrinkles at the initial un-stretched and unstressed length of the base. This relationship has been verified by tracking the change in the deformed profile of the wrinkles. As depicted in Figure 3.10 and Figure 3.11, the shape of the wrinkles is accurately captured by the cosine curve with a period that is given by Eq. (3.3).

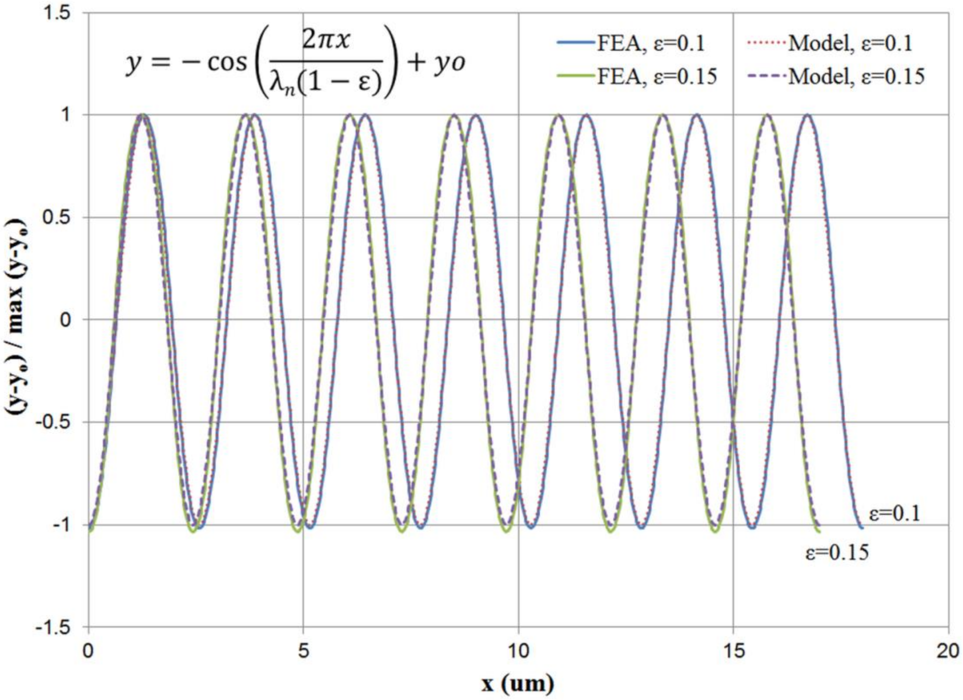

Figure 3.10: Shape of the deformed profile of the wrinkles during compression of bilayer without any base pre-stretch. The profile represents the deformed coordinates of the mid-plane of the top film. Here, film thickness is 24.6 nm and moduli ratio $\boldsymbol{\eta}$ is 78,125.

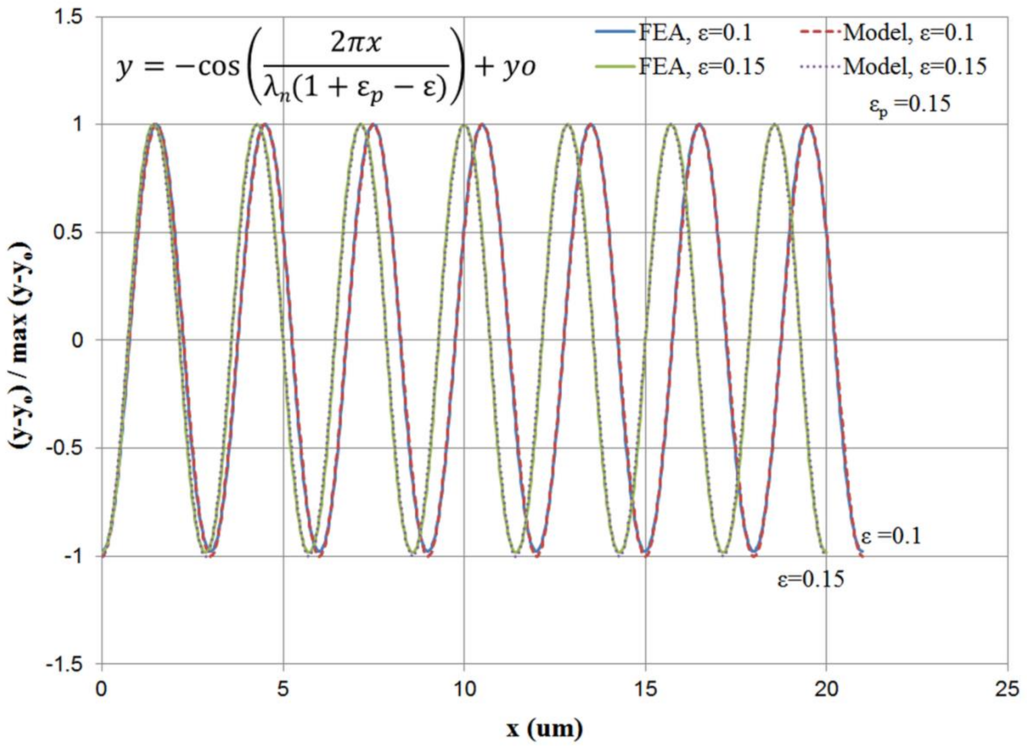

Figure 3.11: Shape of the deformed profile of the wrinkles during pre-stretch release. The profile represents the deformed coordinates of the mid-plane of the top film. Here, film thickness is 24.6 nm and moduli ratio η is 78,125.

The size of the wrinkles is quantified by the amplitude of the deformed profile. The amplitude of the deformed profile is related to the applied compression via kinematics. This is based on the approximation that the lateral compression of the top film is negligible during wrinkling. Thus, the length of the top film remains constant with compression of the bilayer. For small amplitudes, the length of a cosine curve over one period (***l***) can be evaluated in terms of the period and amplitude as:

$$l = \lambda_n\left(1+\left(\frac{\pi A}{\lambda_n}\right)^2\right) \tag{3.4}$$

The length of the top film over one period is also given by:

$$l = \lambda_n(1+\varepsilon) \tag{3.5}$$

From Eq. (3.4) and Eq. (3.5), amplitude of wrinkles (***A***) is obtained as:

$$\frac{A}{\lambda_n} = \frac{1}{\pi} \varepsilon^{0.5} \tag{3.6}$$

Equation (3.6) has been verified against the FEA results as shown in Figure 3.12. Equation (3.6) overestimates the amplitude by about 2% at 5% compression and by about 5% at 15% compression. This error arises out of the approximation of the length of a cosine curve by Eq. (3.4) and can be reduced by including higher order terms in length evaluation or by numerically evaluating the length of a cosine curve. The discrepancy in the case of base prestretch at low compression values is because the onset of bifurcation is delayed in the case of a pre-stretched base. This occurs due to the technique employed to implement base prestretch. The base prestretch is implemented by applying a residual strain to the top layer. This residual strain does not account for large displacement effects. Thus, bifurcation is delayed for large prestretch values.

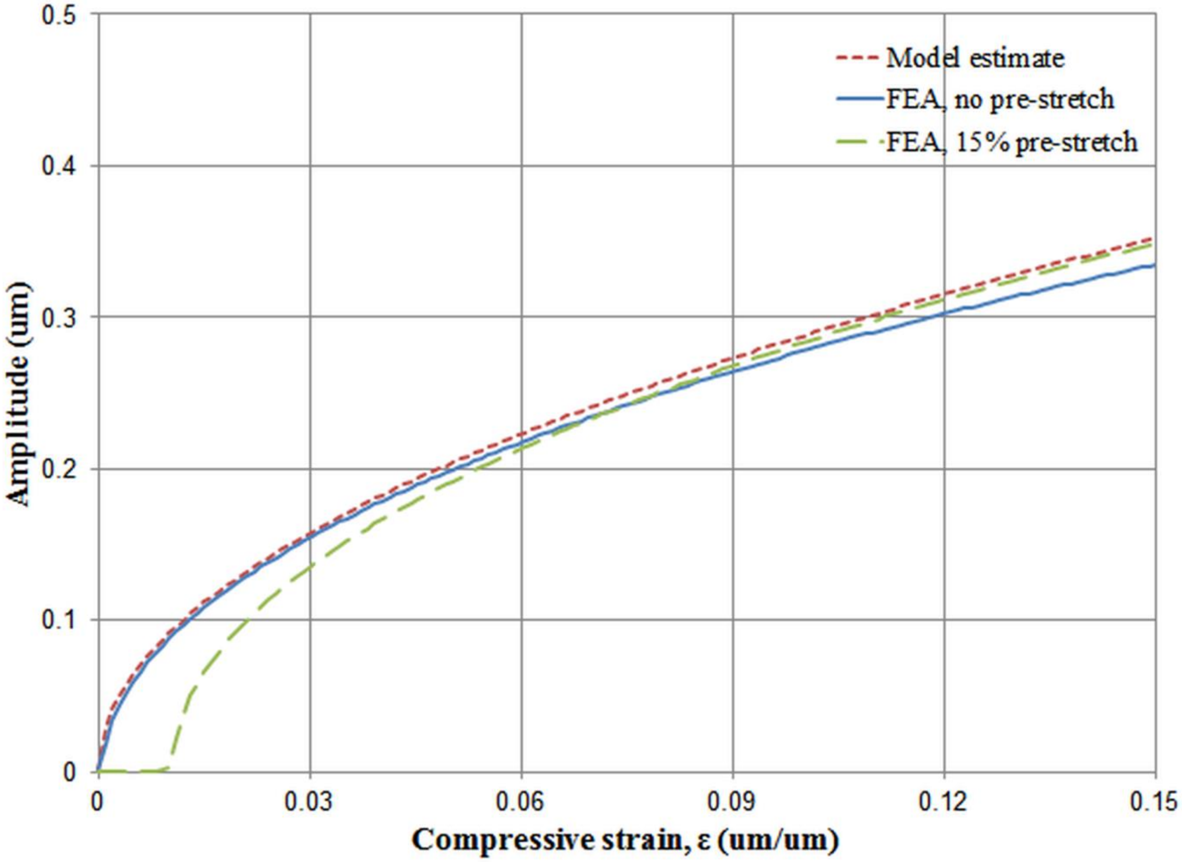

Figure 3.12: Amplitude of the wrinkles during compression with and without base pre-stretch. Here, film thickness is 24.6 nm and moduli ratio η is 78,125.

3.5.3 Mesh convergence

Studies of the effect of mesh density on the amplitude and period were performed to select the appropriate mesh density. The results are shown in Figure 3.13(a). COMSOL pre-set mesh densities were used for these studies. Convergence was achieved for mesh size of ~19,000 nodes. This corresponds to a pre-set setting of ‘extra fine’ mesh. This setting was used for subsequent FEA runs. The corresponding resource utilization in terms of the memory usage and solution time is shown in Figure 3.13(b). As expected, the solution time for convergence and the size of the model increase with an increase in the mesh size.

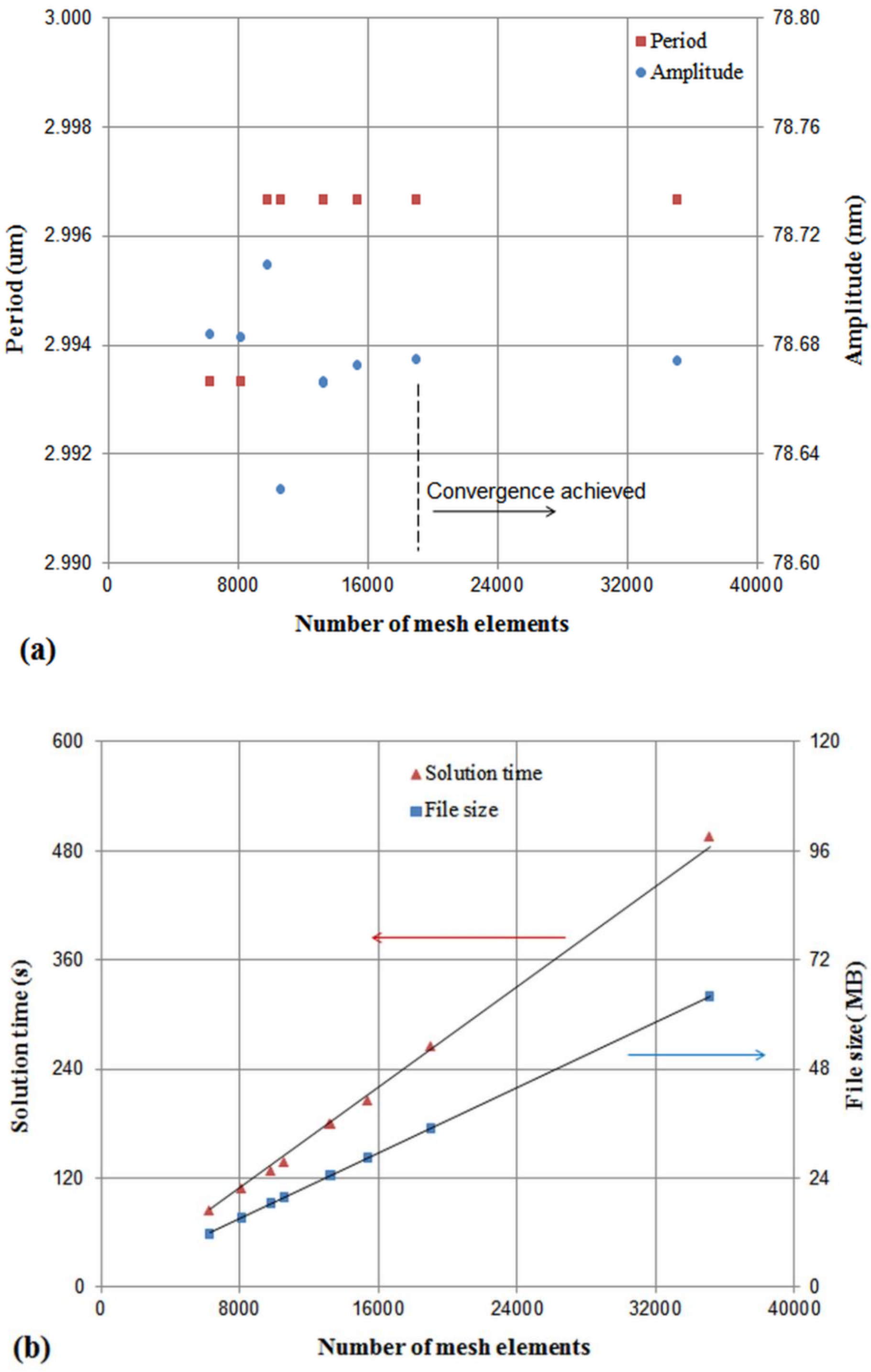

Figure 3.13: Effect of mesh size on accuracy of period and amplitude and resource utilization. (a) Period and amplitude versus mesh size and (b) solution time and file size versus mesh size. Mesh must be sufficiently dense to ensure convergence of solution. Beyond convergence, higher density mesh leads to wastage of computational time and memory. COMSOL pre-set mesh densities were used; from lower to higher density: extremely coarse, extra coarse, coarser, coarse, normal, fine, finer, extra fine, and extremely fine. Here, h=25 nm, η=77, 778, pre-stretch ε_p=0.75%.

3.5.4 Error analysis

Error in period

Errors in period arise due to the quantization imposed by the boundary conditions. The boundaries can only accommodate peaks or valleys due to the imposed symmetry boundary conditions. However, the actual period may lie between a valley and a peak. Thus, the observed period may correspond to the actual period lying between two limits. These limits are given by:

$$\lambda_U = \lambda\left(\frac{1}{1-0.25\lambda/L}\right) \tag{3.7}$$

$$\lambda_L = \lambda\left(\frac{1}{1+0.25\lambda/L}\right) \tag{3.8}$$

Here, $\boldsymbol{\lambda_U}$ is the upper limit of period, $\boldsymbol{\lambda_L}$ is the lower limit of period, and $\boldsymbol{L}$ is the length of the bilayer domain. Equations (3.7) and (3.8) suggest that the bilayer length must be sufficiently high to ensure a low uncertainty in the measured period. For a bilayer that accommodates 10 wrinkles, the uncertainty in measured period is +2.6% and -2.4%.

Error in amplitude

Errors in amplitude arise due to mesh perturbations. Perturbing the mesh transforms the initial undeformed geometry of the bilayer into a non-flat state. The effect of this non-flat initial geometry can be accounted for via an equivalent mesh perturbation compression ($\boldsymbol{\varepsilon_m}$). The equivalent compression is the hypothetical compression that is required to generate the initial non-flat geometry via wrinkling of a flat bilayer. Using Eq. (3.6), the error in amplitude due to mesh perturbations can be estimated as:

$$\delta A = 0.5A\left(\frac{\varepsilon_m}{\varepsilon}\right) \tag{3.9}$$

Here, $\boldsymbol{\delta A}$ is the error in amplitude and $\boldsymbol{\varepsilon_m}$ is the equivalent compression due to mesh perturbation. This equivalent compression is given by:

$$\varepsilon_m = \left(\frac{\pi w h}{\lambda}\right)^2 \tag{3.10}$$

For a weight of 0.05, the error in amplitude is ~0.05% at a compression of 10%. Thus, for practical purposes, the error in amplitude due to such mesh perturbations may be neglected.

3.5.5 Internal consistency tests

Effect of domain size

The period and amplitude of wrinkles are independent of the domain size of the bilayer, i.e., are independent of the length of the bilayer and the thickness of the base layer. This domain size independence can serve as a check for the internal consistency and accuracy of the finite element model. Beyond a threshold value, changes in the thickness of the base layer do not affect the wrinkling process. This threshold layer can be estimated from the response of the system to changes in the base layer thickness. The effect of base layer thickness on the period and amplitude are shown in Figure 3.14(a). For base layers thicker than approximately 100 times the top layer thickness, the base thickness does not have an influence on the wrinkling process. Instead, the base layer is “perceived” as a semi-infinite layer. For thin bases, the approximation of a semi-infinite base is not accurate; this is reflected as a change in the period of the wrinkles.

The effect of length of the bilayers on the period and amplitude are shown in Figure 3.15(b). The amplitude of the wrinkles is linked to the period via kinematics. Thus, the ratio of amplitude to period remains unchanged even when the period changes. It is observed that the period varies as the length of the bilayer is varied, but remains within the uncertainty band given by Eqs. (3.7) and (3.8). The uncertainty depends on the number of wrinkles in the domain and reduces with an increase in the domain size. Thus, to maintain accuracy of period computation one must select a sufficiently long bilayer.

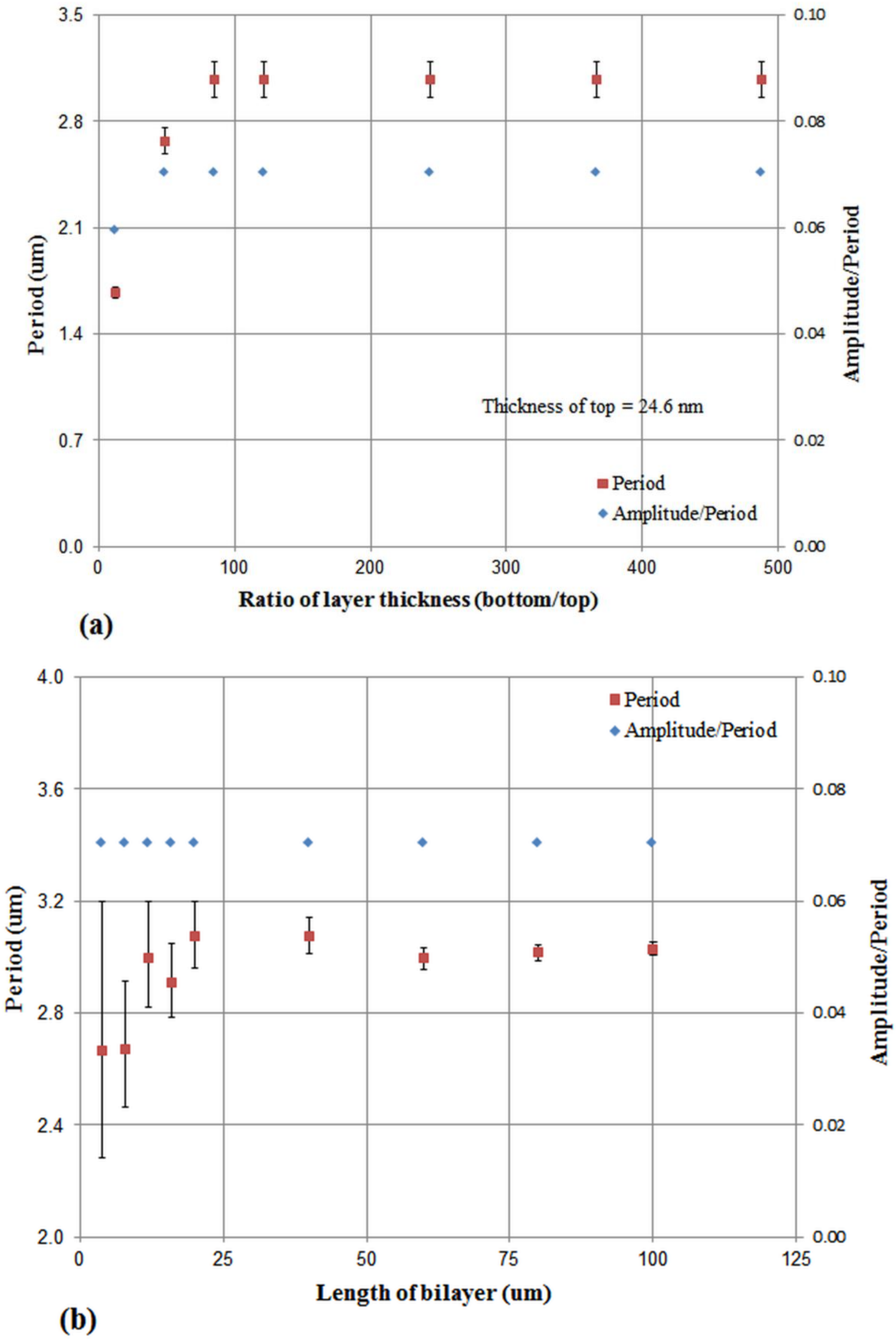

Figure 3.14: Effect of domain size on period and amplitude. (a) Period and amplitude over period ratio versus ratio of thickness of the two layers and (b) period and amplitude over period ratio versus length of bilayer. Period and amplitude should be independent of the domain size for a properly defined system.

For finite element analysis, a smaller domain is preferred so as to reduce the computational time and memory usage. However, the domain size must be sufficiently large to accurately capture the wrinkling phenomenon. Analysis of data shown in Figure 3.14 provides the lower limit of the base thickness and the bilayer length for FEA studies. In this work, the length of the bilayer has been selected to be at least 10 periods long so as to maintain the error in period to be within 5%. The lower limit of base thickness has been set to 100 times the thickness of the top film to ensure that the base acts as a semi-infinite domain.

Amplitude versus period

As the ratio of amplitude to period is determined by kinematics, amplitude over period must be independent of the thickness of the top layer. Also, for large compressions the amplitude over period ratio must be independent of the moduli ratio (η). Instead, the amplitude over period ratio is determined only by the applied compression and is given by Eq. (3.6). Verification of this kinematic relationship between amplitude and period can be used as an internal consistency test to verify that the finite element model has been properly set-up.

The amplitude versus period ratio versus the thickness of the top film and the moduli ratio are shown in Figure 3.15. From the figure it is evident that the period of the wrinkles increases with an increase in the top layer thickness. However, the ratio of amplitude to period remains constant and does not vary with the top layer thickness. The observed amplitude to period ratio differs from the kinematic estimate at low moduli ratio due to the effect of the small pre-buckling lateral compression of the top film. For large compressions of the bilayer, this lateral compression of the top film may be neglected.

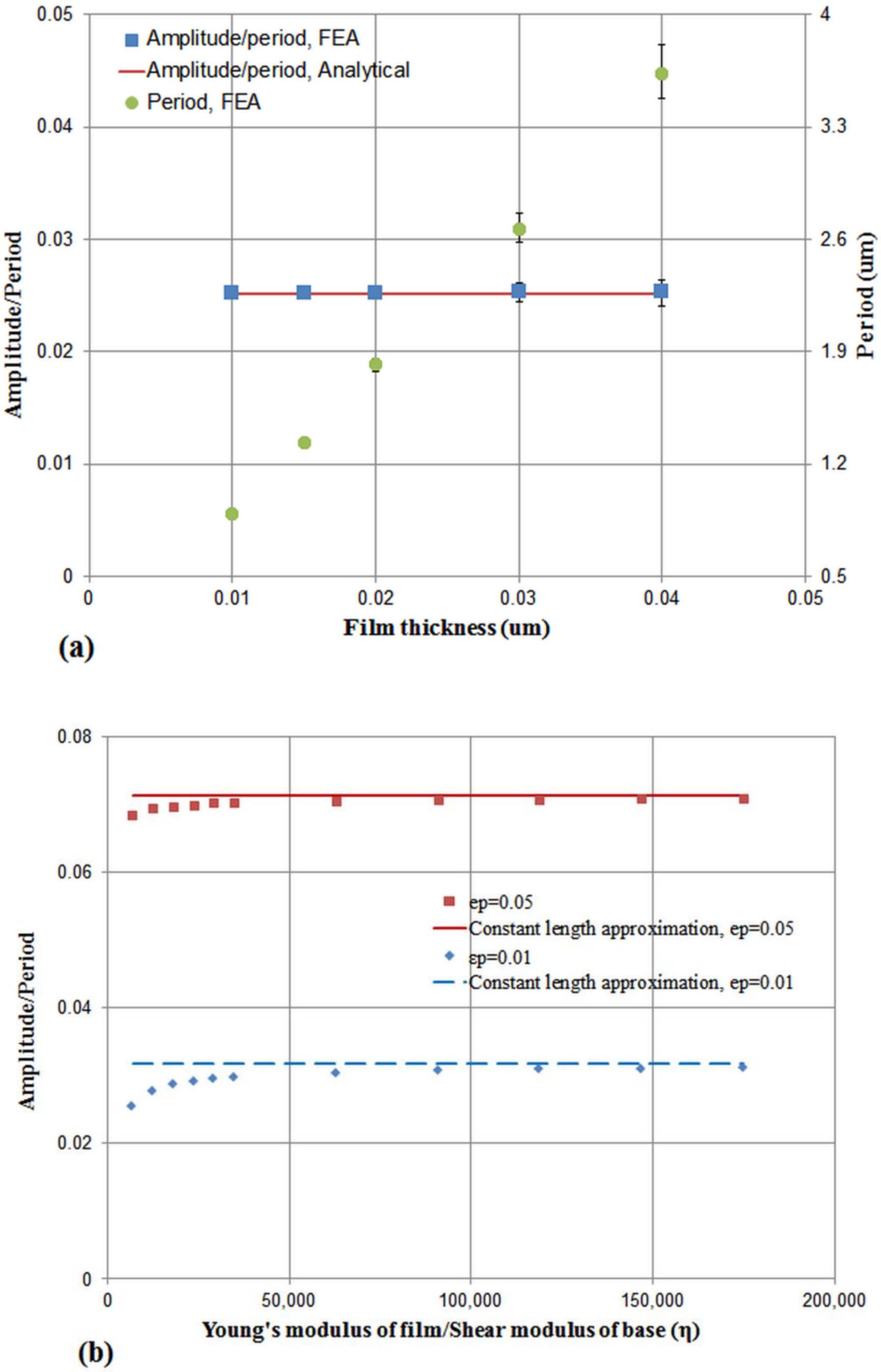

Figure 3.15: Effect of thickness of top film and material properties on the ratio of amplitude and period at a constant pre-stretch release (a) Amplitude over period versus thickness of top film; η=35000, pre-stretch release ε_p = 0.75%, and critical stretch ε_c=0.126% for analytical estimate. (b) Amplitude over period versus material property ratio (η). Amplitude over period ratio is related to the pre-stretch release purely via kinematics and is independent of the thickness of top film. For large pre-stretch release, effect of material properties on amplitude may be neglected with an error of the order of $0.5\varepsilon_c/\varepsilon_p$.

Effect of material properties

The effect of material properties on the period and amplitude is through the ratio of the Young's modulus of the top layer and the shear modulus of the bottom layer. Thus, no changes in the period and amplitude should be observed if the moduli ratio is held constant while the individual moduli are varied. This can be used an internal consistency test to verify the accuracy of the FEA. The effect of changes in moduli on the period when the moduli ratio is held constant is shown in Figure 3.16. From the figure it is evident that the effect of material properties on the period is perceived only through the ratio of the moduli.

The effect of moduli ratio on the period has also been studied. The results are summarized in Figure 3.17. The expected trend from Eq. (2.1) is that the period is proportional to 1/3rd power of the moduli ratio. This power law dependence of period on moduli ratio is supported by the results of the FEA as shown in Figure 3.17.

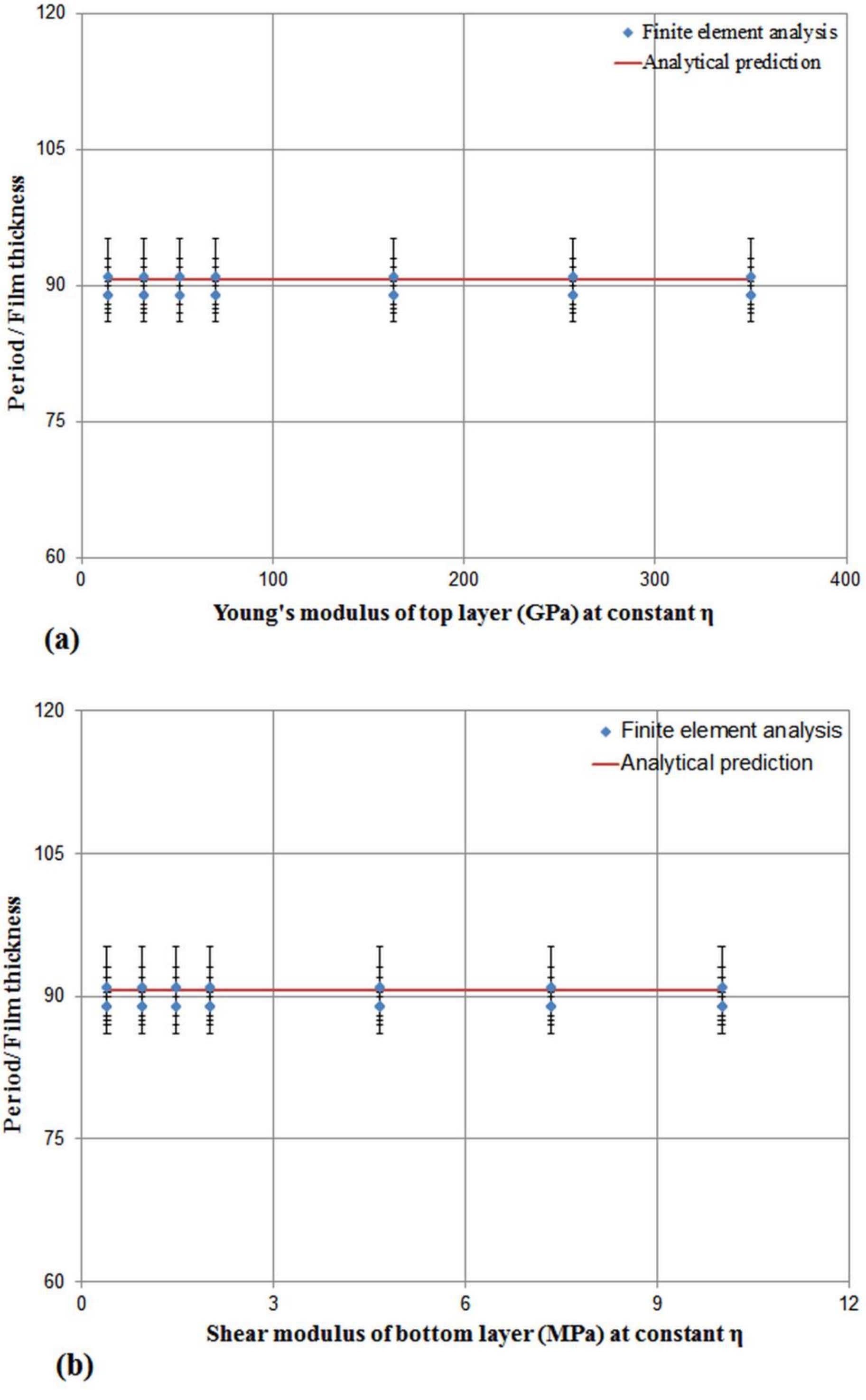

Figure 3.16: Effect of material properties on period when the moduli ratio is held constant. (a) Period over film thickness versus Young's modulus of top film at constant material property ratio (η=35,000). (b) Period over film thickness versus shear modulus of compliant base at constant material property ratio (η=35,000). Film thickness was varied over 10 nm, 15 nm, 20 nm, 30 nm, and 40 nm; pre-stretch to the base was 0.75%. Effect of material properties on period is observed only through the ratio of properties of the top and bottom layers, i.e. through η. Error bars represent the uncertainty in the measured period as given by Eqs. (3.7) and (3.8).

Length of top film

During wrinkling, compression of the bilayer leads to bending of the top film without any lateral compression of the film. Thus, the length of the top film is expected to remain constant with an increase in the bilayer compression. This length constancy property of the wrinkling process can be used as a test to verify the accuracy of the finite element model.

The length of the top film was computed from the FEA results by numerically evaluating the length of the deformed profile of the mid-plane of the top film. The length of the base layer was evaluated directly from the applied compression. The change in length of the two layers of the bilayer with compression is shown in Figure 3.18. As expected, the length of the top film does not change during wrinkling. There is an initial lateral compression of the film prior to buckling bifurcation that is on the order of the critical bifurcation compression. Thus, for practical purposes, the lateral compression of the top film may be neglected. The effect of film thickness and moduli ratio on the length of the wrinkled film is shown in Figure 3.19. As is evident from the figure, the length of the wrinkled film is independent of the film thickness. Also, the lateral compression of the film length may be approximately considered to be independent of the moduli ratio. Thus, the applied compression and the size of the deformed film are linked only via kinematics. This kinematic relationship is an important tool in predictive modeling of wrinkled patterns.

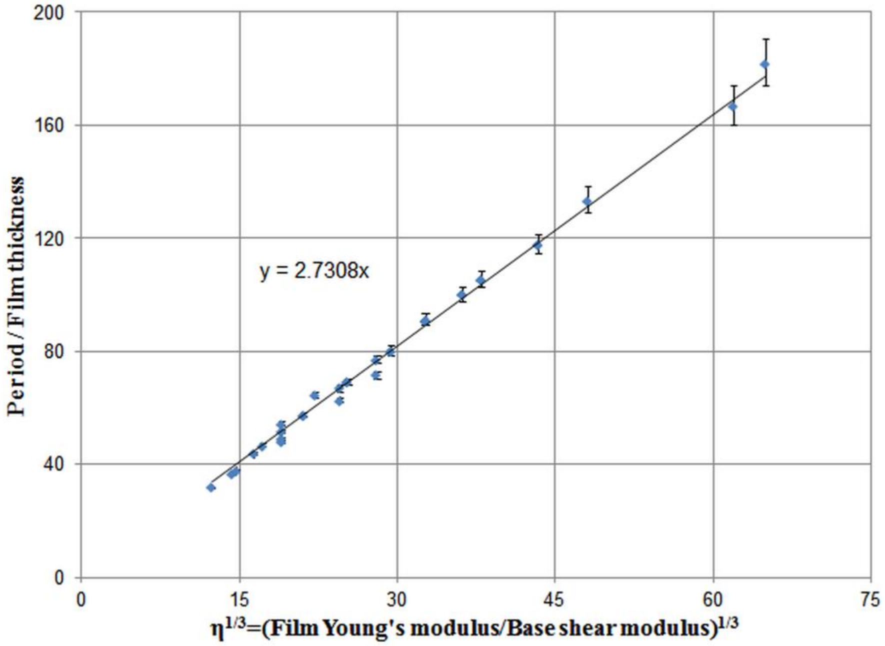

Figure 3.17: Effect of moduli ratio on period over film thickness. Film thickness was varied over 10 nm, 15 nm, 20 nm, 30 nm, and 40 nm; pre-stretch to the base was 0.75%. The moduli ratio was varied by varying the Young's modulus of the top layer over 14-350 GPa and varying the shear modulus of base over 0.4-10 MPa.

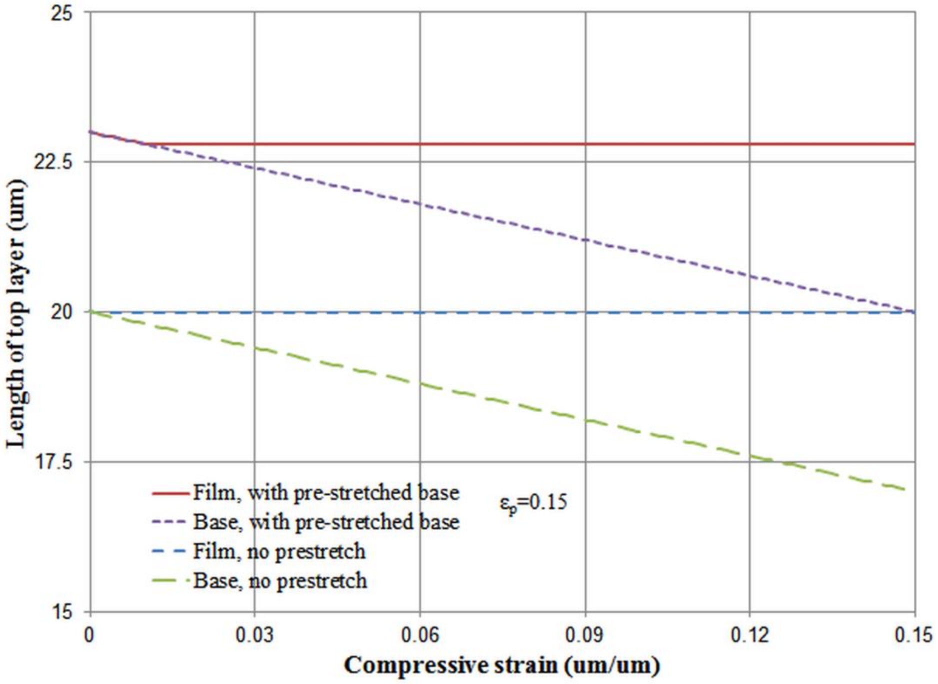

Figure 3.18: Change in length of the two layers as the bilayer is compressed for the cases when the base is pre-stretched and no pre-stretch is applied to the base. The base undergoes lateral compression, whereas the top layer undergoes negligible lateral compression after the onset of bifurcation. Here, thickness of top film is 24.6 nm and the moduli ratio η=78,125.

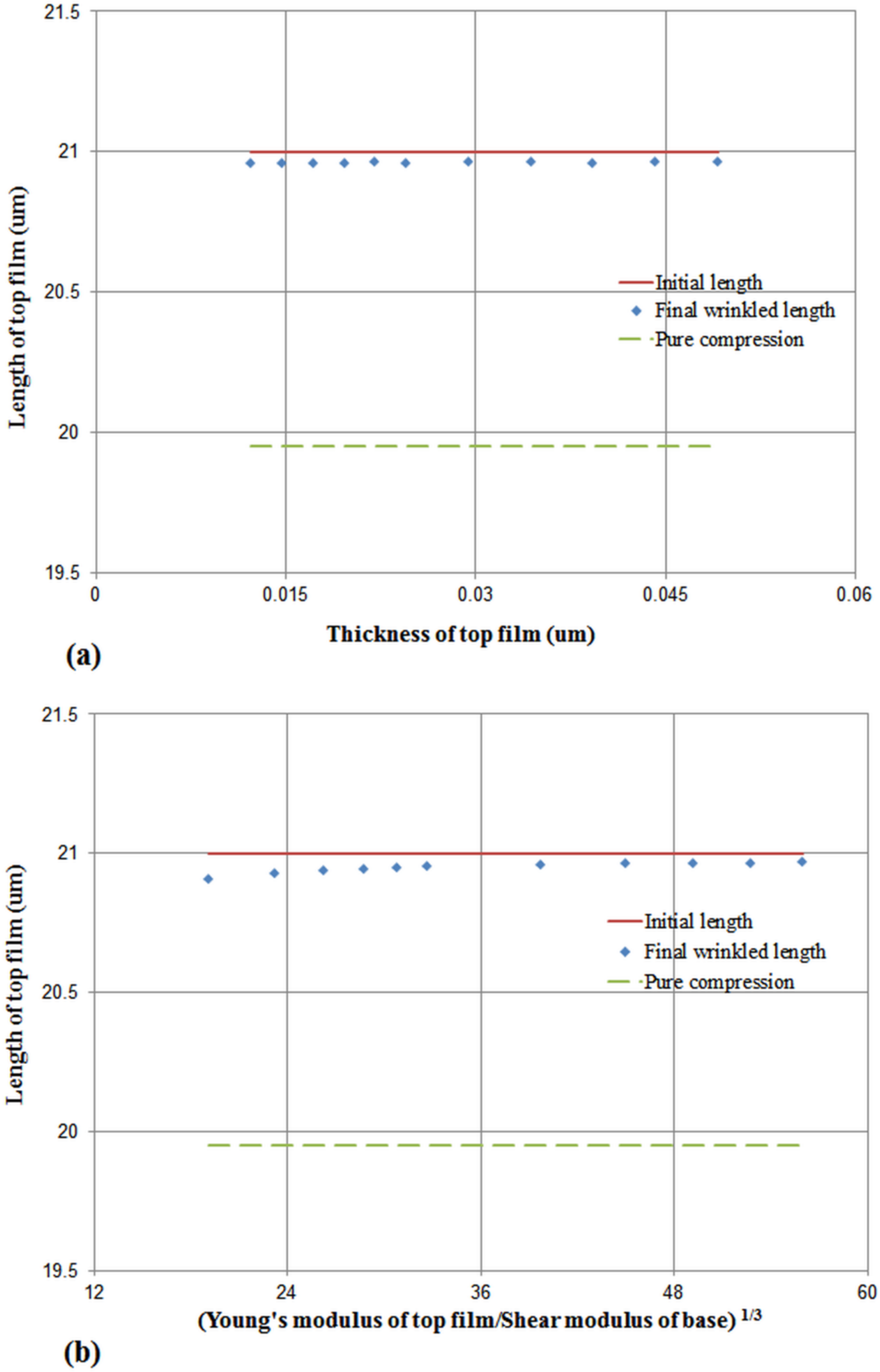

Figure 3.19: Effect of thickness of top film and material properties on the length of the top film during pre-stretch release of the bilayer. (a) Length of top film versus thickness of top film; η=78,125; pre-stretch release ε_p=5%. (b) Length of top film versus material property ratio (η); h=20 nm, pre-stretch release ε_p=5%. For sufficiently large pre-stretch release, the effect of the initial compression of the top film before bifurcation may be neglected with an error of the order of ε_c.

Energy of wrinkles

The energy of the wrinkles can be evaluated by separately evaluating the energy of the two domains: (i) the top film and (ii) the bottom base. For 2-D models, the area energy density is evaluated as the average energy density over the length and width into the plane. The energy density (***E_i***) is evaluated as:

$$E_i = \frac{1}{L}\int_0^{h_i}\int_0^{L} W_s\, dx\, dy \tag{3.11}$$

Here, the subscript ***i*** refers to the ***i^{th}*** domain, i.e., bottom base (1) or the top film (2), ***W_s*** is the volumetric deformation energy density, ***L*** is the length of the bilayer, and ***h_i*** is the thickness of the ***i^{th}*** domain.

The energy of the base layer includes the energy due to wrinkle formation and the energy due to lateral compression of the base. For a sufficiently thick base, the energy due to lateral compression dominates the energy of the base and cannot be neglected. The fraction of energy in the base purely due to wrinkling can be estimated by evaluating the energy of the base in an equivalent compressed bilayer with no imperfections. As a bilayer without imperfections does not undergo wrinkling bifurcation, all of the energy in such a system is due to lateral compression. Thus, the contribution of the base to energy of wrinkling can be evaluated by subtracting this lateral compression-only energy from the total energy of the base.

The evolution of energy of the wrinkled system with compression is shown in Figure 3.20. As expected, the energy of the top film during wrinkling is much lower than the energy during pure lateral compression. Also, during wrinkling the energy of the film varies linearly with compression. This is because the energy of the wrinkled film is determined entirely by the bending of the film without any contribution from film stretching or lateral compression. Before bifurcation, the energy of the film dominates the overall bilayer energy as the deformation energy of such a flat film is determined by stretching or lateral compression.

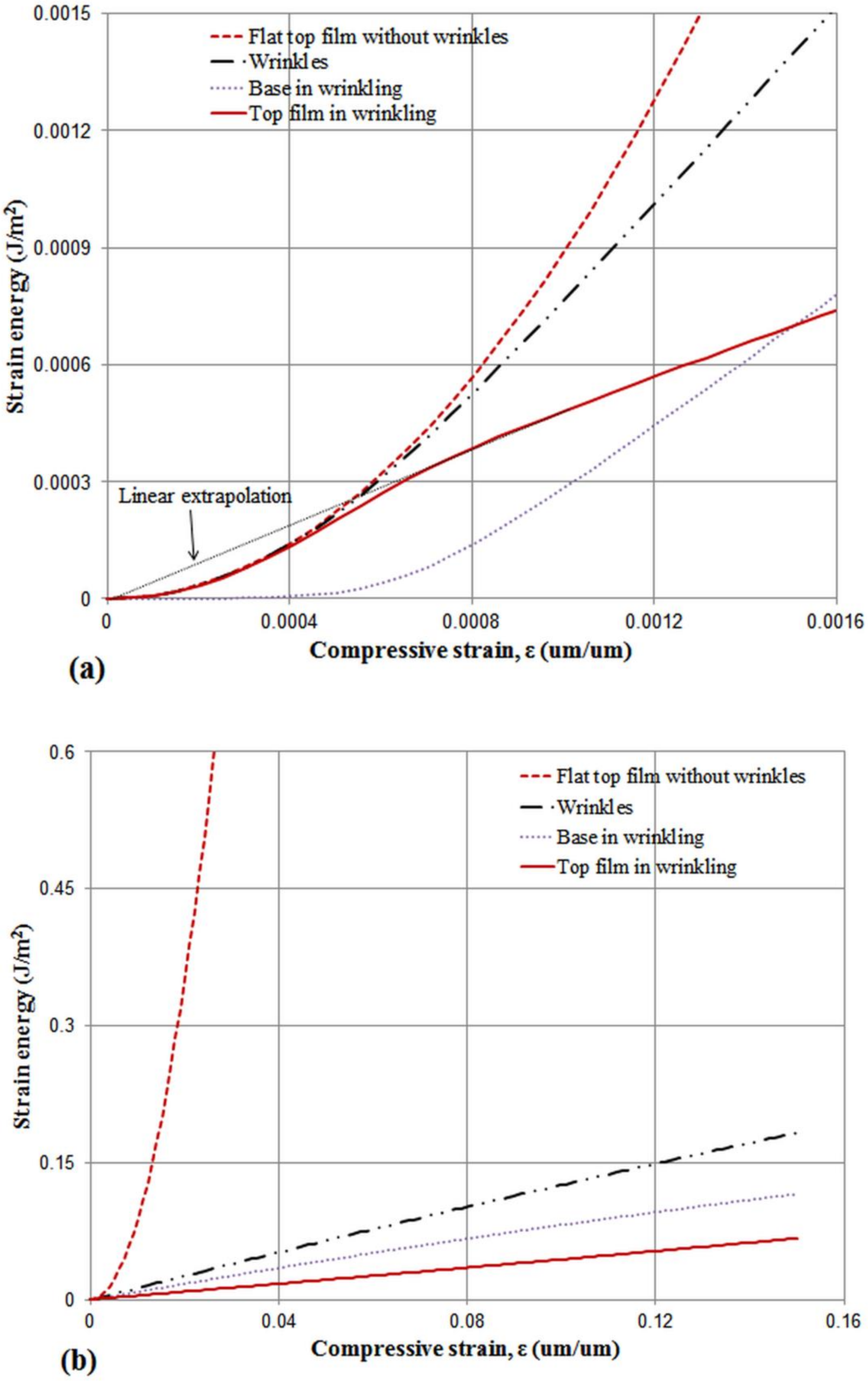

Figure 3.20: Evolution of the strain energy of the bilayer with compression. (a) Strain energy versus strain for small values of strain that are comparable to the bifurcation strain and (b) Strain energy versus strain for high strain values. Here, the thickness of top film is 24.6 nm and the moduli ratio η is 78,125.

Chapter 4

Hierarchical wrinkles: Complexity via geometry

4.1 Introduction

A hierarchical wrinkled pattern is one that comprises more than one spatial frequency, i.e., hierarchical wrinkled patterns demonstrate periodic sinusoidal patterns of one period built on top of patterns of another period. In general, hierarchical patterns may demonstrate hierarchy on several length scales, i.e. patterns with several different periods. Herein, the fabrication and prediction of hierarchical patterns with two spatial periods is presented.

Often, hierarchical structures are fabricated via a combination of two or more substantially different fabrication processes. This leads to manufacturing challenges in terms of throughput, cost, and/or scalability as one needs to satisfy the requirements for multiple processes. The purpose of this work is to develop a scalable and affordable process to fabricate hierarchical structures via a single fabrication process. This has been achieved by performing wrinkling of pre-patterned surfaces wherein the pre-patterned surfaces are also fabricated via wrinkling. Thus, hierarchy of wrinkles is generated via control of the geometry of the bilayers. Presented here is: (i) a fabrication process scheme for generating hierarchical patterns from wrinkling of pre-patterned surfaces, (ii) demonstration of fabrication of tunable hierarchical patterns via this scheme, and (iii) an analytical and finite element model to predict the generation of hierarchical patterns.

4.1.1 Limitations of existing techniques

Although hierarchical wrinkling has been demonstrated in the past [22, 50, 73-76], there are major limitations that prevent one from using the existing techniques in a manufacturing environment. These limitations are: (i) inability to accurately predict the resulting pattern for a given set of process parameters and (ii) inability to perform inverse pattern design; i.e., inability to predictively design and fabricate the desired hierarchical patterns by combining several patterns. For example, Chiche et al. [50] demonstrated the fabrication of “composite” modes that were generated by wrinkling of pre-patterned surfaces. However, due to lack of predictive capability, it’s not possible to perform an inverse pattern design using this scheme. Formation of hierarchical wrinkles has also been demonstrated by Efimenko et al. [22]. In their work, a predictive model for emergence of these wrinkles has also been proposed. However, the process of emergence of hierarchical patterns is fundamentally different as the hierarchy results due to the presence of gradients in material properties that are difficult to control via fabrication process parameters. Thus, it is not possible to generate a wide class of desired hierarchical patterns by tuning/controlling the process parameters. Herein, (i) a fabrication scheme is proposed that enables generating a wide class of hierarchical patterns by tuning the control parameters and (ii) a predictive model is presented that enables inverse design of desired hierarchical patterns.

4.1.2 Behavior of pre-patterned surfaces: quasi-planar wrinkling

When a pre-patterned periodic bilayer is compressed, its behavior is different from that of a planar bilayer. As demonstrated in Chapters 2 and 3, a planar bilayer wrinkles into a single-period natural mode. However, a corresponding quasi-planar bilayer upon compression may (i) wrinkle into the natural mode, (ii) persist with the period of the quasi-planar mode, or (iii) wrinkle into a hierarchical mode that is a combination of the natural mode and the quasi-planar mode. These modes are illustrated in Figure 4.1. The difference between the planar and the pre-patterned quasi-planar bilayer systems is purely geometric, i.e., the two differ only by the presence or absence of a pre-pattern. Wrinkling of quasi-planar bilayers into the natural mode is observed when the amplitude of pre-patterns is low enough for the quasi-planar surface to be considered as a flat surface. However, when the amplitude is not negligible, one observes a mode lock-in phenomenon wherein the amplitude of the pre-patterned mode grows with compression. This mode then eventually transitions into a hierarchical mode beyond a critical threshold compressive strain. The purpose of this work is to develop an analytical and finite element model to predict this critical strain.

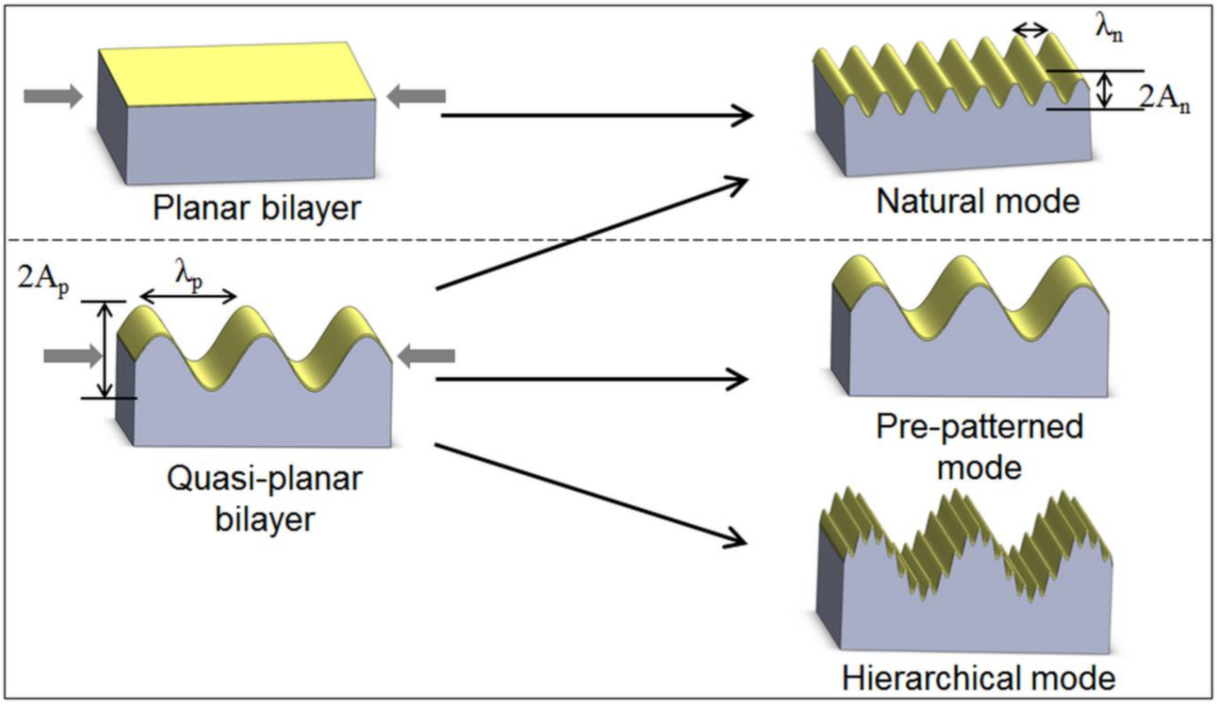

Figure 4.1: Comparison of wrinkling of flat bilayer systems versus quasi-planar bilayers. The two bilayers are identical except for the presence of pre-patterned geometry in quasi-planar bilayers. (a) Flat bilayers wrinkle into the natural mode upon compression. (b) Quasi-planar bilayer systems may wrinkle into the natural mode, pre-patterned mode, or a complex hierarchical mode. The purpose of this work is to predict the wrinkled mode that is obtained upon compression of quasi-planar surfaces.

4.1.3 Modeling and fabrication goals

The modeling goals are:

(i) Analytical and finite element based prediction of mode transition for a given set of process parameters

(ii) Prediction of mode transition for all feasible combinations of pre-patterns and natural patterns

The fabrication goals are:

(i) Development of a fabrication scheme for generating quasi-planar pre-patterns

(ii) Identification and quantification of feasible limits for combination of pre-patterns and natural patterns

Toward these goals, the following are presented here: (i) fabrication process for hierarchical patterns, (ii) limits of process parameters, (iii) finite element modeling technique, (iv) analytical model for predicting mode transition, and (v) verification of the analytical model against experiments and finite element analysis.

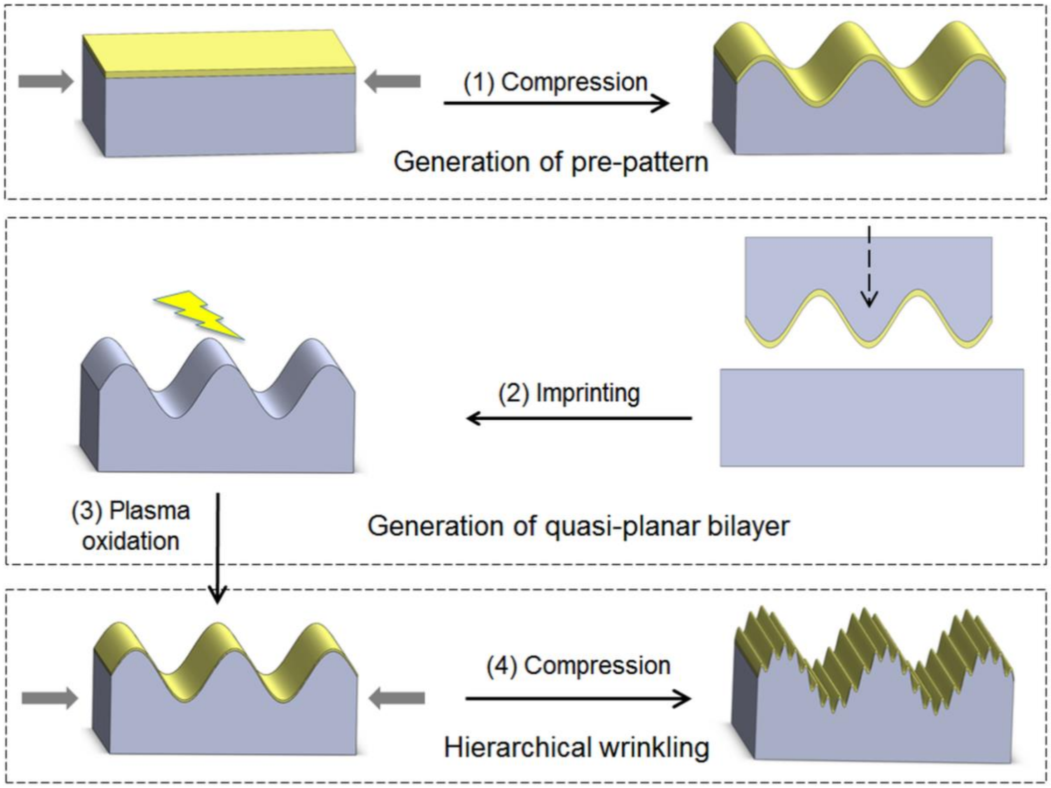

Figure 4.2: Schematic of the fabrication process for generating hierarchical patterns. The steps are (1) Generation of pre-patterns via wrinkling of flat bilayers, (2) transfer of the pre-pattern onto PDMS via imprinting to generate quasi-planar surface, (3) generation of glassy film on top of quasi-planar PDMS to generate quasi-planar bilayer, and (4) compression of quasi-planar bilayer.

4.2 Fabrication process

4.2.1 Process scheme

Quasi-planar surfaces were fabricated on PDMS by using wrinkled surfaces as the molds/templates to generate the PDMS casts as summarized in Figure 4.2. The process steps are (i) generation of the pre-patterns via wrinkling of planar PDMS/glassy bilayers and (ii) replication of these pre-patterns onto a new PDMS sample via casting/curing. The curing protocol for pattern replication is same as discussed in Chapter 2 with the additional step of imprinting the pre-pattern onto the PDMS material during curing. Imprinting is performed by "gently" placing the pre-patterned coupon on top of the exposed surface of the curing PDMS while taking care that the patterned surface is oriented toward the curing material.

4.2.2 Process parameters

The geometric parameters that are relevant to predictive design of hierarchical wrinkles are: (i) the period ($\boldsymbol{\lambda_p}$) of the pre-pattern, (ii) the amplitude of the pre-pattern ($\boldsymbol{A_p}$), (iii) the period of the natural mode ($\boldsymbol{\lambda_n}$), and (iv) the amplitude of the natural pattern ($\boldsymbol{A_n}$). The natural pattern is the hypothetical pattern that would have been observed for a corresponding un-patterned flat bilayer. During design and prediction, the effect of material properties and compression is indirectly accounted for by the natural period and amplitude; whereas the pre-pattern accounts for the geometric effect. As the period and amplitude of the pre-patterns and natural patterns can be independently tuned, a wide range of hierarchical patterns is feasible.

4.2.3 Process protocol

A well-controlled imprinting process is essential to fabricate the desired hierarchical patterns. Factors during imprinting that influence pattern replication are (i) contact force, (ii) uniformity of contact with minimum bubbles/gaps, and (iii) alignment of pre-patterns to the direction of subsequent stretching. To ensure a well-controlled imprinting process, a protocol was developed. This protocol is listed in Table 4.1.

Table 4.1: Protocol for imprinting pre-patterns on PDMS

#	Step	Protocol
1	Mixing of two-part PDMS (resin + curing agent) with curing ratio of 1 part curing agent for 'r' part resin; $r \in [6, 15]$	r =12 or r=15
2	Degassing of the two part mixture under vacuum pressure P_d for t_d minutes	P_d <=-28.5 inHg, t_d =20 minutes
3	Pouring two part mixture onto aluminum mold. The mold is held at constant temperature T_L using a hot plate	T_L =65 ^{0}C
4	Low temperature curing up to gelation point: Mold held at constant temperature T_L for t_l minutes	T_L =65 ^{0}C, t_l=20 min
5	Imprinting pre-pattern onto the top surface of PDMS mold t_i minutes after start of curing	6 min< t_i <8 min
6	High temperature curing: increasing mold temperature to T_H after t_l minutes of pouring and holding this temperature for t_h minutes	T_H =165 ^{0}C, t_h=15 min
7	Taking mold off the heater and then placing it on aluminum thermal sink that is maintained at room temperature for at least t_s minutes	t_s=10 min

In the presence of insufficient contact force, PDMS does not flow into the pre-pattern; whereas high contact force leads to excess flow of PDMS under the pre-pattern and a thinner-than-desired casting. The sensitivity of flow to contact force decreases as curing proceeds due to the increase in viscosity of PDMS. Therefore, delayed imprinting is performed, i.e., imprinting close to, but before, the gelation point instead of at the beginning of the curing process.

To ensure uniform contact and to align the pre-patterns along the stretch direction, a gradual imprinting/alignment scheme was developed. Steps of this scheme are: (i) aligning one of the edges of the pre-patterned coupon to the machined alignment features on the metal mold, (ii) bringing the aligned edge into contact with the curing material, and (iii) gradually bringing the rest of the pre-pattern coupon into contact with the curing material. During gradual contact, alignment is maintained due to no-slip along the initial contact edge and uniform contact can be verified by visual inspection of the moving contact meniscus.

4.2.4 Process constraints

As the pre-patterns are fabricated via wrinkling, only a finite set of pre-patterns is available. This set comprises 1-D sinusoidal periodic patterns over a finite range of period ($\boldsymbol{\lambda_p}$) and amplitude ($\boldsymbol{A_p}$). Herein, (i) the link between feasible range of period and amplitude and the fabrication constraints is established and (ii) upper and lower bounds of the feasible range are quantified.

Fabrication constraints arise due practical limitations such as resolution of vision system, overheating during plasma oxidation, and failure/tearing of PDMS during stretching. During fabrication of wrinkles, period is controlled via the exposure time during plasma oxidation and amplitude is controlled via stretching of PDMS. Thus, fabrication constraints can be linked to the feasible range of period and amplitude by quantifying the feasible range of (i) PDMS stretching ($\boldsymbol{\varepsilon}$) and (ii) exposure time during plasma oxidation.

The maximum stretching ($\boldsymbol{\varepsilon_u}$) is determined by whichever is lower between the failure stretch and the critical stretch release for higher mode transition. Higher modes are experimentally observed at around 18% pre-stretch release versus the failure stretch of around 60%. Hence, the maximum stretching is determined by the transition to second mode for the bilayer systems that were fabricated here. The minimum stretching is determined by the lowest stretch-release at which reliable patterns can be identified under the microscope. This depends on the resolution of the vision system and is given by $\boldsymbol{\varepsilon_l}$. This minimum stretch was observed to be of the order of 2% pre-stretch release. The minimum achievable wavelength ($\boldsymbol{\lambda_l}$) and the maximum wavelength ($\boldsymbol{\lambda_u}$) are determined by shortest and longest feasible exposure time for plasma oxidation. For the plasma oxidation system used here, the typical values for upper and lower wavelengths are approximately 6 um and 0.75 um, respectively.

Due to the process constraints, there is only a finite set of feasible combinations of pre-patterns and natural patterns that can be achieved via this pre-patterning technique. The feasible combinations of wavelengths are given by:

$$\max\left(\frac{\lambda_p}{\lambda_n}\right)=\frac{\lambda_u}{\lambda_l} \tag{4.1}$$

$$\min\left(\frac{\lambda_p}{\lambda_n}\right)=\frac{\lambda_l}{\lambda_u} \tag{4.2}$$

The feasible combinations of amplitudes can be linked to the feasible combinations of wavelengths and the feasible limits of stretching via Eq. (3.6) as:

$$\max\left(\frac{A_p}{A_n}\right)=\left(\frac{\lambda_p}{\lambda_n}\right)\left(\frac{\varepsilon_u}{\varepsilon_l}\right)^{0.5} \tag{4.3}$$

$$\min\left(\frac{A_p}{A_n}\right)=\left(\frac{\lambda_p}{\lambda_n}\right)\left(\frac{\varepsilon_l}{\varepsilon_u}\right)^{0.5} \tag{4.4}$$

The relationships of Eqs. (1.3)-(4.4) are graphically represented in Figure 4.3.

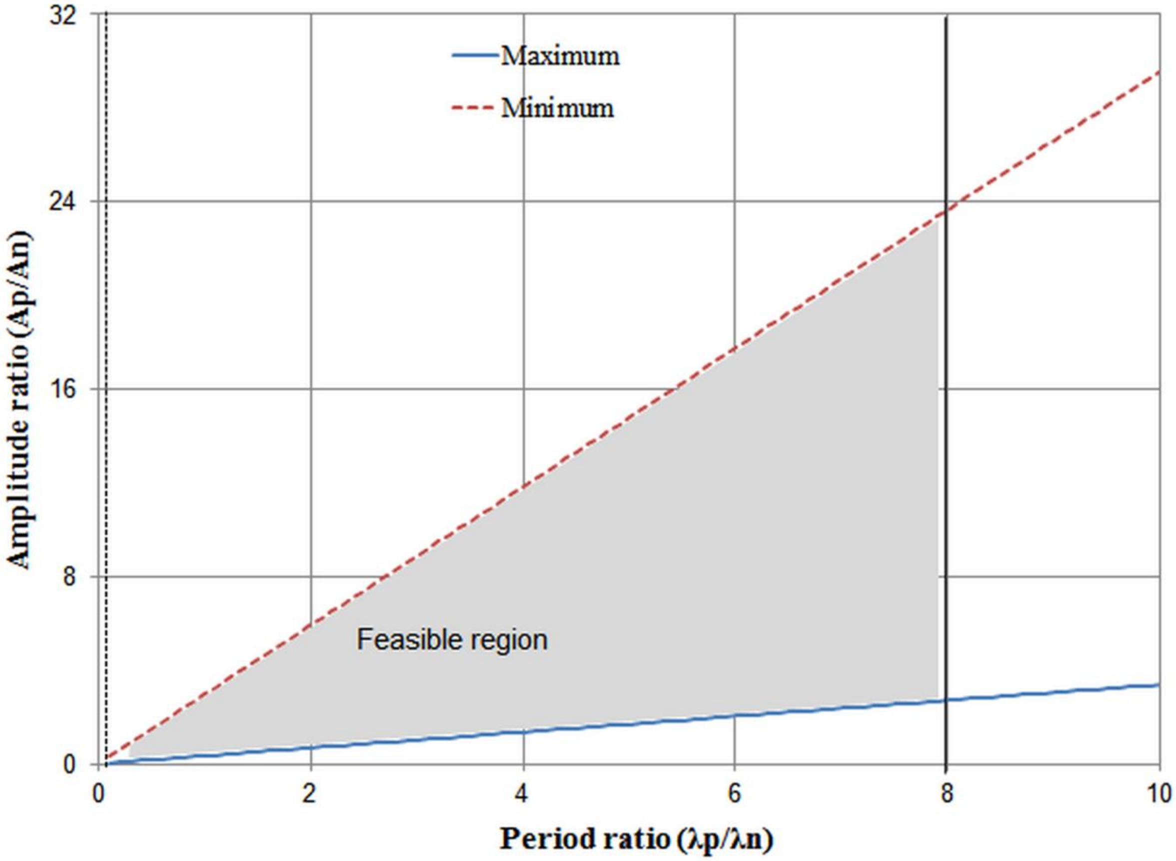

Figure 4.3: Feasible region of geometric process parameters. Only a finite set of the entire design space for hierarchical patterns is experimentally accessible due to practical process constraints. Upper and lower limits of period are determined by the plasma oxidation process. Upper limit of amplitude is determined by the pre-stretch release for transition into higher mode, whereas lower limit is determined by the resolution of microscope.

4.2.5 Fabricated patterns

Patterns that were generated by compression of quasi-planar surfaces are shown in Figure 4.4. The images of the patterns that were obtained via an Atomic Force Microscope (AFM) demonstrate that both mode lock-in and hierarchy are observed. The measurements were performed at the central region of the bilayer coupons away from the edges to ensure that the strain is uniform.

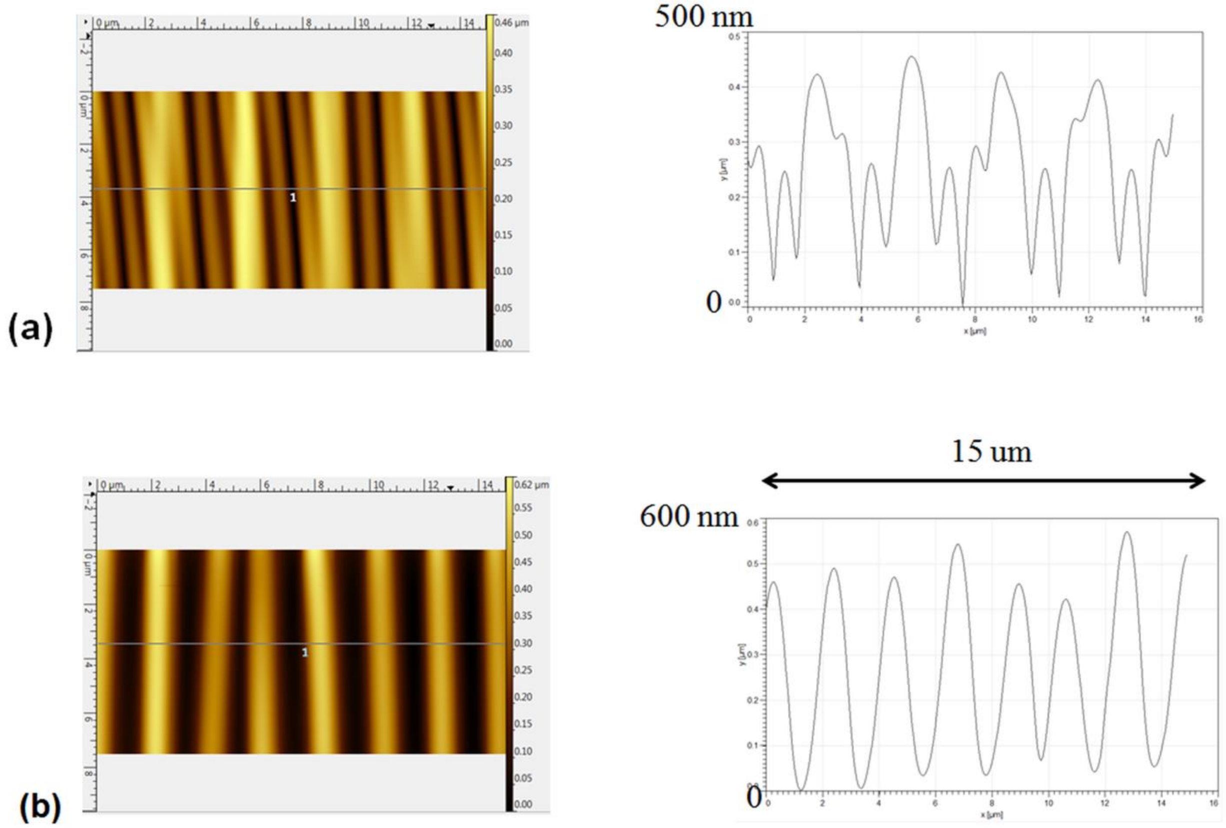

Figure 4.4: (a) Fabricated hierarchical pattern as seen under a 2-D atomic force microscope scan and 1-D cross-sectional view along the stretch direction. Nominal pre-pattern period is 3.35 um and amplitude is 276 nm. Nominal natural period is 1.5 um and amplitude is 182 nm. (b) Fabricated pattern with mode locked into the pre-pattern. Nominal pre-pattern period is 2.23 um and amplitude is 273 nm. Nominal natural period is 1.5 um and amplitude is 182 nm.

4.3 Finite element modeling

4.3.1 Generating pre-patterns

Quasi-planar surfaces were generated by perturbing the mesh points of the planar surfaces. The scheme for perturbing a mesh is described in Sec. 3.3. Mesh perturbation was performed by (i) evaluating the shape functions that are required to morph the flat surface into the desired quasi-planar surface and (ii) adding these shape functions to the mesh points of the flat surface as described by Eq. (3.1). Herein, the methodology to evaluate the mesh perturbations that are required for generating the desired periodic surface is presented; i.e., the methodology to evaluate the shape functions '$\boldsymbol{u}_{i,j}$' and the weight factor '$\boldsymbol{w}$' in Eq. (3.1).

Quasi-planar surfaces were generated by perturbing an existing mesh instead of defining a new geometry via CAD software because this technique (i) has a higher flexibility in generating free-form surfaces due to the ability to independently perturb each mesh point, (ii) conveniently interfaces with the existing codes for post-buckling analysis of flat surfaces, and (iii) reduces the number of processing steps. During generation of quasi-planar surfaces from flat surfaces, the mesh must be sufficiently fine so as to be able to accurately morph into a curved geometry. This requirement is automatically satisfied for cases when the pre-pattern period is higher than the natural period; however, for lower pre-pattern periods a preliminary mesh refinement may be necessary before perturbing the original mesh of the flat geometry.

Shape of top film

The desired shape of the top film is defined by the period (***λ_p***) and the amplitude (***A_p***). It is given by:

$$Y = A_p \cos\left(\frac{2\pi X}{\lambda_p}\right) \tag{4.5}$$

Here, '***X***' and '***Y***' are the spatial coordinates in the *undeformed* coordinate system.

In this scheme, the mesh is perturbed such that the interface between the top and the bottom layers follows the desired shape that is defined by Eq. (4.5). Perturbation for the rest of the film is evaluated by implementing these constraints: (i) thickness of the film is uniform throughout its length and (ii) thickness of the film in the perturbed system is same as that in the flat system. These constraints can be evaluated by generating curves that are parallel to the desired shape of Eq. (4.5). Thus, shape functions for perturbing the top film are given by:

$$u_{1,j} = X_{2,j}\left(\frac{2\pi A_p}{\lambda_p}\right)\left(\frac{\sin\left(2\pi X_{1,j}/\lambda_p\right)}{\sqrt{1+\left(2\pi A_p/\lambda_p\right)^2 \sin^2\left(2\pi X_{1,j}/\lambda_p\right)}}\right) \tag{4.6}$$

$$u_{2,j} = A_p \cos\left(2\pi X_{1,j}/\lambda_p\right) + \left(\frac{X_{2,j}}{\sqrt{1+\left(2\pi A_p/\lambda_p\right)^2 \sin^2\left(2\pi X_{1,j}/\lambda_p\right)}}\right) \tag{4.7}$$

For $\boldsymbol{X_{2,j}} = 0$, i.e., at the interface between the two layers, $\boldsymbol{u_{1,j}} = 0$,i.e., $\boldsymbol{x_{1,j}} = \boldsymbol{X_{1,j}}$ and $\boldsymbol{u_{2,j}} = \boldsymbol{A_p}$ $\cos(\boldsymbol{2\pi X_{1,j}/\lambda_p})$ that is equivalent to the shape function defined by Eq. (4.5). The shape of the mesh perturbations are given by Eqs. (4.6) and (4.7), and the amplitude of the perturbations is given by:

$$A_p = wh \tag{4.8}$$

Here, '$\boldsymbol{w}$' is a non-dimensional weight factor and '$\boldsymbol{h}$' is the thickness of the top film. Thus, all parameters of Eq. (3.1) that are required for performing mesh perturbation of the top layer have been evaluated.

Shape of base

The top edge of the base layer is given by Eq. (4.5) that defines the interface between the two layers. The rest of the base layer must satisfy the following kinematic constraints: (i) edges on the sides and bottom of the base must satisfy the applied displacement boundary conditions and (ii) all mesh points in the perturbed mesh must remain bounded by the edges, i.e., mesh points should not lie outside the domain that is defined by the mesh points of the edge. These two constraints are satisfied by the pre-buckling solution for the special case when the imperfection period is same as the natural period ($\boldsymbol{\lambda_p}$=$\boldsymbol{\lambda_n}$). Thus, the perturbations for the base are obtained by modifying the pre-buckling solution for this case [17] as:

$$u_{1,j} = kX_{2,j}\sin\left(\frac{2\pi X_{1,j}}{\lambda_p}\right)\exp\left(kX_{2,j}\right) \tag{4.9}$$

$$u_{2,j} = \left(1 - kX_{2,j}\right)\cos\left(\frac{2\pi X_{1,j}}{\lambda_p}\right)\exp\left(kX_{2,j}\right) \tag{4.10}$$

Here, $\boldsymbol{k}=2\pi/\boldsymbol{\lambda_n}$ is the wave number corresponding to the natural period of the system.

The displacement field of the pre-buckling solution has these characteristics: (i) exponential decay with vertical distance away from the interface, (ii) maximum amplitude that is determined by the wave number, and (iii) periodic variation along the horizontal direction. The shape functions given by Eqs. (4.9) and (4.10) were obtained from the analytical 'natural' pre-buckling displacement field by (i) replacing the horizontal period by the pre-pattern period $\boldsymbol{\lambda_p}$ and (ii) maintaining the same decay constant and amplitude as in the pre-buckling solution. Additional constraints that are not captured by Eqs. (4.9) and (4.10) are applied to implement the displacement boundary conditions as follows: $\boldsymbol{u_{1,j}}$ = 0 for vertical edges and $\boldsymbol{u_{2,j}}$ = 0 for the horizontal edge at the bottom of the base. The weight factor for the perturbations of the base is same as that for the film. Thus, Eqs. (4.6)-(4.10) define the mesh perturbations for the entire system.

Perturbed mesh

Examples of some perturbed mesh are shown in Figure 4.5 and Figure 4.6. Figure 4.5(a) shows a perturbed mesh for the case when the pre-pattern wavelength is higher than the natural period; whereas Figure 4.5(b) shows the mesh for the case when the wavelength of the pre-pattern is lower than that of the natural pattern. An incorrect mesh shown in Figure 4.6 demonstrates the need to accurately select the perturbation shapes so that all of the mesh points lie within the system boundaries.

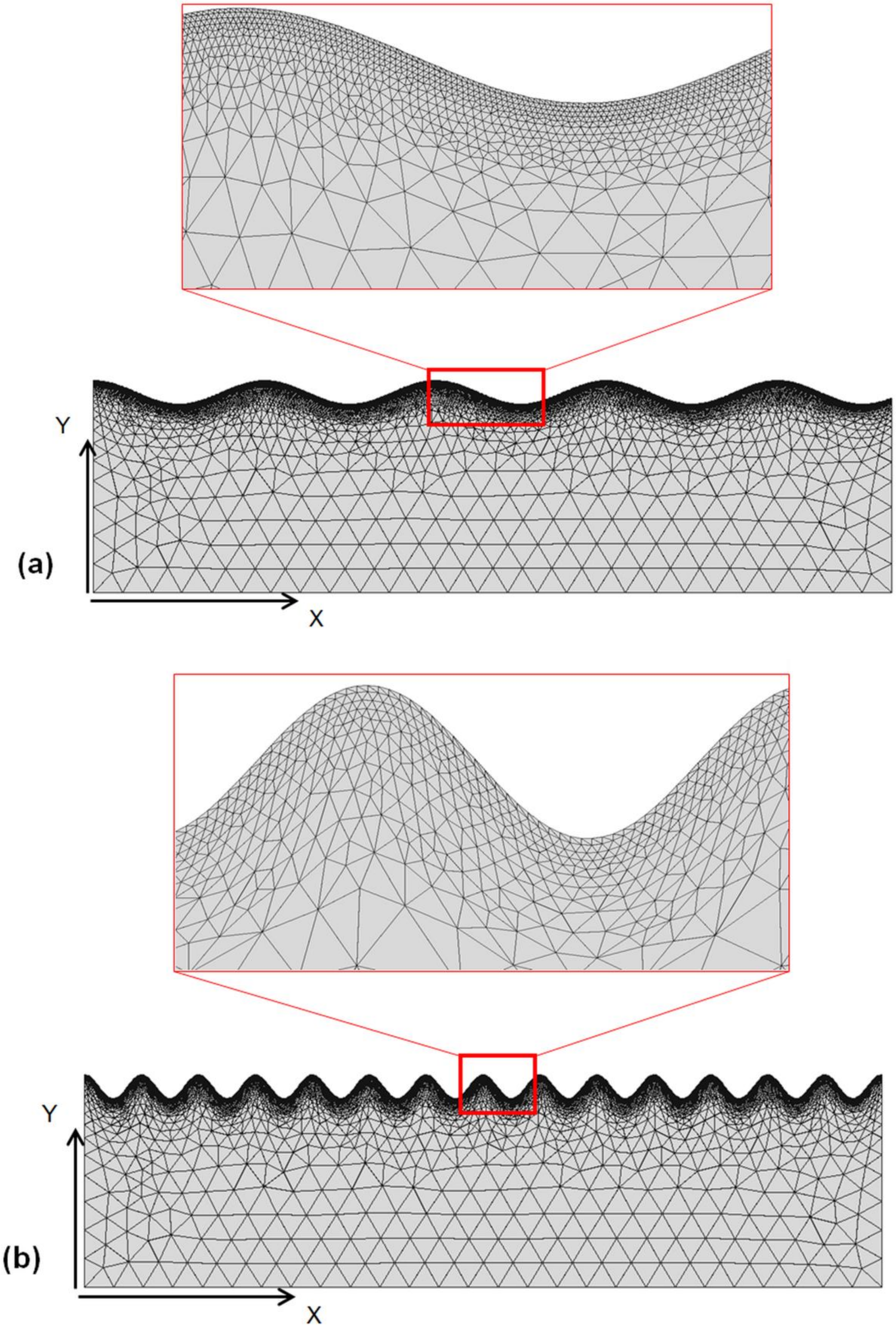

Figure 4.5: Mesh for pre-patterned bilayers that are obtained via mesh perturbations. (a) Pre-pattern period is higher than the natural period; (b) pre-pattern period is lower than the natural period. Top film consists of the elements that have at least one node on the top edge. All other elements in the mesh are part of the base layer.

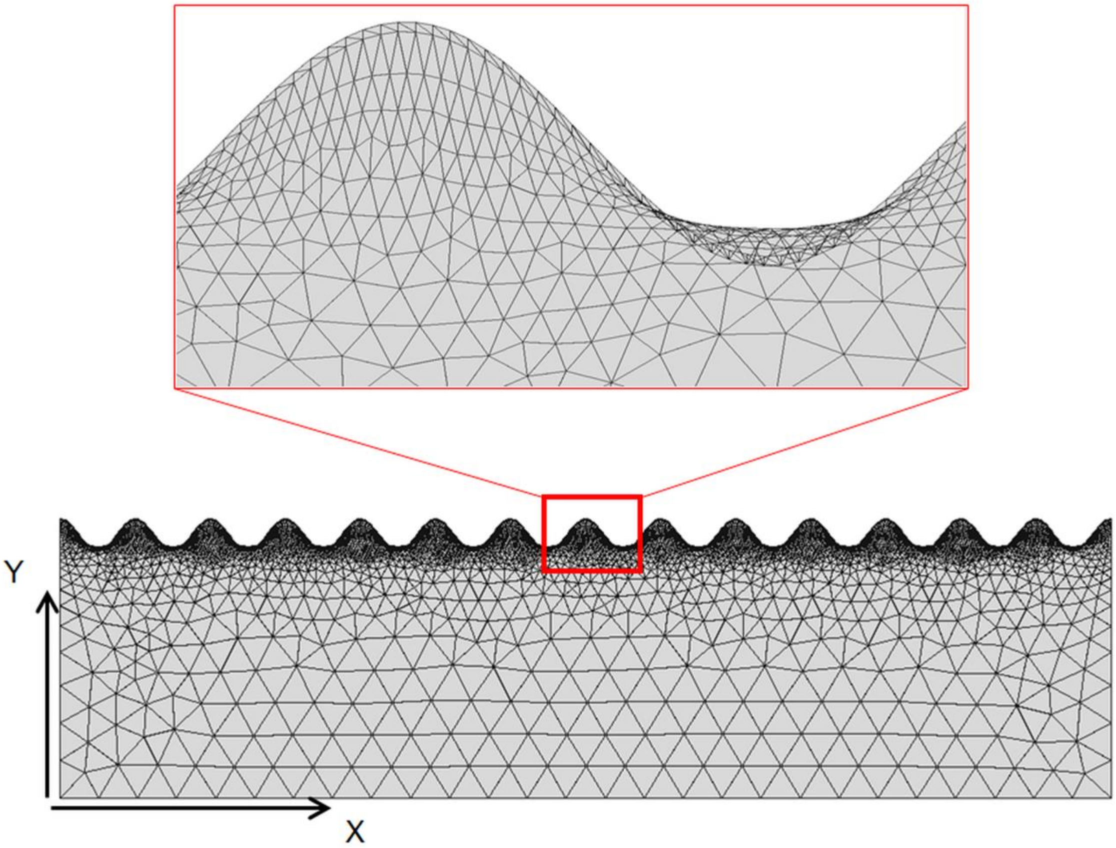

Figure 4.6: Unacceptable mesh with incorrect perturbation. The mesh perturbations must be carefully selected so as to ensure that no mesh points lie outside the system boundaries.

4.3.2 Hierarchical wrinkles via FEA

Hierarchical patterns that were generated by compression of quasi-planar surfaces are shown in Figure 4.7. Hierarchical patterns are observed for both cases: (i) when the pre-pattern period is higher than the natural period and (ii) when the pre-pattern period is lower than the natural period. Upon compression of the pre-pattern, the pre-pattern amplitude is observed to increase with the compression. Beyond a critical compression, the natural mode of the system emerges and a ‘composite’ hierarchical wrinkle profile is observed.

4.3.3 Post-processing hierarchical wrinkles

Two different techniques were used to evaluate the critical compressive strain (ε_t) at which the pre-patterned surfaces transition into the hierarchical mode. These are (i) energy based criterion and (ii) Fast Fourier Transform (FFT) based criterion. These two techniques are discussed here.

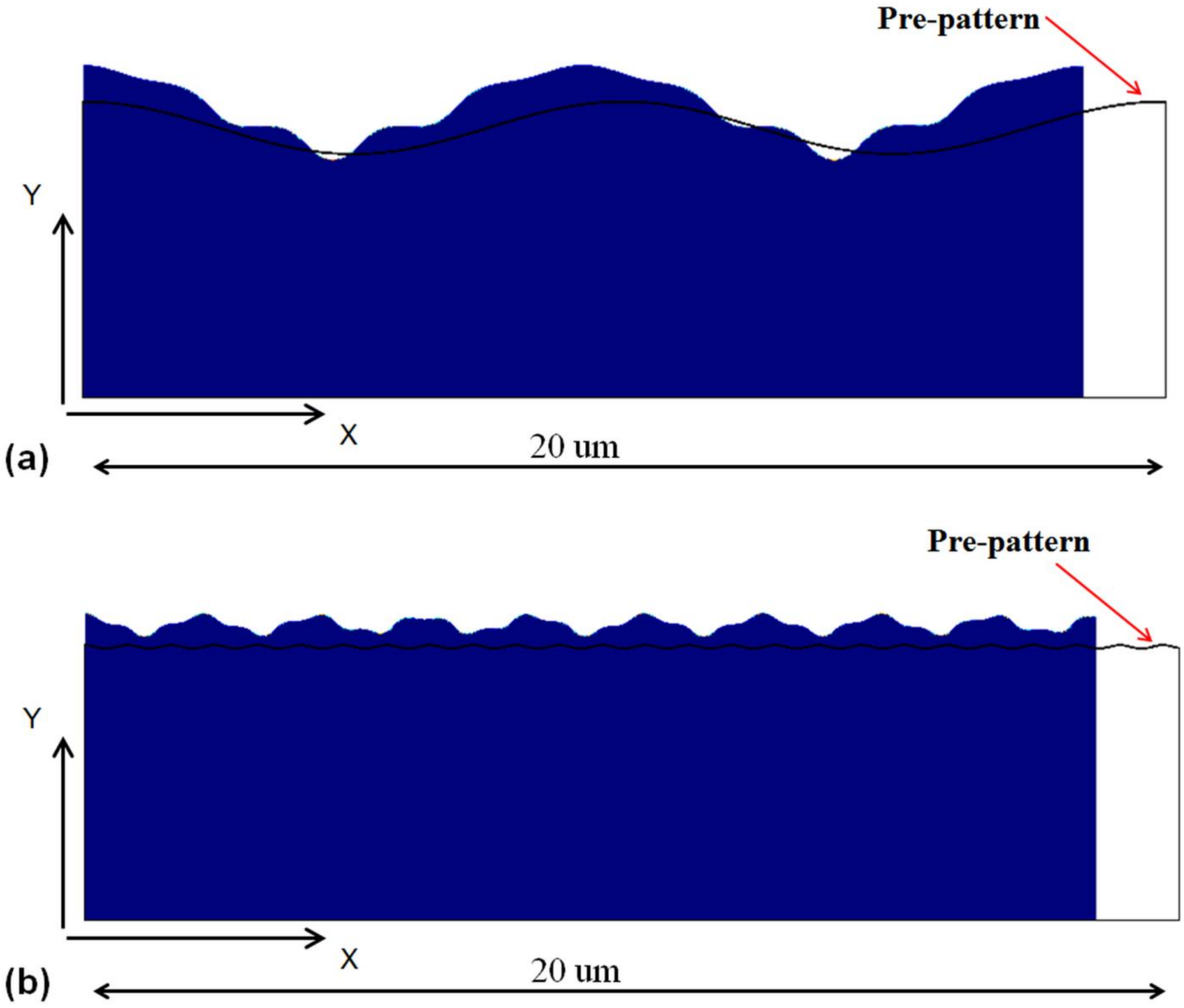

Figure 4.7: Hierarchical patterns obtained during finite element simulations. (a) Pre-pattern period is higher than the natural period. Pre-pattern period is 4.75 times the natural period; natural period is 2.1 um (b) Pre-pattern period is lower than the natural period. Pre-pattern period is 0.375 times the natural period; natural period is 2.1 um.

Energy based criterion

In the energy based criterion, the critical compressive strain is evaluated by tracking the change in the curvature of the energy of the top film versus strain curve. At transition, there is a change in the slope of the energy versus strain curve due to emergence of the natural mode. After transition, the slope increases when the pre-pattern period is higher than the natural period; whereas the slope decreases when the pre-pattern period is lower than the natural period. As the energy versus strain curve is nominally linear, the transition s is recorded as the point of maximum curvature on the energy versus strain curve. This transition strain is illustrated in Figure 4.8.

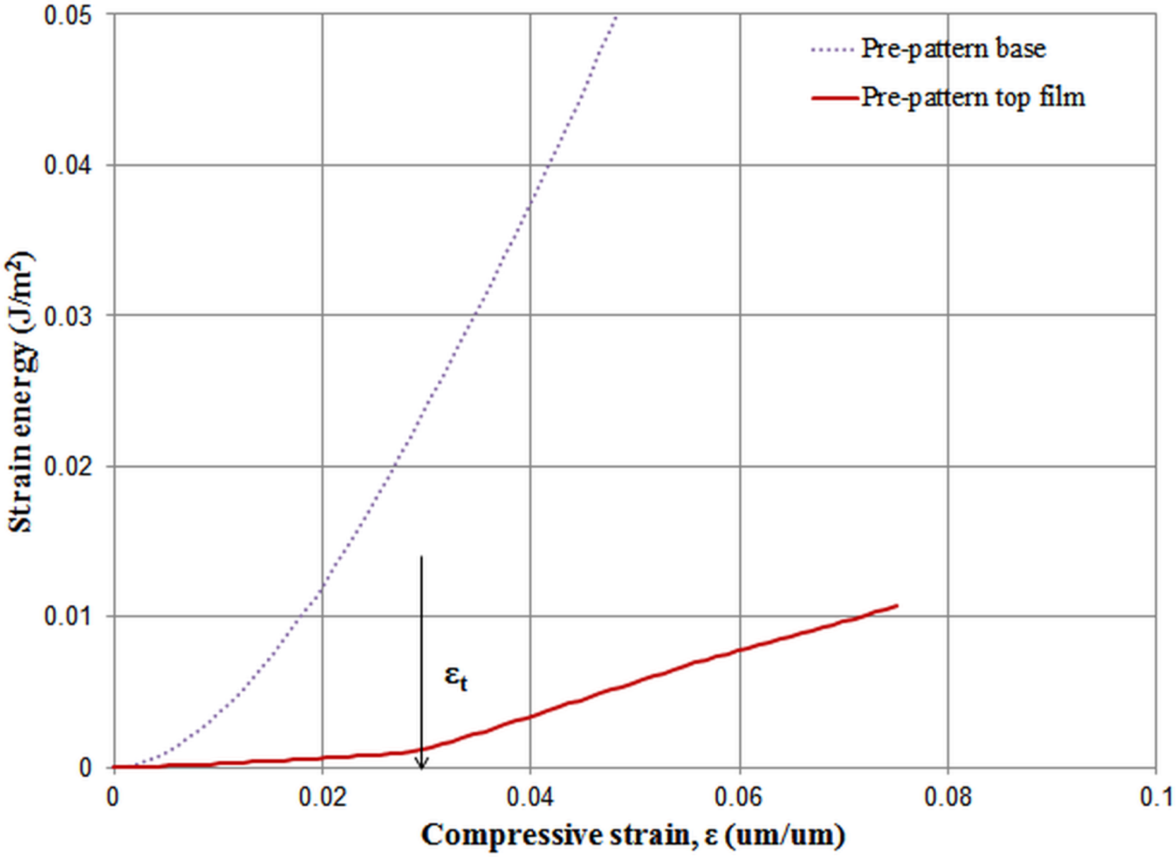

Figure 4.8: Change in energy of the base and the top film as the compressive strain is increased.

FFT based criterion

The critical compressive strain based on spatial frequency of the patterns is evaluated by analyzing the FFT spectrum of the top film. For this purpose, an FFT spectrum is generated for the mid-plane coordinates of the top film at all of the compression steps. These spectrums are then analyzed and the amplitudes of the dominant and second-most dominant modes are evaluated. The evolution of these amplitudes with the strain is then used to generate a bifurcation diagram for compression of pre-patterned surfaces. The critical strain is evaluated as the strain at which the curvature of the amplitude of the pre-pattern versus strain curve is maximum. A representative FFT spectrum and the bifurcation diagram based on an FFT spectrum are shown in Figure 4.9.

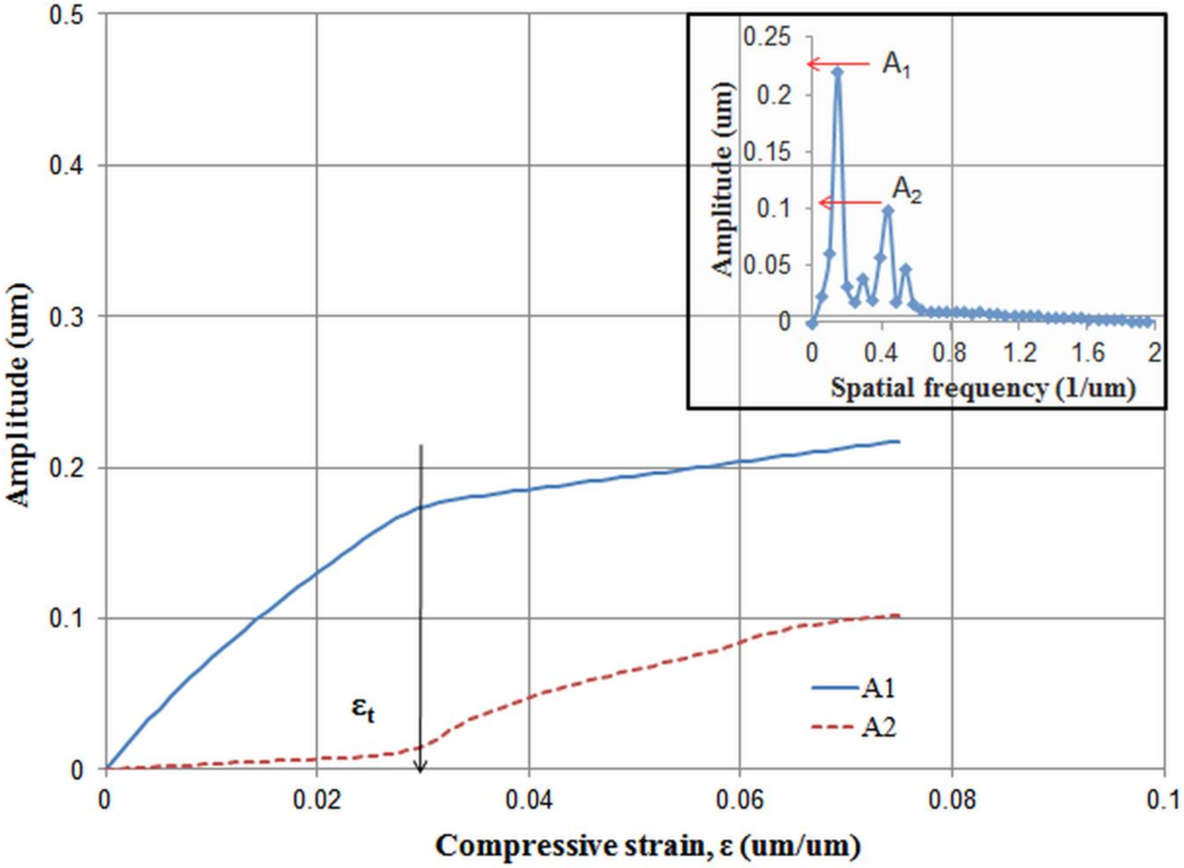

Figure 4.9: Evolution of Fast Fourier Transform (FFT) spectrum of a quasi-planar bilayer system. Inset shows FFT of the displacement of the deformed mid-plane coordinates of the top film. Only one dominant period exists below the transition strain.

4.4 Prediction of hierarchical patterns

4.4.1 Process physics

Tunable hierarchical patterns were generated via compression of pre-patterned bilayers as summarized in Figure 4.2. The process of compressing the pre-patterned bilayer system is similar to the case of compression of flat bilayer systems. In the presence of pre-patterns in the bilayer, hierarchical patterns emerge when the compression reaches a critical threshold. Below the critical threshold, only the pre-patterns are observed; whereas beyond the critical compression hierarchical patterns with multiple periods are observed.

Hierarchical patterns are formed as result of the competition and combination of two distinct modes of the wrinkled system. These two modes are (i) pre-pattern that is imprinted onto the bilayer and (ii) natural mode of the corresponding flat bilayer system. The natural mode of the flat bilayer system is determined by the thickness of the top film, mechanical properties of the bilayer, and the applied pre-stretch release. The contribution of these two modes to the overall mode shape is determined by the applied compression. Below a critical threshold compression, the pre-pattern mode is energetically favorable. Thus, during initial compression of the pre-patterned bilayer a non-hierarchical single period mode is observed. As the compression is increased, the natural mode becomes energetically favorable. Therefore, a combination of the pre-pattern and the natural mode is observed during subsequent compression. The critical compression threshold can be predicted in terms of the pre-pattern and the natural pattern of the bilayer.

Pre-patterning a bilayer system changes the wrinkling process in two ways: (i) pre-patterning the surface provides a lower energy pathway to bending deformation as compared to the case of a flat surface and (ii) pre-patterning with a period that is not the natural period of the bilayer system leads to an energy penalty. The energy penalty arises because the natural period of the bilayer system is by definition the lowest energy mode for a flat system. Thus, pre-patterning causes the imprinted mode to have a lower energy whereas the non-natural pattern causes the imprinted mode to have a higher energy. The energy penalty due to non-natural mode is independent of the applied compression; however, the energy advantage due to pre-patterning decreases with compression. Thus, beyond a critical threshold the pre-patterned mode becomes energetically unfavorable. Beyond this threshold compression, the natural mode emerges in addition to the imprinted pre-pattern mode; thereby, resulting in the formation of a complex hierarchical pattern. This hierarchical pattern can be further tuned by modifying the applied compression.

Herein, an analytical model is presented to predict the critical compression in terms of the pre-pattern and the natural mode of the bilayer. The model is developed by separating out the effects of the pre-pattern and the non-natural mode. For this purpose, two special cases are investigated: (i) the case where the pre-pattern period is same as the natural period and (ii) a hypothetical system without any pre-pattern that bifurcates into an energetically unfavorable non-natural period.

4.4.2 Energy of flat bilayer

The film and the base both contribute to the energy of the bilayer system during wrinkling. The scaling of the deformation energy of the base and the film with the period of the wrinkle (***λ***) and the applied compressive strain (***ε***) are given by [17]:

$$E_w = \varepsilon\left(\alpha\lambda + \frac{\beta}{\lambda^2}\right) \qquad \textbf{(4.11)}$$

Here, $\boldsymbol{E_w}$ is the deformation energy of a flat bilayer system that undergoes wrinkling; $\boldsymbol{\alpha}$ is the contribution due to the base and $\boldsymbol{\beta}$ is the contribution due to the film. The parameters $\boldsymbol{\alpha}$ and $\boldsymbol{\beta}$ depend on the film thickness and material properties of the base and the film and are given by [17]:

$$\alpha = \frac{E_s}{3\pi} \qquad \textbf{(4.12)}$$

$$\beta = \frac{\pi^2}{4}\frac{E_f h^3}{\left(1-\nu_f\right)^2} \qquad \textbf{(4.13)}$$

Here, $\boldsymbol{h}$ is the thickness of the top film, $\boldsymbol{\nu_f}$ is the Poisson's ratio of the top film, $\boldsymbol{E_{f,s}}$ is the Young's modulus, and the subscripts ***f*** and ***s*** refer to the top film and the base, respectively.

This model is based on the approximation that both the base and the top film are linear elastic materials. Although the base of the fabricated bilayer systems has a nonlinear stress versus stretch response, this simplified model provides valuable physical insight into the mode transition phenomenon. Hence, the linear-elastic approximation has been used here to develop the analytical model.

Equation (4.11) is valid across all wrinkle periods, i.e., it holds for both natural and non-natural periods. The natural mode of the system can be obtained by minimizing the energy of the wrinkles with respect to the period; thus, the natural period ($\boldsymbol{\lambda_n}$) is given by:

$$\lambda_n = \left(\frac{2\beta}{\alpha}\right)^{1/3} \qquad \textbf{(4.14)}$$

As the parameters ***α*** and ***β*** depend on the material properties and the thickness of the top film, the natural period of the system indirectly incorporates the effect of these process parameters.

4.4.3 Effect of pre-patterning

Kinematics

The shape of the top surface of the base is determined by the pre-pattern that is imprinted upon the base and is given by:

$$Y = A_p \cos\left(\frac{2\pi X}{\lambda_p}\right) \tag{4.15}$$

The shape of the bilayer pattern during compression is then given by:

$$y = A\cos\left(\frac{2\pi X}{\lambda_p}\right) \tag{4.16}$$

Here, the lower case spatial coordinates (***x*** and ***y***) refer to the coordinates of the deformed configuration; whereas the upper case coordinates (***X*** and ***Y***) refer to the coordinates of the undeformed configuration.

The amplitude of the deformed mode and the amplitude of pre-pattern are kinematically related to the applied compression. With the approximation that there is no lateral compression of the top film, the two amplitudes are related as:

$$\left(\frac{\pi A}{\lambda_p}\right)^2 = \varepsilon + \left(\frac{\pi A_p}{\lambda_p}\right)^2 \tag{4.17}$$

With the substitution of an intermediate variable $\boldsymbol{\varepsilon_p}=(\pi \boldsymbol{A_p}/\boldsymbol{\lambda_p})^2$, Eq. (4.17) reduces to:

$$\left(\frac{\pi A}{\lambda_p}\right)^2 = \varepsilon + \varepsilon_p \tag{4.18}$$

Here, $\boldsymbol{\varepsilon_p}$ has the physical interpretation of being the compressive strain that is required to generate the pre-pattern geometry prior to imprinting. During compression of the pre-patterned bilayer, this equivalent strain does not change when the applied compressive strain $\boldsymbol{\varepsilon}$ is varied.

The relationships defined by Eqs. (4.16)-(4.18) were verified against finite element simulations for the special case when the pre-pattern period is same as the natural period. The results are summarized in Figure 4.10. Figure 4.10(a) demonstrates that the mode shape of the pre-pattern persists during compression. Figure 4.10(b) demonstrates that the amplitude of the mode shape during compression can be accurately predicted by Eq. (4.17) to within an accuracy of 2%.

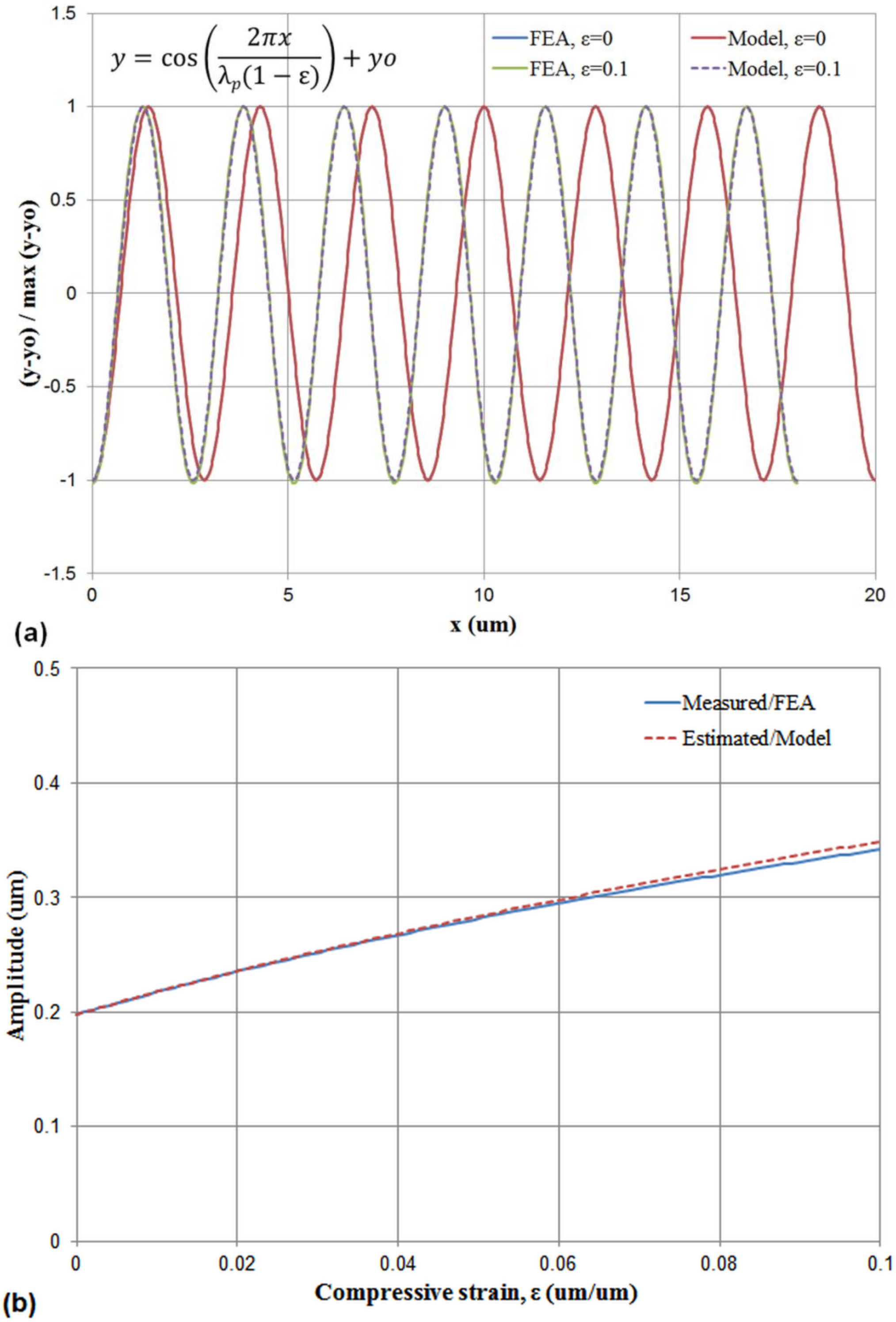

Figure 4.10: Deformation mode that is observed during compression of pre-patterned bilayer for the specific case when the period of pre-patterns is same as the natural period of the system. (a) Comparison of the shape of the observed modes to pre-pattern shape. (b) Comparison of the size of the observed mode to model predictions. The pre-pattern period is 2.86 um and amplitude is 198 nm.

Mode energy

The effect of pre-patterns on the energy of the system can be studied by considering the compression of a hypothetical initially-flat bilayer system. This hypothetical system and the pre-patterned system follow the same energy versus compression path; with one significant difference that the zero energy states for the two systems are at different points on this path. As the energy versus compression relationship for the flat system is already available via Eq. (4.11), the energy versus compression relationship of the pre-patterned system can also be evaluated. For this, one needs to identify the point on the energy versus compression path of the flat system that corresponds to the uncompressed pre-patterned system. This is achieved via the set of kinematic relationships given by Eqs. (4.17) and (4.18). Thus, the energy of the pre-patterned system is evaluated as:

$$E_{w,p}(\varepsilon, \lambda) = \varepsilon\left(\alpha\lambda + \frac{\beta}{\lambda^2}\right) f(\gamma) \tag{4.19}$$

Here, $\boldsymbol{E_{w,p}}$ is deformation energy of wrinkles in a pre-patterned system and the multiplier $\boldsymbol{f(\gamma)}$ is the factor by which the energy of the pre-patterned bilayer is lower than that of the flat bilayer. This factor is:

$$f(\gamma) = 1 - 2\left(\sqrt{\gamma(1+\gamma)} - \gamma\right) \tag{4.20}$$

Here, $\boldsymbol{\gamma}$ is the ratio of equivalent pre-pattern compression to the applied compression and is given by:

$$\gamma = \frac{\varepsilon_p}{\varepsilon} \tag{4.21}$$

The ratio $\boldsymbol{\gamma}$ can also be represented in terms of the pre-pattern and natural period using kinematic relationships as:

$$\gamma = \left(\frac{n}{m}\right)^2 \tag{4.22}$$

Here, ***m*** and ***n*** are ratio of periods and amplitude. These may be represented in terms of the geometric parameters as:

$$m = \frac{\lambda_p}{\lambda_n} \tag{4.23}$$

$$n = \frac{A_p}{A_n} \tag{4.24}$$

For the special case when the pre-pattern period is same as the natural period, the ratio of energy of the pre-patterned ($\boldsymbol{E_{p,n}}$) system to that of the flat system ($\boldsymbol{E_n}$) is evaluated as:

$$\frac{E_{p,n}}{E_n} = f(\gamma) \tag{4.25}$$

This relationship has been verified against finite element simulations as shown in Figure 4.11. The factor $\boldsymbol{f}(\boldsymbol{\gamma})$ is always less than or equal to 1. Thus, pre-patterning leads to an energy advantage; i.e., pre-patterning reduces the energy of the bilayer system. A higher value of $\boldsymbol{f}(\boldsymbol{\gamma})$ indicates a lower energy advantage. As the factor $\boldsymbol{f}(\boldsymbol{\gamma})$ increases with the compression, the energy advantage due to pre-patterning decreases with an increase in the compression.

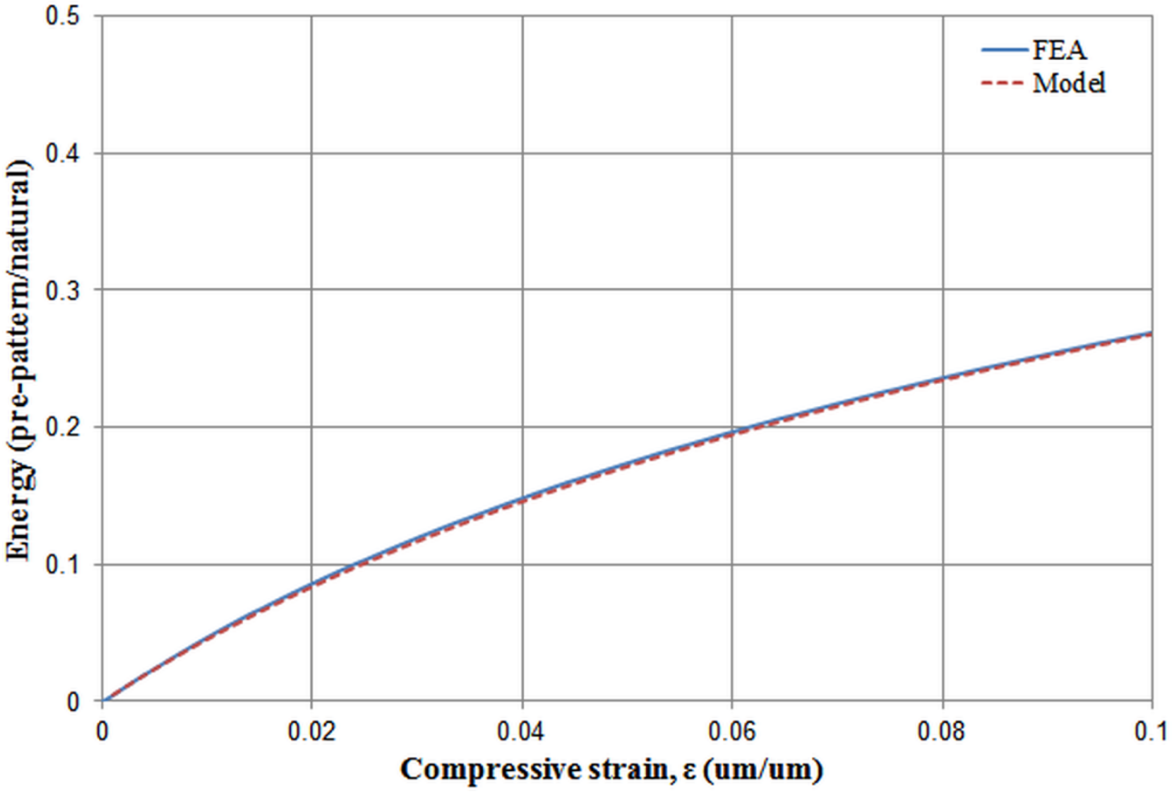

Figure 4.11: Energy of top film during compression of pre-patterned bilayers as compared to energy of the film in a compressed initially-flat bilayer. The pre-pattern period is 2.86 um and amplitude is 198 nm. Pre-patterning with the same period as the natural period of the system results in an "energy advantage". Energy advantage due to pre-patterning decreases with applied compression.

4.4.4 Effect of non-natural mode

Kinematics

The kinematic relationships represented via Eqs. (4.17) and (4.18) are still valid for the general case when the pre-patterned period is different from the natural period. Thus, the same relationships are used with the replacement of the natural period by the non-natural pre-pattern period.

Mode energy

The energy of a non-natural pre-patterned mode can be evaluated via a two-step process: (i) evaluation of energy of non-natural mode for a hypothetical initially-flat bilayer, and (ii) evaluation of energy of pre-patterned non-natural mode. The energy of the flat non-natural mode can be evaluated using Eq. (4.19) by replacing the generic period with the pre-patterned period.

With this substitution, the ratio of energy of the flat non-natural mode (***E$_p$***) and the flat natural mode (***E$_n$***) is given by:

$$\frac{E_p}{E_n}=\frac{2m^3+1}{3m^2} \tag{4.26}$$

This relation is graphically represented in Figure 4.12 and demonstrates the energy penalty due to non-natural mode. The energy penalty is non-symmetric about the point ***m***=1; i.e., modes with periods lower than the natural period experience a larger energy penalty than the modes with periods higher than the natural period. This non-natural mode is not observed in a physical system as the energy of this mode is always higher than the natural mode. However, when the bilayer is pre-patterned, the effect of pre-patterning may lower the energy penalty to such an extent that the energy of this mode falls below the energy of the flat bilayer's natural mode. The ratio of energy of a pre-patterned non-natural mode (***E$_{p,p}$***) to that of the natural mode (***E$_n$***) is:

$$\frac{E_{p,p}}{E_n}=\frac{2m^3+1}{3m^2}f(\gamma) \tag{4.27}$$

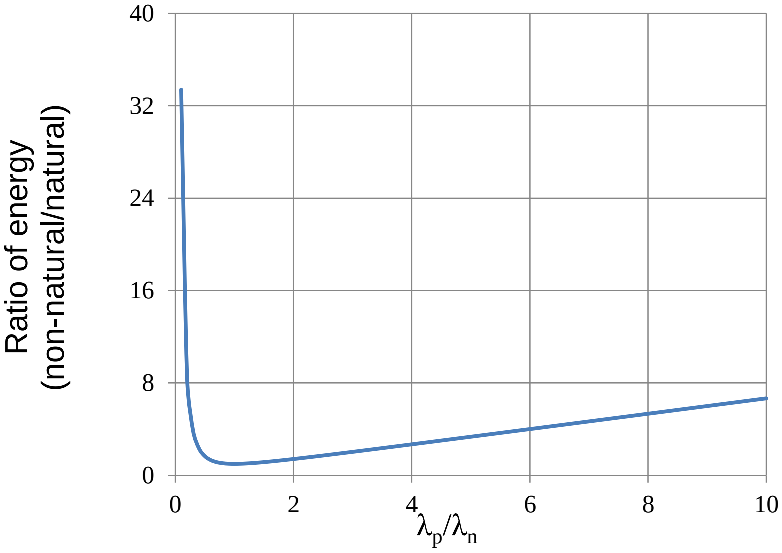

Figure 4.12: Energy of wrinkles during compression of pre-patterned bilayers as compared to energy of wrinkles in a compressed initially-flat bilayer. Pre-patterning with a period that is different from the natural period of the system results in an "energy penalty". Energy penalty due to non-natural pre-pattern mode does not depend on the applied compression.

4.4.5 Prediction of hierarchy transition

Transition criterion

At low compression values, the energy advantage due to pre-patterning dominates the energy penalty effect due to non-natural modes. However, at high compression values the energy penalty due to non-natural mode dominates. Thus, the criterion for transition of pre-patterned modes to hierarchical modes is given by:

$$\frac{E_{p,p}}{E_n} = 1 \qquad \textbf{(4.28)}$$

This condition can be rearranged in terms of the ratio of period and amplitude as:

$$n_t = \frac{\left|1 + 2m^3 - 3m^2\right|}{\sqrt{12\left(1 + 2m^3\right)}} \qquad \textbf{(4.29)}$$

Here $\boldsymbol{n_t}$ is the transition amplitude ratio. For the case when $\boldsymbol{n} > \boldsymbol{n_t}$, the pre-pattern mode persists whereas hierarchical modes are observed for the case when $\boldsymbol{n} < \boldsymbol{n_t}$.

Transition compression

The critical compression may be evaluated from the transition criterion by using Eq. (3.6) as:

$$\varepsilon_t = \left(\frac{\pi A_{n,t}}{\lambda_n}\right)^2 \qquad \textbf{(4.30)}$$

Here, $\boldsymbol{A_{n,t}}$ is the amplitude of the natural mode in the equivalent flat bilayer system at the transition point and is given by:

$$A_{n,t} = n_t A_p \qquad \textbf{(4.31)}$$

Phase diagram

The transition criterion described by Eq. (4.29) can be used to generate a phase diagram for hierarchical wrinkling. This phase diagram is shown in Figure 4.13. The analytical model described by Eq. (4.29) was also verified against finite element simulations and experiments.

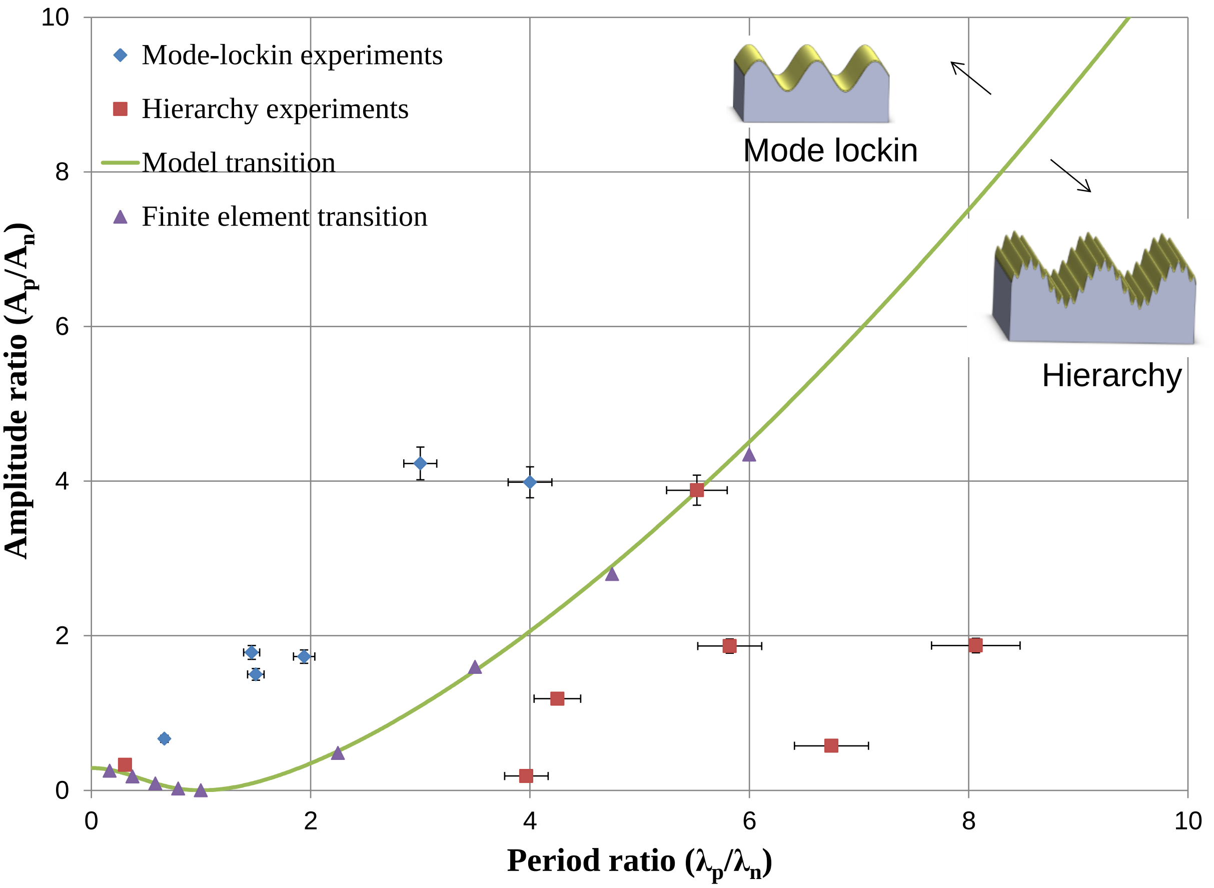

Figure 4.13: Phase diagram for hierarchical wrinkling obtained from analytical models, experiments, and finite element models. The wrinkled pattern has three distinct phases: imprinted pre-pattern, natural pattern, and hierarchical pattern. The phase of the pattern is uniquely determined by the amplitude and period of the pre-pattern and the natural pattern. This phase diagram is invariant under a change in material properties and/or film thickness.

In the phase diagram, the results of finite element simulations represent the critical compression for mode transition. During FEA, the critical compressive strain for transition was obtained by (i) pre-patterning the bilayer with a fixed period (λ_p) and amplitude (A_p) and (ii) increasing the compression of the bilayer. The critical compressive strain was evaluated by tracking the change in slope of the plate energy versus strain curve according to the energy criterion discussed in Sec. 4.3.3. The corresponding natural period (λ_n) and amplitude (A_n) were obtained from a reference flat bilayer system. The reference model is set-up such that it has the same top layer thickness and material properties as those in the pre-patterned system. Different points for the transition curve were obtained by varying the pre-pattern period and amplitude while holding the natural period constant at 2.1 um.

The results of the experiments that are shown in Figure 4.13 were obtained by observing the mode of the final pattern when the pre-stretch in the pre-patterned base is fully released. Thus, these data points do not represent the transition criterion. Instead, the location of the experimental data points on the phase map should be used to verify the accuracy of the analytical transition criterion. Experiments were performed via the following steps (i) pre-patterning the base layer, (ii) stretching the base layer, (iii) plasma oxidation of the pre-stretched base layer, and (iv) full prestretch release. To accurately quantify the pre-pattern geometry, a region of the base layer was physically masked using a 50 um thin metal shim stock during the plasma oxidation step. This preserves the pre-pattern on the bare PDMS as the unexposed regions do not undergo plasma oxidation and bilayer wrinkle formation. Subsequently, after prestretch release of the bilayer, both the pre-pattern and the wrinkled pattern are measured via an atomic force microscope. The natural period is evaluated by counting the number of peaks per unit length of the natural pattern in the hierarchical pattern. The effective local strain of the film is also evaluated from the AFM image profile as discussed later in Sec. 5.2.1. The natural amplitude is then evaluated using Eq. (3.6) with the measured natural period and the measured compression. Uncertainty in the data arises due to spatial variation in the measurement of the pre-pattern. Error bars in the data quantify this uncertainty. The uncertainty due to spatial variation has been previously quantified as discussed in Sec. 2.6.3. A maximum spatial variation of ±5% has been used for both period and amplitude of the pre-patterns.

4.4.6 Relevance to predictive design and fabrication

The phase diagram shown in Figure 4.13 can be used to make several design decisions for fabrication of hierarchical wrinkled patterns.

First, the transition criterion is not symmetric about period ratio of unity. This is because the energy penalty for non-natural modes is not symmetric about the natural period. Therefore, the design space for hierarchical patterns for the case when the pre-pattern is smaller than the natural period is very small. Thus, if hierarchical patterns are desired, one must select the pattern with the higher period as the pre-pattern.

Second, the design space for hierarchical patterns broadens as the ratio of pre-pattern to natural pattern deviates away from unity. This means that it becomes easier to generate hierarchical patterns when the pre-patterns are further apart from the natural pattern.

Third, the phase plot depicted in Figure 4.13 may be used to fabricate tunable patterns that switch between hierarchical and mode-locked patterns. Switching between the two modes is possible by tuning the applied compression. The quantitative data available from the phase plot would enable one to select the appropriate input parameters so that tunable patterns operate close to the transition point.

Chapter 5

Period doubling: Complexity via strain

5.1 Introduction

When compressive strains that are much higher than the first bifurcation strain are applied to the bilayer system, one expects to observe a change in the mode/shape of the wrinkled surface. The possible modes shapes for large strains are (i) natural mode of higher amplitude, (ii) mode with frequency doubling, or (iii) mode with period doubling. These modes are illustrated in Figure 4.1. During buckling of an unsupported beam, frequency doubling is expected at higher compressions. For beam buckling, frequency doubling mode is both kinematically admissible and energetically favorable over the period doubling mode. However, during wrinkling of bilayers, the energy profile is determined by the competition between the top and the bottom layers. When acting alone, period doubling is the energetically favorable mode for bending of the top layer; whereas frequency doubling is the energetically favorable mode for compression of the base layer. In a combined bilayer system, period doubling is found to be the energetically favorable higher mode. This is supported by experimental observations and finite element simulations wherein the period doubling mode is exclusively observed at high compressive strains. The purpose of this work is to (i) predict the onset of period doubling and (ii) predict the shape of this period-doubled mode.

5.1.1 Limitations of existing models/tools

Brau et al. [60] have demonstrated fabrication of period doubling and period quadrupling bifurcations in wrinkling of PDMS with UV exposed top layer when large compressive strains are applied. However, their model is insufficient in capturing the effect of material properties.

Specifically, their model predicts that the critical bifurcation compression is independent of the Young's modulus and the thickness of the top film. This is however incorrect, as supported by both finite element analysis and experiments. Thus, their model is insufficient for predicting period doubling bifurcations.

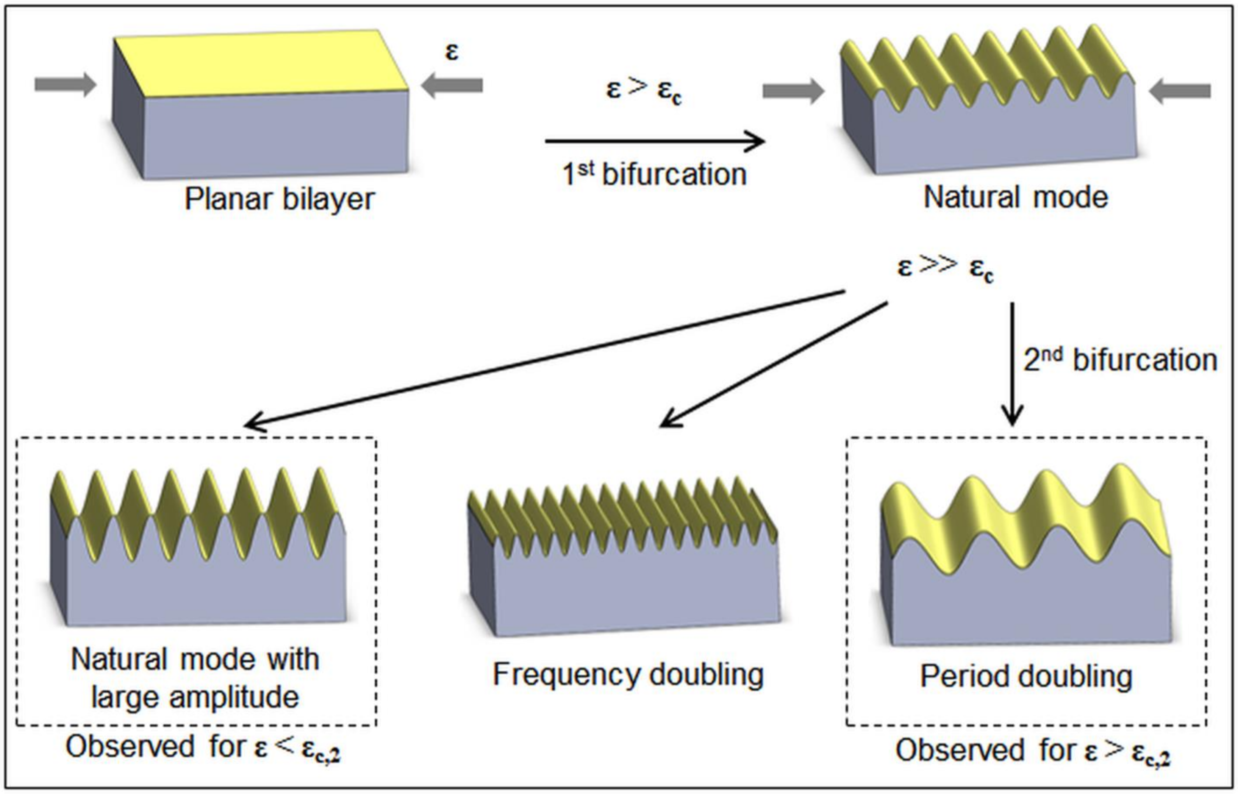

Figure 5.1: 1-D modes that may emerge at higher compressive strain. These modes are (a) higher amplitude natural mode, (b) mode with twice the frequency of the natural mode, and (c) mode with twice the period of the natural mode. During experiments with an initially-flat bilayer, period doubling mode is exclusively observed beyond the critical second bifurcation strain of $\varepsilon_{c,2}$.

Cao et al. [77] have recently demonstrated finite element modeling of period doubling phenomena. They predict that the critical period doubling compression increases with pre-stretch. Under those conditions, period doubling should not be observed at full pre-stretch release in the 20-25% range. However, experimental evidence suggests that this is not true. In fact, during pre-stretch release period doubling is observed at a strain values that are less than 20%.

Period doubling has also been observed experimentally by Sun et al. [63]. However, these patterns were fabricated with metal thin films bonded onto PDMS that exhibit period doubling at strains that are in the 30-40% range. As such large stretches are often not feasible due to material failure during prestretch, usable period-doubled patterns are not available via this technique.

5.1.2 Goals

The goals of this work are to (i) fabricate higher complex wrinkling modes during 1-D compression (ii) predict the nature of higher mode, i.e., period halving versus period doubling; (iii) predict the type of period doubling mode, i.e., valley-moving-up mode versus peak-moving-down based on the material nonlinearity, and (iv) predict the onset of period doubling in terms of material properties and thickness of the top film.

5.2 Period doubling as higher 1-D mode

5.2.1 Fabrication process

The fabrication process for generating period doubling modes is similar to that for generating the natural wrinkles with the exception of the magnitude of the applied compressive strain. Period doubling modes are fabricated by applying a high prestretch to the base and then slowly releasing the prestretch after the plasma oxidation step. As the pre-stretch in the bilayer is released during 1-D loading, one observes period doubling bifurcations in the system beyond a critical threshold. This threshold is observed to be in the range of 15-20% compression of the top layer. One representative sample with the period doubling mode is shown in Figure 5.2. Period doubling manifests as the alternate valleys moving up; i.e., alternate valleys are shallower. This ‘valley moving up’ phenomenon is evident from the cross-sectional profile of an AFM scan of the wrinkled surface. As the compression increases beyond the threshold value, the depth of the moving valley decreases. This behavior is studied later in Sec. 5.3.

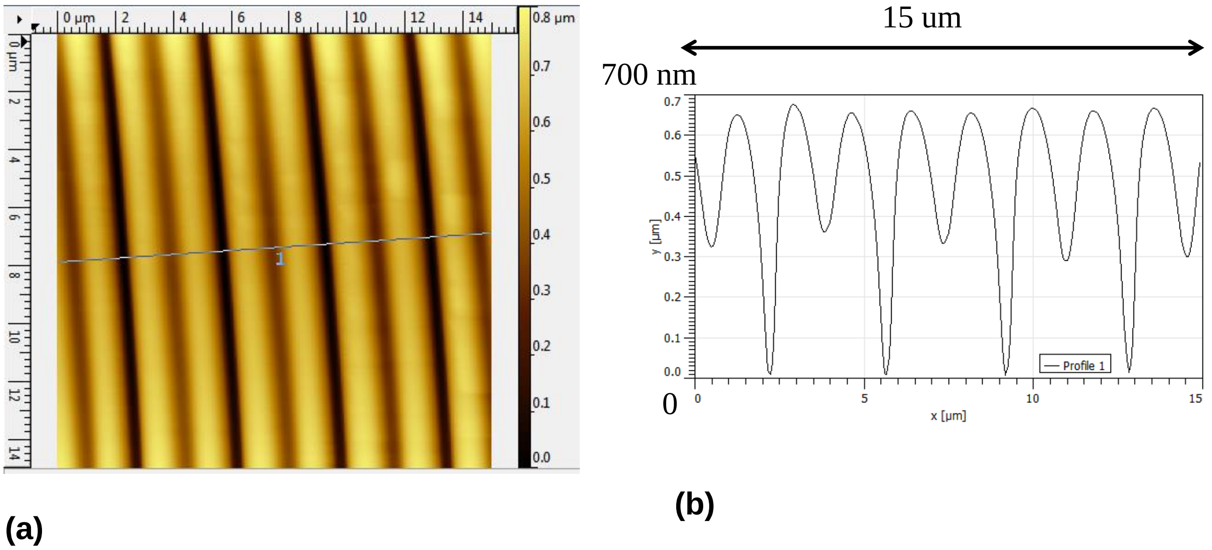

Figure 5.2: Image of fabricated higher mode. (a) Atomic force microscope scan and (b) 1-D profile demonstrating period doubling.

Although wrinkling of plasma oxidized PDMS bilayer systems has been studied extensively in the past, this period doubling phenomenon has not been widely reported. In fact, this period doubling phenomenon is often considered an aberration/exotic mode instead of the expected higher mode. Lack of suitable fabrication tools may partially account for this. For example, period doubling modes are observed only beyond a critical threshold compression. During prestretch release, period doubling would not be observed if the initial maximum pre-stretch is lower than the critical compression that is required for period doubling. As the maximum pre-stretch cannot be tuned after generation of the top film, it is not possible to tune bilayers to demonstrate period doubling if it is not already observed on full pre-stretch release. Additionally, if the compressive strain is not sufficiently higher than the critical strain, the amplitude difference between the alternate valleys may be very small. These small amplitude differences may be incorrectly classified as a result of non-uniformity instead of a distinct period doubling mode. Unequivocal proof for period doubling instead of non-uniformity was available here by tracking the change in amplitude of these modes with the compressive strain. Period doubling as a distinct mode is verified by the increase in the difference in amplitude of alternate valleys that is accompanied with the ‘valley moving up’ phenomenon.

Measuring wrinkle profile with AFM

Atomic force microscope images can be used to measure the period and amplitude of the higher mode wrinkles. Also, the compression of the top film can be evaluated from the wrinkled profile by evaluating the total length of the curved profile. The compressive strain of the top film (***ε***) is related to the scan profile as:

$$\varepsilon = \frac{l_c}{l_x} - 1 \tag{5.1}$$

Here, $\boldsymbol{l_c}$ is the length of the curved profile and $\boldsymbol{l_x}$ is the length of the AFM scan along the scan direction. The length of the curve can be evaluated from the scan profile Y versus X as:

$$l_c = \int_0^{l_x} \sqrt{\left(1 + \left(\frac{\mathrm{d}Y}{\mathrm{dX}}\right)^2\right)} dX \tag{5.2}$$

Here, this technique has been used to evaluate the local strain that is experienced by the top film.

5.2.2 Energetic preference for period doubling

For buckling of unsupported beams, higher buckling modes are usually of higher spatial frequency, i.e., of lower period. However, for bilayer wrinkling it is experimentally observed that the wrinkling mode transitions into higher periods at higher compressions. This behavior can be predicted by the energetic preference of the wrinkled system to buckle into higher periods versus lower periods. The energy of the bilayer system that bifurcates into wrinkles of period (λ) is given by [17]:

$$E_w = \varepsilon \left(\alpha\lambda + \frac{\beta}{\lambda^2} \right) \tag{5.3}$$

Here, the parameter $\boldsymbol{\alpha}$ captures the effect of the base and the parameter $\boldsymbol{\beta}$ captures the effect of the top layer.

The natural period of the system can be obtained by minimizing this energy with respect to the period. There is an energy penalty for any period above or below this natural period.

Interestingly, this energy penalty is not symmetric for periods that are higher or lower than the natural period. The energy penalty can be evaluated as:

$$\frac{\Delta E}{E_n} = \frac{1}{3}\left(\frac{\lambda}{\lambda_n}\right)\left(2+\left(\frac{\lambda_n}{\lambda}\right)^3\right)-1 \qquad \textbf{(5.4)}$$

Here, ***ΔE*** is the net energy penalty due to non-natural mode, $\boldsymbol{E_n}$ is the energy of the natural mode, $\boldsymbol{\lambda_n}$ is the period of the natural mode and $\boldsymbol{\lambda}$ is the non-natural period.

The dependence of energy penalty on the period of wrinkles is graphically summarized in Figure 5.3. The energy penalty for lower periods is much higher than that for higher periods. This suggests that when the compressive strain increases, higher periods are favored. Using Eq. (5.4), ratio of energy for a period that is twice that of the natural period to energy for half the natural period is evaluated to be 0.85. Thus, period doubling is energetically favorable over period halving.

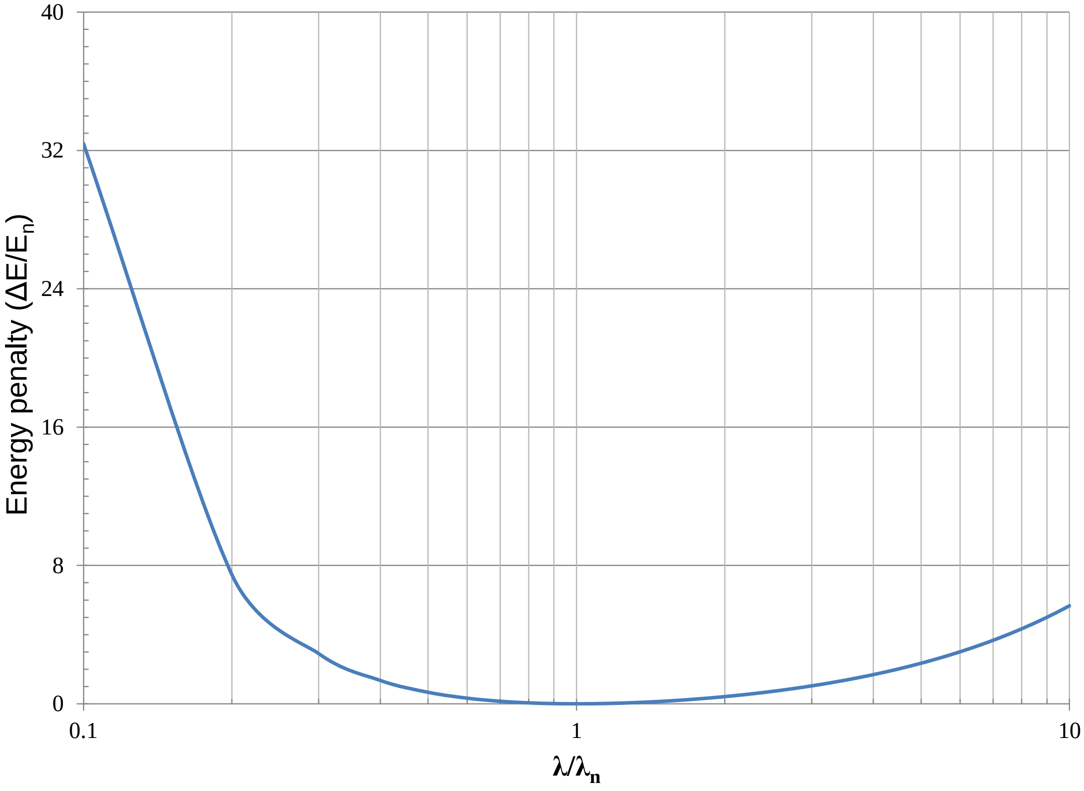

Figure 5.3: Energy penalty of a hypothetical higher mode as compared to the energy of the natural mode. Natural mode is the lowest energy state of a wrinkled system. A mode with a period higher than the natural period is energetically favorable over a mode with a period lower than the natural period.

5.3 Period doubling mode shapes

After the onset of period doubling, the shape of the wrinkled surface is composed of two distinct spatial frequencies. These spatial frequencies correspond to the natural period and twice the natural period. The transition from pure natural period to double period occurs over a range of compression values. In this range, the contribution of the natural period decreases whereas the contribution of the double period increases with an increase in the compression. During this transition, the shape of the wrinkled surface (***y***) may be represented as a sum of these two spatial frequencies as:

$$\frac{y}{y_o} = (-1)^s \left(\cos\left(\frac{2\pi X}{\lambda_n} \right) + k \cos\left(\frac{2\pi X}{2\lambda_n} \right) \right) \tag{5.5}$$

Here, $\boldsymbol{y_o}$ is the amplitude of the natural period, ***s*** is a switching parameter that is either 0 or 1 and ***k*** is a non-dimensional parameter that depends on the compression, thickness of top film, and the material properties of the bilayer.

The effect of the parameter ***k*** on the mode shape is shown in Figure 5.4. The parameter ***k*** is a measure of the "amount" of the higher mode that is present in the complex mode relative to the natural mode. Before the onset of period doubling, this ***k*** parameter is zero. After the onset of period doubling, the ***k*** parameter increases with an increase in the compression. There is a corresponding increase in the deviation of the shape from that of the natural mode with an increase in ***k***. This deviation manifests as either the alternate valleys moving up or the peaks moving down. The effect of sign change in the ***k*** parameter manifests as a phase change in the higher mode. A positive to negative sign change in ***k*** causes a phase lag of one natural period in the higher mode while preserving the valley-moving-up or peak-moving-down behavior.

The valley-moving-up and peak-moving-down phenomenon is determined by the value of the parameter ***s***. The period doubling mode transition can occur in two ways: (i) alternate valleys move up or (ii) alternate peaks move down. In both of these cases, the contribution of the higher period increases with compression. The valley-moving-up phenomenon is observed for the case when ***s*** is 1, whereas the peak-moving-down phenomenon is observed for the case when ***s*** is 0. These two cases are kinematically equivalent and kinematics alone cannot be used to accurately predict the observed behavior. For a real system, the appropriate value of ***s*** is determined by the energetic preference of the system to be in either of these two states. For Neo-Hookean materials, it is observed that the system selects ***s***=1, i.e., the system bifurcates into the period doubling mode via the valley-moving-up transition.

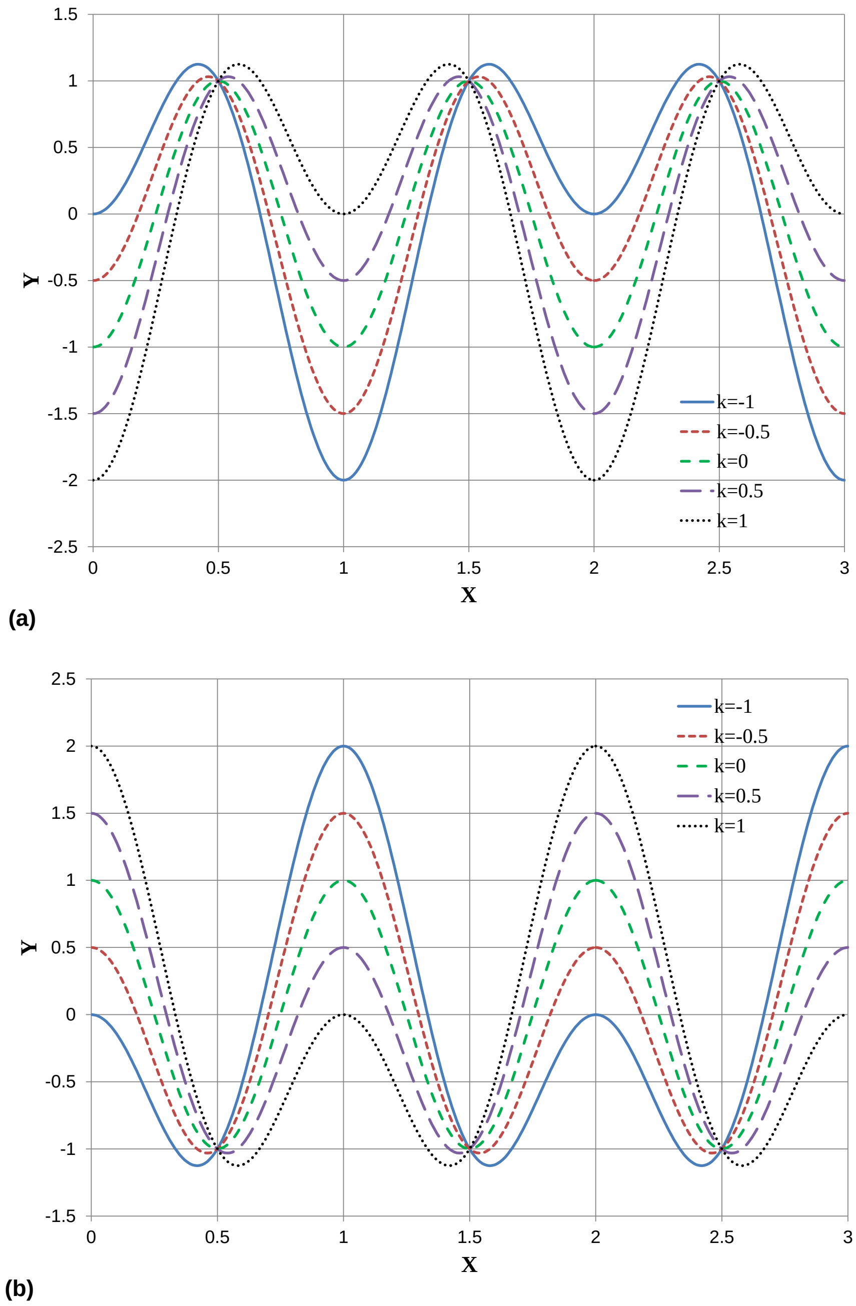

Figure 5.4: Shape and size of the period doubling mode as the contribution of the second mode changes. (a) For the case when the valley moves up, i.e., *s*=1 and (b) For the case when peak moves down, i.e., *s*=0. The two set of curves are mirror images of each other about the *Y*=0 axis.

5.3.1 Energetic preference for ‘valley-moving-up’

To determine whether the valley-moving-up mode is energetically favorable over the peak-moving-down mode, finite element simulations were performed to investigate the effect of the base deformation. The two modes differ in the ‘amount’ of stretching and compression of the base. For the linear elastic material model, the stretching versus strain response and the compression versus strain response is symmetric about the zero strain point. Thus, no difference in the deformation energy is expected for the two modes. However, the two modes are not energetically degenerate for base layers that exhibit nonlinear behavior due to either material nonlinearity or due to geometric nonlinearity. The effect of nonlinear base material was captured by deforming the base layer and recording the deformation energy. To deform the base, a displacement boundary condition was applied at the top surface of the base as summarized in Figure 5.5. The shape of the displacement boundary condition is given by Eq. (5.5).

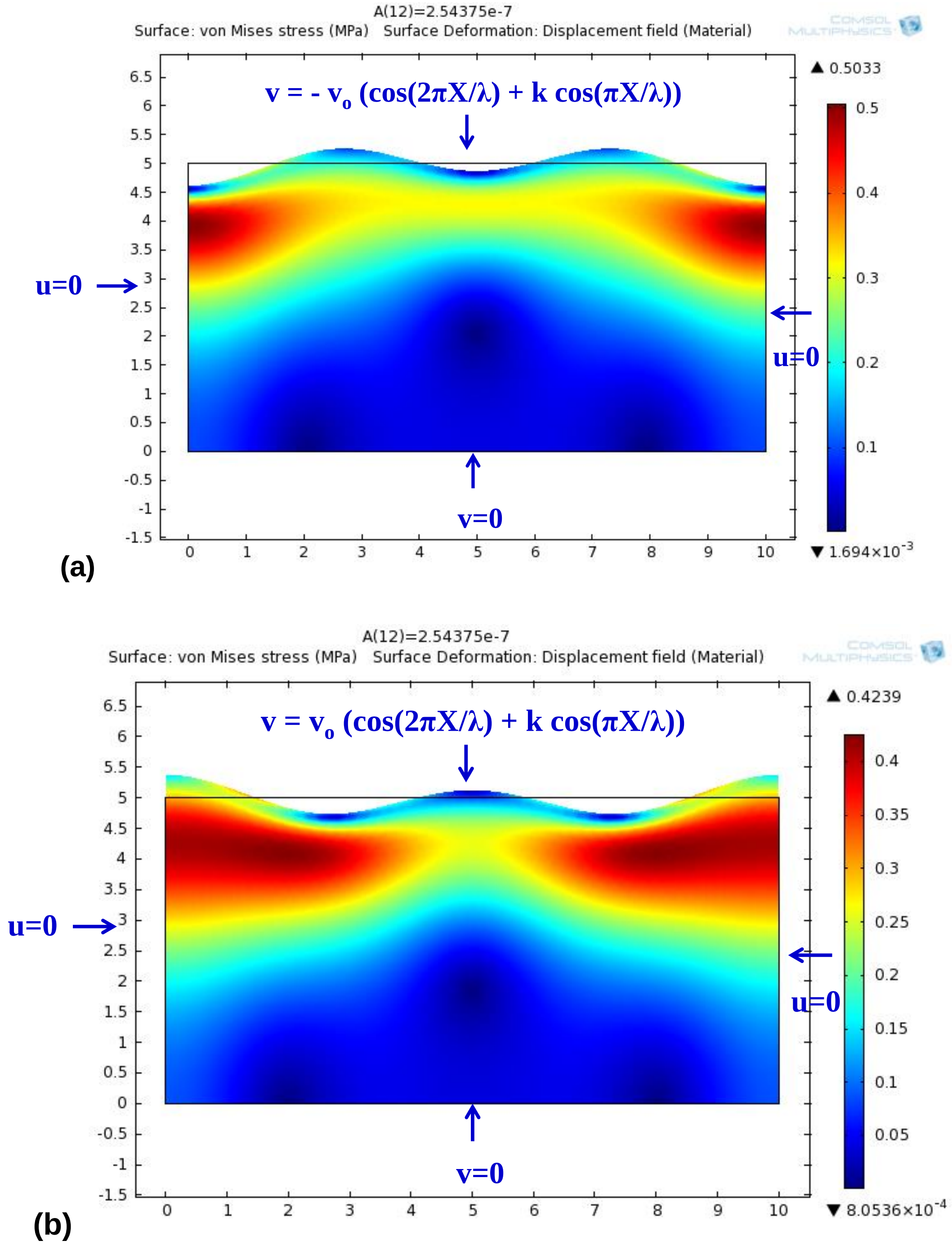

Figure 5.5: Response of the base layer when a prescribed displacement is applied to the top surface as observed via finite element simulations. Two different types of period doubled mode shapes are applied. (a) Response for mode shape with negative amplitude and (b) response for mode shape with positive amplitude. For both cases, the amplitude v_0 is 254 nm, period λ is 5 um and the parameter *k* is 0.5.

The result of the finite element simulations is summarized in Figure 5.6. During simulations, the amplitude of the natural period was held constant as the ***k*** parameter was varied. The energy of the system increases with an increase in the ***k*** parameter. This conforms to the expected trend due to an increase in the net deformation of the system. Interestingly, for low ***k*** values the energy of the valley-moving-up mode is lower than that of the peak-moving-down. This is because of the lower net compression in the valley-moving-up mode. As the energy for compression is higher than the energy for stretching in a Neo-Hookean material, the valley-moving-up mode has a lower energy. Period doubling transition occurs when ***k*** approaches zero. In this limit, the valley-moving-up mode is of lower energy than the peak-moving-down mode. This energetic preference supports the observations of experiments and finite element simulations at large compressive strains wherein valley-moving-up period doubling bifurcations are observed.

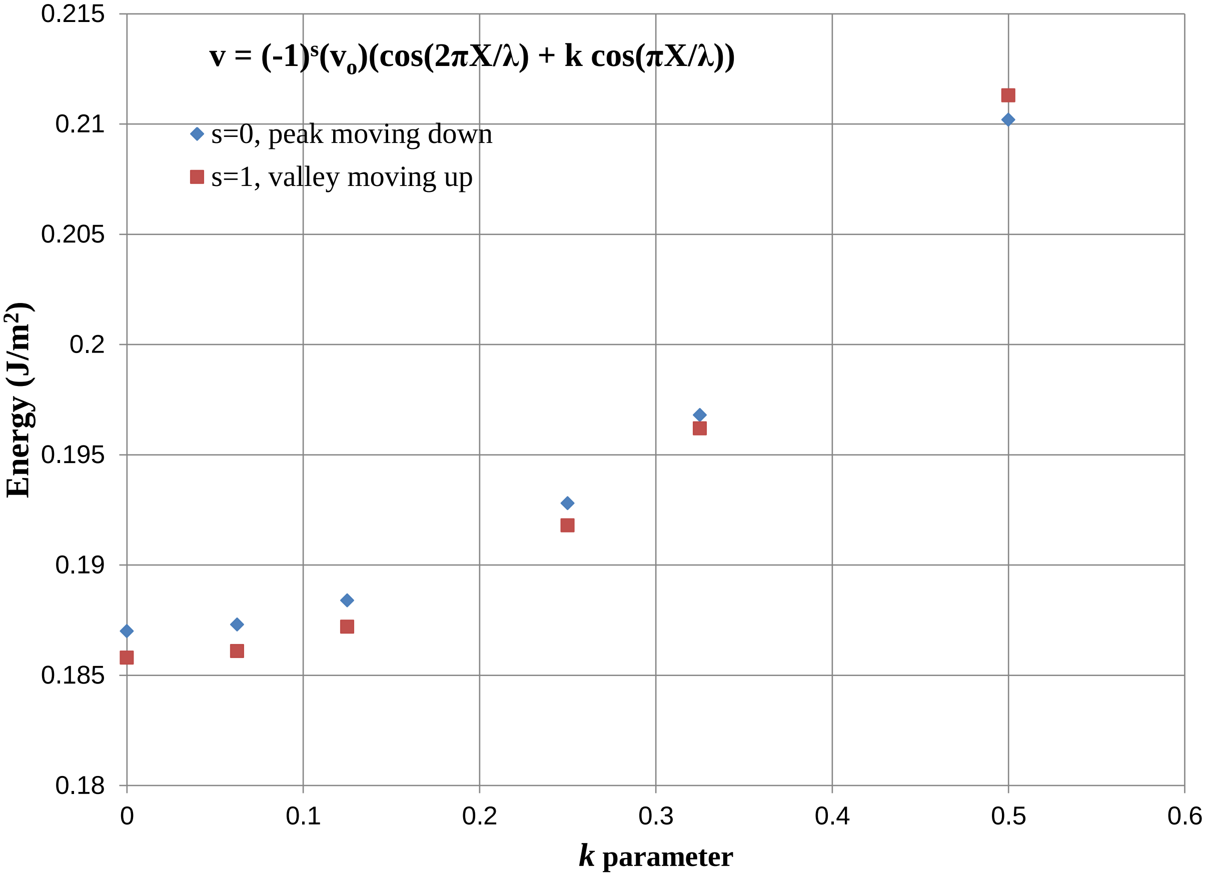

Figure 5.6: Effect of *k* parameter on the deformation energy of the base layer when a prescribed displacement is applied to the top surface. The amplitude of the prescribed displacement v_0 is 555 nm and period λ is 5 um. The energy of the 'valley-moving-up' mode is lower than that of the 'peak-moving-down' mode for low *k* values.

5.3.2 Amplitude of period-doubled mode

The shape of Eq. (5.5) can be used to identify the peaks and heights of these peaks, i.e., the amplitude of the natural and higher modes. Equation (5.5) may be represented in a non-dimensional form as:

$$\bar{y} = (-1)^s \left(\cos(2\pi \bar{X}) + k\cos(\pi \bar{X})\right) \tag{5.6}$$

Here, $\bar{y} = y/y_o$ and $\bar{X} = 2\pi X/\lambda_n$.

In the range $\bar{X} \epsilon$ [0 1], there are three extrema for $\bar{y}$ for the case when $0 \le k \le 4$ and two extrema for the case when $k > 4$. The parameter $\boldsymbol{k}$ increases with an increase in the compressive strain. Before the onset of period doubling $\boldsymbol{k}$ is zero. When $\boldsymbol{k}$=4, the peaks due to natural period are completely “lost”. The locations of the extrema can be determined by differentiating the RHS of Eq. (5.6) with respect to $\bar{X}$ and setting it to zero. The locations of the extrema are given by:

$$\bar{X} = 0, \frac{\theta_o}{\pi}, 1 \tag{5.7}$$

Here, the intermediate location $\boldsymbol{\theta_o}$ is related to parameter $\boldsymbol{k}$ as:

$$\cos(\theta_o) = -\frac{k}{4} \tag{5.8}$$

The amplitudes of the peaks of Eq. (5.6) can be evaluated by evaluating the peak to valley heights as:

$$\bar{A_1} = \frac{\bar{y}(0) - \bar{y}(\theta_o)}{2} \tag{5.9}$$

$$\bar{A_2} = \frac{\bar{y}(1) - \bar{y}(\theta_o)}{2} \tag{5.10}$$

Using Eqs. (5.6), (5.9), and (5.10) , the amplitudes of the profile represented in Eq. (5.5) can be evaluated as:

$$\frac{A_1}{y_o} = 1 + 0.5k + 0.0625k^2 \tag{5.11}$$

$$\frac{A_2}{y_o} = 1 - 0.5k + 0.0625k^2 \tag{5.12}$$

The average of the two amplitudes (***A_d***) is given by:

$$A_d = y_o\left(1 + 0.0625k^2\right) \tag{5.13}$$

The difference of the amplitudes of the two modes (***δA_d***) is given by:

$$\delta A_d = y_o k \tag{5.14}$$

From Eqs.(5.13) and (5.14), the parameter ***k*** can be evaluated as:

$$k = 4\left(\frac{A_d}{\delta A_d} - \sqrt{\left(\frac{A_d}{\delta A_d}\right)^2 - 1}\right) \tag{5.15}$$

As the difference in amplitudes and the average amplitude can be measured from the bifurcation diagram and the experiments, model predictions can be compared to experiments via this ***k*** parameter.

5.4 Finite element modeling

5.4.1 Modeling technique

Period doubling modes are observed during wrinkling when large compressive strains are used. The finite element modeling technique for the case of large compressions is similar to the case for small to moderate compressions discussed in Chapter 3. To ensure that the system bifurcates into the 1st and then the 2nd mode, the step size during compression ramp-up must be at least 3-5 times smaller than the critical strain for 1st bifurcation. If large step sizes are used, the system may not bifurcate into the wrinkled state.

A representative system demonstrating the period doubling behavior is shown in Figure 5.7. Out of the two different types of feasible period doubling modes, the valley-moving-up mode is exclusively observed for Neo-Hookean base layers. This is consistent with the observation that the energy of the valley-moving-up mode is lower than the peak-moving-down mode for Neo-

Hookean materials. During period doubling, two distinct set of valleys can be identified. Period doubling is evident by the observation that the amplitude of every alternate valley is lower than the amplitude of the valleys in the immediate neighborhood. Thus, two distinct amplitudes may be defined as (i) $\boldsymbol{A_1}$, that is the amplitude of the deeper valleys and (ii) $\boldsymbol{A_2}$, that is the amplitude of the shallower valleys. These amplitudes are labeled in Figure 5.7(b). These amplitudes correspond to the amplitudes defined by Eqs. (5.11) and (5.12). Before the onset of period doubling, the two amplitudes are equivalent. After the onset of period doubling, the amplitude of the deeper valleys increases with strain whereas the amplitude of the shallower valleys decreases with strain.

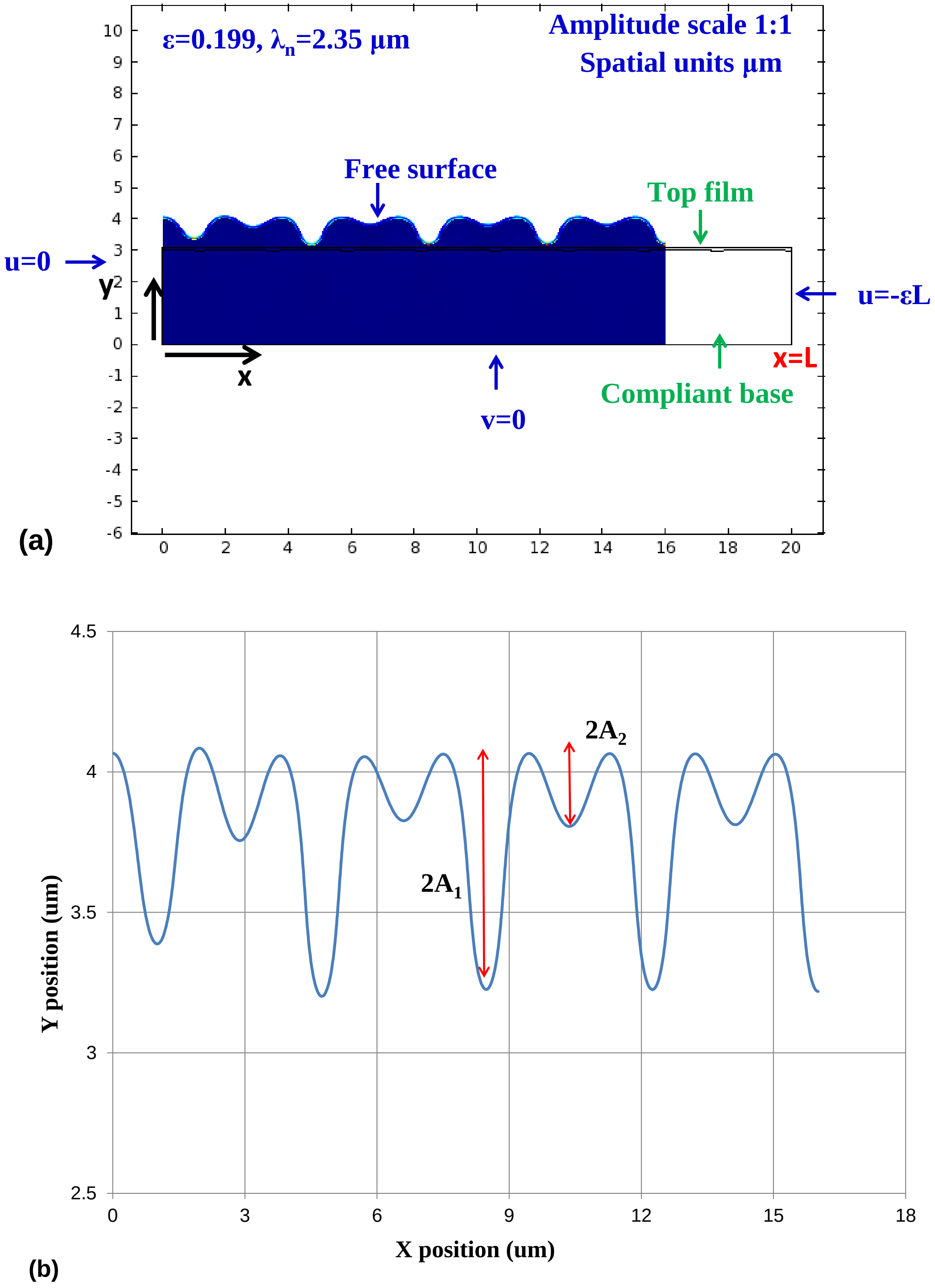

Figure 5.7: Representative result of FEA demonstrating emergence of period doubling beyond a critical strain. (a) 2-D view and (b) profile of the mid-plane coordinates of the top film. Thickness of the top film is 93.8 nm and the moduli ratio η=1116.1. A compression of 19.9% is applied to the bilayer without any base prestretch.

5.4.2 Post-processing

Evaluating amplitude and period

The process of evaluation of amplitude and period of the period-doubled mode is similar to the process of evaluating period and amplitude of the natural mode described in 3.5.1. The amplitude and period are evaluated from the gap and height of the peaks and valleys. To evaluate the two different types of amplitudes, the valleys are first classified as either deep or shallow. The two different amplitudes are then evaluated as the average amplitude of the valleys belonging to the two sets. Details on the post-processing implementation are available in the codes that were generated for performing this operation [68].

FFT analysis

A Fast Fourier Transform (FFT) of the mid-plane coordinates of the top film can be used to identify the spatial frequencies present in the period-doubling mode. An FFT analysis of the mid-plane coordinates of the top film is shown in Figure 5.8. As expected, the period-doubling mode exhibits two distinct spatial frequencies. These correspond to the natural period and twice the natural period. The amplitudes that are obtained from FFT are distinct from the amplitudes $\boldsymbol{A_1}$ and $\boldsymbol{A_2}$ defined by Eqs. (5.11) and (5.12). The amplitudes obtained from FFT are the amplitudes of the periodic cosine terms with the two different periods; whereas the amplitudes defined by Eqs. (5.11) and (5.12) are the amplitudes of the extrema of the deformed profile. During experimental observations, the amplitude that is evaluated from the peaks and valleys in the profile corresponds to the definitions described by Eqs. (5.11) and (5.12).

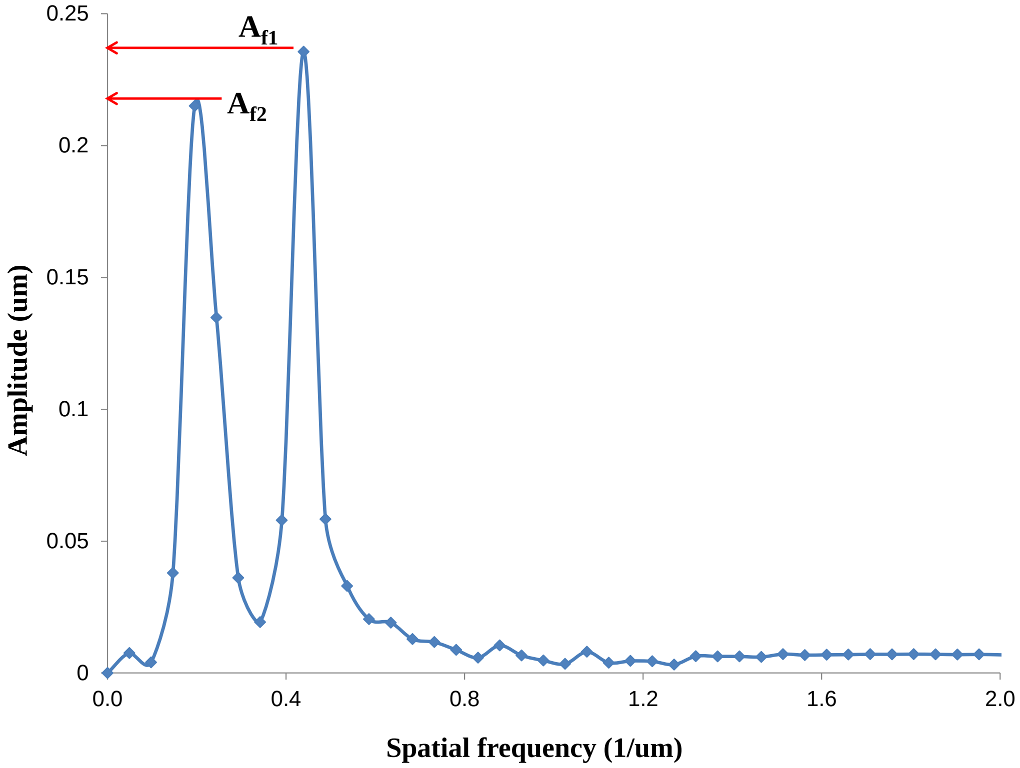

Figure 5.8: Fast Fourier Transform of the mid-plane coordinates of the top film demonstrating the presence of two distinct spatial periods.

Bifurcation diagram

The bifurcation diagram is a graphical representation of the change in amplitude of the distinct amplitudes $\boldsymbol{A_1}$ and $\boldsymbol{A_2}$ with the strain. The bifurcation diagram is obtained by tracking the change in the two amplitudes with an increase in the compression of the bilayer. To generate the bifurcation diagram, amplitudes $\boldsymbol{A_1}$ and $\boldsymbol{A_2}$ are used instead of the amplitudes obtained from the FFT. This is done to ensure that the bifurcation diagram obtained from FEA can be directly compared to observations from experiments.

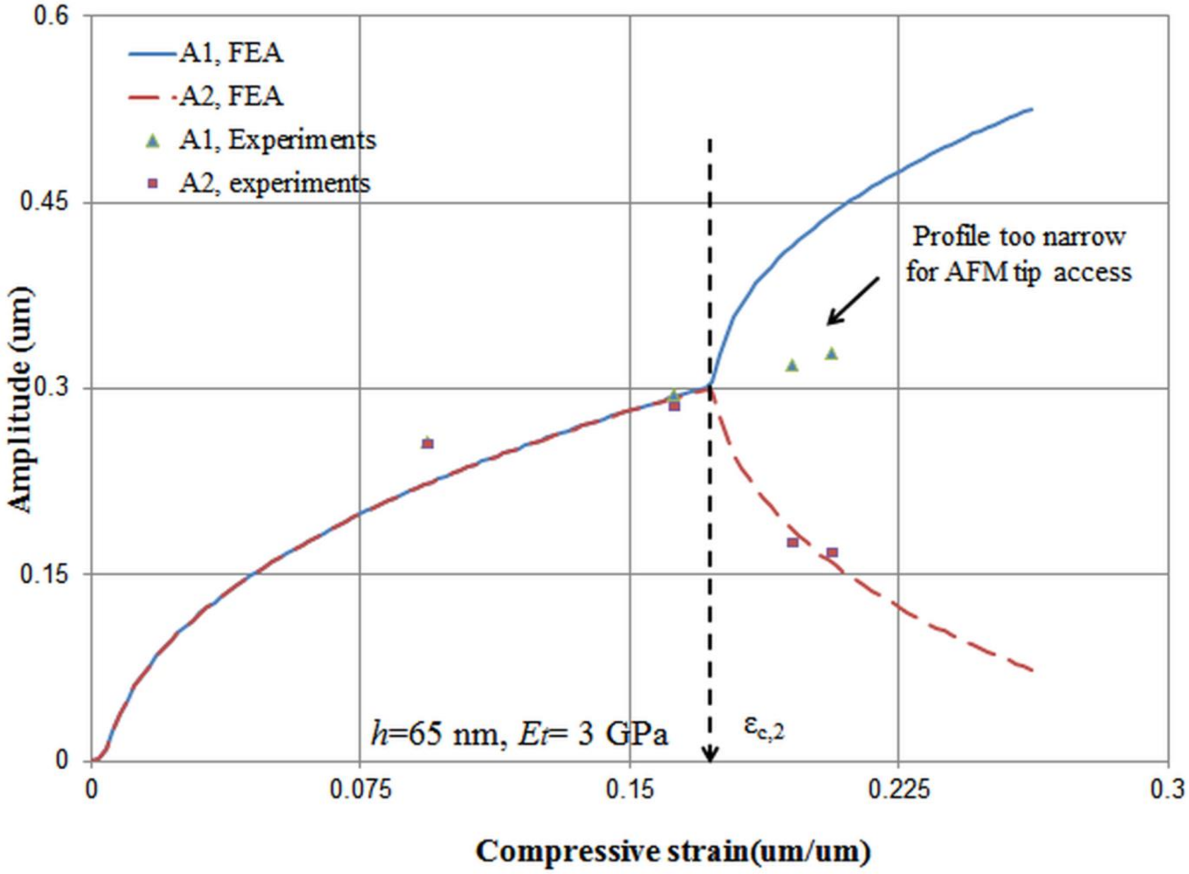

Figure 5.9: Bifurcation diagram for period doubling showing the evolution of amplitude of the modes with the applied compressive strain. Period doubling mode emerges at the critical strain. The critical strain is numerically evaluated as the point of zero slope on the amplitude versus strain curve for the shallower valleys, i.e., for the curve that corresponds to the smaller amplitude.

Evaluating critical strain

Critical strain for the onset of period doubling corresponds to the strain at which the higher mode emerges. During experiments and finite element simulations, the emergence of higher mode is accompanied with a change in the amplitude of alternate valleys. A distinct critical point can be evaluated by analyzing the bifurcation diagram generated from finite element simulations. On the bifurcation diagram, the critical strain corresponds to the point at which the slope of the lower amplitude approaches zero. Before bifurcation, the higher amplitude (A_1) and the lower amplitude (A_2) are equivalent; both of these amplitudes increase with an increase in the strain. After the period doubling bifurcation, the lower amplitude decreases with an increase in compression. This corresponds to alternate valleys moving up. The slope of the lower amplitude versus strain curve is zero at the bifurcation point. The strain at this point is labeled as $\varepsilon_{c,2}$ on the bifurcation diagram that is shown in Figure 5.9.

The second bifurcation point is a sharp and distinct point on the bifurcation diagram. This is in contrast with the first bifurcation observed during transition from the flat state to the wrinkled state. During finite element simulations, the first bifurcation occurs over a small range of compressive strain. Additionally, accurate measurement of the first bifurcation strain is challenging during experiments due to the extremely small values of the critical strain of around 0.1%. In contrast, the period doubling bifurcation occurs at a higher value of about 18% strain. Thus, the period doubling bifurcation behavior provides a convenient experimental technique to extract information about the wrinkling phenomenon.

Measurements from experiments of the period doubling phenomenon are shown alongside finite element simulations in Figure 5.9. The finite element simulation is able to accurately capture the onset of bifurcation. Qualitatively, experiments verify that the first amplitude increase with compression, whereas the second amplitude decreases with compression after the onset of period doubling. The discrepancy in the values of finite element and experiments for the amplitude $\boldsymbol{A_1}$ after bifurcation is possibly due to the inability of a finite sized AFM tip to image the bottom of the deep and narrow valleys.

5.5 Parametric analysis

5.5.1 One parameter at-a-time

Effect of moduli ratio

The effect of changes in the material properties on the critical strain is summarized in Figure 5.10(a). For these studies, the moduli ratio $\boldsymbol{\eta}$ was varied over a large range while holding the top layer thickness at a constant value. Under these conditions, it is observed that the critical compressive strain lies within the range of 18-19% for all values of the moduli ratio. Also, there is no discernable trend to the variation in the critical strain. There are two possible explanations for this behavior: (i) the effect of large deformations is completely decoupled from the effect of the stiffness moduli of the materials or (ii) the effect of large deformations is coupled with both geometry and material properties in a way that leads to a near-constant critical bifurcation. The first hypothesis has been proposed by Brau et al. [60]; whereas the second hypothesis has not been explored and/or tested in the past. To distinguish between the two hypotheses, the effect of geometry on critical compression has been independently investigated. The results of these studies are discussed later in Sec. 5.5.2.

Effect of top layer thickness

The effect of changes in the top layer thickness on the critical strain is summarized in Figure 5.10(b). For these studies, the moduli ratio η was held constant while the top layer thickness was varied. Under these conditions, it is also observed that the critical compression lies within the range of 18-19%. In addition, a slight dip in the critical strain is observed for intermediate values of top layer thickness. This suggests that there is an optimum set of parameters that minimizes the critical compression.

As a first approximation, the parametric analysis of the effect of top layer thickness and moduli ratio suggests that the period doubling behavior is independent of the material properties and the geometry. However, this interpretation may be flawed as changes in the moduli ratio and the top layer thickness are accompanied by changes in period of the wrinkles. If the period doubling behavior is dependent on the period of wrinkles, then the one-parameter-at-a-time approach would not be able to capture the effect of the period. To investigate this, one must first determine the effect of the period on large deformation behavior of the base and then isolate the effect of period on the bifurcation behavior.

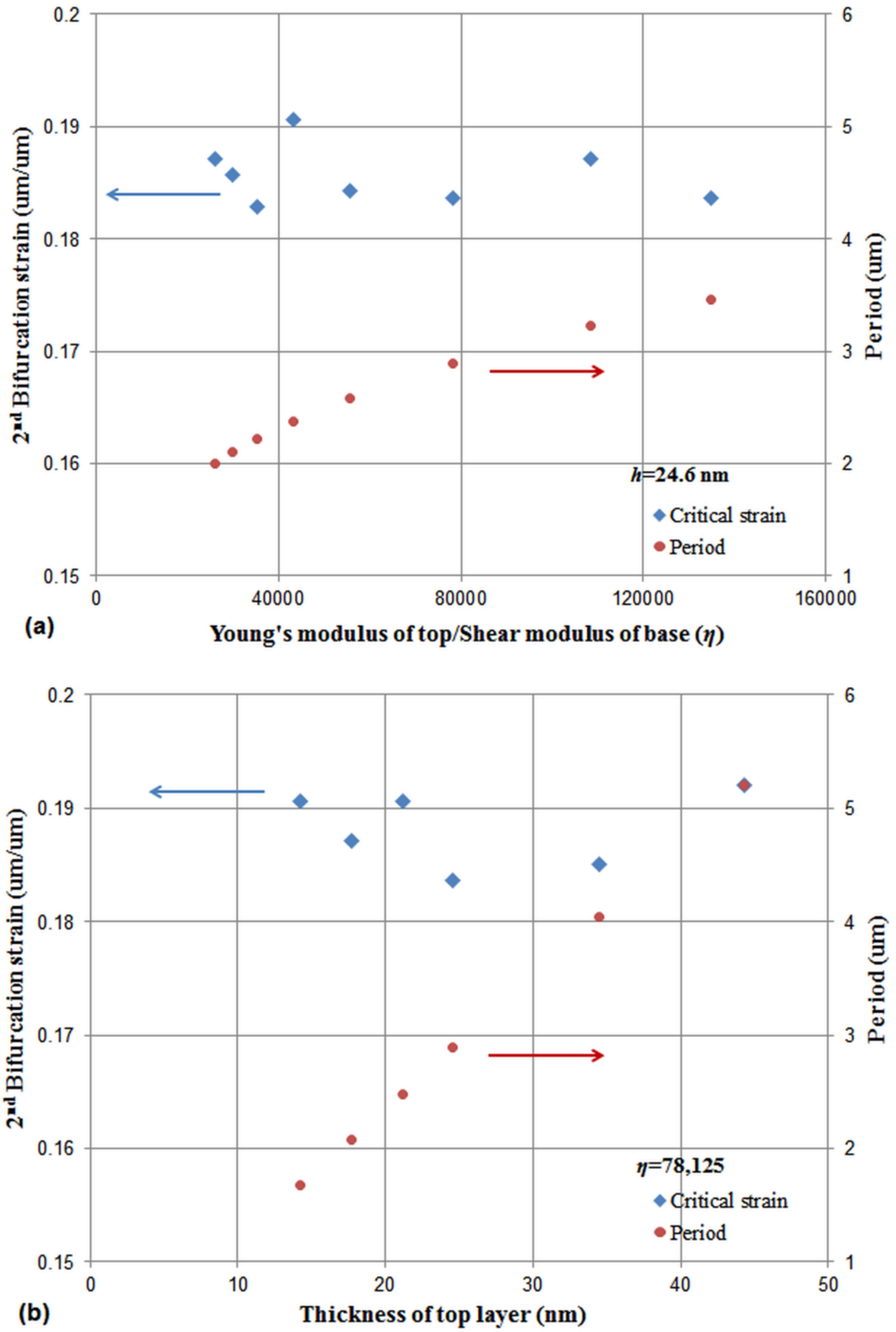

Figure 5.10: Effect of process parameters on the second bifurcation strain and period of wrinkles. (a) Second bifurcation strain and period versus stiffness moduli ratio. (b) Second bifurcation strain and period versus thickness of top film.

5.5.2 Effect of period on energy of base

To investigate the effect of the period of wrinkles on the energy of the base for large deformations, finite element simulations were performed to independently quantify the response of the base layer to a periodic displacement boundary condition. A representative model is shown in Figure 5.12. The effect of wrinkle period on energy is simulated by applying a periodic displacement boundary condition on the top surface of the base layer. The period of the displacement boundary condition is equivalent to the period of the wrinkles. The amplitude of the applied displacement ($\boldsymbol{A_a}$) is varied from zero to a finite value by varying the parameter $\boldsymbol{\varepsilon}$ as:

$$A_a = \frac{\lambda}{\pi}\varepsilon^{0.5} \tag{5.16}$$

Under these conditions, the parameter $\boldsymbol{\varepsilon}$ corresponds to the compression of the bilayer during wrinkle formation. Thus, the results of this simulation can be directly compared to the effect of large compressive strains on energy of the base during wrinkling.

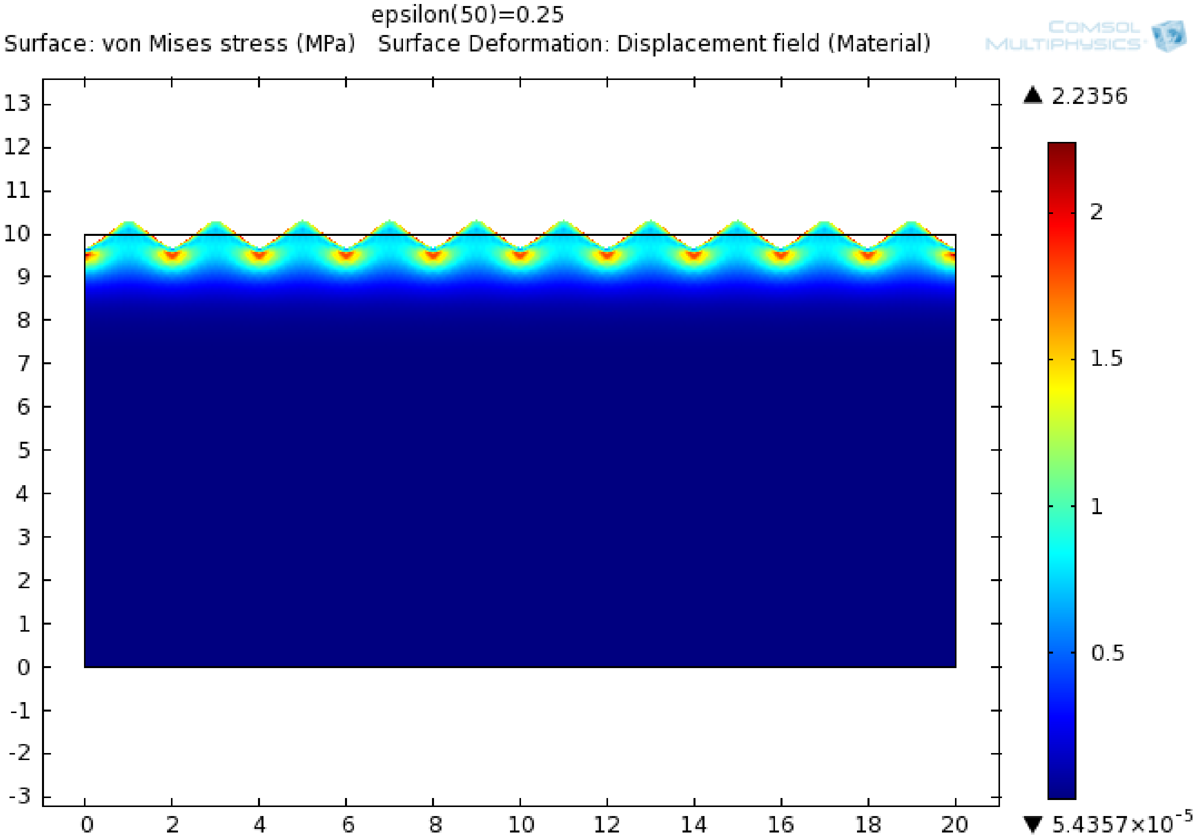

Figure 5.11: Representative model definition for studying the effect of period on the energy in the base for large deformations.

The effect of compression on the energy of the base for different wrinkle periods is summarized in Figure 5.12. Two different studies were performed: (i) base that has a nonlinear Neo-Hookean material response and (ii) base that has a linear material response. For the case with linear material, it is observed that (i) the energy versus compression response is linear and (ii) the base energy increases with the period. These observations are consistent with the linear model for wrinkling as represented by Eq. (5.3). However, the energy versus compression response is nonlinear for the case of a Neo-Hookean base. Additionally, for such a base, the effect of period is coupled with that of the compression such that the energy of the base increases faster for a lower period. The relationship between energy, strain, and period may be represented as:

$$E_b = \alpha_1 \varepsilon \lambda \left(1 + \frac{\alpha_2 \varepsilon}{\lambda^c} \right) \tag{5.17}$$

Here, ***c*** is an exponent that is greater than one and $\boldsymbol{\alpha_1}$ and $\boldsymbol{\alpha_2}$ are material properties. Equation (5.17) is a qualitative representation of the data summarized in Figure 5.12. For linear materials, the parameter $\boldsymbol{\alpha_2}$ is zero. Existing analytical models for large deformation effects that are based on small parameter perturbation analysis [61, 62] do not capture the effect of period on the nonlinear contribution to base energy, i.e., such models erroneously assume that the parameter ***c*** is zero.

When the stiffness moduli ratio is varied, both $\boldsymbol{\alpha_2}$ and $\boldsymbol{\lambda}$ change. This masks the effect of moduli ratio on the critical strain. To separate the effect of the two, constrained parametric analysis was performed by varying the parameters such that the natural period of the wrinkles is held constant.

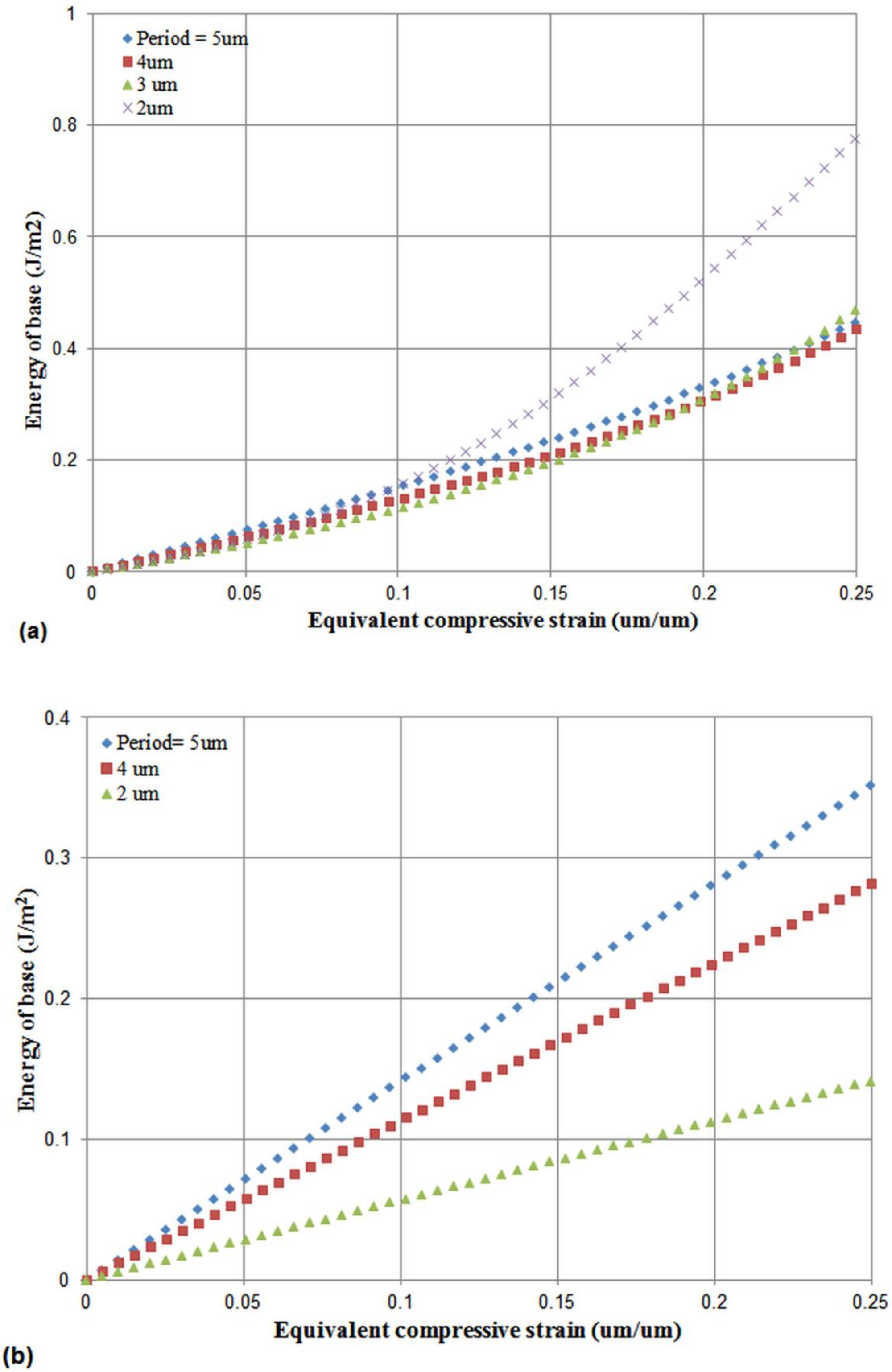

Figure 5.12: Effect of period on energy of base for large deformations. (a) For Neo-Hookean material model. (b) For linear elastic material model. For these studies a periodic displacement boundary condition is applied to the top surface of the base. The equivalent compressive strain (ε) is linked to the amplitude of the applied boundary displacement via Eq. (5.16).

5.5.3 Constrained studies

During constrained parametric studies, the effect of period on bifurcation was eliminated by holding period constant. This was achieved by varying the thickness of the top layer and the moduli ratio such that the two are related as:

$$\eta^{1/3}h = C \tag{5.18}$$

Here, ***C*** is a constant that is determined by the period of the wrinkles and may be evaluated using Eqs. (2.1) and (2.4). The effect of variation in the process parameters on the critical compression is shown in Figure 5.13. For the case when the period is held constant, it is observed that the critical strain for period doubling depends on the moduli ratio and varies from about 17% to 20%. A discernable trend of increase in critical strain with moduli ratio is observed.

The data generated via constrained parametric analysis can be used to estimate the moduli ratio and top layer thickness by comparing the finite element simulations to experimental observations of the critical bifurcation. The data available from experimental observations of the natural mode wrinkling is insufficient to individually evaluate the top layer thickness and the moduli ratio of the bilayer. Mathematically, this occurs because there are more unknown variables than independent equations that link observable parameters to controllable parameters. The period doubling behavior provides additional information that can be used to link observable parameters to all controllable parameters. To do this, one must (i) regenerate the curves depicted in Figure 5.13 for the period that is observed during experiments and (ii) compare the regenerated curves to the experimentally observed period doubling bifurcation compression.

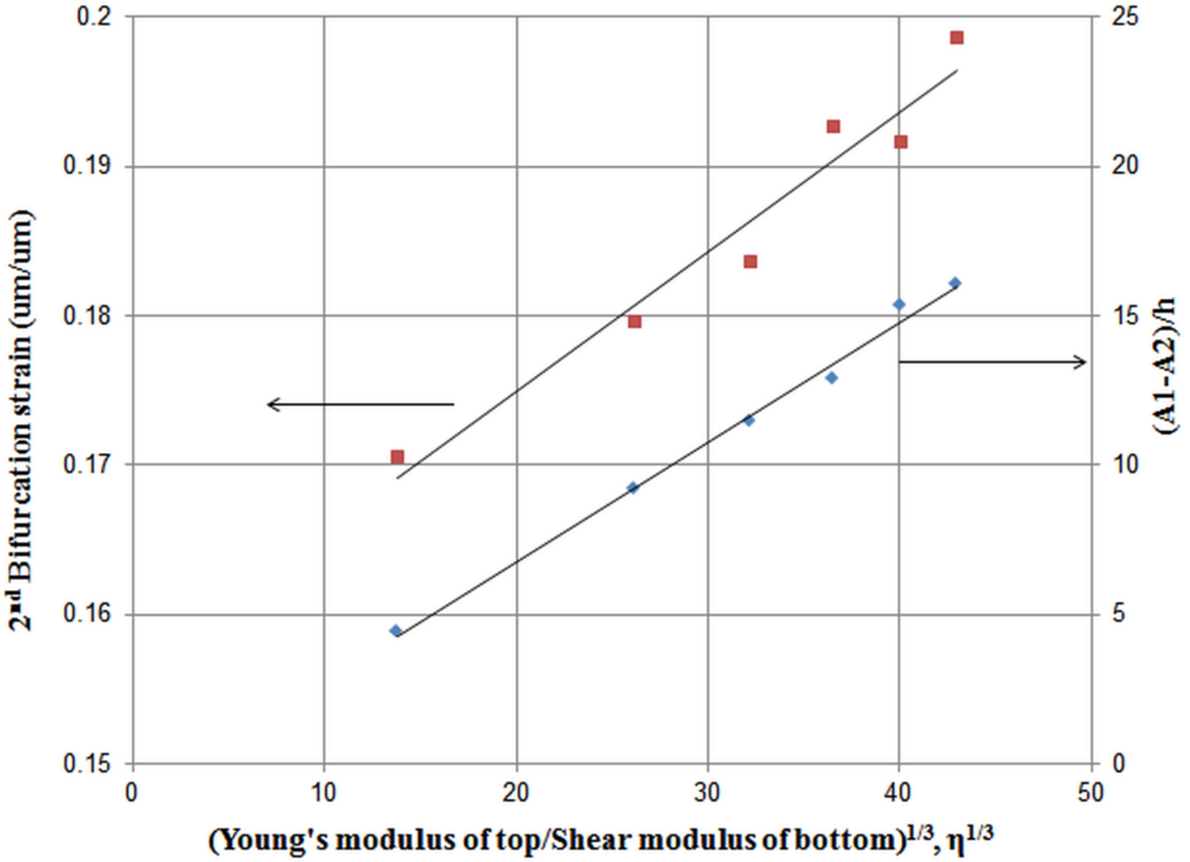

Figure 5.13: Effect of process parameters on critical strain and amplitude difference at 22.5% compressive strain. Lines are linear fit to the data points. The process parameters were constrained such that the natural period is constant for all combinations of the process parameters. The period doubling behavior changes even when the natural period of the systems is held constant.

Chapter 6

Attractors and repellers: Complexity via materials

6.1 Introduction

Non-uniformity in materials generates non-uniform wrinkle patterns. Several experimental techniques that provide a means to rapidly vary material non-uniformity enable one to generate a variety of non-uniform wrinkled patterns. However, due to a lack of predictive models, it is currently not possible to perform predictive design of non-uniform wrinkled patterns. As existing analytical models are based on the approximation of uniform material properties, such models are insufficient in predicting these non-uniform patterns. Thus, predictive design is currently limited to a series of time and resource intensive iterative computational prediction and fabrication cycles. The goal of this work is to (i) identify the building blocks for non-uniform patterns that are formed due to localized material defects and (ii) link properties of building blocks to process/control parameters. This would enable one to rapidly perform predictive design of target patterns via controlled material defects.

6.1.1 Limitations of existing techniques and models

In the past, material non-uniformity in wrinkle formation has been explored within the context of large spatial extent; i.e., on a length scale that is several tens to hundreds of periods. At this scale, the effect of non-uniformity in materials is accounted for by spatial averaging, i.e., by obtaining an average effective modulus for the "defect" zone and then applying conventional 1-D model for wrinkle formation [16]. However, this approach is not appropriate when the defect is too small to be accurately captured as an averaging effect.

Another alternate approach has been to consider the effect of defects as edge effects during 2-D loading [15]. The principal design rule for these systems is that the normal to an edge is traction free. Thus, a nominal 2-D loading is effectively reduced to a 1-D loading at the edges. Although physically accurate, this approach/design rule is of limited practical use as the wrinkle formation away from the edges is still governed by the competition between two principal stretch directions of comparable stretches. Thus, designing non-uniform patterns would require predicting the 2-D wrinkle patterns that arise around defects.

6.1.2 Advantages of bending 1-D wrinkles

Herein, the phenomenon of in-plane bending of 1-D wrinkles due to localized material defects has been investigated to capture the effect of non-uniform material properties. The primary advantage of bending 1-D wrinkles is the simplicity of design and fabrication due to a reduction in the number of independently actuated/stretched directions that arise due to 1-D loading instead of 2-D loading. As 1-D loading is inherently easier to control and manipulate, the scheme of bending wrinkles during 1-D loading is a tractable problem from the perspective of predictive design and fabrication of target features. It simplifies design of equipment, control of parameters, and predictive models that are used to design the patterns. As such, non-uniform wrinkled patterns with 1-D loading has not been extensively studied or used for practical applications. Herein, we demonstrate that non-uniform bent wrinkle is indeed feasible during 1-D loading and the bending phenomenon is tunable via material properties and geometry of localized defects.

6.2 Bending 1-D wrinkles

6.2.1 Bent wrinkles

The ability to bend wrinkles in-plane is necessary when target patterns that are composed of curved features are desired. Also, in-plane bending of wrinkles would open up a design space that is not accessible via uniform materials and simple 1-D loading. The basic building block for curved wrinkles is a bent wrinkle with a non-zero curvature as shown in Figure 4.13. For materials with uniform properties, curvature in wrinkles is not observed. However, for non-uniform material properties there is a finite curvature of wrinkles. The goal of this work is to (i) identify the basic building block for a bent wrinkle, (ii) quantify the building block in terms of geometric parameters, and (iii) link these geometric parameters to control/process parameters.

These studies would enable one to engineer localized defects to direct the generation/fabrication of non-uniform patterns.

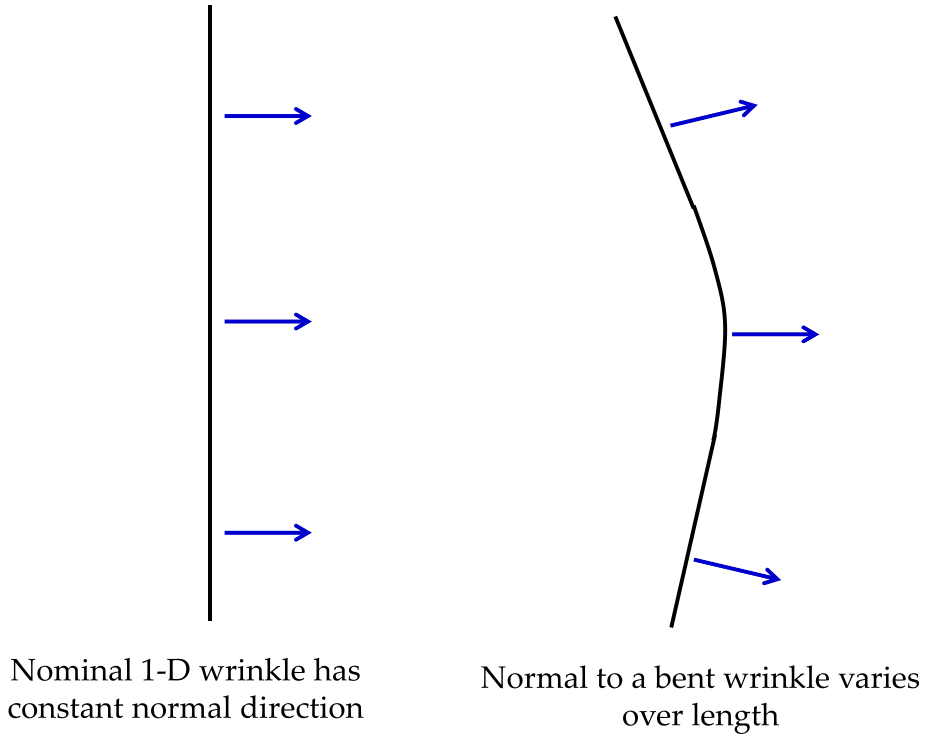

Figure 6.1: Basic building block for a bent wrinkle. Bent wrinkles are necessary when curved wrinkled structures are desired. In the absence of non-uniform material properties, wrinkles do not exhibit in-plane curvature. The figure depicts the building blocks as seen in the top-view of the wrinkled surface. The lines are locus of the peaks of a wrinkled surface.

6.2.2 Edge effects

The phenomenon of bending of wrinkles during 1-D loading was observed at the edges of the PDMS coupon during 1-D loading. In-situ images of the wrinkled surface on various test spots on the PDMS coupon were recorded during stretch release. On analyzing these images, a distinct trend was identified: wrinkles are normal to the principal stretch direction. This is illustrated in Figure 6.2.

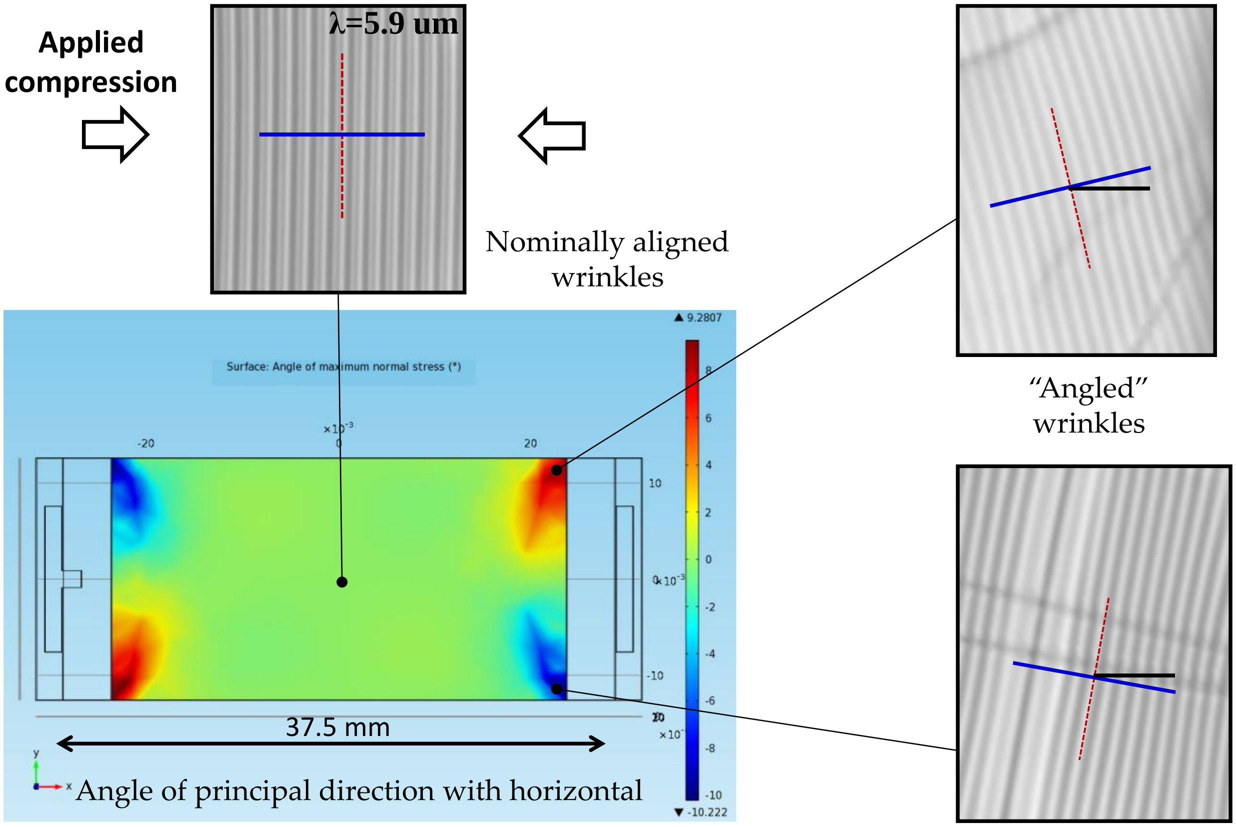

Figure 6.2: Edge effects during wrinkle formation via 1-D loading. Wrinkles at the corners of the film are at an angle to the nominal stretch direction. Dotted red lines indicate the wrinkle profile; solid blue lines indicate the direction of normal to the wrinkle profile; and solid black lines indicate the nominal stretch direction.

At the center of the coupon, wrinkles are observed to be aligned parallel to the nominal stretch direction. However, near the corners of the coupons wrinkles are observed at an angle to the nominal stretch direction. Interestingly, the angles of the non-aligned wrinkles are of opposite sign at the positive and negative y axis positions. This trend matches with the finite element simulation predictions of the angle of the principal stretch direction as shown in Figure 6.2. As these images were recorded in-situ during stretch release, these angles cannot be due to distortions from the coupon unclamping process. This suggests that the non-uniformity in the principal stretch direction during prestretch release is responsible for bending of these wrinkles.

6.3 Attractors and repellers

6.3.1 Concept of attractors and repellers

Attractors and repellers are distinct material defects that alter the direction of wrinkles around them in a specific manner. Attractors are material defects that pull or attract wrinkles toward them; whereas repellers are material defects that push wrinkles away from them. The concept of attraction versus repulsion of wrinkles toward local material defects is a direct consequence of local tracking of wrinkles of the principal stretch direction. Localized material defects in the base material locally alter the principal stretch direction. This change in the principal stretch direction manifests as a change in the normal vector to the wrinkles. As wrinkles track these changes in the normal vector along their length, continuous bent wrinkles that are attracted or repelled by the defects are observed.

The attraction and repulsion effects depend on (i) relative material stiffness moduli of the defect and the base and (ii) geometry of the defect. From experiments and finite element analysis, we observe that the distinction between attractors and repellers is determined entirely by the relative stiffness of the defect and the base. Defects that have a stiffness modulus that is lower than that of the base act as attractors; whereas defects that have a stiffness modulus higher than that of the base act as repellers. Qualitatively, attraction versus repulsion is determined by the ratio of the stiffness moduli of the defect and the base. Thus, voids with zero moduli ratio and rigid inclusions with infinite moduli ratio are two extremes of the attractor-repeller continuum. Voids demonstrate attraction effects, whereas repellers demonstrate repulsion effect. Quantitatively, the "amount" of attraction or repulsion is determined by both the stiffness modulus and the geometry of the defects. Herein, (i) the parameters that quantify the attraction/repulsion effect are identified and (ii) these parameters are linked to the process/control parameters.

6.3.2 Physical basis for attraction versus repulsion

The physical basis for attraction versus repulsion of wrinkles toward material defects is the specific stress field that is generated around these defects. The nature of these stress fields can be visualized in terms of the constant force lines along the defects. The constant force lines around a void are repelled as the void surface acts as a traction free boundary. Constant force lines around a rigid inclusion are attracted toward the inclusion as the inclusion surface acts as a rigid boundary, i.e., a boundary with zero displacement. As the wrinkles are perpendicular to these constant force lines, the effect of voids is to attract wrinkles toward them. Similarly, the effect of rigid inclusions is to repel wrinkles away from them. For the general case of defects with non-zero and non-infinite moduli ratio, the attraction versus repulsion effect is determined by whether the moduli ratio is less than or greater than one. The attraction and repulsion effects are illustrated in Figure 6.3.

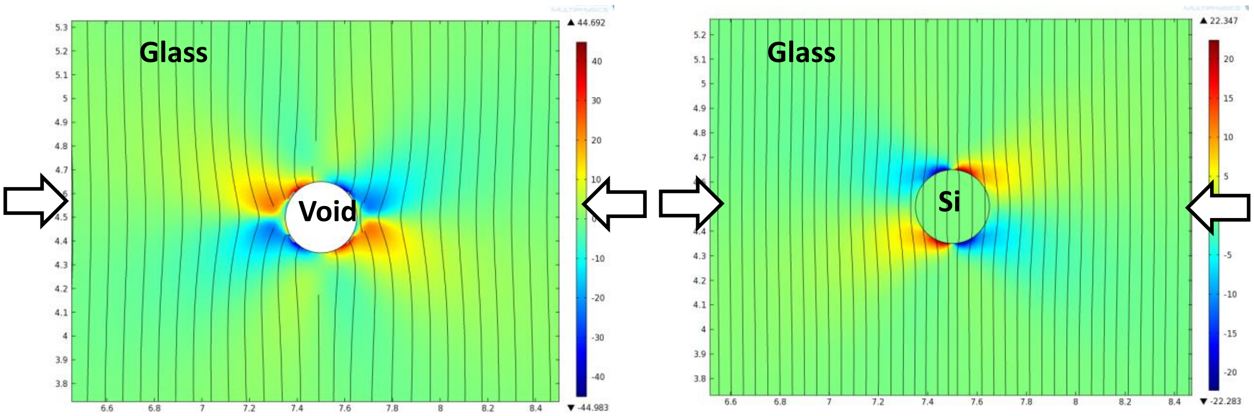

(a) (b)

Figure 6.3: Finite element simulations around material defects demonstrating the attraction and repulsion effect. (a) Void as an attractor of wrinkles. (b) Stiffer silicon inclusion as a repeller of wrinkles. The lines represent the streamlines of principal stress direction. Wrinkles are aligned along these streamlines for a compressed bilayer system. Color information represents the angle of the principal stress direction with respect to the nominal direction of applied compression.

6.3.3 Pattern characterization

The wrinkle patterns around an attractor or repeller may be characterized in terms of the geometric parameters of the building block of an attracted/repelled pattern. The critical parameters are (i) curvature of the wrinkles at the center, (ii) angle of wrinkles at a fixed height from the center line, and (iii) the critical distance from the center line at which the curvature goes to zero. The stress field that determines the direction of 1-D wrinkles can be quantified in terms of these parameters: (i) angle of first principal stress direction and (ii) gradient of the angle of the first principal stress direction.

6.3.4 Physical attractors

To experimentally demonstrate the concept of an attractor, voids were used as material defects. Voids were formed by generating an air bubble close to the top surface of the PDMS before curing. During curing, the bubble migrates to the top surface and bursts to generate a surface void in the cured PDMS. From the wrinkle patterns that are observed around a void, it is evident that a void acts as an attractor of wrinkles. The wrinkle pattern around a void is shown in Figure 6.4. Quantitatively, the extent of attraction, i.e., the curvature of the wrinkles can be predicted if the geometry of the void is accurately known. However, the edges of the void are non-uniform. Thus, the angle of the wrinkles cannot be accurately predicted for this system.

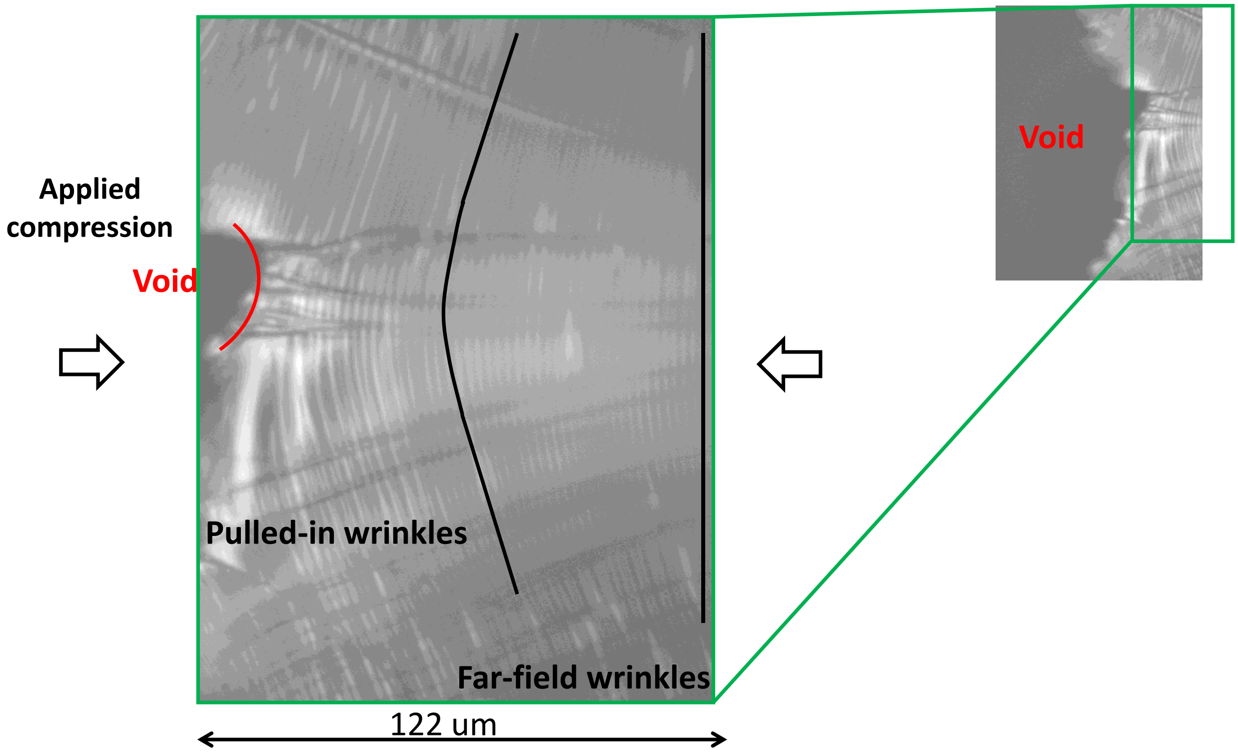

Figure 6.4: Demonstration of void as a physical attractor. Wrinkles are attracted toward the edges of the void. The radius of the void is 175 um.

6.3.5 Physical repellers

To experimentally demonstrate the concept of repellers, stiff inclusions were introduced in the base PDMS. This was performed by sprinkling spherical micro scale glass beads on top of the uncured PDMS followed by curing of the PDMS. The glass beads get embedded into the PDMS base and act as stiff inclusions during wrinkle formation. The wrinkled pattern that is observed around the glass beads is shown in Figure 6.5. From the patterns it is evident that the wrinkles are repelled by the glass beads that are stiffer than the PDMS base material. A quantitative verification of the angle of the wrinkles requires an accurate measurement of the embedded depth of the glass beads. As this depth is not accurately known, the angle cannot be accurately predicted for this system. Nevertheless, this system conclusively demonstrates the concept of repellers.

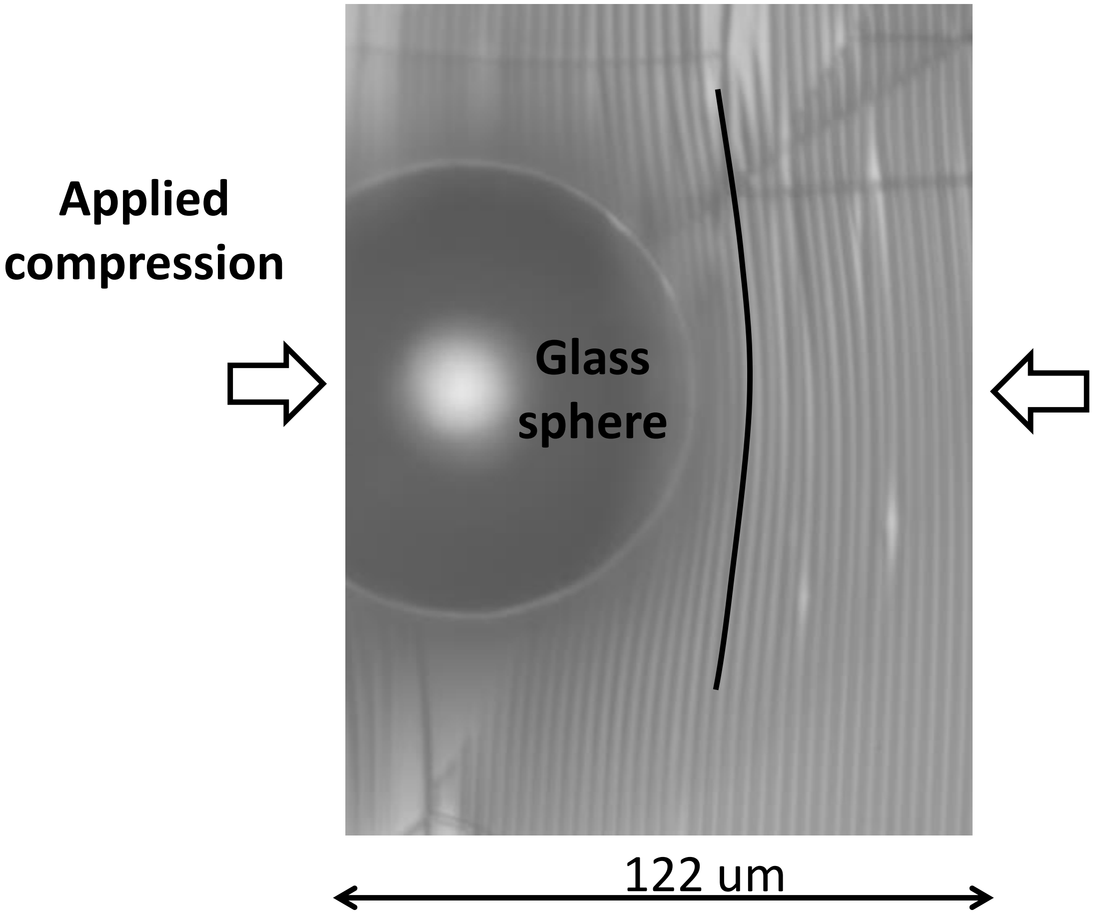

Figure 6.5: Demonstration of a stiff inclusion as a physical repeller. Wrinkles are repelled away from the inclusion. The stiff inclusion is a solid glass microsphere of diameter 75 um.

6.4 Parametric analysis

Finite element analysis based parametric studies were performed to link the properties of the defect to its attraction/repulsion effect. A representative model that was generated to perform these studies is shown in Figure 6.6. For these studies, a spherical inclusion was fully embedded in the base material at a depth of 10 um from the top surface. Finite element simulations were then performed to generate the stress field around the inclusion when the system is uniaxially compressed along the ***X*** axis. Symmetry boundary conditions have been applied to the negative ***X*** and ***Y*** faces to reduce the size of the model.

The curvature of the principal stress direction was measured at a point on the top surface that is located on the negative ***Y*** face and at the radius of the defect along the ***X*** axis. The curvature quantifies the 'amount' of attraction or repulsion. Due to circular symmetry of the spherical defect, the first principal stress direction is oriented along the X axis at the measurement point.

Thus, attraction is quantified by a negative curvature, whereas repulsion is quantified by a positive curvature. The curvature ($\boldsymbol{\kappa_d}$) is quantified as:

$$\kappa_d = \frac{\partial}{\partial Y}\left(0.5\tan^{-1}\left(\frac{2\sigma_{xy}}{\sigma_{xx}-\sigma_{yy}}\right)\right) \tag{6.1}$$

Here, $\boldsymbol{\sigma_{xy}}$ is the in-plane shear stress and $\boldsymbol{\sigma_{xx}}$ and $\boldsymbol{\sigma_{yy}}$ are the normal stresses along $\boldsymbol{X}$ and $\boldsymbol{Y}$. The curvature ($\boldsymbol{\kappa_d}$) is the $\boldsymbol{Y}$ gradient of the direction of principal stress. As the normal to the wrinkles is determined by the direction of principal stress, the curvature of the wrinkle profiles is determined by the gradient of the direction of principal stress. A $\boldsymbol{\kappa_d}$ value of zero indicates that there is no change in the direction of principal stress along the $\boldsymbol{Y}$ axis. In such a case, there would be no in-plane bending of the wrinkles; instead a linear wrinkle profile would be observed. Thus, the parameter $\boldsymbol{\kappa_d}$ quantifies the amount of attraction or repulsion due to a localized defect. A system with uniform material properties has a $\boldsymbol{\kappa_d}$ value of zero over the entire surface.

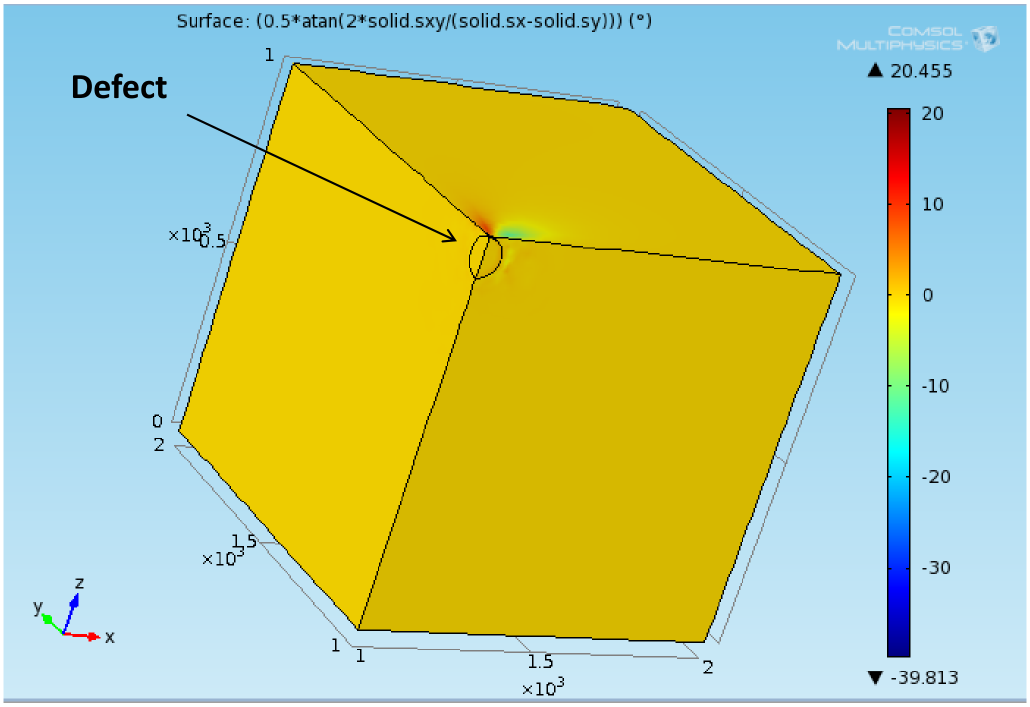

Figure 6.6: Finite element model of a fully embedded defect in the base material. The stress field on the top surface is analyzed to quantify the attraction/repulsion effect. Color bar represents the angle of the first principal stress direction with respect to the X axis.

6.4.1 Attractor versus repeller

The effect of Young's modulus of an inclusion on the attraction/repulsion effect is shown in Figure 6.7. From the figure, it is evident that attraction versus repulsion effect is dependent on the ratio of Young's modulus of the inclusion to the base. For the case when this ratio is less than one, the inclusion acts as an attractor. The inclusion acts as a repeller when this ratio is greater than one. This is consistent with the limiting cases: (i) voids that have a zero moduli ratio and act as attractors and (ii) rigid inclusions that have an infinite moduli ratio and act as repellers. For defects that have the same size and shape, the attraction versus repulsion effect is not symmetric about the unity moduli ratio. The attraction effect is stronger than the repulsion effect for defects of the same size and shape.

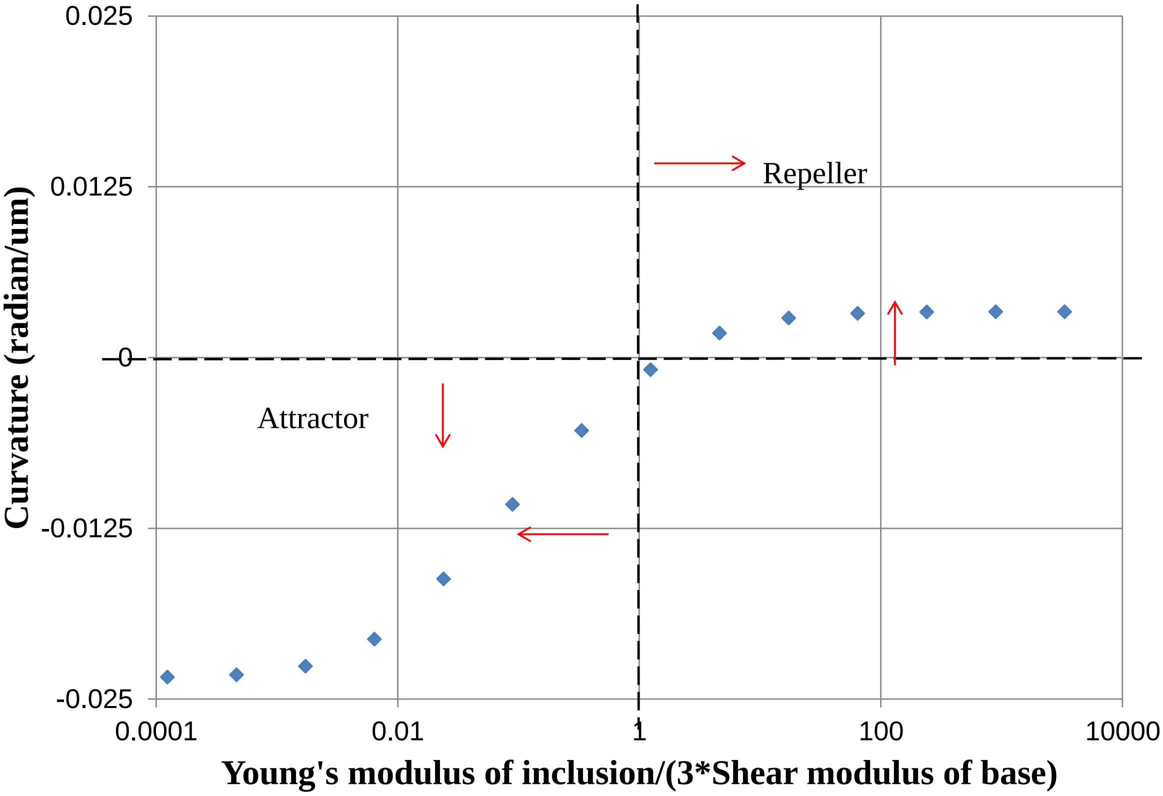

Figure 6.7: Effect of Young's modulus of the defect on the attraction/repulsion effect. The defect diameter is 100 um.

6.4.2 Effect of defect size

The effect of defect size on the gradient of principal stress direction is summarized in Figure 6.8. As the gradient of the principal stress direction decreases with the size of the defect, the repulsion effect decreases with increasing defect size. This occurs because the gradient of the stress field decreases with an increase in the size of the defect; i.e., the stress field becomes more uniform as the defect size increases. This leads to two limiting cases: (a) when the defect size is extremely large and (b) the defect size is extremely small. For the case of an extremely large defect, the attraction/repulsion effect is averaged over several wrinkles such that the net effect is generation of wrinkle profiles with negligible curvature. For the case of an extremely small defect, the gradients are high; however, the spatial extent of the effect is small. Under such a condition, the attraction/repulsion effect of the defect would not be captured even over a single wrinkle period. Thus, there is a "sweet spot" range of defect sizes over which the attraction/repulsion effect manifests as curved wrinkles. Here, the terms 'large' and 'small' defect size are relative and scale with the period of the wrinkles.

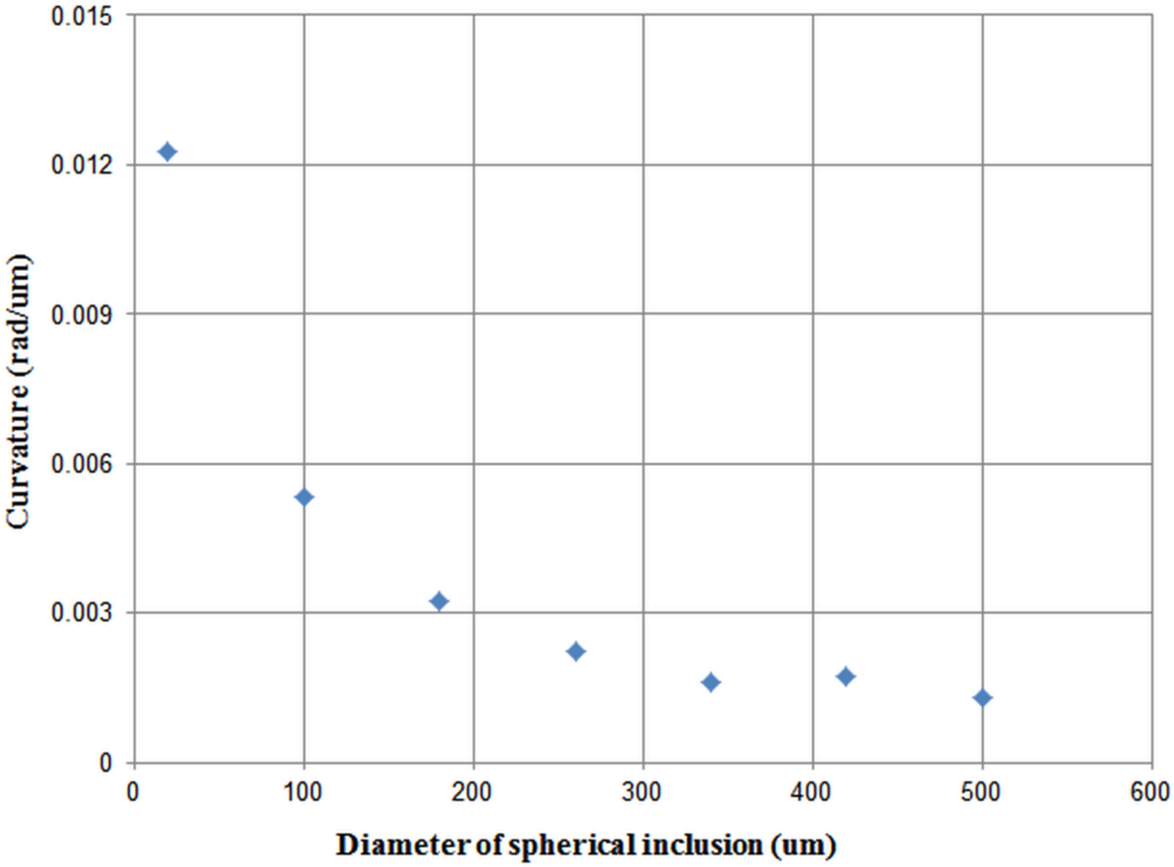

Figure 6.8: Effect of defect size on the repulsion effect. Young's modulus of the defect is three times higher than that of the base material.

Chapter 7

Conclusions

7.1 Thesis within context

At present, wrinkling of thin films is an active area of research around the world. The focus of a majority of research groups is on (i) understanding and exploring the mechanics of wrinkle formation for a given set of parameters and/or (ii) applying elementary wrinkle patterns to tune surface properties by linking periodic structures to novel properties. In combination, these two approaches are advancing the adoption of the wrinkling process as an alternate low-cost laboratory scale fabrication technique. However, further adoption of wrinkling as a scalable and affordable manufacturing process requires an additional research effort: predictive design and fabrication of desired *complex* wrinkled patterns. In the absence of such work, one is limited to design and prediction of only a small set of elementary patterns. Additionally, it is not possible to determine whether fabricating a desired pattern is feasible within the manufacturing constraints. Without this knowledge base, it is impossible to transition wrinkling-based processes to industrial scale manufacturing. This thesis fulfils the need for this knowledge base by contributing to the science and engineering of predictive pattern design via wrinkling.

The work summarized in this thesis has been performed from the vantage point of scalable manufacturing. This has led to an alternate set of research questions and solution approaches. For example, this vantage point necessitates the study of the fabrication process steps in conjunction with the analysis of the complex wrinkled patterns. Thus, instead of focusing on analyzing a specific set of complex wrinkled patterns that were generated via uncontrolled non-uniform process parameters, the focus here has been to systematically investigate the contribution of each controllable process parameter to overall pattern complexity. This approach enables one to develop a set of predictive tools and fabrication techniques to perform inverse pattern design, i.e., to select the appropriate set of process parameters that would generate a desired complex pattern. To support this approach, tools and techniques were developed that enable one to individually tune the process parameters and to probe their effect on the pattern complexity. One such representative tool is illustrated in Figure 7.1. Apart from supplementing the research efforts underway elsewhere, this thesis provides an alternate perspective to research in this field by demonstrating the fundamental advances that must be made to transform a laboratory scale fabrication process to industrial scale manufacturing.

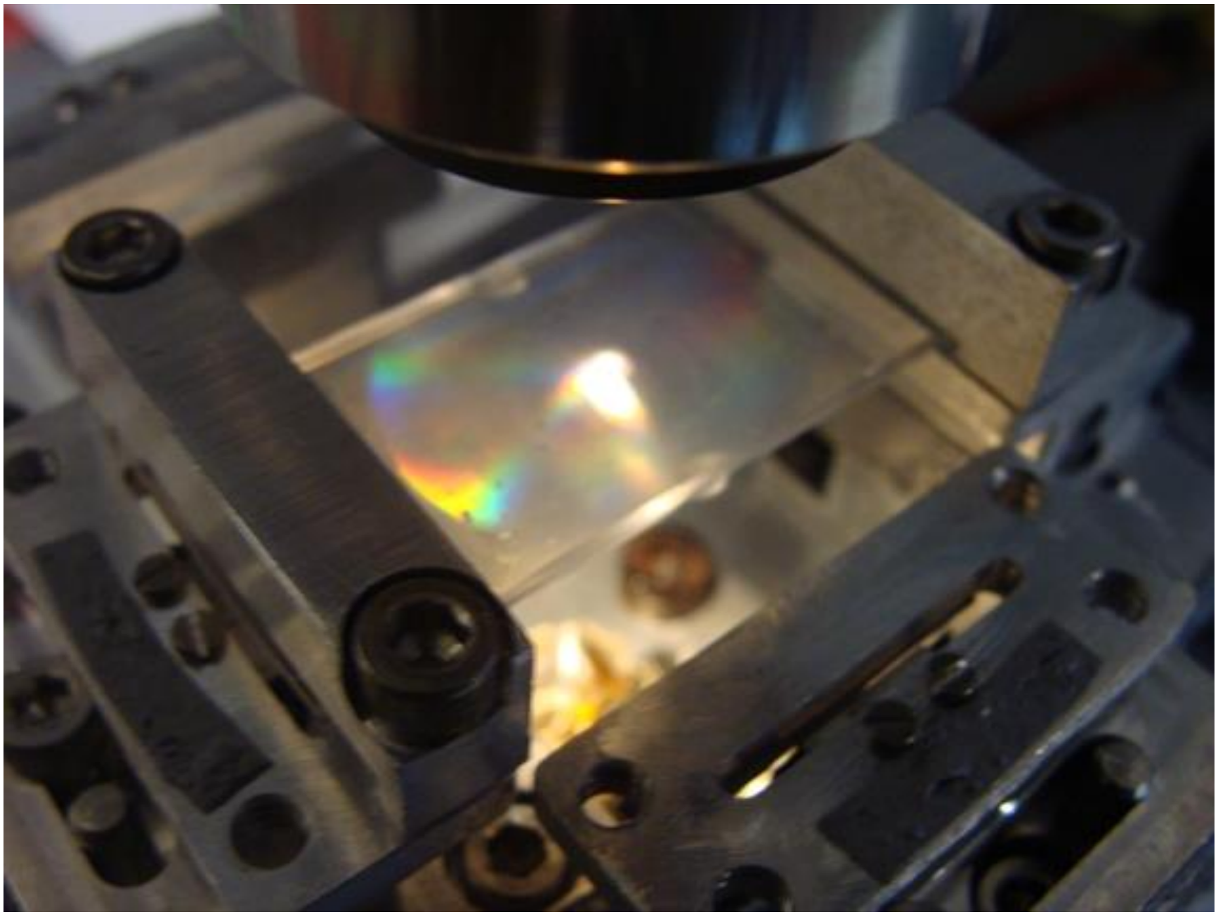

Figure 7.1: Close-up view of a bilayer with partial prestretch release. For scale, the bolt head in the foreground belongs to a standard 6-32 bolt. Iridescence on the PDMS surface occurs due to the presence of wrinkle patterns. Tools developed here enable one to tune the process parameters and to observe the effect of the process parameters on the wrinkle patterns.

7.2 Summary of contributions

The goal of this work was to enable predictive design and fabrication of complex wrinkled patterns for affordable and scalable manufacturing. Toward this goal, two types of contributions have been made: (i) engineering tools to fabricate and predict wrinkles and (ii) predictive process knowledge. These are summarized in this section.

7.2.1 Tools

Fabrication tools

To enable fabrication of wrinkled patterns, a compact biaxial stretch stage was designed and built. This stage provides the means to apply accurate, large, non-equibiaxial stretch to PDMS films within a small device footprint. This makes it feasible to predictively fabricate desired wrinkled patterns via affordable metal deposition or plasma oxidation processes. Additionally, the process steps in wrinkle fabrication were standardized and characterized so as to reduce and quantify process variations. This enables fabricating accurate micro/nano scale patterns via low-cost non-cleanroom fabrication techniques.

Computational tools

Mesh perturbation is a necessary requirement for performing post-buckling simulations. However, this functionality is not available in commercially available finite element packages. Here, a mesh perturbation tool box has been developed, characterized, and verified to perform accurate predictions of wrinkle patterns via finite element methods. This toolbox enables one to study the sensitivity of the bifurcation process to a variety of predetermined geometric perturbations. This functionality is essential to be able to accurately predict the onset of complex hierarchical modes when pre-patterned bilayers are compressed.

7.2.2 Process knowledge

Complexity via geometry

Herein, complex hierarchical wrinkled structures were fabricated by geometrically patterning the bilayers to an initially non-flat state. To enable low-cost deterministic geometric patterning, a fabrication scheme was developed to perform pre-patterning via replication of wrinkled patterns. Based on studies of hierarchical wrinkled structures, the following process knowledge has been generated:

(1) Compressing a pre-patterned bilayer is energetically favorable over compressing a flat bilayer.
(2) Compressing a pre-patterned bilayer with a non-natural period leads to an energy penalty with respect to compressing a pre-patterned bilayer with the natural period.
(3) A pre-patterned bilayer transitions from the pre-patterned state into the hierarchical state when the compressive strain exceeds a threshold value.
(4) The critical compressive strain for transition into hierarchical mode is determined by the competition between the energy advantage due to pre-patterning and the energy penalty due to non-natural period.

Based on the above process knowledge, an analytical model was generated to accurately predict the transition of pre-patterned bilayers into hierarchical modes. This model has been verified against finite element simulations and experiments. The model enables one to predictively design tunable hierarchical patterns by selecting the appropriate process parameters that are required to generate the desired pattern.

Complexity via loading

Complex higher mode wrinkles emerge when large compressive strains are applied. Out of several feasible higher modes, the immediate higher mode for wrinkling manifests as period doubling with the valley-moving-up mode. Currently available models in the literature cannot predict this mode selection at higher compressive strains. Here, finite element simulations have been performed to predict the effect of material non-linearity in the base on the selected higher mode. These simulations have been verified against experiments that demonstrate period doubling via valley-moving-up phenomenon. The following process knowledge has been generated:

(1) Unlike an unsupported beam, period doubling is energetically favorable over period halving during compression of bilayers.
(2) Period doubling via the valley-moving-up mode is energetically favorable over the peak-moving-down mode for Neo-Hookean base materials due to non-symmetric stress versus strain response in compression versus in tension.

(3) The effect of nonlinear base material that determines the critical strain for transition into period doubling depends on the period of the wrinkles and the stiffness modulus of the base.
(4) When the wrinkle period is held constant, the critical strain increases with an increase in the moduli ratio of the bilayers.

The knowledge generated here about the period doubling phenomenon can be used to separately predict the moduli ratio and the top layer thickness of the bilayers from observable process parameters. As this prediction is not feasible from the observation of the first bifurcation into the natural mode, the period doubling prediction enables one to perform predictive design and fabrication of patterns via low-cost plasma oxidation processes.

Complexity via material properties

Non-uniformity in material properties leads to deviations in the wrinkle pattern from the natural mode. In the past, complex patterns have been fabricated via 2-D loading of bilayers with material non-uniformity. For such systems, predictive design is currently not feasible because the effect of non-uniformity is confounded by interaction of 2-D loading with material non-uniformity. Here, the problem has been simplified by applying 1-D loading with localized material defects. This enables one to construct elegant design rules for tuning the in-plane direction of wrinkles during 1-D loading. The following knowledge has been generated during this process:

(1) There are two distinct types of localized material defects: attractors and repellers. Attractors pull wrinkles toward them, whereas repellers push wrinkles away from them.
(2) The attraction versus repulsion effect is determined by the ratio of stiffness modulus of the defect with respect to the base material. Defects with a ratio less than unity act as attractors, whereas defects with a ratio higher than unity act as repellers.
(3) The attraction/repulsion effect increases as the moduli ratio deviates away from unity.
(4) Maximum attraction is observed for a void and maximum repulsion is observed for a rigid inclusion.
(5) For attractors and repellers of the same size and shape, the attraction effect is higher than the repulsion effect.

7.3 Future work

The work presented in this thesis is necessary but not sufficient to develop wrinkling as a robust affordable and scalable manufacturing process. To achieve this goal, further research in this field is necessary. These research directions are listed in this section.

7.3.1 Thin film generation

In this work, bilayers have been generated by plasma oxidation of PDMS films. This is a low-cost technique for generating thin nanometer scale films on top of PDMS. However, at present the process knowledge about the plasma oxidation step is limited. Specifically, it is not possible to separately quantify and/or predict the thickness and the stiffness modulus of the oxidized films based on the controllable process parameters. Here, nano-indentation measurements were performed to quantify the stiffness modulus of the film that suggested that the film property is not uniform across its thickness. Thus, there is a need to implement alternate film generation techniques that are based on depositing metal or polymer thin films. With such techniques, a-priori information about the film thickness and stiffness modulus would provide additional predictive capability. At present, such techniques are of limited practical use due to (i) delamination of the deposited film, (ii) high temperatures during deposition, and/or (iii) extremely slow deposition process. These issues must be overcome to enable scalable manufacturing via wrinkling. Nevertheless, deposition based techniques may be used at the laboratory scale to investigate the wrinkling process and to generate predictive models for complex patterning. Once these models are available, plasma oxidation based processes may be used to scale-up manufacturing.

7.3.2 Hierarchical wrinkling

In this work, hierarchical wrinkling has been predicted and demonstrated for the special case of (i) patterns with two spatial frequencies and (ii) patterns in which the two periods are aligned along the same axis. There are two logical extensions to this work: (i) patterns that have hierarchies on more than one length scale and (ii) demonstration and prediction of cross-aligned patterns, i.e., patterns that are aligned to each other at an angle. The case of cross-aligned patterns can also be used to study the effect of 2-D loading on pre-patterned surfaces. Fabricating and predicting these patterns would also require tackling engineering issues such as tolerance of alignment of the two patterns to each other.

7.3.3 Period doubling

Here, the effect of nonlinear base on the period doubling behavior has been investigated for a specific set of bilayer materials. As a logical extension to the work presented here, generalized analytical or numerical models for large deformations of the base must be developed. Such models would enable one to predict the onset of period doubling across different material systems. For example, period doubling has not been observed for the silicon/PDMS bilayer system even at large strains. Large deformation models would provide insight into material selection when period doubling is a desired or undesired behavior. Currently available analytical models that predict the effect of base nonlinearity are based on perturbation analysis techniques. These analyses are insufficient to predict the behavior of nonlinear base material for large deformations that lead to period doubling behavior.

7.3.4 Attractors and repellers

Herein, the concept of attractors and repellers as distinct material defects has been proposed and experimentally verified. To enable the generation of complex patterns via these defects, the next step is to develop the tools to systematically combine multiple attractors and/or repellers on the same surface. This requires one to develop (i) fabrication techniques to generate multiple micro scale material defects and (ii) the ability to tune the location of individual defects with respect to each other. Additionally, one must also develop a set of predictive models to capture the effect of interacting attractors and/or repellers.

Here, defects with circular symmetry have been used to demonstrate the attraction and repulsion effect. The nature of attraction versus repulsion effect is qualitatively preserved for other shapes that include sharp corners. However, new quantitative design maps must be generated for shapes that differ from circular/spherical defects.

In this work, the principal stress direction has been used as a proxy to predict the direction of wrinkles in the presence of localized material defects. This approximation has been verified to be accurate for locations that are at a moderate to large distance away from the defects. However, during experiments it has been observed that sometimes the wrinkles become discontinuous for regions that are very close to the defects. This arises due to competition between large gradients in the principal stress direction and the stress concentration. To accurately capture this effect, one must develop analytical and/or finite element techniques to directly predict the wrinkles close to the defect boundaries. Direct prediction of wrinkles around defects has posed a significant numerical challenge due to the large difference in length scale of the top film and the defect. As the size of the two features differs by about 10,000 times, it poses challenges in successfully setting up the mesh for finite element simulations.

7.3.5 Loading path dependence in wrinkling

Although not discussed earlier in this thesis, preliminary experiments performed here demonstrate that the loading path has a significant effect on the pattern geometry during biaxial compression. For example, sequential compression along orthogonal directions can be used to generate two sets of zig-zag patterns that are orthogonal to each other by altering the ordering of the applied compressions. Further work must be done to fully explore the effect of loading path on the wrinkle patterns. The biaxial stretch stage that was designed and developed here can be used to perform such studies. In addition to flat bilayer surfaces, path dependence studies may also be performed on pre-patterned surfaces. As pre-patterning leads to an energetic preference for deformation along the pre-patterned axis, pre-patterning breaks the in-plane symmetry of the bilayer system. For a biaxially loaded system, this may lead to complex wrinkle patterns that are not accessible via compression of flat bilayers.

7.3.6 Composite complex patterning

The focus of this work has been on individually linking the effect of geometry, material properties, and loading to the complexity of the wrinkled pattern. A set of more complex patterns can now be generated by combining the complexity arising out of these three independent process parameters. Further work must be performed to develop predictive models that systematically combine the effect of these parameters.

References

1. Malshe, A.P., et al., *Tip-based nanomanufacturing by electrical, chemical, mechanical and thermal processes.* CIRP Annals - Manufacturing Technology, 2010. **59**(2): p. 628-651.
2. Rosi, N.L. and C.A. Mirkin, *Nanostructures in biodiagnostics.* Chemical reviews, 2005. **105**(4): p. 1547-1562.
3. Boukany, P.E., et al., *Nanochannel electroporation delivers precise amounts of biomolecules into living cells.* Nat Nano, 2011. **6**(11): p. 747-754.
4. Kahl, M., et al., *Periodically structured metallic substrates for SERS.* Sensors and Actuators B: Chemical, 1998. **51**(1–3): p. 285-291.
5. Anker, J.N., et al., *Biosensing with plasmonic nanosensors.* Nat Mater, 2008. **7**(6): p. 442-453.
6. Paronyan, T.M., et al., *Formation of ripples in graphene as a result of interfacial instabilities.* ACS Nano, 2011. **5**(12): p. 9619-27.
7. Singamaneni, S. and V.V. Tsukruk, *Buckling instabilities in periodic composite polymeric materials.* Soft Matter. **6**(22): p. 5681-5692.
8. Vandeparre, H., et al., *Confined wrinkling: impact on pattern morphology and periodicity.* Soft Matter. **7**(15): p. 6878-6882.
9. Vandeparre, H., et al., *Wrinkling Hierarchy in Constrained Thin Sheets from Suspended Graphene to Curtains.* Physical Review Letters. **106**(22): p. 224301.
10. Wang, L., C.E. Castro, and M.C. Boyce, *Growth strain-induced wrinkled membrane morphology of white blood cells.* Soft Matter. **7**(24): p. 11319-11324.
11. Zheng, X.-P., et al., *Surface wrinkling of nanostructured thin films on a compliant substrate.* Computational Materials Science. **49**(4): p. 767-772.
12. Ghosh, S.K., *Experiments of buckling of multilayers which permit interlayer gliding.* Tectonophysics, 1968. **6**(3): p. 207-249.
13. Chan, H.C. and O. Foo, *Buckling of multi-layer sandwich plates by the finite strip method.* International Journal of Mechanical Sciences, 1977. **19**(8): p. 447-456.
14. Bowden, N., et al., *Spontaneous formation of ordered structures in thin films of metals supported on an elastomeric polymer.* Nature, 1998. **393**(6681): p. 146-149.
15. Bowden, N., et al., *The controlled formation of ordered, sinusoidal structures by plasma oxidation of an elastomeric polymer.* Applied Physics Letters, 1999. **75**(17): p. 2557-2559.
16. Huck, W.T.S., et al., *Ordering of Spontaneously Formed Buckles on Planar Surfaces.* Langmuir, 2000. **16**(7): p. 3497-3501.

17. Groenewold, J., *Wrinkling of plates coupled with soft elastic media.* Physica A: Statistical Mechanics and its Applications, 2001. **298**(1-2): p. 32-45.

18. Sridhar, N., D.J. Srolovitz, and Z. Suo, *Kinetics of buckling of a compressed film on a viscous substrate.* Applied Physics Letters, 2001. **78**(17): p. 2482-2484.

19. Cerda, E., K. Ravi-Chandar, and L. Mahadevan, *Thin films: Wrinkling of an elastic sheet under tension.* Nature, 2002. **419**(6907): p. 579-580.

20. Cerda, E. and L. Mahadevan, *Geometry and Physics of Wrinkling.* Physical Review Letters, 2003. **90**(7): p. 074302.

21. Yoo, P.J. and H.H. Lee, *Evolution of a Stress-Driven Pattern in Thin Bilayer Films: Spinodal Wrinkling.* Physical Review Letters, 2003. **91**(15): p. 154502.

22. Efimenko, K., et al., *Nested self-similar wrinkling patterns in skins.* Nature Materials, 2005. **4**(4): p. 293-297.

23. Smoukov, S.K., et al., *Nano- and Microscopic Surface Wrinkles of Linearly Increasing Heights Prepared by Periodic Precipitation.* Journal of the American Chemical Society, 2005. **127**(50): p. 17803-17807.

24. Chan, E.P. and A.J. Crosby, *Spontaneous formation of stable aligned wrinkling patterns.* Soft Matter, 2006. **2**(4): p. 324-328.

25. Genzer, J. and J. Groenewold, *Soft matter with hard skin: From skin wrinkles to templating and material characterization.* Soft Matter, 2006. **2**(4): p. 310-323.

26. Jiang, C., et al., *Complex Buckling Instability Patterns of Nanomembranes with Encapsulated Gold Nanoparticle Arrays.* Nano Letters, 2006. **6**(10): p. 2254-2259.

27. Huang, J., et al., *Capillary Wrinkling of Floating Thin Polymer Films.* Science, 2007. **317**(5838): p. 650-653.

28. Lin, P.-C. and S. Yang, *Spontaneous formation of one-dimensional ripples in transit to highly ordered two-dimensional herringbone structures through sequential and unequal biaxial mechanical stretching*. Vol. 90. 2007: AIP. 241903.

29. Chiche, A., C.M. Stafford, and J.T. Cabral, *Complex micropatterning of periodic structures on elastomeric surfaces.* Soft Matter, 2008. **4**(12): p. 2360-2364.

30. Holmes, D.P., M. Ursiny, and A.J. Crosby, *Crumpled surface structures.* Soft Matter, 2008. **4**(1): p. 82-85.

31. Pandit, M.K., B.N. Singh, and A.H. Sheikh, *Buckling of laminated sandwich plates with soft core based on an improved higher order zigzag theory.* Thin-Walled Structures, 2008. **46**(11): p. 1183-1191.

32. Pretzl, M., et al., *A Lithography-Free Pathway for Chemical Microstructuring of Macromolecules from Aqueous Solution Based on Wrinkling.* Langmuir, 2008. **24**(22): p. 12748-12753.

33. Rand, C.J., et al., *Fracture-induced alignment of surface wrinkles.* Soft Matter, 2008. **4**(9): p. 1805-1807.

34. Song, J., et al., *Buckling of a stiff thin film on a compliant substrate in large deformation.* International Journal of Solids and Structures, 2008. **45**(10): p. 3107-3121.

35. Evensen, H.T., et al., *Transformations in Wrinkle Patterns: Cooperation between Nanoscale Cross-Linked Surface Layers and the Submicrometer Bulk in Wafer-Spun, Plasma-Treated Polydimethylsiloxane.* Nano Letters, 2009. **9**(8): p. 2884-2890.

36. Flynn, C.O. and B.A.O. McCormack, *A three-layer model of skin and its application in simulating wrinkling.* Computer Methods in Biomechanics and Biomedical Engineering, 2009. **12**(2): p. 125 - 134.

37. Guvendiren, M., S. Yang, and J.A. Burdick, *Swelling-Induced Surface Patterns in Hydrogels with Gradient Crosslinking Density.* Advanced Functional Materials, 2009. **19**(19): p. 3038-3045.

38. Khang, D.-Y., J.A. Rogers, and H.H. Lee, *Mechanical Buckling: Mechanics, Metrology, and Stretchable Electronics.* Advanced Functional Materials, 2009. **19**(10): p. 1526-1536.

39. Pai, C.-L., M.C. Boyce, and G.C. Rutledge, *Morphology of Porous and Wrinkled Fibers of Polystyrene Electrospun from Dimethylformamide.* Macromolecules, 2009. **42**(6): p. 2102-2114.

40. Schweikart, A. and A. Fery, *Controlled wrinkling as a novel method for the fabrication of patterned surfaces.* Microchimica Acta, 2009. **165**(3): p. 249-263.

41. Wang, L., et al., *Wrinkled surface topographies of electrospun polymer fibers.* Applied Physics Letters, 2009. **94**(15): p. 151916-3.

42. Yin, J., X. Chen, and I. Sheinman, *Anisotropic buckling patterns in spheroidal film/substrate systems and their implications in some natural and biological systems.* Journal of the Mechanics and Physics of Solids, 2009. **57**(9): p. 1470-1484.

43. Chen, X. and J. Yin, *Buckling patterns of thin films on curved compliant substrates with applications to morphogenesis and three-dimensional micro-fabrication.* Soft Matter, 2010. **6**(22): p. 5667-5680.

44. Mei, Y., et al., *Principles and applications of micro and nanoscale wrinkles.* Materials Science and Engineering: R: Reports, 2010. **70**(3-6): p. 209-224.

45. Breid, D. and A.J. Crosby, *Effect of stress state on wrinkle morphology.* Soft Matter, 2011.

46. Cai, S., et al., *Periodic patterns and energy states of buckled films on compliant substrates.* Journal of the Mechanics and Physics of Solids, 2011. **59**(5): p. 1094-1114.

47. Chung, J.Y., et al., *Stiffness, Strength, and Ductility of Nanoscale Thin Films and Membranes: A Combined Wrinklingâ€“Cracking Methodology.* Nano Letters, 2011. **11**(8): p. 3361–3365.

48. Mei, Y., et al., *Principles and applications of micro and nanoscale wrinkles.* Materials Science and Engineering: R: Reports. **70**(3-6): p. 209-224.

49. Hendricks, T.R., W. Wang, and I. Lee, *Buckling in nanomechanical films.* Soft Matter. **6**(16): p. 3701-3706.

50. Chiche, A., C.M. Stafford, and J.T. Cabral, *Complex micropatterning of periodic structures on elastomeric surfaces*, in *Soft Matter*. 2008, The Royal Society of Chemistry. p. 2360-2364.

51. Bar-Yam, Y., *General Features of Complex Systems*, in *Encyclopedia of Life Support Systems*. 2002, UNESCO Publishers: Oxford, UK.

52. Han, M., et al., *Quantum-dot-tagged microbeads for multiplexed optical coding of biomolecules.* Nat Biotech, 2001. **19**(7): p. 631-635.

53. Saha, S.K. and M.L. Culpepper, *A surface diffusion model for Dip Pen Nanolithography line writing.* Applied Physics Letters, 2010. **96**(24): p. 243105.

54. Saha, S.K. and M.L. Culpepper, *An Ink Transport Model for Prediction of Feature Size in Dip Pen Nanolithography.* Journal of Physical Chemistry C, 2010. **114**(36): p. 15364-15369.

55. Saha, S.K. and M.L. Culpepper, *Characterization of the Dip Pen Nanolithography Process for Nanomanufacturing.* Journal of Manufacturing Science and Engineering-Transactions of the Asme, 2011. **133**(4): p. 041005.

56. Stafford, C.M., et al., *Combinatorial and high-throughput measurements of the modulus of thin polymer films.* Review of Scientific Instruments, 2005. **76**(6): p. 062207-5.

57. Huang, R. and Z. Suo, *Wrinkling of a compressed elastic film on a viscous layer.* Journal of Applied Physics, 2002. **91**(3): p. 1135-1142.

58. Huang, R., *Kinetic wrinkling of an elastic film on a viscoelastic substrate.* Journal of the Mechanics and Physics of Solids, 2005. **53**(1): p. 63-89.

59. Hobart, K., et al., *Compliant substrates: A comparative study of the relaxation mechanisms of strained films bonded to high and low viscosity oxides.* Journal of Electronic Materials, 2000. **29**(7): p. 897-900.

60. Brau, F., et al., *Multiple-length-scale elastic instability mimics parametric resonance of nonlinear oscillators.* Nat Phys, 2011. **7**(1): p. 56-60.

61. Jiang, H., et al., *Finite deformation mechanics in buckled thin films on compliant supports.* Proceedings of the National Academy of Sciences, 2007. **104**(40): p. 15607-15612.

62. Hutchinson, J.W., *The role of nonlinear substrate elasticity in the wrinkling of thin films.* Philosophical Transactions of the Royal Society A: Mathematical, Physical and Engineering Sciences, 2013. **371**(1993).

63. Sun, J.-Y., et al., *Folding wrinkles of a thin stiff layer on a soft substrate.* Proceedings of the Royal Society A: Mathematical, Physical and Engineering Science, 2011.

64. Yin, J., et al., *Deterministic Order in Surface Micro-Topologies through Sequential Wrinkling.* Advanced Materials, 2012. **24**(40): p. 5441-5446.

65. Yin, J., et al., *Bi-axially Mechanical Tuning of 2-D Reversible and Irreversible Surface Topologies through Simultaneous and Sequential Wrinkling.* ACS Applied Materials & Interfaces, 2014.

66. Wong, E.J., *Modeling and Control of Rapid Cure in Polydimethylsiloxane (PDMS) for Microfluidic Device Applications*, in *Mechanical Engineering*. 2010, Massachusetts Institute of Technology: Boston, MA. p. 151.

67. Lee, J.-B., S.-S. Yoon, and D.-Y. Khang, *The importance of interfacial adhesion in the buckling-based mechanical characterization of materials.* RSC Advances, 2013. **3**(38): p. 17364-17372.

68. Saha, S.K. and M.L. Culpepper. *MeshPerturb: MATLAB codes for mesh perturbation and automated pre and post processing of post-bifurcation analyses via COMSOL*. 2014; Available from: http://hdl.handle.net/1721.1/86934.

69. *Structural Mechanics Module User's Guide COMSOL 4.2 installation documentation*.

70. *The COMSOL File Formats*, in *COMSOL Multiphysics Reference Guide*, *COMSOL 4.2 installation documentation*. p. 481.

71. *Building a COMSOL Model*, in *COMSOL Multiphysics User's Guide, COMSOL 4.2 installation documentation*. p. 357.

72. *LiveLink for MATLAB User's Guide, COMSOL 4.2 installation documentation.*

73. Chen, C.-M., J.C. Reed, and S. Yang, *Guided wrinkling in swollen, pre-patterned photoresist thin films with a crosslinking gradient.* Soft Matter, 2013. **9**(46): p. 11007-11013.

74. Yin, J. and C. Lu, *Hierarchical surface wrinkles directed by wrinkled templates.* Soft Matter, 2012. **8**(24): p. 2528-2534.

75. Zhang, Z., et al., *Strain-Controlled Switching of Hierarchically Wrinkled Surfaces between Superhydrophobicity and Superhydrophilicity*. Langmuir, 2011. **28**(5): p. 2753-2760.

76. Yu, S.-J., et al., *Spontaneous formation of hierarchical wrinkles in Cr films deposited on silicone oil drops with constrained edges.* Physical Review E, 2013. **88**(4): p. 042401.

77. Cao, Y. and J.W. Hutchinson, *Wrinkling Phenomena in Neo-Hookean Film/Substrate Bilayers.* Journal of Applied Mechanics, 2012. **79**(3): p. 031019-9.